AORTIC VALVE MECHANOBIOLOGY – ROLE OF ALTERED HEMODYNAMICS IN MEDIATING AORTIC VALVE INFLAMMATION AND CALCIFICATION

A Thesis

Presented to

The Academic Faculty

by

Swetha Rathan

In Partial Fulfillment

of the Requirements for the Degree

Doctor of Philosophy in the

School of Chemical and Biomolecular Engineering

Georgia Institute of Technology

May 2016

AORTIC VALVE MECHANOBIOLOGY-
ROLE OF ALTERED HEMODYNAMICS IN MEDIATING
AORTIC VALVE INFLAMMATION AND CALCIFICATION

Approved by:

Ajit P. Yoganathan, PhD, Advisor
School of Chemical and Biomolecular Engineering
Georgia Institute of Technology

Hanjoong Jo, PhD
The Wallace H. Coulter Department of Biomedical Engineering
Georgia Institute of Technology and Emory University

W. Robert Taylor, MD, PhD
The Wallace H. Coulter Department of Biomedical Engineering
Georgia Institute of Technology and Emory University

Robert M. Nerem, PhD
School of Chemical and Biomolecular Engineering
Georgia Institute of Technology

Julie A. Champion, PhD
School of Chemical and Biomolecular Engineering
Georgia Institute of Technology

Date Approved: 09/29/2015

This thesis is dedicated to Mom,
Dad, Swathi and Sai Kiran.

ACKNOWLEDGEMENTS

Firstly, I thank my parents Vijayasree and Ram Prasad, and siblings Swathi and Sai Kiran for their unconditional love and encouragement. I thank my fiancé Vamsi for always being supportive. His constant motivation helped me survive the tough times in grad school. I feel fortunate to have my extended family Shashi, Sapna, Kapil, and Archana here in US. I cannot thank them enough for their support. My cute little niece Ananya and nephew Pranav are my most favorite stress busters.

I thank my thesis advisor Dr. Ajit P. Yoganathan for picking me into his world famous CFM lab and allowing me to pursue my interest and passion as a graduate student. I feel grateful to him for introducing me to the exciting field of valve biology and a wide-range of translational biomedical research. Being a chemical engineer, biological research was definitely not my comfort zone. But, I am actually amazed at the confidence he had in me as a fresh graduate student, when he assigned me the heart valve mechanobiology project. Thanks to him, I met several great scientists in the field of biomedical engineering and was able to travel to different parts of the world to present my research. His advisement played an important role in my professional development. He always emphasized on striving for excellence and encouraged me to do my best. I am better for having worked with him. Also special thanks to his family Tripti, Anila and Aadi

for inviting me to Diwali and Christmas parties every year, which always made me feel at home.

I thank all my committee members for their guidance in pursuing the research during my doctoral program. Their recommendation letters for my AHA fellowship and job applications are invaluable. Special thanks to Dr. Hanjoong Jo and Dr. Robert Nerem. Their timely feedback has been extremely instrumental in shaping my thesis. Besides, I will always be grateful to them for letting me work in their labs whenever needed and constantly guide me to be on track. Thanks to Dr. Taylor for encouraging me to look into other aspects of valve calcification. Because of this project, I had an opportunity to work with Dr. Charles O'Neill at Emory University, which has been an amazing experience.

I am grateful to Mr.Holifield for donating porcine hearts. Without his generous donations, this research would not have been possible. I thank my funding sources: American Heart Association pre-doctoral fellowship and National Institute of Health. Also, thanks to Gurley family for their donations to the lab.

Sincere thanks to the administrative staff Janice Whatley, Juanita Freeman, Claudia Clarkson, Sandra Maffey, Pat Jordan, Tracie Dinkins for their help in patiently dealing with my travel and other paper work. Thanks to Sally Gerrish for her career advises. Thanks to IBB core facility staff: Aqua, and Andrew for answering my innumerable questions with regards to histology and microscopy.

Thanks to Steve Woodard and Julian Dorsey for their efforts in putting together the new core facility at TEP. Special thanks to the ChBE machine shop crew: Jeff Andrews and Bradley Parker, ME electrical engineer: Kyle French, VWR stockroom sales reps: Jason Robinson and Kevin Brantley.

Thanks to all my wonderful friends in CFM lab and Jo lab, who patiently reviewed this thesis and had invaluable feedback/ revisions to refine it further. I also made some good friends in this lab especially Elaine, Ikay, Milan, Eric, Joan, Maria, Vrishank, Yap, Tim, Prem, Phillip, Charlie, Shiva, Neela, Lucia, Arvind, Paul, Ewa, Mike, Brian, Min, Diana, Kartik(s) and Alan. These folks made my stay in lab more enjoyable and memorable. Most importantly Elaine and Ikay have been my rock. Eric's constant reminders to take iron pills definitely helped me stay healthy. I also want to thank Jo lab members for teaching me all the biology stuff, especially Casey, Randy, Sandeep, Rachel, and Jessy. I want to thank my diligent undergraduate students: Harika, Anita, Samiya, Ruth, Shan, Heesu, Elsa, Pouria and tech temps Laurel and Ann. Without their help, I am sure I would have taken longer to finish this thesis. Thanks to Anastassia, Alex and Julia, who always had time for a quick chat during coffee/tea breaks.

I want to thank all my wonderful roommates especially Anupama, Swathi, Dharani, Anusha, Prajakta, Hima, Anita, Sonali and Keerthi for being so supportive. Special thanks to Vishy, Sandeep, Bala, Bhanu, Bhanupriya, Ketki, Sricharan, Lina, Loice, Haider, Rajiv, Prasad, Swapna, CV, Aravind, Ranjini and

Anirudh. I also want to thank my friends in India: Hima Bindu, Krishna and Shashank for all the love and support. Last but not the least, I want to thank God for all the strength and guidance in ways I have never imagined.

TABLE OF CONTENTS

LIST OF TABLES

LIST OF FIGURES

LIST OF SYMBOLS AND ABBREVIATIONS

18S	Ribosomal RNA
5HT	5-hydroxytryptamine
ALP	Alkaline phosphatase
AR	Aortic regurgitation
AS	Aortic stenosis
ATP	Adenosine triphosphate
AV	aortic valve
BCL2L11	BCL2 like 11 (apoptosis facilitator)
BMP	Bone morphogenic protein
BSA	Bovine serum albumin
CKD	Chronic kidney disease
Col1a1	Collagen type 1
CTNNB1	Catherin-associated protein, Beta1
DAPI	4', 6-Diamidino-2-phenylindole
DEPC	Diethyl pyrocarbonate
DMEM	Dulbecco's modified eagle medium
DNA	Deoxyribonucleic acid
DPBS	Dulbecco's phosphate buffered saline
EC	Endothelial cell
ECM	Extracellular matrix
Endo-MT	Endothelial to mesenchymal transition
Enos	Endothelial nitric oxide synthase 3
ENPP1	Ectonucleotide pyrophosphatase/phosphodiesterase 1
F	Fibrosa

GAGs	Glycosaminoglycans
HAVEC	Human aortic valve endothelial cells
HBSS	Hank's balanced buffer solution
HUVEC	Human umbilical vein endothelial cells
IC	Interstitial cell
ICAM1	Intercellular adhesion molecule 1
IP	Inorganic pyrophosphatase
KLF4	Kruppel-like factor 4
LDL	Low density lipoprotein
LDV	Laser doppler velocimetry
LS	Unidirectional pulsatile shear stress
MAPK	Mitogen activated protein kinase
MCP1/CCL2	Monocyte chemoattractant protein 1
MGP	Matrix γ-carboxyglutamic acid Gla protein
miRNA	Micro ribonucleic acid
MMP	Matrix metalloproteinase
mRNA	Messenger ribonucleic acid
MTT	Methylthiazoletetrazolium
NF-κB	Nuclear factor Kappa B
ob	Osteoblast
OCT	Optimal cutting temperature
OS	Oscillatory shear stress
PFA	Paraformaldehyde
PKA	Protein kinase A
PPi	Inorganic pyrophosphate
RISC	RNA-induced silencing complex

RNU6B	Small nuclear ribonucleic acid
RT-qPCR	Real-time quantitative polymerase chain reaction
RUNX2	Runt-related transcription factor 2
S	Spongiosa
SMA	Alpha smooth muscle actin
TGF-β1	Transforming growth factor beta 1
TIMP	Tissue inhibitor of matrix metalloproteinase
TNAP	Tissue non-specific alkaline phosphatase
TNFα	Tumor necrosis factor-alpha
tRNA	Transfer ribonucleic acid
TUNEL	Terminal deoxynucleotidyl transferase mediated dUTP Nick End Labeling
UDP	Uridine-5'-diphosphate
V	Ventricularis
VCAM1	Vascular adhesion molecule 1
VE-Cadherin	Vascular endothelial cadherin
VEC	Aortic valve endothelial cell
VIC	Aortic valve interstitial cell
VSMC	Vascular smooth muscle cell
vWF	von Willebrand Factor

SUMMARY

Calcific aortic valve (AV) disease is a progressive disease that ranges from mild thickening (sclerosis) to severe calcification with impaired leaflet motion (stenosis) (*1*). AV calcification is a multifactorial disease involving different types of calcification, including inflammation-driven calcification (*2*), ectopic calcification (*3, 4*), and passive accumulation of hydroxyapatite crystals (*5, 6*). AV calcification is one of the major causes of cardiovascular related deaths and shares the risk factors associated with atherosclerosis of blood vessels (*7, 8*). Calcified AVs show signs of endothelial injury, extensive lipid deposition, fractured extracellular matrix fibers and inflammation. These markers occur preferentially in the fibrosa side of the valve(*9*). This side dependency can be attributed to the mechanical environment, matrix composition, and underlying gene expression that differ on either side of the valve (*10*).

The objective of this dissertation was to understand the molecular mechanisms involved in this side-dependent calcific AV disease. We hypothesized that *"sclerosis, inflammation, and calcification preferentially occur in the fibrosa compared to the ventricularis due to differential gene expression and oscillatory shear stress".* Using an *ex vivo* approach and porcine AVs, three specific aims were designed to test this hypothesis: 1) to identify side- and shear-dependent microRNAs (miRNA) involved in AV sclerosis, inflammation and calcification, 2) to determine the relationship between a key side- and shear-dependent miRNA

and AV pathogenesis, and 3) to investigate the role of pyrophosphate in AV calcification. Aims 1 and 2 addressed the shear-dependent mechanisms while Aim 3 focused on the chemical imbalance aspect of side-specific AV pathogenesis.

In aim 1, we developed a side-dependent sclerosis and calcification model of AV disease and used it to identify the miRNAs and mRNAs that are potentially involved. We showed that low magnitude oscillatory shear stress (OS) induced changes in the ECM (increased collagen crimping, disrupted elastin fibers), and increased thickness of the fibrosa layer and collagen turnover consistent with the characteristic features in the fibrosa of sclerotic and calcified valves (*9, 11*). We also showed that two out of four side-dependent miRNAs, miR-181a and miR-214 showed significantly higher expression in the fibrosa compared to the ventricularis in the presence of OS. We performed a bioinformatics analysis and identified 26 and 16 potential side- and shear-dependent targets of miR-181a and miR-214, respectively. These filtered targets are well known for their involvement in AV pathogenesis. Since miR-214 is associated with fibrosis (*12, 13*), inflammation, osteogenic differentiation (*14*) and coronary artery disease (*15*), we reported that miR-214 could be a key side- and shear-dependent miRNA involved in calcific AV disease.

In aim 2, we chose to investigate the functional role of miR-214 in AV pathogenesis. Five potential target genes (*Klf4, Enos*, *Ctnnb1*, *Bcl2l11, Sma*)

showed an inverse relationship with miR-214 in the fibrosa when exposed to OS. Further a down regulating trend of these markers in the fibrosa when exposed to OS is indicative of the OS induced pro-inflammatory environment. We developed an *ex vivo* miRNA silencing protocol and knocked down the expression of miR-214. Silencing miR-214 in the fibrosa exposed to OS, significantly upregulated *Klf4* while downregulating *Tgfβ1*. Silencing of miR-214 alone, however, was not sufficient to affect AV inflammation and calcification in fibrosa exposed to OS. This suggests the possibility that other miRNAs and cytokines may be involved. This work shows that miR-214 could be involved in OS induced AV endothelial-to-mesenchymal transition and fibrosis by regulating *Klf4* and *Tgfβ1* in a side- and shear-dependent manner.

In aim 3, we developed an *ex vivo* AV calcification model to understand the role of an endogenous inhibitor (pyrophosphate, PPi) of calcification. Freshly isolated porcine AV leaflets were cultured in serum-free medium under static conditions for up to 8 days. As a result, calcification occurred predominantly in the fibrosa side, and required both a high phosphate concentration (3.8 mM) and removal of PPi with alkaline phosphatase (ALP) or inorganic pyrophosphatase (IP). Calcification was arrested by etidronate (bisphosphonate), a non-hydrolyzable analog of PPi. AV leaflets actively produced PPi when the tissue non-specific alkaline phosphatase (TNAP) was inhibited. The AV leaflets also synthesized PPi from extracellular ATP, which was reduced by β, γ-methylene-ATP, an inhibitor of ENPP1. We thus showed that the extracellular PPi is a key endogenous inhibitor

of calcification and its levels appear to be controlled through synthesis by ENPP1 and hydrolysis by TNAP. Future investigations on preventative therapeutics to treat AV disease could be similarly based on bisphosphonates or inhibitors of TNAP.

In conclusion, we determined the side- and shear-dependent miRNAs (miR-214 and miR-181a), which may serve as master regulators of AV biology and disease. Further, we began to understand the role of miR-214 in regulating targets that are involved in tissue remodeling, inflammation and calcification, processes that lead to calcific AV disease. We also demonstrated the potential of synthetic analogs of PPi for use as a drug to inhibit AV calcification. These findings improve our current understanding of the molecular mechanisms involved in AV inflammation and calcification. Moreover, based on these findings, we have proposed hypotheses and research directions that emphasize the great potential of this field.

CHAPTER 1 INTRODUCTION

Calcification of AV results in stenosis and regurgitation that requires clinical intervention when detected(*16*). To date, the gross pathological changes and surgical treatments of sclerotic valves have received much attention while the molecular mechanisms underlying AV disease have not been well studied or understood. Further, identification of biomarkers that can be used to detect early stage AV disease is also understudied but vital to successfully preventing and/or treating AV disease. This work focuses on understanding the mechanobiology of AV disease, particularly the role of adverse patterns of shear stresses *ex vivo*.

This work mainly focuses on identifying the shear-dependent miRNA(s) and mRNAs that are associated with the AV disease *ex vivo*. The functional studies carried out in this work aim to link the mechanosensitive miRNAs to the genes involved in inflammation, endothelial-to-mesenchymal transition, and cell apoptosis etc, which eventually causes AV leaflets to calcify. These mechanosensitive miRNAs could be potentially used as disease biomarkers and in the development of drugs for non-surgical treatments.

Moreover, this work also aims to evaluate the role of shear stresses in inducing side-dependent AV calcification. This particular study allows us to understand the extent of calcification induced by shear stresses compared to that of pathological stretch (*17*) and pressure. Further, an *ex vivo* AV calcification model was also

developed to understand the role of endogenous pro- and anti-calcification factors, such as inorganic pyrophosphate, orthophosphate, and alkaline phosphatase.

This chapter discusses the relevant background and the clinical rationale for this thesis work. Initial sections are focused on the anatomy, hemodynamics, and cellular components of the AV. A section is also dedicated to highlight the prevalence and significance of calcific AV disease and its molecular pathways. The next subsections outline the literature review on the micromechanical environment experienced by the valve and mechanobiology (stretch, shear and pressure) with respect to the degenerative AV disease. The final section will discuss the miRNAs and their function in the cardiovascular system. In CHAPTER 2, the rationale for this research and the hypothesis is discussed. The specific aims designed to test this hypothesis are also discussed. The next three chapters address each specific aim in detail. The approach, methodology, results, discussion, conclusions and limitations of each specific aim are discussed in detail. Briefly, in CHAPTER 3, the side- and shear-specific miRNAs involved in AV pathogenesis are identified and in CHAPTER 4, the relationship between a key miRNA, miR-214 and AV pathogenesis is investigated. CHAPTER 5 determines the role of pyrophosphate, an endogenous inhibitor of calcification in AV ectopic calcification. In CHAPTER 6, all the key results are discussed in the context of the overall rationale and hypothesis of this thesis work. CHAPTER 7 presents the conclusions of this research work and the potential impact of this

thesis work. With CHAPTER 8, this dissertation concludes with the recommendations and the future work based on the findings in this thesis work.

1.1 Aortic valve anatomy

The aortic valve is one of the semilunar or outflow tract valves of the heart and regulates the blood flow direction between the left ventricle and aorta. A healthy AV (Figure 1.1) is comprised of three semilunar cusps, each of which is attached to the fibrous annulus ring at the base. Directly behind each cusp is an elliptical depression called the sinus of valsalva or aortic sinuses. Two of the sinuses give rise to coronary arteries that branch off the aorta, providing blood supply to the heart itself. The AV sinuses and the corresponding valve leaflets are named according to the presence of the coronaries. The sinuses with the right and left coronary artery ostium are known as the right and left coronary sinuses respectively, and the corresponding leaflets are known as right and left coronary leaflets. The sinus without any coronary attachment is the non-coronary sinus, and the associated leaflet is the non-coronary leaflet. The superior base of the leaflet is connected to the valve commissure, which inserts into the surrounding aortic root. The aortic valve commissures provide load-bearing support to the leaflets when they are closed to resist high transvalvular pressures.

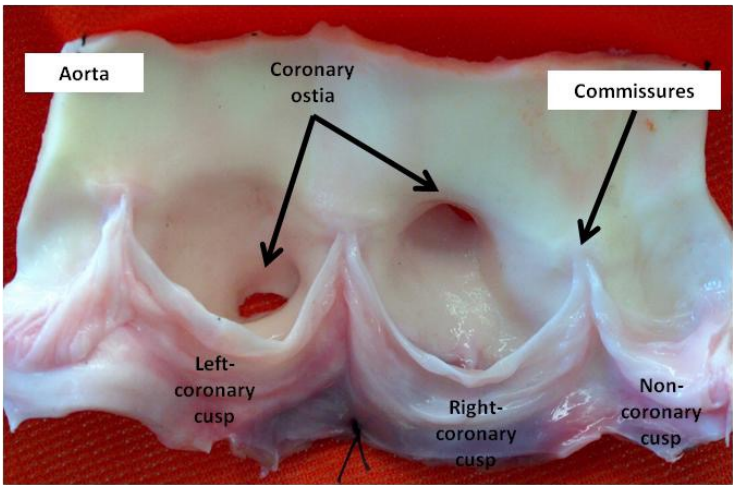

Figure 1.1 The AV, cut open along the axial line demonstrating the anatomy of the valve (*18*).

1.2 Aortic valve hemodynamics

The structure and function of the AV is influenced by its surrounding hemodynamics and mechanical microenvironment as shown in the Figure 1.2. At the beginning of systole, the valve leaflets rapidly open, and blood accelerates through the valve with a positive gradient (higher pressure upstream in the ventricle than downstream in the aorta). Forward flow velocities are at their peak value of 1.35 $\pm$ 0.35 m/s (*19*), during the first third of systole. At the end of systole, when the ventricular pressure drops below aortic pressure, the valve starts to close as the forward flow begins to decelerate to zero, with very little flow reversal. The adverse axial pressure difference across the valve causes the low inertia flow in the developing boundary layer along the aortic wall to decelerate, and then to reverse direction resulting in vortices in the sinuses behind the AV leaflets. This action forces the leaflet tips towards a closed position, resulting in a very fast and efficient closure of the leaflets. During

diastole, when the left ventricle relaxes, the valve remains completely closed. The flow patterns in the outflow tract of the valve depend on the valve geometry and can be used to evaluate the function and health of the valve (*20*). Thus, the AV is a highly dynamic organ, opening and closing approximately one billion times during the average human lifetime, experiencing transvalvular pressures, pulsatile and oscillatory shear stresses, as well as bending and axial stress (Figure 1.2).

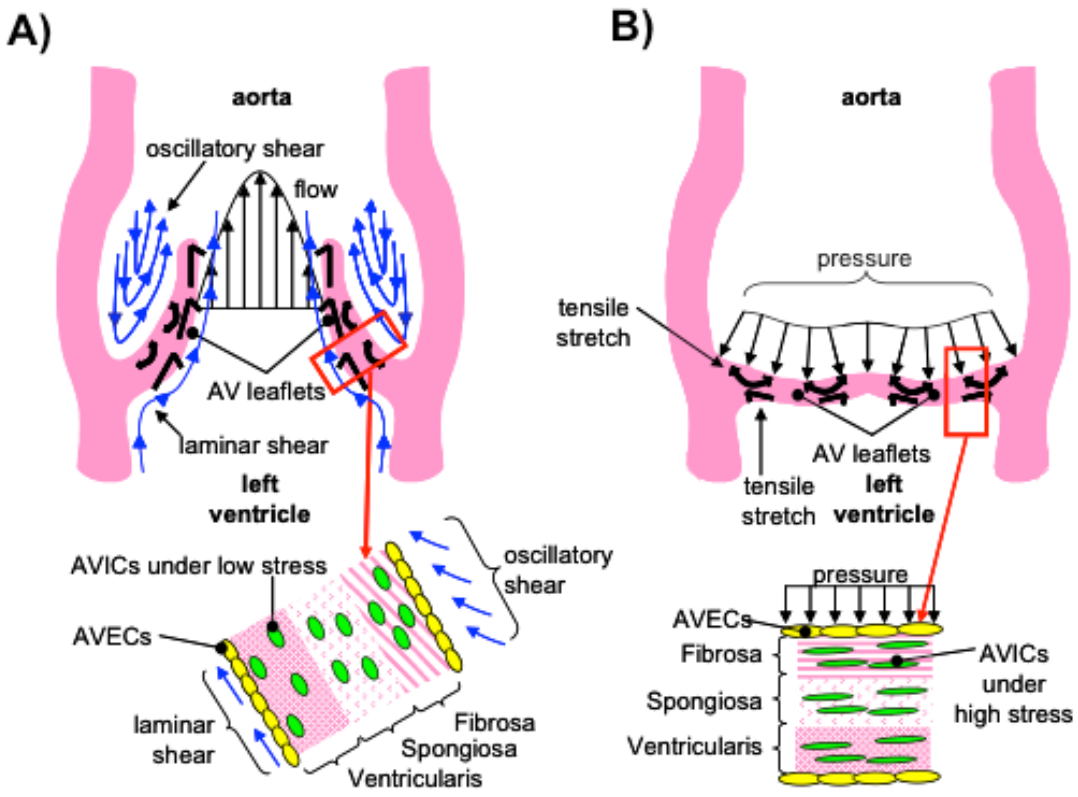

Figure 1.2 Schematic of different mechanical stimuli experienced by the AV during a cardiac cycle: a) Systolic mechanical forces, b) Diastolic mechanical forces.

1.3 Aortic valve tissue structure and cell types

Each aortic valve leaflet cusp is comprised of three layers: fibrosa - facing the aorta; ventricularis - facing the left ventricle; and spongiosa - the layer between the fibrosa and ventricularis (Figure 1.3A). These three layers vary in their organization of extracellular matrix (ECM) components (collagen and elastin), especially along the radial direction. The fibrosa is predominantly made of type I fibrillar collagen that is arranged in circumferential direction in parallel bundles, surrounded by a matrix of elastins. The ventricularis is mostly comprised of elastin fibers oriented along the radial direction, while the spongiosa is primarily made up of glycosaminoglycans, which act as shock absorbers and provide the deformability function of the valve leaflets (*21*).

The AV leaflets are composed of two cell types - interstitial cells (ICs), which make up the majority of the valve, and endothelial cells (ECs), which line the AV along the fibrosa as well as the ventricularis. The ECs form single cell monolayers, express Von Willebrand factor, produce vasoactive agents such as endothelin-1 and nitric oxide, and exhibit prostacyclin activity. The ICs are a heterogeneous (three phenotypes: myofibroblasts, fibroblasts, smooth muscle cell like phenotype) and dynamic population of cells responsible for the constant renewal of ECM (*21*). The ICs play a critical role in normal functioning of the

valve and in the initiation and progression of valve pathology. Both complex genetic programming as well as local hemodynamic factors such as leaflet strain and surface shear stresses influences the phenotype of ICs. Human AV ECs align parallel to the direction of the flow (*22*), although this alignment has been observed to be species specific because the porcine AV ECs align perpendicular to the direction of blood flow (*23*). Valvular ECs share some similarities with vascular ECs in terms of responses to mechanical stimuli, however they are genetically different and have a higher propensity to undergo endothelial to mesenchymal transition.

Aortic valve ECs on either side of the leaflets show differential gene expression profiles, which could be attributed to the conditioning due to different microenvironments on either side. Particularly, the genes that inhibit local and global calcification such as OPG, CNP, PTH, chordin etc., are expressed at significantly lower levels on the fibrosa endothelium compared to that on the ventricularis, indicating that fibrosa has a higher susceptibility to calcify. On the contrary, fibrosa endothelium also shows higher expression of the antioxidative markers such as MGST2, NOS3, PRDX2 etc., which could be protecting the fibrosa from oxidative stress induced inflammation (*24*). Interestingly, the ECs on fibrosa are characterized by an elongated shape and are more compliant than that on the ventricularis side, and are attributed to the stiffness of the underlying ECM (*25*).

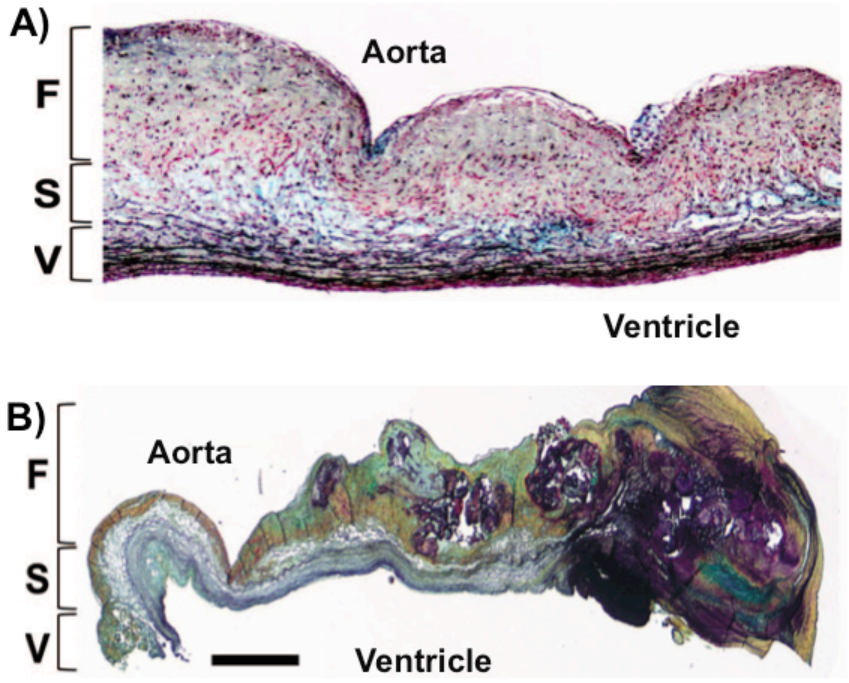

Figure 1.3 AV structure and composition.
A) Trilayered structure of the healthy porcine AV consisting of fibrosa (F), spongiosa (S), and ventricularis (V). B) A calcified human AV showing obvious signs of altered ECM, preferentially on the fibrosa (F) (*26*).

1.4 Aortic valve disease: prevalence and clinical significance

A normally functioning AV ensures the uni-directionality of blood flow from the left ventricle to aorta, with physiological hemodynamics. Abnormalities of the valve (Figure 1.3B) arise due to a variety of risk factors such as hypertension, high LDL content, old age, hyperphosphatemia, diabetes, obesity, smoking etc (*27*). These abnormalities of valve range from mild thickening to severe calcification with impaired leaflet motion (Figure 1.4). AV stenosis refers to narrowing of the AV opening during systole and leads to greater pressure gradient across the valve (*28*) AV stenosis is caused by both age-related progressive calcification and

congenital malformations such as bicuspid AV (BAV), a congenital condition occurring in 1-2% of all live births (*29*). Elevated levels of turbulence measured downstream of the stenosed valve are enough to cause significant damage to the endothelial layer of ascending aorta (*30*). The classic symptoms of the AS are syncope, angina and congestive heart failure.

Aortic regurgitation (AR) is a condition when there is a backflow of the blood into the left ventricle. Around 50% of the cases of aortic insufficiency are due to dilatation of the aortic root, which is idiopathic in most instances. In about 15% of regurgitation cases, the cause is innate BAV, while another 15% of the cases are due to retraction of the cusps as part of post-inflammatory processes of endocarditis in rheumatic fever and various collagen vascular diseases (*31*).

Thus, calcific AV disease is a strong risk factor for cardiovascular related deaths (*9, 32, 33*) and is a significant source of mortality worldwide, with the number of patients requiring AV surgery expected to triple from 250,000 to 850,000 by 2050 (*34*). The most common forms of the AV disease can be distinguished clinically by age at the onset and by their characteristic echocardiographic findings. Currently, one of the viable options is to treat AV disease is to surgically replace the diseased valve with a mechanical or biological valve. Recent developments are aimed towards the use of transcather AV replacement of the diseased valve, especially in elderly patients who are not qualified for a surgery. However, as of now, no proven medical therapies exist for the treatment of calcified AV leaflets.

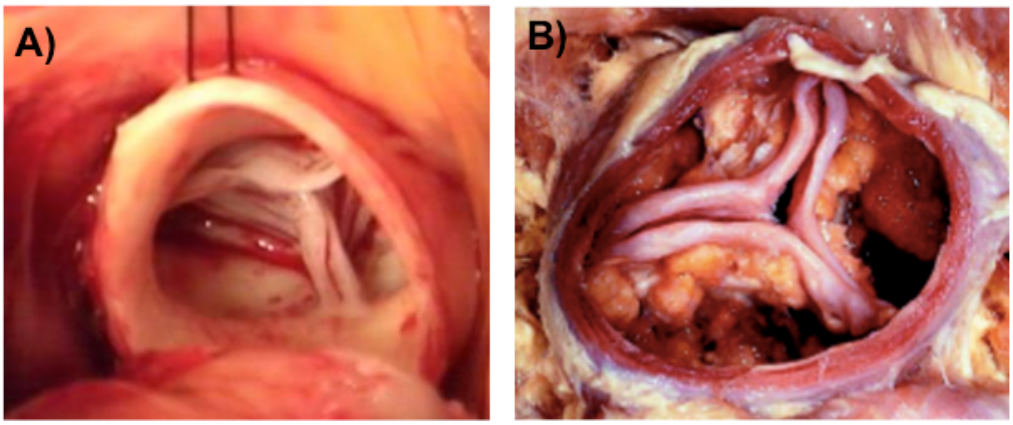

Figure 1.4 Native and diseased AV.
A) Healthy AV and B) Severely calcified AV (adapted from deptmed.queensu.ca/blog/?p=248).

1.5 Aortic valve pathology

1.5.1 Molecular pathways

Calcific AV disease is a slowly progressive disorder with a disease continuum that ranges from mild thickening of the valve to severe calcification with impaired leaflet motion. Calcification of the AV is a side-dependent disease, preferentially occurring on the fibrosa of the AV. It is typically characterized by inflammation, fractured matrix fibers, thrombus formations, sclerotic and calcific lesions (Figure 1.3). The cellular and molecular events leading to AV disease are interdependent and entwined with extracellular matrix maladaptation. Endothelial dysfunction or leakage is speculated to be one of the first events triggered when VECs are subjected to an insult, be it abnormal hemodynamics or mechanical stress or pathological injury (Figure 1.5) (*35*). Mechanotransducers in the extracellular

matrix transmit these stimuli to the quiescent VICs (qVICs), and activate them. Following this activation is the deposition of low density lipoprotein (LDL) particles, infiltration of inflammatory cells, and release of inflammatory cytokines. These events lead to abnormal collagen synthesis and ECM remodeling by collagenases, matrix metalloproteinases (MMPs) and tissue inhibitors of matrix metalloproteinases (TIMPs), cathepsins (*36*). Hyperphosphatemia, a condition seen in CKD, upregulates the expression of Runx2/ Cbfa-1, an osteogenic transcription factor (*37*). In the presence of such factors, cells exhibit markers of the osteogenic or chondrogenic lineage, resulting in osteoblast VICs (obVICs) that actively participate in the valve calcification process. In addition, hyperphosphatemia enhances production of apoptotic bodies and matrix vesicles that nucleate vascular mineral deposition (*38*). The transforming growth factor (TGF)-β/ TGF-like cytokine and TGF-β1 can also enhance the osteogenic phenotype (*17*). On the other hand, Fetuin-A, an abundant plasma protein prevents extracellular and intravesicular basic calcium phosphate growth in matrix vesicles and thus reduces calcium-induced apoptosis in vascular smooth muscle cells. In the absence of extracellular Fetuin-A, cells fail to properly handle a high mineral load because of elevated extracellular calcium phosphate and succumb to apoptosis (*39*). Apoptotic bodies containing high amounts of mineral-like matrix vesicles readily mineralize and form a potent nidus for further extracellular matrix calcification. Unlike matrix vesicle mediated mineralization, AB-mediated mineralization does not require alkaline phosphatase and annexins**.** Apart from TGF-β1 and BMP family, other pathways that can promote the

transcription by RunX2 are Mitogen activated protein kinase (MAPK) and Protein Kinase-A (PKA) pathways, indicating that RUNX2 is a focal point for the integration of a variety of signals affecting osteoblast activity (*40*).

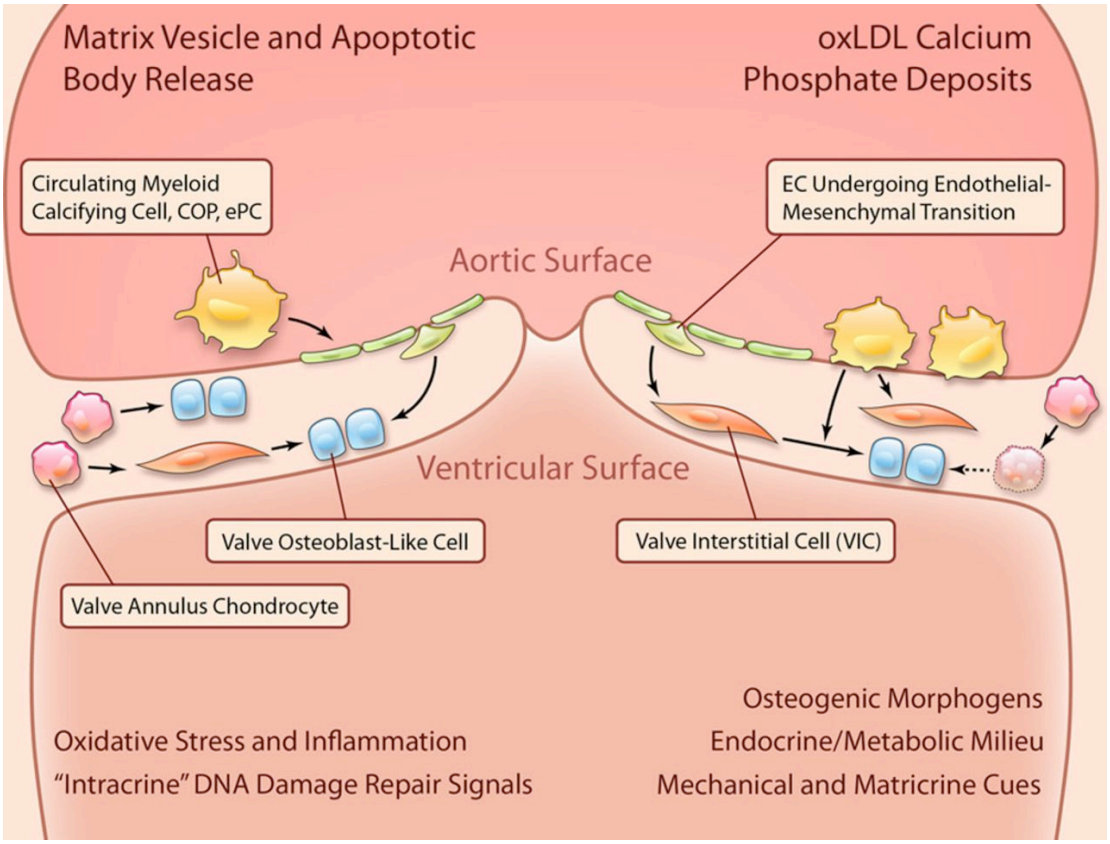

Figure 1.5 Molecular mechanisms involved in AV disease.
The osteogenic differentiation of the valve cells can be initiated by a myriad of sources such as endothelial mesenchymal transition of ECs, circulating macrophages, trans-differentiation of the valve ICs into osteoblast like phenotype to name a few (*41*).

1.5.2 Soft tissue calcification

There are distinct types of calcification processes identified in the soft tissues (vessels, valves) and the end result of all these calcification processes is the same, which is bone formation. From a pathomorphological perspective (*5*),

calcification can be distinguished into four types on the basis of location, association with plaque, and mode of formation: 1) Dystrophic or passive calcification (minor form of widespread non-specific organ and soft tissue calcification as a result of abnormal Ca/P products) 2) Calcification of cardiac valves, 3) Calcification in arterial intimal layers in association with macrophages, lipids and vascular smooth muscle cells (VSMCs) as in classical atherosclerosis, popularly referred as intimal calcification, and 4) Calcification in arterial medial layers as a result of elastin fiber mineralization, VSMCs degeneration, and upregulation of osteogenic programs as in chronic kidney disease or diabetes, popularly referred as medial calcification. The last three types of calcification are all occur in the absence of raised Ca/P levels and are actively regulated mechanisms, which require complex regulatory networks that involve 1) Positive and negative regulators; 2) temporal expression or activation of modulators; 3) multiple amplification or suppressive feedback loops that orchestrate cell recruitment, differentiation, function, survival, and interactions with other cells or matrix molecules. Osteopontin, osteoprotegerin (inhibitor of osteoclastogenesis), matrix-gla protein, Fetuin A, inorganic pyrophosphate that prevent calcification and tissue non specific alkaline phosphatase, receptor activator of NF-KB (induces maturation of osteoclast progenitors) or NF-KB ligand are some of the compounds that play a major role in promoting calcification (*4*). Intraperitoneal delivery of PPi for duration of a few hours can inhibit aortic calcification in uremia without affecting the bone formation (*42*). Thus, by understanding mechanisms underlying calcification, it is feasible to slow down the progression of calcification.

1.6 Aortic valve mechanobiology

AV degradation is not a passive process brought about by wear and tear due to aging but an active process involving perturbation of valvular ECs and ICs by the local mechanical forces such as strain, shear, and transvalvular pressure (*43*). *Ex vivo* studies have shown that different mechanical forces act in synergy to modulate and maintain a normal cellular phenotype. Another important aspect of AV cellular mechanobiology is the interactions between ECs and ICs. There are relatively few co-culture studies performed on AV cells or tissues. Butcher et al. developed a 3D model of the AV leaflet comprising both ICs and ECs and determined the cellular responses when exposed to different luminal flow patterns and suggested that ECs are necessary to regulate the ICs phenotype and ECM synthesis (*44*). The significance of interactions between ECM and valvular cells has been investigated as well. The following sections describe individual mechanical stimuli experienced by the native AV, under normal and pathological conditions, with an emphasis on their relevance to AV mechanobiology.

1.6.1 Shear stress

Physiologically, shear stress occurs on AV leaflet surface due to friction with flowing blood. Shear stresses experienced by the AV depend on flow conditions through the valve as well as cyclic dynamic leaflet motion. Shear stresses directly affect the ECs lining each valve cusp, which in turn transmit the signal to the underlying matrix and ICs. Different shear stress patterns are known to elicit different EC responses, and disturbed flow has been shown to promote cell

proliferation, as well as morphology and gene expression dissimilar to laminar flow in ECs (*45*). Further, shear stresses on the valve can also change with developing pathology. Thus, an accurate estimation of shear stresses experienced by the AV under both physiological and pathological hemodynamics is critical for mechanobiology studies.

Fluid mechanics of AV such as flow profiles, Reynolds shear stresses, and turbulence characteristics, have been estimated using both experimental techniques (laser doppler velocimetry, hot film anemometry, PIV, MRI, doppler ultrasound) as well as computational modeling (*46-49*). Recently, Yap et al. measured shear stresses on both the fibrosa and ventricularis of the leaflet using two-component Laser Doppler Velocimetry. The ventricularis shear stress resembled a half-sinusoid during systole with peak magnitude of 64-71 dyn/cm^{2,} and the direction of this shear reversed during late systole with a significant magnitude of 40-51 dyn/cm^2. In contrary to the popular belief, fibrosa do not experience oscillatory shear stress profile, rather a profile similar to a half sine wave with little or no reverse flow, with a magnitude of up to 20dyn/cm^2. These shear stresses are dependent on cardiac output and heart rate. As alterations in the hemodynamics such as high heart rate and low cardiac output have been shown to affect several stages of cardiovascular disease continuum such as endothelial dysfunction, plaque rupture and myocardial infarction, the shear stresses under these altered conditions can be used in mechanobiology studies to gain more insights into AV pathobiology.

A growing body of evidence suggests that the morphology of BAV can lead to adverse hemodynamics both near the valve as well as in the ascending aorta resulting in turbulence and higher leaflet surface shear stresses compared to that of normal TAV (*30, 50*). Both systolic and diastolic shear stresses were higher on non-fused leaflet than the fused leaflet. Although genetic factors have been implicated in the formation of BAVs, this altered microenvironment due to the BAV morphology itself could be the reason behind accelerated progression of the disease condition.

1.6.2 Shear stress: mechanobiology

Shear stress regulates expression of proteins in ECs that control many opposing functions such as vasodilation and vasoconstriction, thrombo-resistance and thrombogenesis, and normal cell morphology and atherosclerosis. The morphological changes of ECs under shear were induced by the assembly and re-orientation of the stress fibers, accompanied by translocation and remodeling of cell substrate adhesion complexes, and transient formation of punctate cell-cell adherent junctions, that may signal the nucleus to elicit a specific cellular response. Several studies have characterized the role of shear stresses on vascular biology and indicated that low and oscillatory shear stress is atheroprone; whereas, high shear is atheroprotective (*45*). It is also speculated that the reduced shear stresses on the non-coronary leaflet of the AV due to the lack of coronary flow is responsible for the increased susceptibility to calcification of that leaflet (*1*).

Although AV stenosis may be akin to atherosclerosis, there exist distinct differences in the phenotypes of both the cell types, warranting further studies on AV cells and its biology. Further, compared to vasculature, there have been very few studies on the effects of shear stress on AV. Two types of shear stress bioreactors – parallel plate system (*51*) and cone and plate viscometer (*52*) have have been used thus far to investigate the role of shear stress in AV biology and pathobiology, both *in vitro* and *ex vivo*. The parallel plate system is typically used to apply a uniform laminar shear stress while the cone and plate device can be used to impose uni-directional laminar shear or oscillatory and much more complex shear stress variations. Recently Sun et al. refined the design of the original cone and plate device to be able to expose either sides of AV to different shear stresses simultaneously that closely mimics the *in vivo* scenario (*53*). Using parallel plate flow chamber, earlier studies clearly demonstrated that changes in shear stress patterns (steady or pulsatile) are capable of affecting the ECM protease and protein turnover balance in short durations (*51, 54*).

As discussed in the previous section, the magnitude and nature of shear stress experienced by either side of the valve differs greatly and is perhaps responsible for the differential gene transcription profiles observed in healthy, porcine AVs (*24*). Gene profiling of porcine AV ECs showed that the expression of protective markers such as osteoprotegerin (key regulator of inflammation), parathyroid hormone (regulates Ca+2 level and osteogenesis), c-type natriuretic peptide (cardiac and smooth muscle cell growth regulator) and chordin (BMP antagonist)

that regulate the ectopic calcification were relatively low on fibrosa suggesting that fibrosa is more prone to disease initiation compared to ventricularis. This difference is more pronounced in the calcified valves, where the expression of the markers related to canonical BMP pathway such as phosphorylated SMAD-1/5/8 were found to be higher on the fibrosa endothelium corroborating the fact that fibrosa is more prone to disease initiation and progression (*55*). Side- and shear-specific expression on fibrosa side was also seen in response to altered shear stresses, where inflammation markers such as VCAM-1, ICAM-1, TGFβ-1, and BMP-2, 4 were significantly upregulated compared to ventricularis and were detected in the endothelial and sub-endothelial regions . Expression of these markers on fibrosa endothelium in the presence of altered shear stresses indicates that the disease initiation could be side-specific and shear-dependent and could be potentially mediated by BMP-dependent pathway. Holliday et al. investigated the side- and shear-dependent miRNA and mRNA expression in human AV ECs and identified some of the mechanosensitive-miRNAs, which were found to be important in remodeling, inflammation, cell proliferation and migration (*22*).

One of the studies that looked at the biological implications of the altered shear stresses due to BAV morphology was by Sun et al. Wall shear stresses experienced by the non-fused leaflet of BAV maintained homeostasis whereas the shear stress of fused leaflet of BAV activated the fibrosa endothelium by up-regulating the expression of ECM proteases, inflammatory markers as well as

osteogenesis related proteins (*56*). These findings demonstrate that altered shear stresses can significantly alter the valve cell phenotype, inducing inflammation, osteogenic differentiation in a side specific manner and thus eventually cause valve degeneration and calcification, apart from the underlying genetic factors.

1.6.3 Stretch

The mechanics of valve tissue is complex with a highly non-linear stress-strain relationship. During the course of each cardiac cycle, the AV undergoes a combination of normal, bending, tensile, compressive, and shear stresses. A majority of these stresses and strains are induced by a complex interplay between blood flow dynamics and valve cusp tissue. The stress distribution in the leaflet is majorly affected by the internal changes induced by strain. Bending stress in AV is both tensile and compressive, with the inflow-side experiencing tensile stress while the outflow-side experiences compressive stress. Indeed, the curvature of the leaflet is integral in ensuring proper coaptation and long-term functionality and viability of the valve cusp (*57*). Ragaert et al. have characterized the flexural mechanical properties of porcine AV leaflets (coronary and non-coronary) using indentation and static rupture tests, and quantified the maximum extension before breaking (~3mm), stiffness (~6N/mm) and maximum load before rupture (~13N) (*58*). Layer specific flexural properties have been extensively studied as well (*59*).

The AV leaflets exhibit anisotropic strain because the collagen in the circumferential direction provides greater tensile strength. Leaflet strain may be rapidly lost as the tissues become less extensible with increasing age. This is primarily because continued collagen fibrillogenesis over the lifetime of an individual increases the diameter of some of the constituent fibrils, requiring greater force to produce the same extension (*60*). This progressively reduces the AV strain with age, with drastic reduction occurring before the age of 25 (*61*). The radial direction, which is mainly composed of elastic fibers, shows higher strain. It has been reported *in vivo* AV leaflet strains are approximately 10% and 40% in the circumferential and radial directions (*62, 63*), respectively and is comparable across different species. Yap et al. measured the strains on porcine AV cusps under different hypertensive pressure conditions in an *ex vivo* flow loop system by tracking markers on leaflet surface using stereo photogrammetry (*64*). In terms of strain profile, the diastolic strain of the leaflets followed the transvalvular pressure gradient and the systolic strain followed the flow curve. These dynamic strain characteristics were used as the reference value for various physiological and pathophysiological *ex vivo* studies from the same investigators, as explained in the next section. Efforts are underway to measure strain in surgically stitched BAV models. Sacks et al. have characterized the biaxial mechanical behavior of fibrosa and ventricularis layers separately and found out that these layers exhibit different nonlinear anisotropic (quasi-elastic) behavior (*65*). The fibrosa behaved similar to the intact native tissue, but less compliant, biaxial loading. They also inferred that the ventricularis dominates the mechanical response of the intact

tissue in the radial direction at higher stress levels. This biomechanics study sheds light on the layer specific properties of the AV leaflets, which is very critical in developing constitutive models of the AV for numerical studies.

Numerical models are gaining prominence in recent times to characterize the stress distribution on native AV leaflets and malformed (bicuspid) leaflets (*66*). Weinberg et al. also developed a multiscale finite element model for comparing BAV and normal TAV and they observed that cellular deformations between these two are not significantly different. Stenotic bicuspid valve experiences more bending strain compared to that of the stenotic tricuspid valve and this strain was more pronounced on the central region of the fused leaflets of BAV (*67*).

1.6.4 Stretch: mechanobiology

Ex vivo and *in vitro s*tretch simulation studies on AV leaflets have been focused on two main areas: Effect of cyclic strain on 1) native leaflets in terms of remodeling, inflammation and calcification markers 2) isolated AV cells loaded in scaffolds, and studying them from tissue engineering perspective. Native porcine AV leaflets when subjected to varying stretch magnitudes, the responses were either biphasic in terms of MMP activity and TIMP expression, or reached a plateau. Elevated cyclic stretch also increased the collagenase and gelatinase activity. However, there was an overall increase in the collagen content with increased stretch levels, pointing out that the leaflets adapt to altered mechanical

loading by either increasing synthesis, or decreasing degradation of collagen (*68*).

In terms of ECM remodeling enzymes, it was observed that cathepsin L expression was reduced by elevated cyclic stretch, while cathepsin S and K expression was increased and similar expression was also observed in stenotic aortic valves (*69*). Further, pathological level of stretch has been shown to induce AV calcification in a BMP-dependent manner (*17*). BMPs have been established as markers in early calcification progression in cultured vascular and valvular cells. It was also observed that the BMP antagonist noggin was able to downregulate the stretch induced osteogenic and calcification events (ALP activity, Runx2 expression and calcium levels in the leaflets). On the other hand, the fibrosis effect of neurotransmitter serotonin (5-hydroxytryptamine, 5HT) on heart valves has been well documented. Peña-Silva et al. reported that elevated serotonin levels can result in increased oxidative stress in the valve cusp potentially leading to stenotic valve disease (*70*). 5-HT-induced valve stiffening may occur throughout the valve cusp resulting in reduced valve curvature and ability of the valve to coapt effectively (*71*).

Cell level cyclic strain studies have been garnering lot of interest from the tissue engineering and regenerative medicine community. These cell level models have progressed from 2D strain (*72*) application to 3D cultures (*73*). Valve fibroblasts in these 3D models have shown cell differentiation and matrix synthesis. Different

substrates (fibrin, collagen based) for tissue engineered heart valves were investigated and their mechanical behavior, fiber orientation and resultant ECM of the construct in response to mechanical conditioning have been reported (*74*). On the other hand, it was found that a synergistic combination of biological (BMP4) and mechanical forces are required to induce the same level of SMA, runx2 and OPN expressions in human valvular ICs populated scaffolds as that of isolated cells (*75*). Butcher et al. demonstrated that cyclic strain induces time dependent (48 hours, 96 hours) valvular IC orientation and collagen alignment, which in turn influenced α-SMA levels (*73*). Recent gene expression studies by Warnock et al. indicated that 15% cyclic strain reduces expression of pro-inflammatory genes by ICs loaded in collagen constructs (*76*). Any other strain value induced inflammatory response by the valvular ICs as measured by inflammatory marker VCAM-1 and mechanosensitive gene OPN. Thus, leaflet strain plays a significant role in maintaining valve phenotype and ECM structure, and when increased, can trigger pathways that lead to AV inflammation and calcification.

1.6.5 Pressure

During the course of a single cardiac cycle, the pressure on the aortic cusps cyclically varies changing the stress and the strain in the leaflet tissue. In healthy individuals, the AV offers negligible resistance to the forward flow of blood (systole) and the pressure drop across the valve is under a few mmHg. In mild stenosis cases, the mean systolic pressure drop is around 20mmHg during

systole. In severe cases, the mean systolic pressure drop is higher than 40mmHg (*77*). During diastole, a closed AV endures a transvalvular pressure gradient of approximately 80-100 mmHg acting normal to the leaflet area. With systemic hypertension, the transvalvular gradient can reach as high as 180-200 mmHg during diastole. This normal force is supported by the AV leaflets' fibrosa layer and transmitted from the collagen fibers to the preferentially aligned ICs (*60, 63*).

1.6.6 Pressure: mechanobiology

Hypertension plays an important role in the initial stages of aortic stenosis as it is found in one-third of patients with symptomatic aortic stenosis. Elevated pressures experienced during mild to severe hypertension increase the mechanical strain experienced by the leaflets and may play a key role in activation of several complex biological networks that induce endothelial dysfunction, altered remodeling, and inflammation (*78*). Apoptosis, ECM composition and stiffness, cell proliferation signaling and adhesion are influenced by pressure and the modulation levels of these processes are mixed depending on the pressure level (*79-82*). However, it is unclear as to how hypertensive pressure is involved in early AV disease pathophysiology.

In vitro studies have progressed from static pressure experiments to investigating the effects of dynamic pressure on AV mechanobiology. One of the early studies that examined the effects of pressure on AV leaflets demonstrated an increase in

pressure decreased the α-SMA expression whereas the isolated pathological stretch on the other hand increased the α-SMA expression (*83*). The opposing effects of stretch and pressure on α-SMA expression therefore suggest that the combined normal physiological hemodynamic forces may act to maintain the quiescent phenotype and prevent expression of activated contractile phenotype which was also shown using a novel *ex vivo* stretch and pressure bioreactor. Calponin and Caldesmon, associated with the actin bundling and polymerization, showed similar trends to that of α-SMA, indicating that these markers play a role in maintaining the valve IC phenotype. Vimentin, a protective cytoskeletal component that provides stiffness, also decreased at combined pathological stretch and pressure, indicating that its protective function may be compromised under pathological conditions. Hypertensive pressure significantly reduced cathepsin L activity and down regulated MMP-2/9 expression moderately, indicating the pressure-dependent regulation of these proteases (*54*), and further, thickness of fibrosa and spongiosa increased relative to ventricularis in case of pathological stretch and pressure conditions, owing to altered ECM remodeling. Warnock et al. investigated the immediate response of the elevated pressure on valve ICs, and found significant up regulation of VCAM-1 (inflammatory marker) and down regulation of osteopontin (endogenous downregulator of ectopic calcification) (*84*). Further, gene array results indicated that approximately 50% of the genes including MMP-1, MMP-3, Interleukin (IL)-6 and Pentraxin-3 that are involved in Tumor necrosis factor (TNF)-alpha network were impacted by the hypertensive conditions. In a separate study by the same

group using AV ICs on collagen constructs, it was found that cyclic strain up regulated the expression of VCAM-1, suggesting that cyclic strain might be a more significant stimulus in evoking this response (*76*). These markers are known to be involved in inflammation, tissue remodeling, and calcification, and indicate that the pathological processes can be triggered due to hypertensive pressures. Thus these studies indicate that hypertensive pressures alter the inflammatory and remodeling responses mediated by valvular ICs, and thus contribute to the AV disease progression.

Although the above studies have investigated the mechanobiological effects of pressure in isolation, it must be noted that pressure causes increased stretch on the leaflets through tensile-compressive and bending forces. Hence, future studies must investigate these two forces in combination, rather than in isolation.

1.6.7 Combined mechanical stimuli: mechanobiology

Independent mechanobiology studies of AV in the presence of each of the isolated mechanical stimuli (shear, stretch or pressure) aid in understanding how each mechanical stimulus plays a role in regulating AV biology and pathology. Knowledge gained from the studies where the AV is subjected to the combined mechanical stimuli, i.e., mimicking its native *in vivo* state is as critical and helps us understand the interplay of each stimulus in regulating the AV health. There have been recent initiatives to study the mechanobiological effects of combined stimuli. One such attempt was made by Konduri et al. using an *ex vivo* pulsatile

organ culture system, subjecting a native AV along with its root to its physiological hemodynamics (*85*). ECM composition (sGAG, elastin and collagen content), cell viability, proliferation as well as the **α-**SMA content were preserved in cultured leaflets. However, under static conditions, a decrease in sGAG, elastin and **α**-SMA content with significant cell death compared to fresh and cultured AVs was seen indicating that mechanical stimuli are indeed required to preserve native composition and function of the AV leaflets. Warnock et al. studied the inflammatory response of AV ICs when subjected to cyclic strain and pressure together (*76*), and found the synergistic response to be different than the individual response in terms of inflammatory markers such as VCAM and OPN mechanosensitive genes. Another group developed a flexure, stretch and flow bioreactor where each of these stimuli can be independently controlled and can be used for studying the mechanobiological responses to physiological and pathological stimuli (*86*). Apart from understanding the effect of complex mechanical stimuli on AV biology, bioreactors like these could potentially be used to mechanically condition the tissue-engineered AVs to develop the natural ECM and also assess the resultant deformations experienced by the valves using real time non-invasive measurement techniques (*87*).

1.7 MicroRNAs and cardiovascular diseases

1.7.1 Biogenesis of microRNAs

MicroRNAs (miRNAs) comprise a novel class of endogenous, small, non-coding RNAs that negatively regulate gene expression via degradation or translational

inhibition of their target mRNAs. The miRNAs are transcribed as long primary transcripts termed pri-miRNAs, which are then trimmed into approximately 70-nucleotide stem loop forms called pre-miRNAs in the nucleus by RNase III type protein, Drosha. After this initial processing, pre-miRNAs are exported to cytoplasm by Exportin-5 and processed to generate 18 to 22 nucleotide mature duplex miRNAs by Dicer, another RNase III type protein. The duplex is then loaded into the miRNA associated multiprotein RNA-induced silencing complex (miRISC), where one strand of miRNA is preferentially retained in the complex and becomes the mature miRNA and the opposite strand, known as the passenger strand miRNA is eliminated from the complex (*88*) (Figure 1.6). Another biogenesis of miRNAs is the mirtron dependent noncanonical pathway and is microprocessor independent (*89*). Mirtrons are a type of miRNAs that arise from spliced out introns and is initiated by splicing and debranching into a pre-miR hairpin, cleaved by Dicer and directly incorporated into silencing complexes. Another possibility is by bypassing the Drosha processing to produce miRNAs by Dicer. Small nucleolar RNAs (snoRNAs), endogenous short-hairpin RNAs (endo-shRNAs) and tRNA precursors also provide a secondary source of pre-miRNAs that is independent of the microprocessor-mediated processing (*90*). Improper functioning or genetic mutation of Drosha or Dicer can impair the miRNA biogenesis (*91, 92*). In order for a miRNAs to regulate mRNAs, the seed region of the miRNAs on 5' end (2 to 8 nucleotides), must have exact base pairing with the 3' untranslated region of mRNAs and partial complementarity with the rest of the mRNA sequence. Mature miRNAs can negatively modulate gene expression

by either degrading or blocking the mRNA depending on the degree of complementarity between the miRNAs and target mRNAs. Also, the upstream and downstream signaling is different for miRNAs as both miRNA-regulator and miRNA-target availability often differs in cells and especially during disease initiation and progression (*93*).

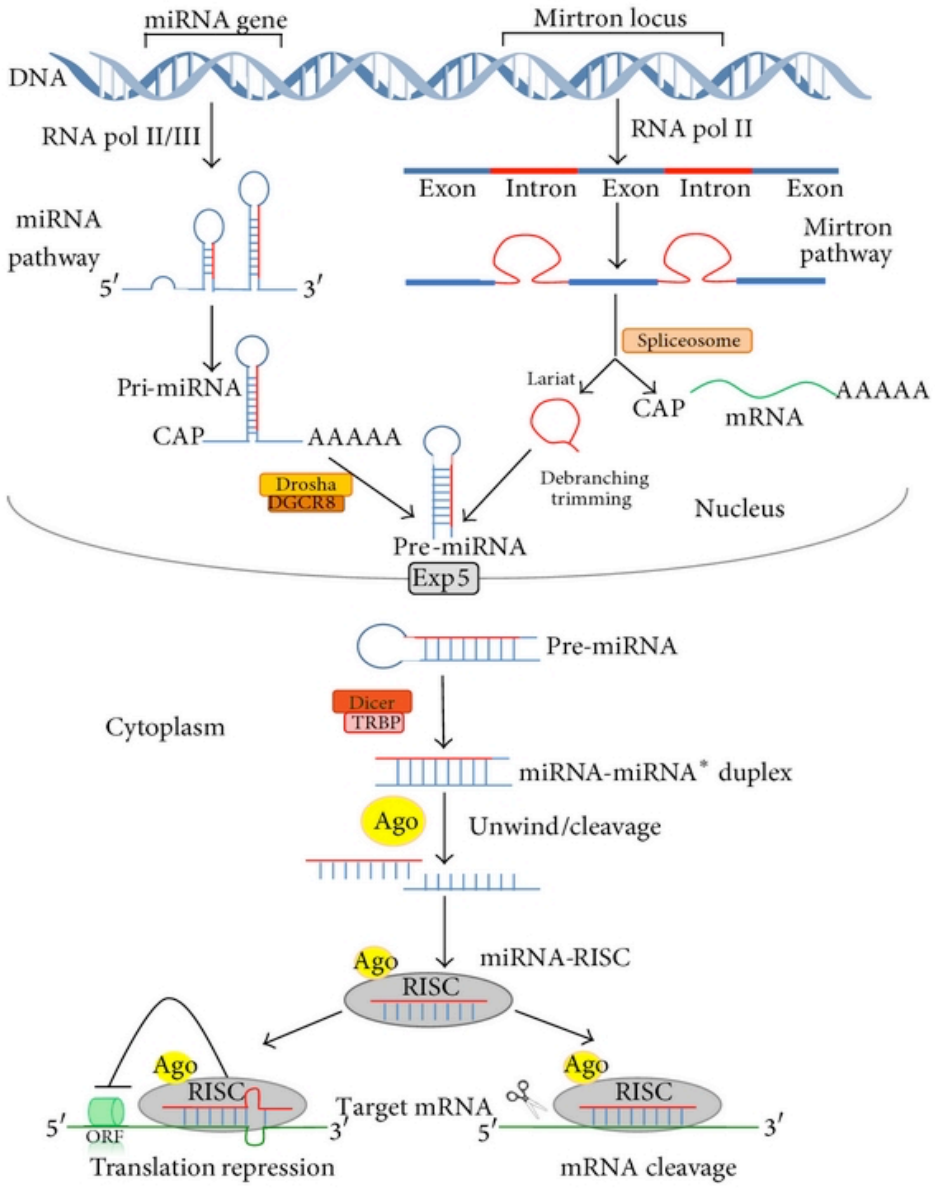

Figure 1.6 Biogenesis of miRNAs: canonical and non-canonical pathways. The canonical pathway produces pri-miRNA transcript from miRNA genes by RNA polymerase II/III followed by DROSHA processing of the pri-miRNA transcript into pre-miRNA. Noncanonical pathways are mirtron pathway, by passing the DROSHA pathway. Pre-miRNAs generated by both pathways are exported into the cytoplasm by exportin, followed by formation of miRNA-miRNA* duplex and cleavage into mature form of miRNA by DICER and Argonaute proteins (Ago). The RNA-silencing inducing complex (RISC) incorporates the mature miRNA and interacts with the 3'-UTR of the target mRNA and regulates gene expression by translational inhibition or mRNA degradation (*94*).

1.7.2 Role of miRNAs in cardiovascular diseases

The miRNAs have emerged as key players in cardiovascular development especially during embryogenesis, and cardiovascular diseases such as myocardial infarction, cardiac arrhythmia, cardiac hypertrophy, heart failure, cardiac fibrosis, ischemia, and atherosclerosis, thus can serve as potential targets for cardiovascular disease prevention, diagnostics and therapy. Several miRNAs such as miR-1, miR21, miR-29, miR-92a, miR-133, miR-199a and miR-320 are involved in ischemic injury, cardiac remodeling via MMP-9 and collagen synthesis, TGF-β - BMP-4 and SMAD pathway (*95, 96*). MiRNAs-1, 133 are anti-hypertrophic and 129, 18b, 195, 21, 23a, 23b, 24, 208 and 212 are pro-hypertrophic (*97*). Further, over expression of miR-221/222, miR-92a inhibits tube formation, migration, and wound healing by possibly regulating the expression of several pro-angiogenic genes (*98*). MiR-126 has been shown to regulate the expression of TNF-alpha stimulated VCAM-1 expression, thus playing a role in vascular inflammation (*99*). A recent study on human AV endothelial cells (HAVEC) has shown that miR-139-3p, miR-187, and miR-486-5p are shear sensitive indicating that there are indeed mechanosensitive miRNAs (*22*). Further, it was also shown that shear responsive miRNAs in HUVECs, i.e., miR-23b and miR-19a are not found in HAVECs, supporting the idea that shear regulation of miRNAs in HAVECs is unique from HUVECs. Further, circulating levels of serum miRNAs such as miR-126, 92a, 133a etc., are also associated with various types of cardiovascular diseases and might serve as

potential biomarkers (*94*). Thus the miRNA family involved in cardiovascular diseases is growing rapidly, however, many unsolved issues remain, and our present understanding of the regulation of individual miRNAs in physiology and pathophysiology of AV is in its infancy. This work proposes the identification and characterization of miRNAs that are shear responsive and side dependent in porcine AV leaflets *ex vivo*.

CHAPTER 2 HYPOTHESIS AND SPECIFIC AIMS

2.1 Rationale and hypothesis

Calcific AV disease is a strong risk factor for cardiovascular related deaths and is a significant source of mortality worldwide, with the number of patients requiring AV surgery expected to increase from 250,000 to 850,000 by 2050 (*34*). Explanted calcified valves show signs of endothelial damage, inflammation, disrupted ECM, angiogenesis, and ossification in the fibrosa side of the leaflets, while the ventricularis side remains relatively unaffected (*9, 100*). Spatial differences in complex genetic programming and local hemodynamics could be strong factors in this side-dependent calcific valve disease (*22*). When valvular endothelial cells are subjected to injury due to abnormal hemodynamics or humoral insult, a cascade of events leads to the triggering of inflammation. These events include infiltration of macrophages and increased expression of adhesion molecules, cytokines, growth factors, and enzymes (*2*). As a result, endothelial cells become activated and display a myofibroblast-like phenotype via endothelial mesenchymal transition. Eventually, inflammatory cells and cytokines invade the ECM and degrade the collagen and elastin. This causes phenotypic changes of valve interstitial cells and leads to ossification and calcification. Understanding the basis for the increased susceptibility of the fibrosa to inflammation and calcification can provide important clues about the regulatory mechanisms involved in AV disease.

Another common form of calcification is ectopic calcification. It occurs when there is a loss of mineralization inhibitors such as pyrophosphate (PPi), matrix γ-carboxyglutamic acid Gla protein (MGP), fetuin, and osteopontin, or when there is increased expression of mineralization promoters such as tissue non-specific alkaline phosphatase, phosphates, or both (*3, 4, 35, 101*). However, the exact mechanisms of how these calcification inhibitors and promoters participate in the AV calcification process are not well understood. Thus, calcification of aortic valves may occur through overlapping yet distinct molecular mechanisms, each with different clinical implications.

Shear stress is a mechanical stimulus that greatly differs on either side of the valve and plays an important role in this side-dependent disease. It is speculated that the reduced shear stresses on the non-coronary leaflet of the AV due to the lack of coronary flow is responsible for the increased susceptibility to calcification of that leaflet (*1, 8*). Altered shear stresses induce increases in inflammatory markers such as VCAM1, ICAM1, TGFβ1 BMP4 in the fibrosa than the ventricularis in endothelial and sub-endothelial regions (*102*). Shear stresses are also known to regulate the expression of MicroRNAs (miRNAs) (*22, 103, 104*). MiRNAs are partially complementary to one or more messenger RNA (mRNA) molecules, and their main function is to downregulate gene expression in a variety of manners, including translational repression, mRNA cleavage, and deadenylation.

MiRNAs are emerging as potential master regulators as well as biomarkers for various cardiovascular diseases such as atherosclerosis, myocardial infarction, coronary artery disease, diabetes mellitus, hypertension, aortic stenosis, and bicuspid aortic valve (*35*). Shear dependency of miRNA expression in human AV endothelial cells was demonstrated by a recent study which discovered miRNAs (miR-187, miR-214, miR-199a-5p, miR-181a, miR-181b, and miR-486-5p) that could potentially regulate key cellular processes in AV disease progression (*22*). Fang, et al. showed that miR-10a regulates a pro-inflammatory state in endothelium susceptible to atherosclerosis both *in vivo* in porcine aortic ECs and *in vitro* in human aortic ECs (*105*). Moreover, Nigam, et al. has identified miRNAs expressed differently in aortic stenosis and aortic insufficiency (miR-26a, miR-30b, and miR-195) *in vivo* using whole, bicuspid valves. In addition, they linked them to calcification-related genes, such as *Smad1/3*, *Runx2*, and *Bmp2* in AV interstitial cells *in vitro* (*106*). Recently Yanagawa et al. showed that miR-141a regulates the BMP-2 pathway as well, and it restores the valvular interstitial cell activation induced by TGF-β1 (*107*). Although there is a growing body of evidence suggesting the involvement of miRNAs in side-dependent AV disease, the function of these miRNAs remains largely unknown. Understanding the function of miRNAs can uncover potential molecular mechanisms underlying AV disease. Further, secreted, circulating miRNAs could act as potential biomarkers for AV disease.

The current standard of care for AV calcification is to replace the calcified valve with a prosthetic heart valve via surgery or transcatheter implantation. Lack of effective therapeutic treatment of AV calcification is attributed to the scarcity of in-depth understanding of AV disease mechanisms. This thesis aims to address this issue by specifically focusing on the initial events such as extracellular matrix remodeling, inflammation etc., which lead to AV calcification.

The overall hypothesis of this work is ***"sclerosis, inflammation and calcification preferentially occurs in the fibrosa compared to the ventricularis due to differential gene expression and oscillatory shear stress"***.

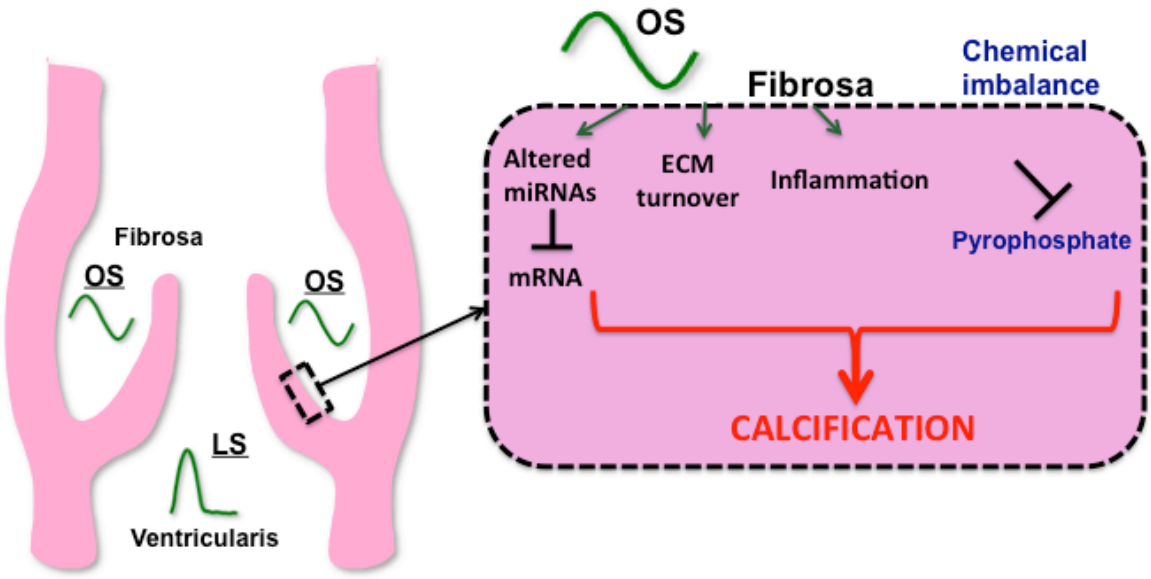

Figure 2.1 Schematic of overall hypothesis of this thesis.

Three aims are designed to test this hypothesis using an *ex vivo* approach. They are:

1. Identification of side- and shear-dependent miRNAs involved in aortic valve sclerosis, inflammation and calcification
2. Determination of the relationship between a key side- and shear-dependent miRNA and aortic valve pathogenesis
3. Investigation of the role of pyrophosphate in aortic valve calcification

2.2 General approach

Porcine AVs will be used in this study because of their anatomical and structural similarity to human AVs and ease of availability. A validated *ex vivo* cone and plate viscometer will be utilized to study the effects of shear stresses on AV tissue (*52*). These *ex vivo* studies provide a critical experimental platform to determine the role of shear in a side-dependent manner, while excluding naturally occurring confounding factors including pressure, strain and circulating factors found in blood. In addition, this system enables experimental conditions that are difficult to achieve in *in vitro* systems such as natural ECM and valvular interstitial cells.

2.3 Specific aims

The approach to address each of the specific aims is described in detail as follows.

Specific Aim 1: Identification of side- and shear-dependent miRNAs involved in aortic valve sclerosis, inflammation and calcification.

The hypothesis of this specific aim is that *oscillatory shear stresses induce altered gene expression, preferentially in the fibrosa side, that leads to aortic valve sclerosis, inflammation and calcification.*

The popularly used idealized shear stress paradigm is where the fibrosa (F) experiences oscillatory shear stress and the ventricularis (V) side experiences unidirectional pulsatile shear stress (*48*). Physiological pulsatile unidirectional shear stress (LS) of 0-79 dyne/cm^2 with peak magnitude 79dyne/cm^2 was used to investigate the mechanobiology in the ventricularis side. Oscillatory shear stress of low magnitude ± 5 dyne/cm^2 at 1 Hz (OS) was chosen to study the mechanobiology in the fibrosa side (*108*). Tissues from four conditions will be investigated: 1) fibrosa exposed to OS, 2) fibrosa exposed to LS, 3) ventricularis exposed to OS, and 4) ventricularis exposed to LS. These four conditions will help us understand if the preferential calcification in the fibrosa side is a result of its inherent matrix and cellular composition or the shear it experiences (OS or LS) or both. These four shear conditions will be investigated for 48 hours and AV tissue morphology (collagen and elastin stain) will be assessed upon completion. The valve cell phenotype (*Sma*) and collagen turnover marker (*Col1a1*) will also be assessed via qPCR. To further understand the role of shear stress in AV calcification, freshly isolated porcine AV leaflets will be exposed to OS in the presence of osteogenic medium (*17*). A time course study for 3 and 7 days will

be carried out. A calcium assay and stain will be performed to quantify calcification, and TUNEL stains will be done to identify apoptosis.

To identify the key miRNAs that are side- and shear-dependent, four miRNAs (181a, 181b, 214 and 199a-5p) are chosen. These miRNAs are preferentially upregulated in the fibrosa side in porcine AV leaflets *in vivo*, but nothing is known about their role in AV disease progression. Fibrosa and ventricularis will be exposed to OS or LS like mentioned earlier. Total RNA will be isolated and qPCR analysis will be performed to identify the side- dependency (fibrosa exposed to OS vs. ventricularis exposed to LS) and shear-dependency (fibrosa exposed to OS vs. LS, ventricularis exposed to OS vs. LS) of these miRNAs. Freshly isolated and or statically cultured AV tissues will be used as controls as needed. *In silico* analysis will be performed using programs such as miRWalk (*109*), miRTarBase (*110*) to identify potential mRNA targets of the side- and shear-dependent miRNAs. These mRNA targets will be filtered using existing mRNA databases to finalize the targets that are also major transcription regulators and related to altered remodeling, apoptosis, inflammation and calcification.

Specific Aim 2*:* Determination of the relationship between a key side- and shear-dependent miRNA and AV pathogenesis.

This specific aim will focus on investigation of the functional role of a key miRNA (identified in specific aim 1) in AV sclerosis, inflammation and calcification and the hypothesis of this specific aim is that *side- and shear-dependent miRNA*

modulates mRNA with sclerosis, inflammatory and calcific AV disease implications.

Selected mRNA targets of this key miRNA, identified in specific aim 1 will be experimentally validated with qPCR analysis. AV leaflets will be sheared and the mRNA targets that show an inverse relationship with the miRNA expression will be chosen. To further understand the role of this key miRNA, and to validate its target mRNAs, the levels of this miRNA will be modulated using a miRNA inhibitor. Transfection protocol of miRNA inhibition in statically cultured AV tissues will be optimized using fluorescently-tagged, non-targeting anti-miRNA. The extent of transfection will be visualized using confocal microscopy and the effect of transfection will be assessed using qPCR. This optimized transfection protocol and qPCR will then be used to determine dosage of anti-miRNA of the key miRNA for its successful inhibition in statically cultured AV tissues. The same dosage will then be used to inhibit miRNA in sheared samples as well. After successful inhibition of the key miRNA, qPCR will be done to quantify the expression of the target mRNA genes that were identified previously. Additional functional studies will be performed by assessing the extent of inflammation, endothelial-mesenchymal transition, and calcification after knocking down this key miRNA. Furthermore, based on the results, a pathway will be proposed to link this miRNA to the existing pathways involved in AV disease progression.

Specific Aim 3*:* Investigation of the role of pyrophosphate in aortic valve calcification.

The hypothesis of this specific aim is that *loss of mineralization inhibitors such as pyrophosphate results in ectopic calcification of AV.*

An *ex vivo* model of AV calcification will be developed in order to understand the protective role of pyrophosphate in ectopic calcification of the AV. AV leaflets will be statically cultured in a serum-free media with different dosages of phosphate (0.8, 2.6, 3.2, 3.8 mM) and pyrophosphate inhibitor. A calcium assay and stain will be performed to quantify calcification, and TUNEL stains will be done to identify apoptosis. Tissue architecture will be assessed with elastin stain. Furthermore, experiments will be performed to assess if the AV leaflets actively produce PPi. The synthesis of PPi from statically cultured AV leaflets will be assessed using a PPi production assay. Enzymatic production of PPi from extracellular ATP by ectonucleotide pyrophosphatase/phosphodiesterase 1 (ENPP1) will also be investigated using autoradiography analysis. Finally, therapeutic benefit of supplementing etidronate (a non-hydrolyzable synthetic form of PPi) to treat AV ectopic calcification will be investigated as well.

CHAPTER 3 IDENTIFICATION OF SIDE- AND SHEAR-DEPENDENT MIRNAS INVOLVED IN AORTIC VALVE SCLEROSIS, INFLAMMATION AND CALCIFICATION

3.1 Summary

Aortic valve calcification preferentially occurs in the fibrosa side; it is hypothesized that the disturbed shear stress experienced by the fibrosa could contribute to this side-dependent disease. Low magnitude oscillatory shear stress induced calcification in the fibrosa compared to the ventricularis. This preferential calcification in the fibrosa required the existence of both low magnitude (5 dyne/cm^2) and oscillatory nature (+/-) of the shear stress. Also, low magnitude oscillatory shear stress induced changes in the collagen, elastin and phenotype of the AV, which were otherwise preserved by the unidirectional pulsatile shear stress. To investigate the changes induced by the low oscillatory shear stress at the miRNA level, four miRNAs (miR-181a, miR-181b, miR-199a-5p, and miR-214) were selected based on their involvement in the cellular processes related to the AV pathophysiology. Two out of four miRNAs tested, miR-214 and miR-181a were highly expressed in the fibrosa exposed to OS compared to other shear conditions, and showed side- and shear-dependency in the fibrosa but not the ventricularis. Further miR-214 has potential targets that play critical roles in early and later stages of AV disease progression and thus was classified as a key miRNA.

3.2 Introduction

AV calcification is a side-dependent disease that primarily affects the fibrosa side and is typically characterized by inflammation, fractured matrix fibers, thrombus formations, and calcific lesions (*6*). The mechanical environment, matrix composition and underlying gene expression that differ on either side of the valve are believed to play a role in this side-dependent disease (*10*).

AV experiences shear stresses that drastically differ on either side. It is possible that this differing shear stress is responsible for the differential gene transcription profiles observed in healthy, porcine AVs (*24*). Furthermore, shear stresses experienced by the fibrosa can also change with developing pathology such as high heart rate or low cardiac output (*111*). Shear stresses when altered, can create a pro-inflammatory environment in the fibrosa but not the ventricularis (*112*). Disturbed or non-uniform shear stresses can also cause altered extracellular matrix remodeling, which in turn can affect the cell phenotype and gene expression (*45*). Another possible mechanism is via preferential activation of the miRNAs and mRNAs involved in remodeling, inflammation, and calcification on the fibrosa (*22*). However, the functional role of miRNAs regulated by shear stresses in a side-dependent manner, is not well understood. This information can uncover potential molecular mechanisms underlying AV disease and can be a crucial step towards developing medical therapies to treat AV calcification.

3.3 Hypothesis

The hypothesis of this specific aim is that the *side-dependent AV calcification occurs due to low, unsteady shear stresses present on the fibrosa, which induces differential expression of mechanosensitive miRNAs compared to the ventricularis. These mechanosensitive miRNAs in turn regulate their target mRNAs that are involved in shear induced AV inflammation and calcification*.

3.4 Materials and Methods

The overall workflow of this specific aim is outlined in Figure 3.1

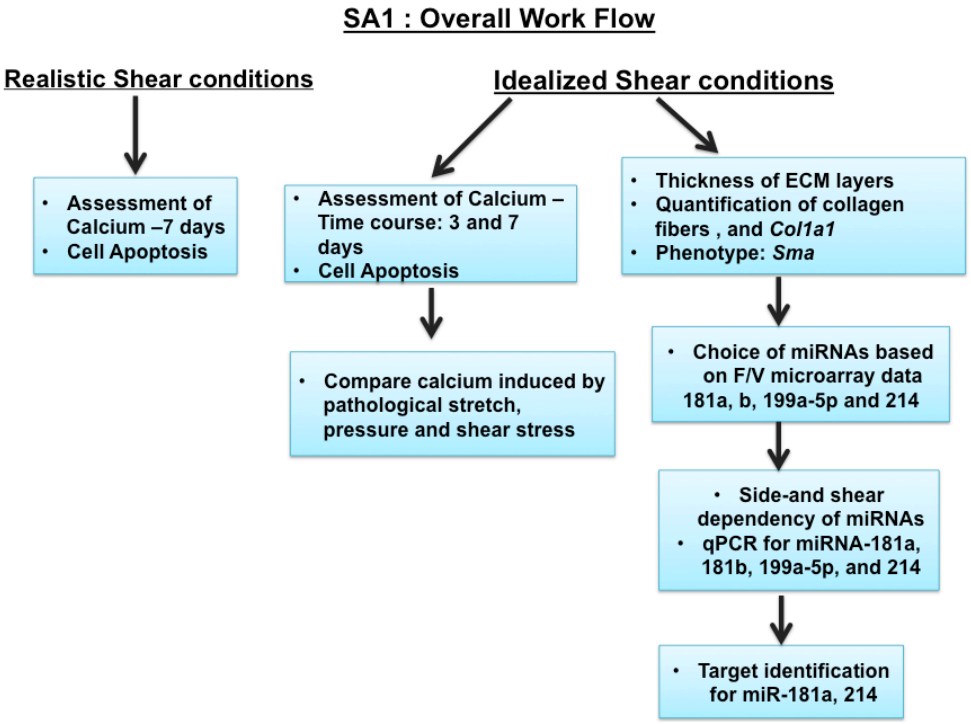

Figure 3.1 The overall workflow of specific aim-1.
The effect of idealized and realistic shear stress profiles on AV calcification was determined. Based on calcification studies, the effect of idealized shear stress on AV ECM, phenotype, and miRNAs was investigated.

3.4.1 Aortic valve tissue harvest for this ex vivo *study*

Hearts were obtained from healthy, female, non-pregnant pigs (aged 6 to 12 months) immediately after slaughter from a local abattoir (Holifield Farms, Covington, GA). The AV leaflets were immediately excised and thoroughly rinsed in sterile nuclease-free Dulbecco's phosphate buffered solution (dPBS; Sigma-Aldrich, MO) at 4 ^{o}C. Valves were placed in nuclease-free dPBS on ice and transported back to the laboratory. Upon arrival in the laboratory, dissected AVs were transferred to clean, sterile dPBS at 4 ^{o}C under the sterile laminar flow hood and processed accordingly.

3.4.2 Shear stress and aortic valve calcification

To determine the role of shear stress in inducing AV calcification, an *ex vivo* shear stress bioreactor was used. To investigate the mechanobiological implications of shear stress alterations, currently two shear stress paradigms are available in the literature: idealized (computational) (*48*) and realistic (experimental) (*113*). It is important to use the shear stress profile that can induce changes at macroscopic (changes of ECM) as well as microscopic (calcification, mRNAs, miRNAs) levels within a reasonable time frame *ex vivo*. Both types of shear stress profiles were tested in this specific aim. The profile that induced preferential calcification in the fibrosa was chosen as the shear stress model for further investigation. The shear stress bioreactor and shear stress conditions are described in detail in sections3.4.2.1, 3.4.2.2, and 3.4.2.3, followed by the details of the experimental set up in section 3.4.2.4**.** Calcification

assays were carried out as described in the sections 3.4.2.5, 3.4.2.6 and 3.4.2.7**.** AV cell apoptosis was assessed using TUNEL stain as detailed in the section 3.4.2.8. An attempt was made to understand the contribution of shear stress to AV calcification, compared to other mechanical stimuli (stretch and pressure). Complete details of the calcification study carried out using the *ex vivo* stretch and pressure bioreactor is not described in this specific aim and is compiled as a separate appendix A.23.

3.4.2.1 Ex vivo cone and plate shear stress bioreactor

An *ex vivo* shear stress bioreactor was used to study the effect of shear stresses on the AV leaflets in a side-dependent manner. This bioreactor has been designed and extensively validated to expose AV tissues to well-defined shear stress profiles (*52*). It is a modification of the cone and plate viscometer. Briefly, as shown in Figure 3.2, the bioreactor consists of a dish with a plate at the bottom, where the valve leaflet tissues are held. In addition, a cone angled at 0.5^{o} is placed at 200 μm above the plate. A programmable servomotor is coupled to this cone and it rotates the cone depending on the specific shear stress program. The device can hold 9 tissue samples of diameter 7 mm. The motors were programmed by the Motion Planner© software (version 4.3.2.0, Parker Hannifin Corp, CA). A perfusion system consisting of a reservoir of media, powered by a slow moving peristaltic pump (Model SP202.100, APT Instruments, IL) was installed to continually re-circulate the media within the cone and plate bioreactor.

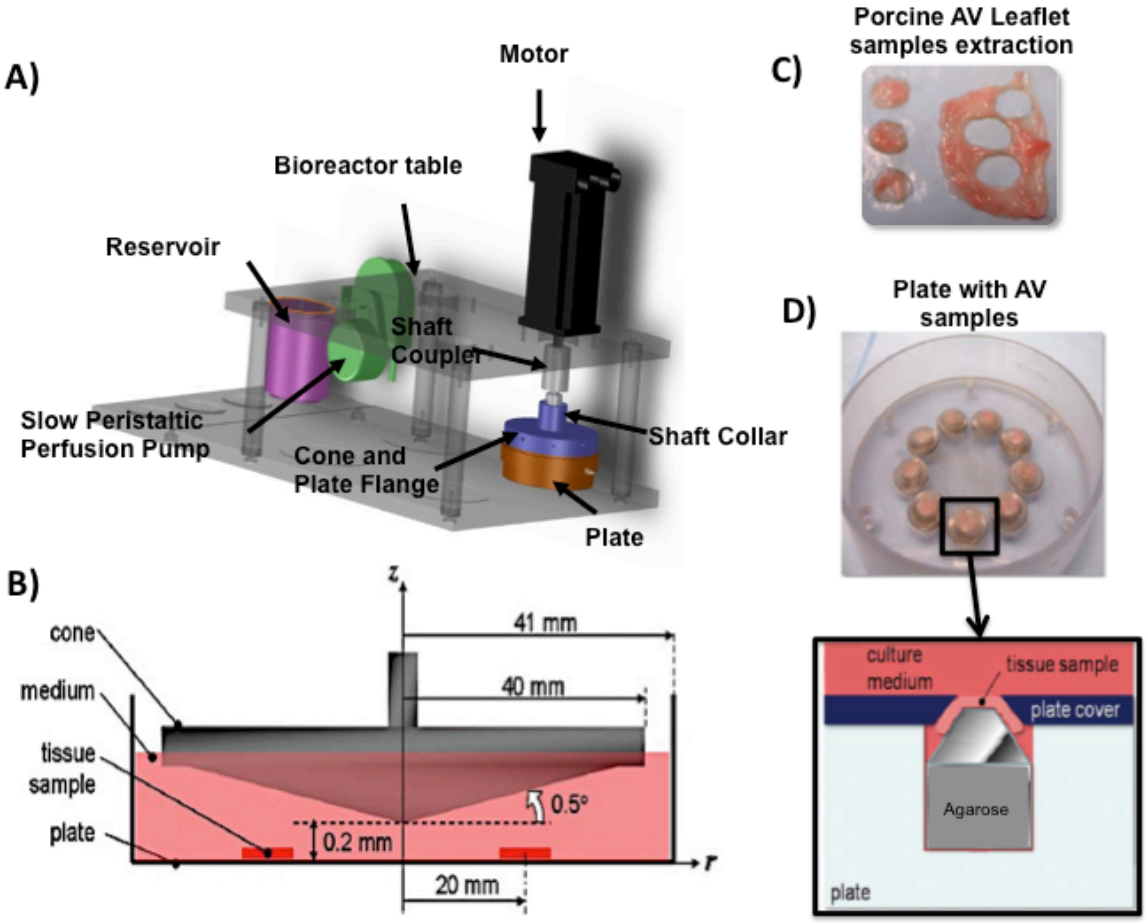

Figure 3.2 Ex vivo cone and plate shear system.
A) The cone and plate bioreactor setup. It consists of a rotating cone (via motor) on top of a stationary plate (with AV samples). The perfusion system maintains constant flow of media in the cone and plate set up. The whole set up is held in a bioreactor table and can be placed in an incubator. B) Schematic of the cone and plate only. The plate can fit 9 AV samples, all placed at a radial distance of 20 mm from the center of the cone. C) Samples extracted from AV leaflet tissue. D) Plate with 9 samples and the highlighted portion shows agarose filled into the well that holds tissue samples.

The rotating cone rotates the media between the cone and plate and imparts the shear stress to the surface of the AV tissues in the circumferential direction.

Shear stress on the plate is calculated by the formula, $\tau_w = \rho \nu \omega \left| \frac{r}{h + r\alpha} \right|$, where τ_w is the wall shear stress, ρ and v are the density and the viscosity of the fluid, ω is the angular velocity of the cone, and *r* is the radial coordinate of shear stress calculation on the plate, *h* is the gap between the apex of the cone and the plate, and α is the cone taper angle, which is 0.5^{o}. This equation for calculating shear stress experienced by the plate has been validated by computational fluid dynamics simulations of the cone and plate bioreactor, as well as by Laser Doppler Velocimetry measurements of the apparatus (*52*). Further, the actual rotational velocity measured by the tachometer on the motor was shown to match the desired velocity programmed into the controller. The cone was coupled to a servomotor (Model SM232AE-NPSN Brushless Servo Motor, Parker Hannifin Corp., Rohnert Park, CA), which was controlled by a servo drive (Model GV6K Gemini Servo, Parker Hannifin Corp., Rohnert Park, CA). Additional details of this bioreactor are explained in-depth in appendices A.1 and A.2.

3.4.2.2 Idealized shear stress profile

The most commonly used idealized shear stress paradigm (Figure 3.3) is the one where the fibrosa (F) experiences oscillatory shear stress and the ventricularis (V) experiences unidirectional pulsatile shear stress (*48, 102, 112*). As per this paradigm, the ventricularis side experiences pulsatile unidirectional shear stress (LS) of 0-79 dyne/cm^2, with a peak magnitude 79 dyne/cm^2.

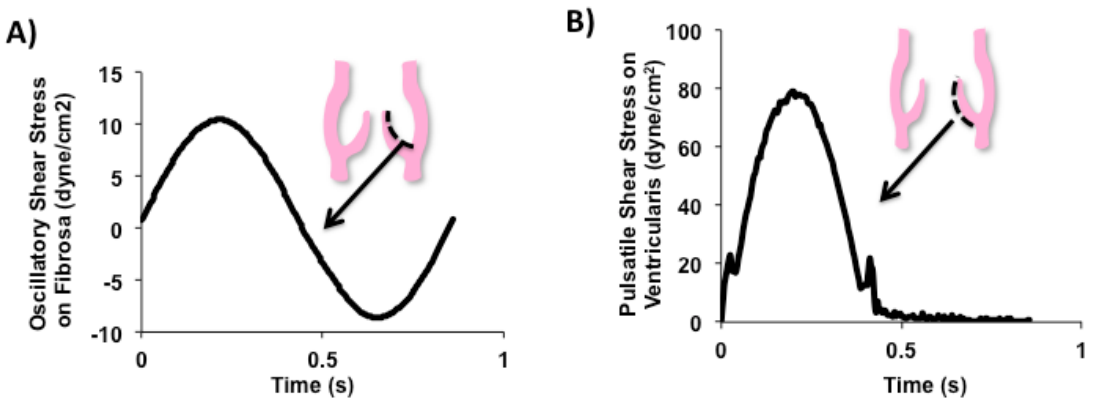

Figure 3.3 Idealized shear stress profile.
A) Fibrosa experiences an oscillatory shear stress (OS). B) Ventricularis experiences a pulsatile shear stress (LS).

A recent study showed that maximum calcification in the fibrosa was observed when exposed to ± 5 dyne/cm^2 (low magnitude) compared to ±10 dyne/cm^2 (physiological) and ± 25 dyne/cm^2 (high magnitude), within 3 days of culture in osteogenic media (*114*). Thus, oscillatory shear stress of low magnitude ± 5 dyne/cm^2 at 1 Hz (OS) was chosen to study the mechanobiology in the fibrosa. Samples were exposed to a steady shear stress of 5 dyne/cm^2 to test if the calcification induced in the fibrosa was due to the oscillatory nature (+/-) or the low magnitude (5 dyne/cm^2) of the oscillatory shear stress. Then to determine if the calcification induced by OS was side-dependent, the ventricularis side was also exposed to OS. Although the ventricularis side never sees the low magnitude shear stress, this particular experiment will help us understand how the endothelial cells on the ventricularis side will respond to this calcification inducing OS. As the oscillatory shear stress did not induce calcification in the ventricularis side, this control experiment was not done on the ventricularis side.

Physiologically, ventricularis experiences LS and does not calcify as much as the fibrosa side, the LS shear was not tested in this calcification model, but was tested in the other experiments.

To investigate AV ECM, phenotype, and expression of miRNAs, tissues from four conditions were used: 1) fibrosa exposed to OS, 2) fibrosa exposed to LS, 3) ventricularis exposed to OS, and 4) ventricularis exposed to LS. Fibrosa exposed to OS and ventricularis exposed to LS are physiologically relevant as the sides' fibrosa/ventricularis are exposed to their respective shear stresses. Thus the fibrosa exposed to OS vs. ventricularis exposed to LS comparison indicates side-dependency. Fibrosa exposed to LS and ventricularis exposed to OS are referred to as altered conditions as the physiological shear stress profiles are switched between the two sides. Fibrosa exposed to OS vs. LS and ventricularis exposed to OS vs. LS comparisons were used to compare the shear dependency of the fibrosa and the ventricularis, respectively. Thus, these four shear conditions were used to understand if the preferential calcification in the fibrosa is a result of its inherent extracellular matrix and cellular composition, or the shear it experiences (OS or LS), or both.

3.4.2.3 Realistic shear stress profile

Recently, dynamic shear stress data obtained from Laser Doppler Velocimetry measurements on AV under normal and altered hemodynamics (*111, 113*) showed that shear stresses experienced by fibrosa changes with the

hemodynamics. According to this study, as shown in the Figure 3.4A, the fibrosa experiences a peak shear stress of about 15 dyne/cm^2 under physiological hemodynamics (4.7 L/min, 70 beats/min). Under altered hemodynamics, the fibrosa experiences a peak shear stress of 6.4 dyne/cm^2 (low cardiac output, CO: 3 L/min, 70 beats/min) and 78 dyne/cm^2 (high heart rate, HR: 90 beats/min, 4.9 L/min). The ventricularis side, as shown in the Figure 3.4B, experiences a peak shear stress of 64 dyne/cm^2 and beyond this peak, the shear stress decreases rapidly and experiences a peak negative of -40 dyne/cm^2. One of the most striking features of this realistic shear stress profile is that the shear stress on the fibrosa side is unidirectional and the ventricularis side is oscillatory unlike the idealized shear stress profile described in section **3.4.2.2.**

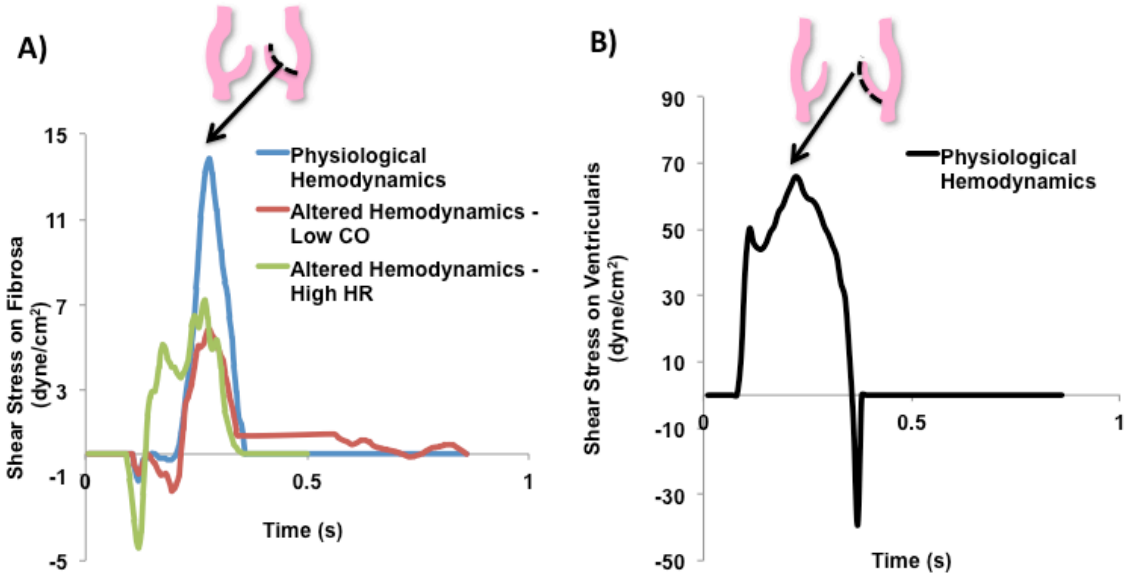

Figure 3.4 Realistic shear stress profile.
A) Shear stress experienced by fibrosa at physiological and altered hemodynamics. B) Shear stress experienced by ventricularis at physiological hemodynamics.

In this study, fibrosa was exposed to the shear stresses at physiological and altered hemodynamic conditions. High HR and low CO are known to affect several stages of the cardiovascular disease continuum such as endothelial dysfunction, plaque rupture and myocardial infarction (*115-117*). Calcification experiments were carried out for 7 days using osteogenic media. Freshly isolated AV tissues were used as controls. Since the ventricularis side did not show calcification compared to the fibrosa side in our idealized shear stress study, the ventricularis side was not tested as part of this preliminary study. However, the future studies should include the calcification experiments on the ventricularis side as well.

3.4.2.4 Shear stress experimental setup

In the laboratory, circular 7-mm radius samples were cut aseptically from the basal region of each leaflet under the sterile laminar flow hood. As detailed by Sucosky et al (*52*), each well of the shear stress bioreactor was filled with approximately 750 µL of 1.2% agarose (Agarose, Thermo Fisher Scientific, NJ), which acted as a tissue holder, and the circularly cut tissue samples were placed on top of the agarose bed (Figure 3.2C, D). Since the thickness of the AV tissue slightly varies from pig to pig, the height of this agarose bed must be adjusted based on the thickness of the tissue. This is to ensure that the tissue samples are flush mounted, i.e., are placed at the same level as the plate that holds all the tissues in place. To verify this, a micro-cover-slide can be slided from the center of the plate to the top of the tissue. If the micro-cover-slide does not move

smoothly over the tissue (which happens when the tissues are not flush mounted), the height of the agarose bed must be re-adjusted. These steps are crucial because if the level of the tissue increases relative to the plate (e.g. by 0.1 mm), it decreases the height between the cone and the plate. This variation of the tissue height significantly increases the shear stress experienced by the tissues (1.36 times). This calculation is based on the fact that there are no secondary flows in this cone and plate system and that the velocity profile is linear as detailed by Sucosky et al (*52*). Additional details are also available in Appendix: Cone and Plate manual A.2

Either the fibrosa or the ventricularis side was exposed to the shear stress during an experiment. Statically cultured tissues and/or freshly isolated AV leaflets were used as a control. To investigate the changes in gene expression (miRNA and mRNA) and valve histology, leaflets were cultured for 48 h using regular DMEM media (*118*). We chose a 48 h culture duration, as it is well known that this culture duration is sufficient to induce changes in gene expression and makes it possible to investigate the early onset of AV disease (*102*).

For calcification-related studies, leaflets were sheared for a time course of 3 and 7 days to determine the time at which detectable calcification occurs. To accelerate the calcification process that occurs over decades *in vivo*, an osteogenic media was used. This osteogenic media contained normal DMEM supplemented with 1 mmol/L glycerophosphate, 10μmol/L dexamethasone, 3.8

mmol/L PO_4^{3-}, and 1 ng/ml TGF-β1. This media has been previously validated to accelerate the calcification of the porcine AV leaflets in the presence of cyclic stretch (*17*).

Media (osteogenic) was changed every 48 h to replenish the nutrients. The entire setup was placed in a 5% CO_2 incubator at 37 °C. Post-culture, the portion of the tissue unexposed to shear stress was carefully excised (without touching the exposed tissue) using sterile tools under the sterile laminar flow hood. Tissues were briefly rinsed in multiple changes of sterile nuclease-free dPBS maintained at 4 ^{o}C until the media was completely removed.

To prepare paraffin sections, the tissues were fixed in 10% neutral buffered formalin (Fisher Scientific, PA) for at least 24 h, saturated in 70% ethanol (VWR, GA), processed in ascending grades of ethanol, embedded in paraffin, and cut into 5 μm sections. The blocks and the tissue sections were stored at room temperature. The cryopreserved tissue blocks were prepared by embedding the tissue in optimal cutting temperature (OCT) medium (Electron Microscopy Sciences, PA) and freezing it using liquid nitrogen. Sections with thicknesses of 5 to 7 μm were cut. The blocks and tissue sections were stored at -80 ^{o}C.

3.4.2.5 Calcium arsenazo assay

Total calcium content in tissue samples was quantified using the calcium arsenazo assay. This was used as a marker to represent calcification of the

tissue. At a neutral pH, the Ca^{2+} forms with arsenazo III a purple-colored complex, the color intensity of which is directly proportional to the concentration of calcium in the sample. Tissue samples from calcification experiments were pulverized by mortar and pestle in liquid nitrogen, and collected in pre-weighed vials. After sample collection, the vials were re-weighed before and after drying the samples overnight at 37 ^{o}C. The dry weights of the tissue were then computed. Subsequently, the ground samples were incubated in 1 M acetic acid at 4 ^{o}C for 24 h, to solubilize calcium. The samples were then centrifuged at 15,000 rpm for 9 min, and the supernatant was collected. The supernatant as well as calcium standards were assayed for calcium content by using a calcium specific Arsenazo dye reagent (Fisher-Scientific, MA): 25 µL of the supernatant or the calcium standard was mixed with 300 µL of Arsenazo solution in a 96 well plate.

The absorbance of the various samples at a wavelength of 650 nm was measured through spectrophotometry, using a 96 well plate reader (BioTek, VT). The absorption calibration curve was established with the calcium standard spectrophotometry readings, and was thereafter applied to readings from the samples. The amount of total calcium per dry weight of sample tissue was calculated. Total calcium content induced by each shear condition was normalized to the mean of the fresh AV leaflets and expressed as relative calcium content.

3.4.2.6 Von Kossa mineralization stain

Von Kossa staining was performed to visualize tissue mineralization. In this method, cryopreserved tissue sections were treated with a silver nitrate solution and the silver is deposited by replacing the calcium reduced by ultraviolet light, thereby visualized as metallic silver. Frozen sections were allowed to warm to room temperature, and were hydrated in PBS for 2 min. They slides were then incubated in 1% silver nitrate solution in a clear glass coplin jar placed under ultraviolet light for 2 h. After washing in several changes of distilled water, excess silver nitrate was removed by incubating in 5% sodium thiosulfate for 5 min. The slides were rinsed in distilled water, dehydrated through graded alcohol and cleared in xylene before being mounted in a resinous medium and coverslipped. Calcium deposits appeared black when viewed under normal white light.

3.4.2.7 Alizarin Red stain

Alizarin Red was used to stain for tissue calcification. Alizarin Red S, an anthraquinone derivative, may be used to identify calcium in tissue sections. The reaction is not strictly specific for calcium, since magnesium, manganese, barium, strontium, and iron may interfere, but these elements usually do not occur in sufficient concentration to interfere with the staining. Calcium forms an Alizarin Red S-calcium complex in a chelation process, and the end product is birefringent. Deparaffinized slides were hydrated and stained in 2% Alizarin Red solution (pH: 4.1 - 4.3) for 5 min while checking for staining microscopically. The slides were then dehydrated in acetone- xylene, cleared in xylene before being

mounted in a resinous medium and coverslipped. Calcium deposits appeared orange-red when viewed under normal white light. Slides were stored in a dry place at room temperature.

3.4.2.8 Aortic valve apoptosis stain

A cell apoptosis stain was performed to assess the cell death and viability of samples from calcification and miR-214 inhibition studies. This staining was done using the In Situ Cell Death Detection Kit; TMR red, TUNEL kit (Roche Diagnostics, Germany). Cryopreserved tissue sections were fixed with 4% paraformaldehyde (Sigma-Aldrich, MO) in dPBS (pH 7.4) for 20 min, rinsed with dPBS for 30 min, permeabilized with 0.1% Triton X-100 (Sigma-Aldrich, MO) in dPBS (2 min at 4 ^{o}C), and rinsed twice with dPBS. Staining was performed by incubating tissue sections for 1 h at 37 °C in a humidified chamber in the dark in 50 µL of TUNEL reaction mixture followed by counterstaining with DAPI for 5 min. A positive control was prepared by incubating the fixed and permeabilized tissue section with DNAse-I solution (3-3000U/ml RNAse free DNAse-I (Qiagen, CA) in 50mM TrisCl (Sigma-Aldrich, MO), pH 7.5, 1mg/mL BSA (Fisher Scientific, PA) for 10 min prior to labeling with TUNEL reaction mixture. A negative control was prepared by incubating fixed and permeabilized tissue sections in 50 µl of TUNEL label solution (without terminal transferase). Apoptotic cells appeared red and nuclei appeared blue under fluorescence microscopy.

3.4.3 Shear stress and aortic valve extracellular matrix

Alterations in the extracellular matrix can activate valvular interstitial cells (*119*) and thus, affect the valve cell phenotype. Further, stress induced changes in the extracellular matrix can dictate various signaling pathways that regulate the miRNA expression (*120, 121*). In this specific aim, the shear stress induced changes to the AV ECM was investigated to understand if these changes are possibly related to the shear induced expression of miRNA(s) (investigated in the later sections). Changes in the AV ECM were assessed using the Verhoeff-Van Gieson elastin stain and picrosirius red collagen stain and is described in detail in sections 3.4.3.1, 3.4.3.2, and 3.4.3.3. The activation of AV interstitial cells was assessed using smooth muscle α-actin*, Sma*, as there is no reliable marker to directly assess the changes in its native (quiescent) phenotype. An ECM related gene (collagen type-I, *Col1a1*) was also assessed at the mRNA level. These two markers were assessed using methods listed in sections 3.4.3.4 through 3.4.3.7.

3.4.3.1 Verhoeff-Van Gieson elastin stain

To visualize the elastin fibers as well as the assess the overall thickness of the fibrosa, spongiosa and ventricularis layers of the AV ECM, a Verhoeff-Van Gieson elastin stain was performed. AV leaflet samples stained with this elastin stain distinctly show the tri-layered components of the AV ECM: fibrosa, spongiosa and ventricularis layers. Elastin fibers stain blue-black to black, nuclei stains blue to black, collagen stains red, and muscle and other matrix

components stain yellow. ACCUSTAIN Elastic kit (Sigma-Aldrich, MO) was used according to the manufacturer's directions.

The thickness of each of these layers was measured using ImageJ software (*83*). Briefly, fibrosa thickness was measured from the edge of the tissue to where the collagen ends. The thickness of ventricularis was measured from the start of the black elastin lines to the edge of the tissue. The remaining thickness of the tissue was measured and reported as the thickness of spongiosa. Each layer was measured at the thickest and thinnest in each image and was averaged. For consistency, the data was normalized with respect to itself by dividing the average percent thickness of each layer by the sum of the average percent thicknesses of all three layers so that the percent thicknesses add up to 1.

3.4.3.2 Picrosirius Red collagen stain

Picrosirius red staining was performed to examine collagen fiber structure and morphology. In bright-field microscopy collagen is red on a pale yellow background. Nuclei, if stained, are ideally black but may often be grey or brown. The long incubation time in picrosirius red solution causes appreciable destaining of the nuclei. When examined through a circularly polarized filter the larger collagen fibers are bright yellow or orange, and the thinner ones, including reticular fibers, are green. This birefringence is highly specific for collagen (*122*). A few materials, including Type IV collagen in basement membranes, keratohyaline granules and some types of mucus, are stained red but are not

birefringent. Deparaffinized slides were stained in picrosirius red solution (saturated picric acid solution, ready to use, Sigma-Aldrich, MO) for one hour. The slides were then washed in 0.5% acidified water (5 mL glacial acetic acid in 995 mL distilled water), three changes of 100% ethanol, and xylene before being mounted in a resinous medium and coverslipped.

The relative proportion of the collagen fibers in the sheared AV leaflets was quantified using a custom Matlab (The Mathworks, Natick, MA) code (*18*). Picrosirius red images were first imported into Matlab R2009b and converted into their hue, saturation and value components. Only the hue components were retained, and a histogram of hue frequency was obtained from the 8-bit hue images that contained 256 possible colors. The colors were defined as follows: red 2 to 9 and 230 to 256; orange 10 to 38; yellow 39 to 51; and green 52 to 128 (*123*). All other hue values corresponded to interstitial space and were confirmed by visual inspection. The number of pixels within each hue range were determined and expressed as a percentage of the total number of collagen pixels (sum of all pixels) and plotted. Since the red and orange correspond to the mature collagen, their percentages were combined for analysis in this study.

3.4.3.3 Imaging

A Zeiss Axioscope A1 (Germany) was used for brightfield and fluorescence imaging. Circular polarizer, analyzer and a rotating stage were used with this microscope to image the tissue sections stained with picrosirius red.

3.4.3.4 RNA isolation

From 48 h shear experiments, total RNA was isolated from whole tissue (both endothelial and interstitial tissue) using the miRNeasy kit (Qiagen, CA). It was not feasible to isolate endothelial-enriched RNA from the sheared AV samples and it was more practical to isolate total RNA from entire tissue (interstitial and endothelial cells). To achieve sufficient RNA yield for qPCR, three sheared tissues were pooled per isolation. In the case of static culture, it was sufficient to pool just two tissues.

Post experiment, media from the tissues was completely removed by washing the tissues with sterile nuclease-free dPBS, as mentioned earlier. The tissues were then incubated in 700 µL of Qiazol for about 5 min at room temperature. The phenol-chloroform extraction was done and subsequent purification steps were performed as per the manufacturer's protocol. Alternatively, the tissue can be pulverized, homogenized as opposed to direct incubation with the Qiazol. The concentration and the purity of the samples were measured using the Take 3 plate attachment of Synergy H4 Hybrid Reader (Biotek, VT). Samples showed 260/280 and 260/320 ratios in the range 1.2 to 1.8 and had concentrations ranging from 10-30 ng/ µL (sheared samples) and 100-500 ng/ µL (statically cultured samples).

3.4.3.5 Preparation of mRNA and miRNA cDNA

To prepare cDNA for mRNA, High-Capacity cDNA Reverse Transcription kit with RNAse inhibitor kit (Life Technologies, NY) was used. To prepare cDNA for miRNA, miScript II RT kit (Qiagen, CA) was used. A Veriti® 96-Well Thermal Cycler (Life Technologies, NY) was used for this purpose.

3.4.3.6 Real-time qPCR

Real-time qPCR was used to test the AV cell phenotype (*Sma*), collagen type-I (*Col1a1*), and shear- and side-dependency of the four shortlisted miRNAs. The primers for *Sma* and *Col1a1* were designed and ordered from Integrated DNA Technologies (IA). The primer sequence is listed in Table 3-1. The primers for miRNAs were purchased from Qiagen (CA).

Table 3-1 Porcine specific primers to test AV cell phenotype changes.

Gene	**Forward Primer**	**Reverse Primer**
Col1a1	5-GGCCAAGAAGAAGACATCCCA-3	5-ACAACACATTGCCGTTGTCG-3
Sma	5-GGTGGGAATGGGACAAAAAGAC-3	5-TGGTGATGATGCCGTGTTCTATT-3
18S	5-CCCCAACTTCTTAGAGGGACAAG-3	5-AGGGCATCACAGACCTGTTATTG-3

The qPCR analysis of miRNAs in sheared AV samples was carried out with miScript SYBR Green PCR kit (Qiagen, CA). RNU6B included in this PCR kit was used as the endogenous control. The expression of *Sma* and *Col1a1* was also assessed via qPCR using the VeriQuest Fast SYBR Green (Affymetrix, CA).

StepOnePlus™ Real-Time PCR system (Life Technologies, NY) was used to run the qPCR analysis.

3.4.3.7 Analysis of qPCR data

A sample size of at least 3 to a maximum of 12 was used for data analysis. As mentioned earlier, each sample infact represents 2 or 3 tissue samples (due pooling of tissues). To analyze qPCR data for all other experiments, ΔCT method was used and fold changes (2^(-ΔCT)) were calculated. When comparing two groups, e.g. fibrosa exposed to OS vs. LS, the fold changes were normalized to the mean of the second group (here fibrosa exposed to LS) (which was set as the baseline) (*14*).

3.4.4 Shear stress and expression of miRNAs in aortic valve

As previously discussed, shear stress can influence the expression of miRNAs. The miRNAs chosen for this study are discussed in detail in 3.4.4.1 and their expression was assessed using real-time qPCR, as detailed in the sections 3.4.3.4 through 3.4.3.7. To identify and investigate the function of key miRNAs involved in AV sclerosis, inflammation and calcification, their potential targets must be determined. For this purpose, a systems biological analysis was carried out (3.4.4.2).

3.4.4.1 Selection of MiRNAs Involved in Sclerosis, Inflammation and Calcification Pathways

Side-specific miRNAs identified in sheared human AV ECs (*in vitro*) (*22*) and freshly isolated porcine AVs (*in vivo*) (*124*) were selected for further investigation in this specific aim. Since there are several miRNAs that are potentially involved in AV inflammation and calcification, the miRNAs investigated in this specific aim were prioritized based on the following criteria: 1) have potential mRNA targets that are expressed in early stages of calcific AV disease progression; 2) regulate fundamental cellular functions such as cell proliferation, adhesion, cycle, growth, migration, death, inflammation etc; and 3) scientific evidence of the function of selected miRNAs in AV or cardiovascular system. The miRNAs that met all of the above criteria were miR-181 a/b, miR-199a, and miR-214 and thus were chosen for further investigation in this specific aim. These four miRNAs are also conserved in humans.

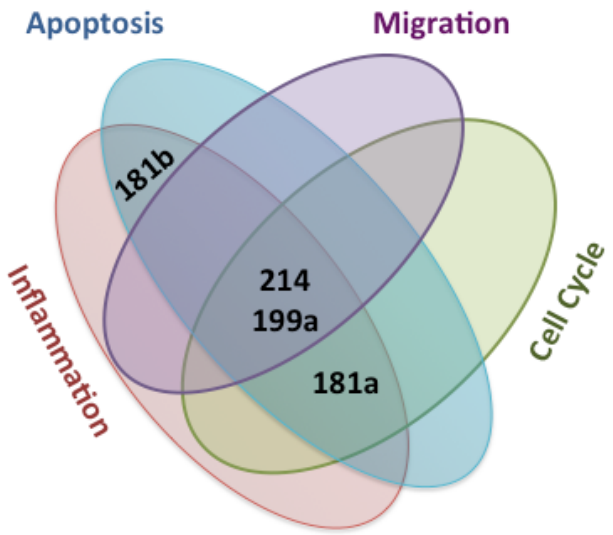

Figure 3.5 Categorization of miRNAs.
The miRNAs were sorted based on their role in the cellular processes that are related to AV disease.

Sufficient evidence exists in the current literature that links these four miRNAs to cellular processes that are involved in a variety of diseases such as cancer, cardiac injury, renal fibrosis, coronary artery disease. Based on their function, these miRNAs were categorized and shown in Figure 3.5. Briefly, miR-181a is involved in lipid metabolism (*125*), epithelial-to-mesenchymal transformation (*126*), angiogenesis (*127*), apoptosis (*128*), and inflammation (*129*) and calcification (osteopontin) (*130*). Moreover, miR-181b contributes to inflammation (*131*), growth changes and apoptosis (*132*) as well. MiR-199a plays a role in growth (*133*), proliferation (*134*), cell cycle and apoptosis (*135*), migration (*133, 134*), inflammation(*136*), and calcification (BMP2/SMAD1) (*137*). MiR-214 plays a role in proliferation (*138, 139*), cell death (*136, 140, 141*), cell cycle (*138*),

migration (*140, 142*), and inflammation (*136, 139, 141*). The low circulating level of miR-214 is also a biomarker for coronary artery disease (*15*).

3.4.4.2 Bioinformatics analysis to identify potential targets of side- and shear-dependent miRNA

It is known that miRNAs control gene expression by inversely regulating the expression of mRNA genes. This logic was applied to identify the potential mRNA targets of side- and shear- dependent miRNA(s); an in-depth bioinformatics analysis was carried out as outlined in the Figure 3.6. Most of the sequence-based mRNA target databases are available only for 3 species: human, mouse and rat. These two miRNAs, miR-181a, and miR-214 are homologous with human miR-181a and miR-214-3p. The experimentally validated mRNA target list of human miR-214-3p, miR-181a was obtained from the two most popular databases miRWalk (*109*) and miRTarBase (*110*).

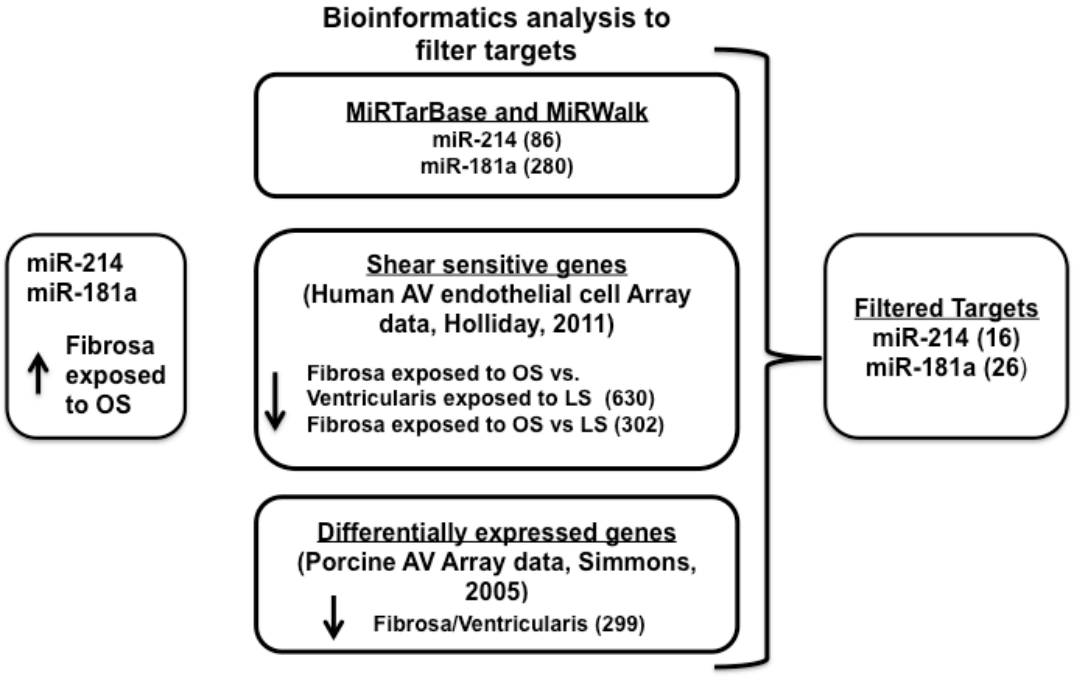

Figure 3.6 Bioinformatics analysis and target filtration scheme.
The targets identified using two programs (MiRWalk and MiRTarBase) were filtered using two databases. The filtered targets identified using this scheme were 26 for miR-181a and 16 for miR-214.

To filter the extensive target list, two additional data sets were used. The first one was the validated side-dependent genes from mRNA microarray data of fresh porcine AV endothelial cells published by Simmons et al (*24*). From this data set, the list of mRNA genes (299) that had significantly lower expression in the fibrosa compared to the ventricularis only was considered. The second data set was the mRNA genes list of sheared human AV ECs from our previous experimental data (*22*). Since miR-214 and miR-181a are upregulated in fibrosa exposed to OS vs. LS and compared to ventricularis exposed to LS, only mRNA genes that were

downregulated in the corresponding data sets were chosen, also shown in the Figure 3.6. The number of downregulated genes in these two experimental data sets was 302 and 630 respectively with a false discovery rate of $\leq$ 5%. Specifically, the mRNA targets filtered and chosen for further investigation are known to play a role in processes such as cell proliferation, apoptosis, inflammation, endothelial dysfunction, development, and endothelial-to-mesenchymal transition that lead to AV calcification.

3.4.5 Statistical analysis

Data was expressed as mean $\pm$ standard error. All the statistical analyses were done using SPSS Statistics for Mac (Version 20.0, IBM Corp, NY). The normality of all the data was tested using the Anderson-Darling method. Student t-test was used when only two groups were being compared. Two-way ANOVA was used for analyzing independent sample sets with Tukey's post-hoc test for comparisons between multiple groups. If the data was not normally distributed, Mann-Whitney and Friedman tests were used in place of the student t-tests and ANOVA, respectively. The groups were considered to be significantly different or show trends if the p-value was less than or equal to 0.05 and 0.10, respectively.

3.5 Results

Raw data for all the results are included in Appendix A.18.

3.5.1 Effect of idealized shear stresses on AV calcification

As shown in the Figure 3.7, calcification in the fibrosa was significantly higher ($p<0.05$) when exposed to OS but not steady shear stress of the same magnitude. Also, statically incubated tissues did not calcify compared to the fresh tissues. This shows that both the low magnitude (5 dyne/cm^2) and oscillatory nature (+/-) of the shear stress or flow disturbance is needed to trigger calcification.

Further, this response proved to be side-dependent, as calcification was observed only when the fibrosa was exposed to OS. This side-dependent calcification continued to increase after 7d ($p<0.05$) (Figure 3.8A). Consistent with this quantitative result, the Von Kossa mineralization stain also showed localization of black calcium nodules in the fibrosa side exposed to OS but not ventricularis (Figure 3.8B).

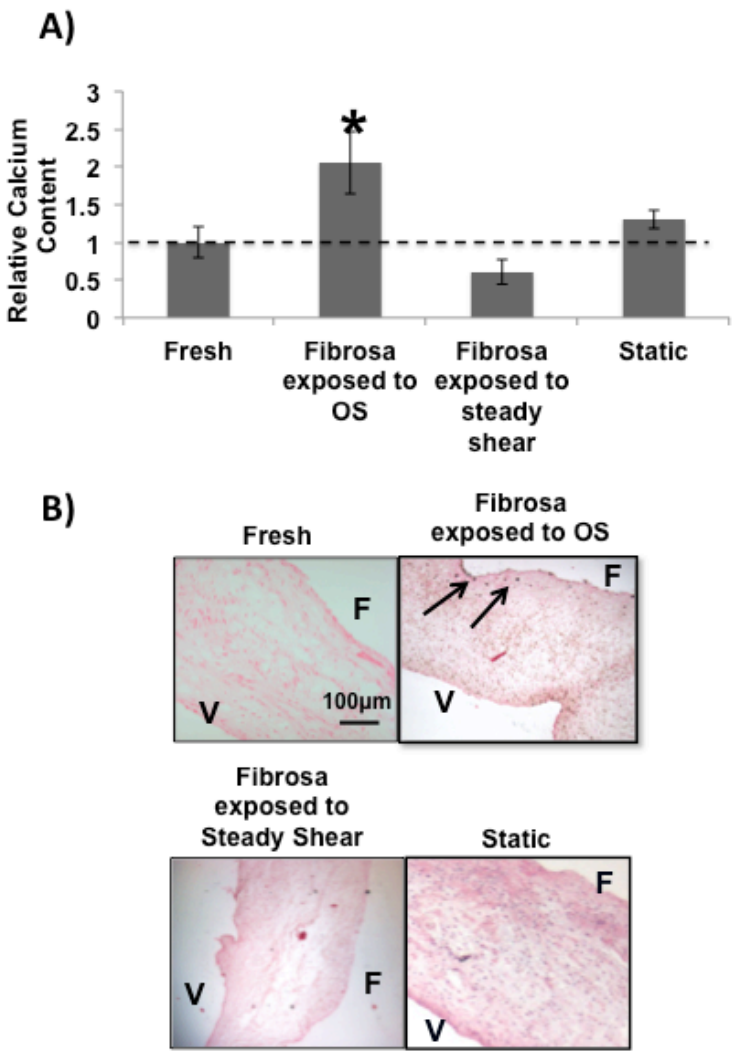

Figure 3.7 Calcification of AV induced by OS and steady shear.
A) No calcium levels were observed in fibrosa exposed to steady shear compared to OS. n=8, *p<0.05. B) Consistent with the quantitative result, fibrosa exposed to a steady shear of 5 dyne/cm^2 showed no calcification suggesting that calcification is dependent on the oscillatory nature of the shear stress. Calcium nodules appeared black (arrows). F: fibrosa, V: ventricularis. n=6. Representative scale bar is shown only on fresh sample.

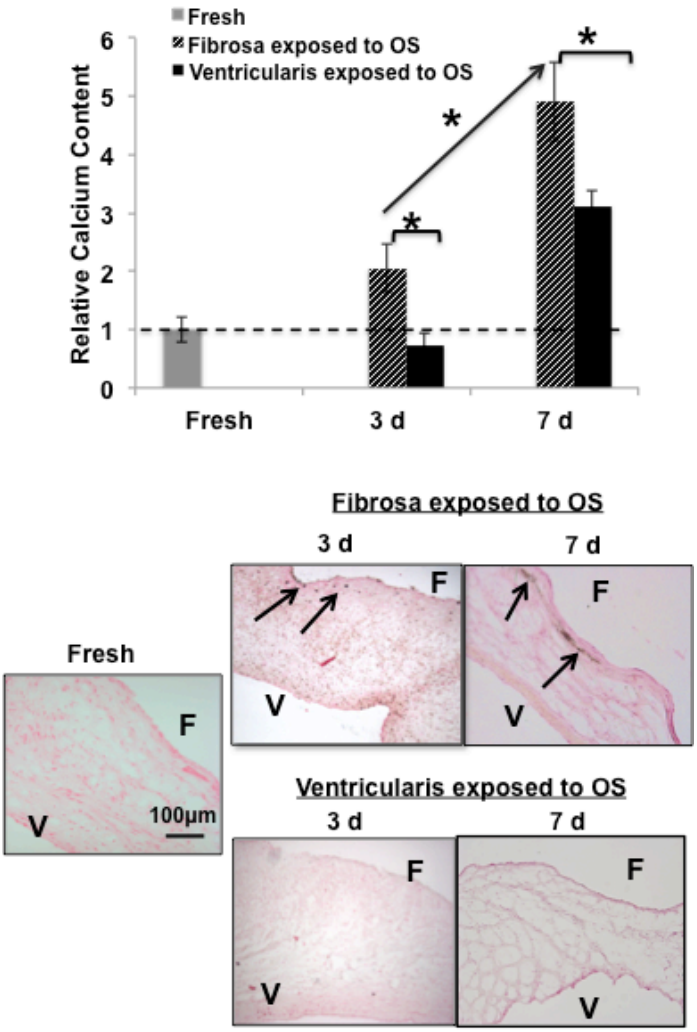

Figure 3.8 Time course of side-dependent AV calcification induced by OS. A) The amount of calcium induced in the fibrosa when exposed to OS is significantly higher than that in ventricularis and continued to increase after 7 days. n=8-10, *p<0.05. B) Consistent with the quantitative result, calcium nodules were observed in fibrosa when exposed to OS but not ventricularis, indicating that the calcification induced by OS is side-specific. Calcium nodules appeared black (arrows). F: fibrosa, V: ventricularis. n=6. Representative scale bar is shown only on fresh sample.

3.5.2 Effect of realistic shear stresses on AV calcification

Tissues exposed to shear stress under low CO had significantly higher calcium compared to those exposed to the physiological condition ($p<0.05$), but not significantly different compared to the fresh control (Figure 3.9). However, qualitatively, calcium nodules were not observed within the tissue (as evident by the calcium stains). The fresh samples in this experiment had calcium levels higher than that observed in the previous results. This could be due to the variability of the pigs in the slaughterhouse.

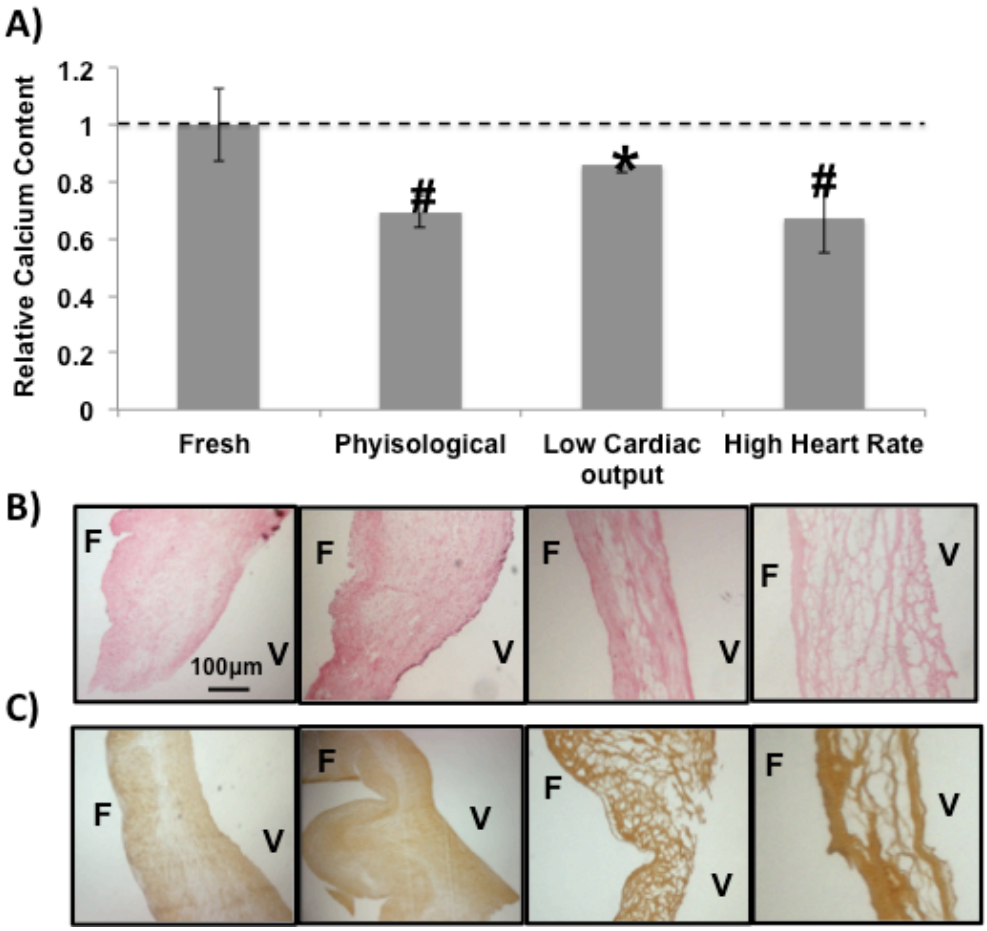

Figure 3.9 Realistic shear stress and AV calcification.
A) Calcium content in the fresh tissue tended to be higher than tissues exposed to physiological and high HR conditions (n=8, #p<0.1), but not the low CO condition. Calcium content in tissue exposed to the low CO condition was significantly higher compared to that of the physiological condition. n=8, *p<0.05. B) and C) Von Kossa and Alizarin Red stain confirmed that there was no calcification in tissues exposed to realistic shear stresses. Fresh AV samples were included as controls. F: fibrosa, V: ventricularis. n=4. Representative scale bar is shown only on fresh sample.

3.5.3 Calcification induced by shear stress compared to stretch and pressure

The extent of AV calcium induced by the low magnitude oscillatory shear stress was compared to that of elevated (15%) cyclic stretch or hypertensive (160/100 mm Hg) pressure (Figure 3.10). The calcium induced by the hypertensive

pressure or elevated stretch was significantly higher than that induced by low magnitude shear stress ($p<0.05$). The calcium induced by the hypertensive pressure, however was higher than that of elevated stretch ($p<0.1$), but did not reach statistical significance of 0.05. Significantly higher amount of calcium was observed when the AV leaflets were subjected to combined elevated stretch and hypertensive pressure ($p<0.05$).

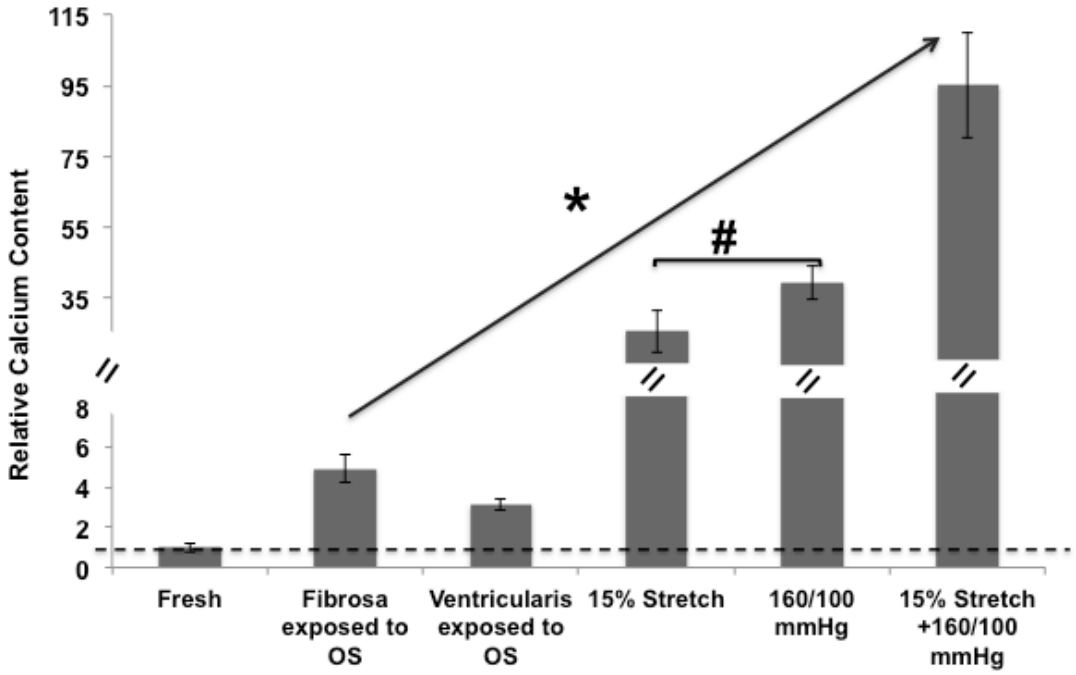

Figure 3.10 AV calcification induced by stretch, pressure and shear stress. Calcium levels induced by 15% (elevated) stretch or 160/100 mmHg (hypertensive) pressure or combined stretch and pressure was significantly higher than that induced by the low oscillatory shear stress. n=4-8, *$p<0.05$. The calcification induced by 160/100 mmHg (hypertensive) pressure tended (#$p<0.1$) to be higher than 15% (elevated) stretch alone. Shear experiments were run for 7 days whereas the stretch and pressure data was from 8 days experiments.

3.5.4 Cell apoptosis of AV exposed to idealized shear stress

Apoptosis of cells in tissues cultured in osteogenic media was investigated (Figure 3.11). After 3 days in culture, fibrosa or ventricularis exposed to OS showed no apoptotic cells. Increased apoptotic cells were observed in fibrosa exposed to OS after 7 days of culture.

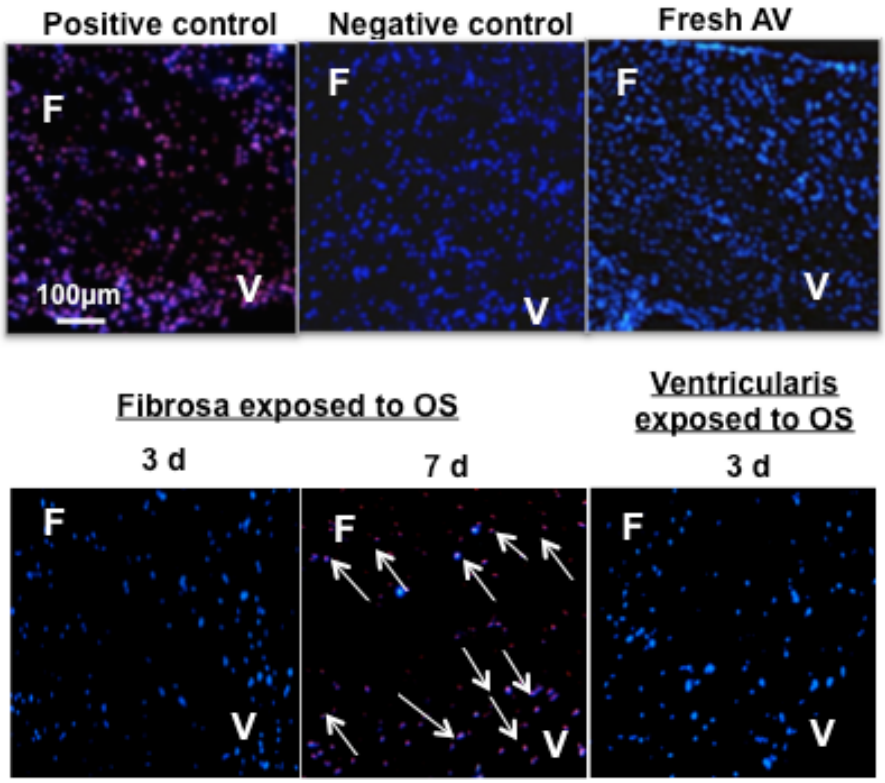

Figure 3.11 Shear stress and AV apoptosis.
Idealized shear stress and apoptosis Positive control for TUNEL showed excessive apoptosis (red). Negative control for TUNEL stain showed no signs of apoptosis. No apoptotic cells were observed when fibrosa or ventricularis was exposed to OS for 3 days in osteogenic media. However, after 7 days, tissues in fibrosa when exposed to OS had quite a few apoptotic cells (arrows point to red). Fresh sample in included as a control and show no signs of apoptosis. F: fibrosa, V: ventricularis. n=3. Representative scale bar is shown only on positive control.

3.5.5 Effect of idealized shear stress on AV extracellular matrix structure

The Verhoeff-Van Gieson elastin stain shows that the tri-layered composition of the AV extracellular matrix was overall preserved between all culture conditions (Figure 3.12A and B). Compared to the fresh AV leaflets, the collagen fiber bundles appeared more loosely packed when fibrosa was exposed to OS or LS. These collagen bundles were also aligned along the length of the tissue, when the fibrosa was exposed to LS. Quantitatively, the thickness of fibrosa layer exposed to OS increased ($p=0.0571$) compared to that of fresh or statically cultured tissue by 15.4% and 17.8% respectively. LS did not change the thickness of the fibrosa.

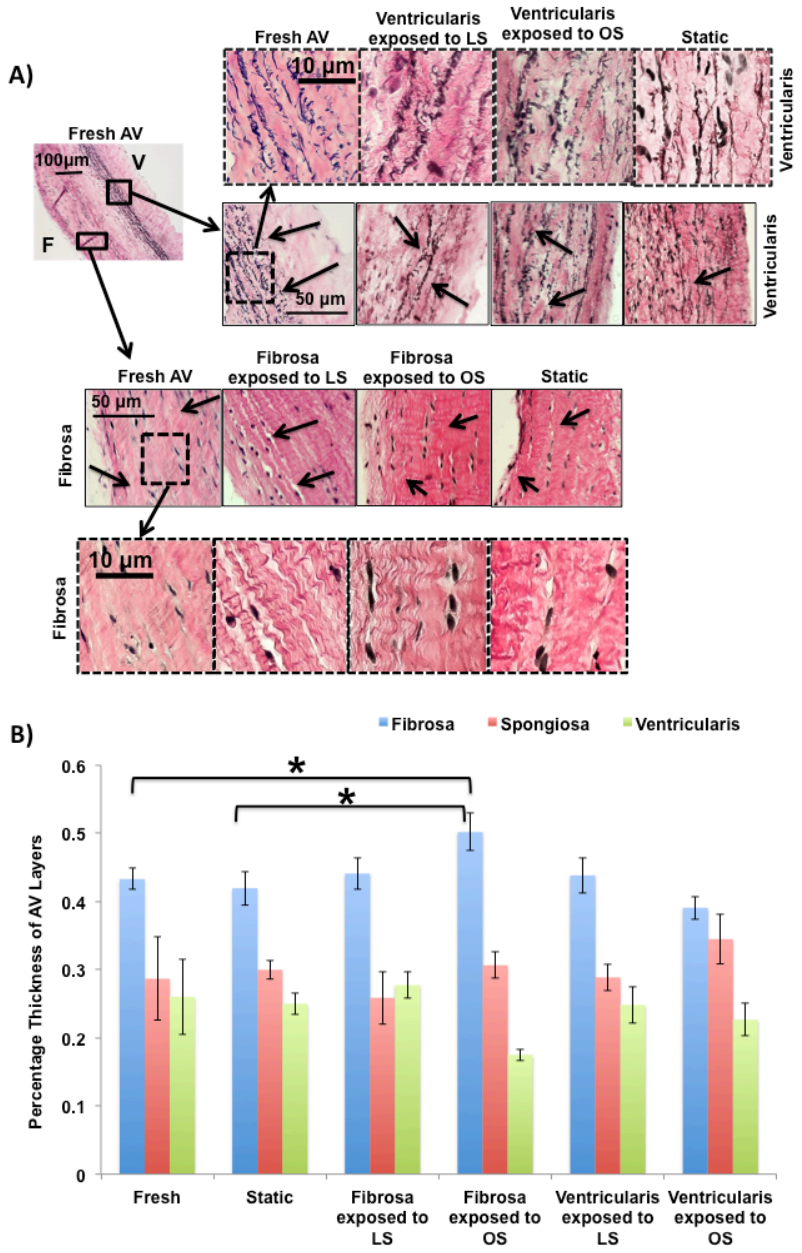

Figure 3.12 Shear stress and AV ECM.

A) Fibrosa or ventricularis side of the AV exposed to OS and LS displayed histological changes in collagen and elastin fiber distribution compared to fresh and statically cultured tissue samples. The higher magnification images highlight these changes. B) Quantification of each of the three layers of AV ECM in response to OS and LS. Thickness of the fibrosa increased significantly in fibrosa exposed to OS compared to the fresh or static (*p=0.0571), while the thickness of ventricularis and spongiosa remained unaltered. (n=4). Representative scale bar is shown only on fresh samples.

The elastin fibers were aligned along the length of the valve tissue and the alignment was preserved when the ventricularis side was exposed to LS. Elastin fibers appeared fragmented, and spaced out, when the ventricularis was exposed to OS. The thickness of the ventricularis layer, however, remained unaffected when exposed to OS or LS, compared to the fresh and statically cultured tissue. The spongiosa was preserved in all shear conditions both qualitatively and quantitatively. Although, the thickness of all three layers was preserved in static culture compared to the fresh tissues, the architecture of the layers however, differed slightly.

Picrosirius red collagen stain showed that the percentages of different collagen fibers varied in response to different shear stresses (Figure 3.13A and B). As indicated earlier, the red/orange, yellow and green fibers represent mature/thick, young and nascent collagen fibers respectively. No significant differences were observed between the static culture and fresh AV leaflets. Fibrosa exposed to OS showed most changes in the maturity of the collagen fibers. Specifically, young collagen fiber content increased in fibrosa exposed to OS compared to ventricularis exposed to OS (1.95 fold, #p=0.09) and statically cultured AVs (1.04 fold, *p=0.041). The mature and nascent collagen fiber content was preserved in all culture conditions. Thus, overall, OS induced most changes in the collagen fiber maturity compared to the LS.

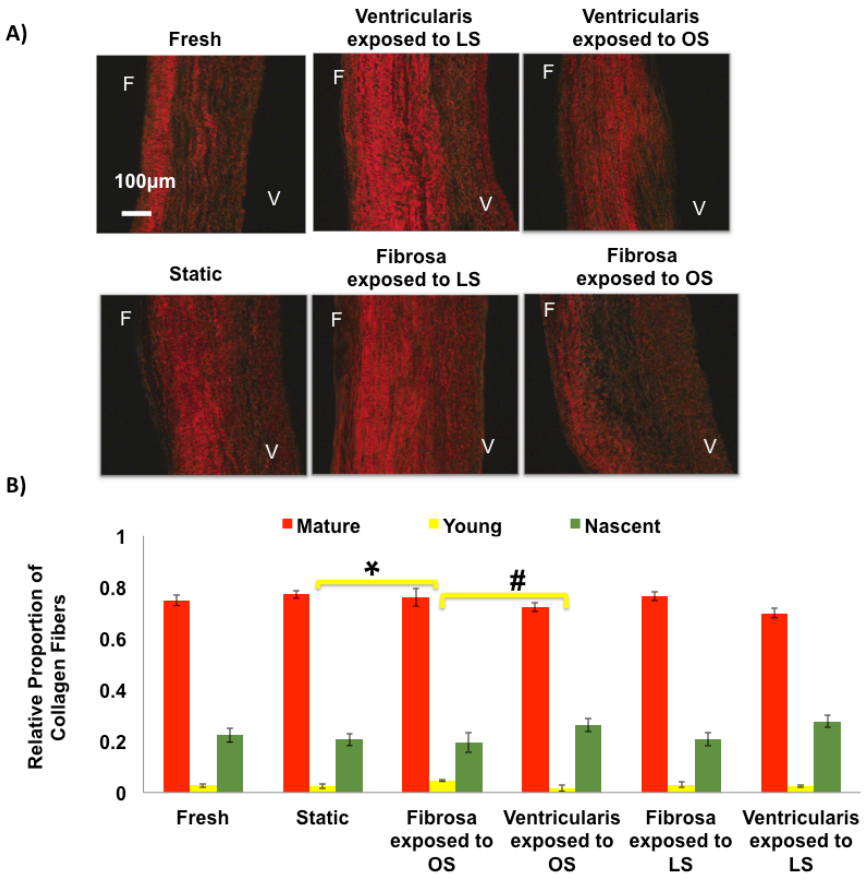

Figure 3.13 Shear stress and AV collagen distribution.
A) Picrosirius red staining showed different proportions of collagen fibers (red, yellow and green) in AV tissues exposed to different shear conditions. F: fibrosa, V: ventricularis. B) Quantification of relative proportions of collagen fibers showed that most changes were observed in fibrosa when exposed to OS. Specifically, young collagen fiber content increased in fibrosa exposed to OS compared to ventricularis exposed to OS (1.95 fold, #p=0.09) and statically cultured AVs (1.04 fold, *p=0.041). The mature and nascent collagen fiber content was preserved in all culture conditions. n=6. Representative scale bar is shown only on fresh sample.

3.5.6 Gene expression changes in AV in response to idealized shear stresses

The AV cell phenotypic change was assessed with smooth muscle α-actin, *Sma*. The change in ECM was also assessed with collagen type-I (*Col1a1*). As shown in the Figure 3.14A, *Col1a1* was upregulated in fibrosa when exposed to OS, but

not LS (p=0.1). This increased expression of *Col1a1* could possibly be the explanation for the previously observed increased thickness of fibrosa in response to OS compared to other conditions. As shown in Figure 3.14B, *Sma* was downregulated in a side-dependent manner in the fibrosa compared to the ventricularis, when exposed to their respective shear stresses (p=0.1). The expression of *Sma* or *Col1a1* did not change in the ventricularis when exposed to OS or LS (Figure 3.14C and D).

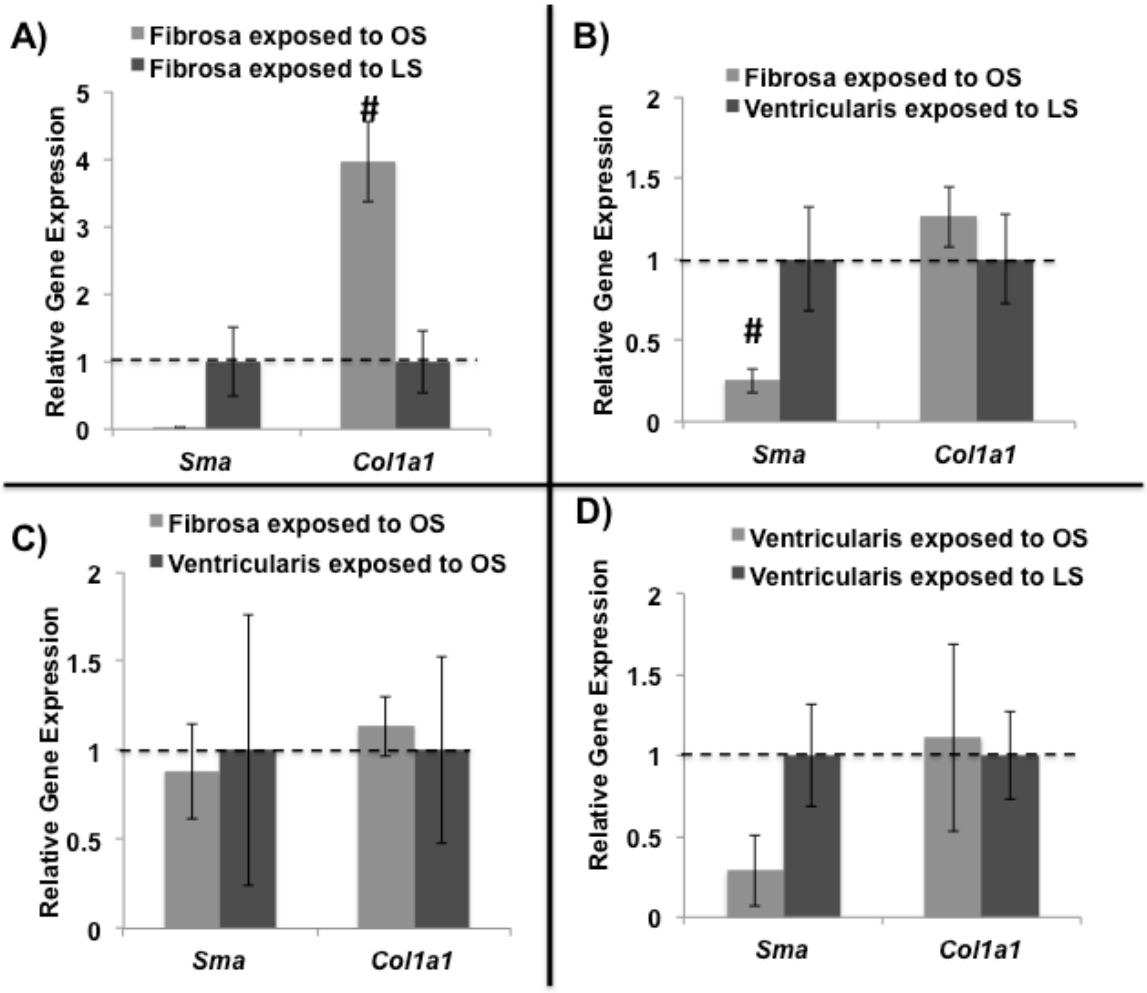

Figure 3.14 Shear stress and AV phenotype and collagen turnover.
A) High expression trend of *Col1a1* was observed only in fibrosa exposed to OS vs. LS. B) Low expression trend of *Sma* was observed only in fibrosa exposed to

OS compared to ventricularis exposed to LS. C) and D) No changes observed in *Sma* and *Col1a1*. n=3 (pooled 3 samples/isolation), #p< 0.1.

3.5.7 Identification of side – and shear – dependent miRNAs in AV

The expression of miRNAs 181a, 181b, 214 and 199a-5p was determined in AV leaflets when exposed to idealized shear stresses *ex vivo*. As shown in the Figure 3.15A the expression of miR-181a and miR-214 was upregulated in fibrosa when exposed to OS vs. LS. Interestingly, this OS effect was not observed in the ventricularis (Figure 3.15B). When compared to the ventricularis samples (LS or OS), fibrosa under OS showed significantly higher miR-214 and miR-181a expression (Figure 3.15C and D). This result indicates that miR-214 and miR-181a are preferentially upregulated in fibrosa, but not in ventricularis, consistent with the array data using fresh porcine AV leaflets (*124*). However, only miR-199a-5p showed significantly higher expression in ventricularis, in a shear-dependent manner, in response to OS vs. LS (Figure 3.15B).

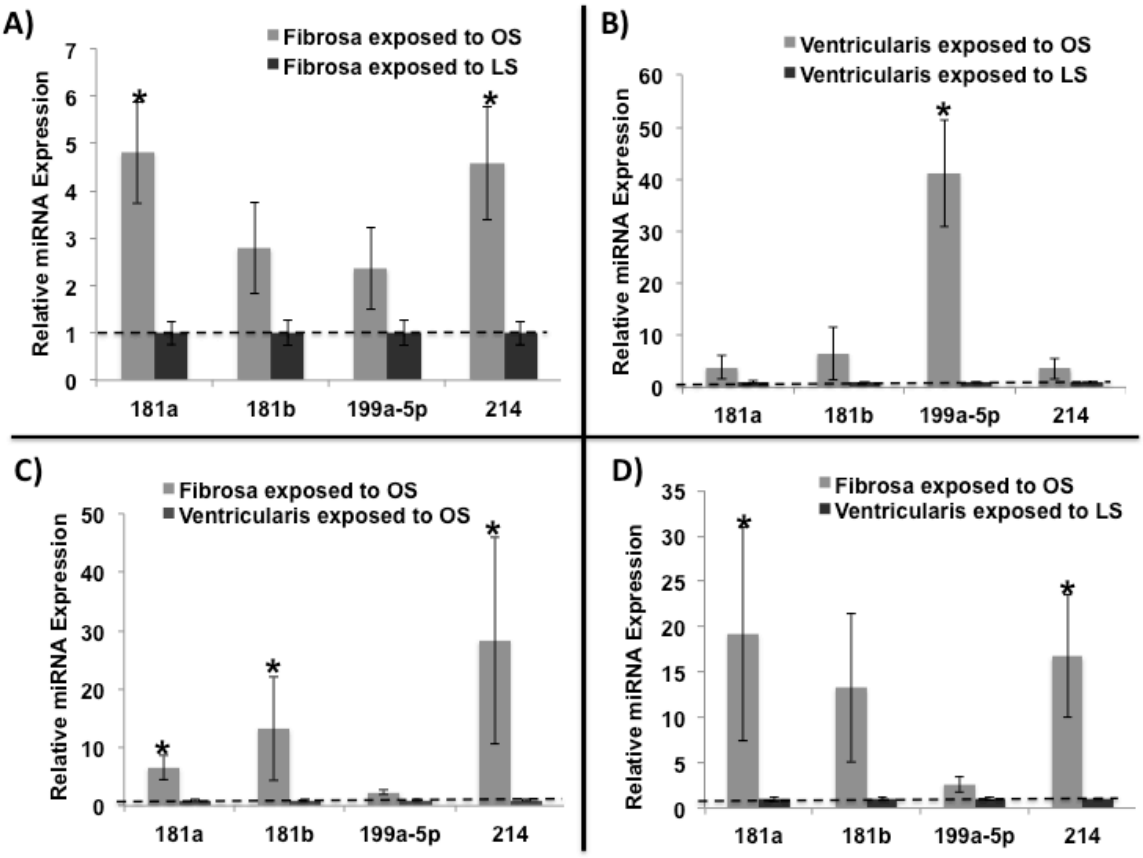

Figure 3.15 Shear- and side-dependent miRNAs in AV.
A and B) Two out of four miRNAs, miR-214 and miR-181a were expressed significantly higher in fibrosa but not ventricularis when exposed to OS vs. LS. C and D) Compared to ventricularis exposed to OS or LS, fibrosa exposed to OS showed significantly high expression of miR-214 and miR-181a. n=6 (pooled 3 samples/isolation), *p<0.05.

The expression of miRNAs (181a, 181b, 199a-5p and 214) in fibrosa when exposed to OS was compared to statically cultured and freshly isolated AVs as well (Figure 3.16). Only this shear condition was chosen because the expression of miRNAs changed the most compared to other shear conditions (Figure 3.15). Only miR-199a-5p showed significantly higher expression ($p<0.05$) in fibrosa

exposed to OS compared to static condition. However miRNAs, miR-181a and miR-214 showed significantly higher expression in fibrosa exposed to OS compared to fresh samples. Between fresh and statically cultured samples, miR-199a-5p expression decreased in static samples ($p<0.1$) whereas the expression of miR-214 was significantly higher ($p<0.05$) in static culture.

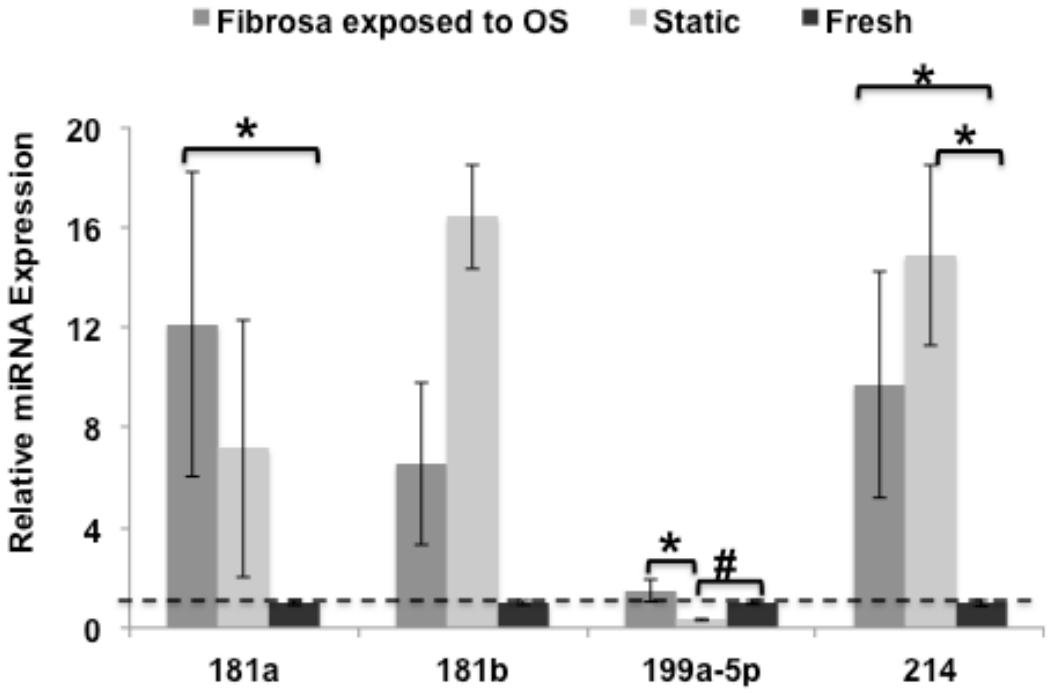

Figure 3.16 Expression of mirNAs in fresh and static AV tissues.
Only two miRNAs-181a and 214 were significantly higher in fibrosa when exposed to OS compared to fresh AV tissues. Only miR-199a-5p showed significantly higher expression in fibrosa exposed to OS condition compared to static culture. Fibrosa exposed to OS: n=6 (pooled 3 samples/isolation), static and fresh: n=3 (pooled 2 samples/isolation) *$p<0.05$, #=0.1.

Thus, overall, miR-181a and miR-214 were expressed significantly higher in fibrosa only when exposed to OS compared to all other conditions and fresh samples. These two miRNAs thus showed side-dependency (fibrosa exposed to OS vs. ventricularis exposed to LS) and shear-dependency in fibrosa side (OS vs. LS), but not in ventricularis (OS vs. LS). Hence miR-181a and miR-214 were chosen for further investigation.

3.5.8 Identification of potential mRNA targets of side- and shear-dependent miRNAs

To discover potential, shear-sensitive, side-specific mRNAs that are regulated by miR-181a and miR-214, an in-depth bioinformatics analysis was carried out, as outlined in the Figure 3.6. Following this approach, the mRNA targets filtered for miR-181a and miR-214 were 26 and 16 respectively and are listed in Table 3-2. The miRs-214 and 181a potentially regulate very critical genes that are well known to be involved in AV pathophysiology. As evident from Table 3-2, most of the targets of miR-214 are well known and involved in AV cell phenotype, apoptosis, development, extracellular matrix regulation, inflammation and calcification, the events that are very important in AV disease. Based on this observation, miR-214 was chosen for further investigation.

Table 3-2 Filtered Targets of miR-181a and miR-214.

miR-181a	**miR-214**
AHSA1	TGFBR2
IL6	KLF4
KRAS	JAG1
LYN	IKBKB
RGS4	COL1A1
SCD	NOS3
TGFBI	ACTA2
TLR4	KRAS
TRIM13	CTNNB1
OPN	BCL2L11
ATM	EZH2
BCL2	MAP2K3
BCL2L11	MAPK8
MCL1	PTEN
CDKN1B	SRGAP2
GATA6	TWIST1
NLK	
SIRT1	
FOS	
PLAG1	
CDX2	
HIPK2	
RALA	
LFNG	
PUM1	
NTS	

To further understand the function of miR-214 in this side-dependent AV disease, six mRNA targets were chosen from its filtered targets. These mRNA targets are *Sma*, *Ctnnb1*, *Enos*, *Klf4*, *Bcl2l11*, and *Col1a1* and the related Kyoto Encyclopedia of Genes and Genomes, (KEGG) pathways are listed in Table 3-3.

Table 3-3 KEGG pathways related to selected mRNA targets.

Gene	**KEGG Pathway(s)**
NOS3 or *Enos*	Arginine and proline metabolism, Calcium signaling pathway, VEGF signaling pathway
BCL2L11	FOXO signaling pathway, Non-alcoholic fatty liver disease, PI3K-Akt signaling pathway
ACTA2 or *Sma*	Vascular smooth muscle contraction
COL1A1	Focal adhesion, ECM-receptor interaction
KLF4	Signaling pathways regulating pluripotency of stem cells
CTNNB1	Wnt signaling pathway, Focal adhesion, Adherens junction, Tight junction, Leukocyte transendothelial migration, Melanogenesis, Pathogenic Escherichia coli infection, Pathways in cancer, Colorectal cancer, Endometrial cancer, Prostate cancer, Thyroid cancer, Basal cell carcinoma, Arrhythmogenic right ventricular cardiomyopathy

These targets are well known for their functional role in AV pathology. Briefly, *Sma*, determines the contractility and phenotype of valvular cells (*143*). Catenin beta-1 or β-catenin **(***Ctnnb1*) is required in embryonic cushion development of the AV (*144*), but its increased expression can induce pathogenesis in adult valves (*145*). A well-known atheroprotective gene, nitric oxide synthase 3 or *Enos*, is anti-inflammatory, and protects the valvular endothelium from calcification (*146*). Apoptosis facilitator, *Bim* or *Bcl2l11* belongs to the family of *Bcl2* and activates the production of reactive oxygen species (*147*). Kruppel-like factor 4, *Klf4* regulates the promoter activity of anti-inflammatory and anti-thrombotic factors and thus, protects vascular endothelium (*148*). Flow-dependent differential expression of *klf4* is also observed in bicuspid compared to tricuspid AV valve (*149*). Finally collagen type I, *Col1a1*, is predominant in AV matrix and its increased expression (observed in calcified AV tissues) indicates high ECM turnover (*150*).

3.6 Discussion

The major findings of this chapter are 1) Low magnitude oscillatory shear stress induced calcification in the fibrosa compared to the ventricularis, but this calcification was not as severe as that induced by elevated stretch or hypertensive pressure; 2) Most changes in the AV ECM and cell phenotype were induced by OS; 3) two out of four miRNAs, miR-214 and miR-181a were highly expressed in the fibrosa exposed to OS compared to other shear conditions and showed side- and shear-dependency in the fibrosa side; and 4) bioinformatics

analysis showed that miR-214 had potential targets that are involved in early stages of AV disease progression.

3.6.1 OS induced side-dependent AV calcification

The aortic valve experiences differing shear stress profiles on either sides of the valve that could play a potential role in its side-dependent calcific AV disease. Both idealized (or theoretical) and realistic (or experimental) shear stress paradigms exist in the literature and have been tested in this chapter to establish a calcification model using shear stress *ex vivo*. The objective of developing this model was to be able to induce early and later stages of AV calcification in a side-dependent manner. Our results showed that using an established osteogenic media, the idealized shear stress paradigm works very well in developing calcification preferentially in the fibrosa compared to the ventricularis. This preferential calcification in the fibrosa required both low magnitude (5 dyne/cm^2) and oscillatory nature (+/-) of the shear stress, as no calcification was observed when the fibrosa was exposed to the steady shear stress alone (5 dyne/cm^2). Increased apoptosis of AV with the increased calcification could be mediated by TGF-β1 (present in the osteogenic media), as demonstrated by Jian et al (*151*). However, the hypertensive pressure and elevated stretch can cause greater damage to the valve leaflets than the low magnitude oscillatory shear stresses. On the contrary, this low magnitude oscillatory shear stress is the primary stimuli involved in the atherosclerosis of blood vessels (*152*). This is an important distinction and further investigation can help us understand the

mechanistic differences between the shear stress induced calcification in the AV compared to the atherosclerosis in the blood vessels.

On the other hand, the realistic (or experimental) shear stresses did not induce any calcification in AV leaflets, which could be attributed to the lack of flow reversal in the shear stresses experienced by the fibrosa side. These results also suggest that the calcification media used in this specific aim must be reformulated in order to develop a side-dependent calcification model using the realistic shear stress paradigm. So, based on the calcification results, idealized shear stress profile was chosen for further investigation in this specific aim.

3.6.2 OS Induced most changes in the AV ECM

Early changes induced in AV leaflets when exposed to the idealized shear stress profile were investigated by assessing the changes in the AV extracellular matrix and cell phenotype. The components of AV ECM provide much needed mechanical strength to maintain the functionality of the valve under rigorous conditions of the cardiac cycle. Overall tri-layered structure of the AV tissues was preserved in all shear and static conditions; but microscopically, noticeable histological changes within these layers were observed.

On the ventricularis side, LS maintained the native structure of elastin fibers while OS caused its disruption. Although physiologically, the fibrosa and the ventricularis side never experience LS and OS respectively, these results

reiterate the sensitivity of the valve extracellular matrix to the changes in its mechanical environment.

Low oscillatory shear stress reduced the activation of valvular interstitial cells as evident by the low expression of *Sma* in the fibrosa in a side-dependent manner (fibrosa exposed to OS vs ventricularis exposed to LS), consistent with a previous study (*153*). Cyclic pressure also had the same effect as OS, and decreased the protein expression of SMA (*83*), which was restored, only when combined with the elevated cyclic stretch. While the valve interstitial cells continuously attempt to respond and adapt to its mechanical environment, similar to the calcification result observed in Figure 3.10, different mechanical stimuli (shear, pressure and stretch) act in synergy to maintain the overall expression of *Sma*.

Thus changes in valve cell phenotype (*Sma),* collagen fibers, increased collagen type-1 (*Col1a1*), combined with increased thickness of fibrosa (all being the indicators of valve ECM remodeling), were noticed only in fibrosa in response to OS but not LS. These changes observed in the ECM composition and its related genes can also potentially affect the miRNA expression and vice versa (*121*).

3.6.3 OS induced most changes in miRNA(s) expression in fibrosa

Native AV leaflets express inflammation and calcification markers on the fibrosa, making it predisposed to disease (*24*). This differential gene expression on either

sides of the valve could be in part be regulated by the side-dependent miRNAs, identified in a recent study (*124*). Our results showed that, of the four miRNAs tested, two miRNAs, miR-181a and miR-214 showed significant side- and shear-dependency in the fibrosa but not the ventricularis. Although miR-199a and miR-214 are clustered(*154*), it appears that only miR-214 is shear-responsive in AV leaflets. Further, these two miRNAs, miR-214 and miR-181a, as discussed earlier, are heavily involved in the processes that are relevant to AV disease such as inflammation, apoptosis, cell differentiation, migration and calcification (*12, 13, 125, 126, 129, 141, 142*). Their increased expression in the fibrosa side in response to OS could either be an adverse or a protective response; suggesting their possible involvement in side-dependent AV disease. This idea is supported by their lower expression on the ventricularis, which was consistently maintained regardless of the shear stress (OS or LS). These two miRNAs are perhaps not shear-sensitive in the ventricularis side and support the observation that the gene expression of endothelial cells is different on either side of the aortic valve (*22, 24*).

3.6.4 Side- and shear- dependent miRNA, miR-214 is potentially involved in AV pathology

The experimentally validated targets of miR-214 and miR-181a were identified and filtered using the existing shear and side-dependent mRNA databases to identify one key miRNA for further investigation. Interestingly, miR-214 has potential targets such as *Ctnnb1, Sma, and Col1a1* that are highly expressed in

the calcified AV leaflets (*143, 145, 150*). The oscillatory shear stress induced changes in the expression of *Col1a1* and *Sma* observed in the previous section 3.5.6, is probably associated with the changes in the miR-214 expression as well. Thus, in the presence of OS, miR-214 can potentially be involved in a feedback mechanism with the changes in the ECM structure (Figure 3.13) and its related genes. Since miR-214 also inhibits the bone formation (*14*) and is associated with the coronary artery disease (*15*), it could play a similarly important role in AV calcification. All of this evidence allows us to hypothesize that the miR-214 is a key side- and shear- dependent miRNA that plays an important role in the fibrosa side, by potentially targeting the genes involved in the pathogenesis of side-dependent AV disease.

3.7 Limitations

No calcification was observed when the AV leaflets were exposed to altered hemodynamics that could be attributed to the lack of flow reversal on the fibrosa side. Thus, there is a need to modify the existing osteogenic media to develop a side-dependent calcification model using the physiologically relevant realistic shear stresses. In this case, culture durations longer than 7 days may be necessary to induce calcification (*17*). Also, the miRNAs identified using the idealized shear stress paradigm may behave differently in *in vivo* scenario, where the stretch and pressure are also present. Despite these limitations, our *ex vivo* shear studies provide a critical experimental platform to determine the role of shear in regulating gene expression in a side-dependent manner, while excluding

numerous other complex systemic changes that occur *in vivo* such as blood and circulating factors.

3.8 Conclusions

The results of this study demonstrated that low magnitude oscillatory shear stress preferentially alters the extracellular matrix architecture, and cell phenotype on the fibrosa. The OS also created a pro-calcific environment that predisposed the fibrosa to early onset of disease compared to the ventricularis. The impact of low magnitude oscillatory shear stress on AV calcification was not as severe as that of pathological stretch or hypertensive pressure.

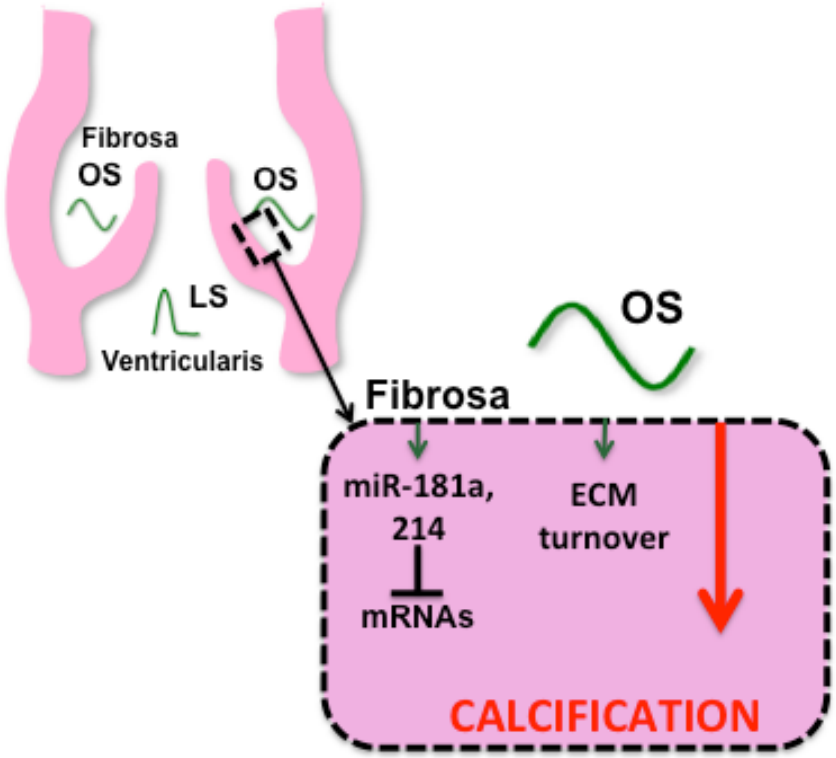

Figure 3.17 Schematic showing the conclusions of specific aim 1.

Thus, pathological stretch and pressure can induce even greater damage to AV compared to OS. Two miRNAs, miR-214 and 181a were side- and shear-dependent in the fibrosa side compared to the ventricularis. Based on the targets regulated by these miRNAs, the miR-214 could be a key miRNA involved in this side-dependent AV disease.

CHAPTER 4 DETERMINATION OF THE RELATIONSHIP BETWEEN A KEY SIDE- AND SHEAR-DEPENDENT MIRNA AND AORTIC VALVE PATHOGENESIS

4.1 Summary

The oscillatory shear stress can induce the side-specific aortic valve disease via microRNA(s) (miRNA) dependent pathway. Identification of these miRNAs and its regulated genes could uncover potential mechanisms involved in AV inflammation and calcification. A key miRNA, miR-214, that is also both side- and shear-dependent in AV (identified in specific aim-1), was selected to investigate this possibility. Selected gene targets of miR-214 were tested for their side- and shear-dependency as well. Of these 6 potential targets, overall 5 genes (*Klf4, Enos*, *Ctnnb1*, *Bcl2l11, Sma*) showed a downregulation in fibrosa when exposed to OS, also indicative of the pro-inflammatory environment induced by OS. These genes also displayed an inverse relationship with miR-214 in fibrosa exposed to OS. Further, a successful miRNA silencing protocol was developed to validate these gene targets and to investigate the functional role of miR-214 in AV. Silencing miR-214 in the fibrosa exposed to OS, significantly upregulated *Klf4* and tended to increase *Sma.* Further miR-214 in fibrosa exposed to OS, also tended to increase *VE-Cadherin* and significantly decreased *Tgfβ1,* suggesting its role in AV fibrosa and sclerosis. The silencing of miR-214, however, did not have a significant effect on AV inflammation and

calcification in fibrosa, induced by OS. Thus, miR-214 could play an important role in AV fibrosis and sclerosis.

4.2 Introduction

Calcific AV disease preferentially occurs in the fibrosa and can be attributed to the higher expression of pro-inflammatory and pro-calcific genes observed in the fibrosa as compared to the ventricularis (*24*). The oscillatory shear stresses observed in the fibrosa, can further enhance the expression of these genes and induce inflammation, endothelial-to-mesenchymal transition (Endo-MT), and increased oxidative stress (*44, 114, 146, 155*). However, the mechanisms by which the oscillatory shear stress initiates these pathological changes in a side-dependent manner are not well understood. Lack of therapeutic treatment of AV calcification places an increasing demand on uncovering these disease mechanisms.

The miRNAs are master regulators of gene expression and their involvement in various cardiovascular diseases is recognized (*156, 157*). Recent studies have reported the contribution of miRNAs in AV disease as well (*106*). Similar to the vascular endothelial cells (*157*), the AV endothelial cells respond to disturbed or uniform flow by varying the expression of miRNAs (*124*). Although there is a growing body of evidence suggesting the involvement of miRNAs in AV calcification, the function of these miRNAs remains largely unknown. One such key miRNA is miR-214, which was identified in specific aim-1 as shear- and side-dependent regulator in AV. The expression of miR-214 is significantly increased

in fibrosa in response to the oscillatory shear stress; however, the downstream mechanisms regulated by miR-214 in AV are unknown. Based on the literature evidence, miR-214 is involved in key cellular processes that are very relevant to calcific AV disease progression. Briefly, miR-214 plays a role in cell proliferation (*138, 139*), cell death(*136, 140, 141*), cell cycle (*138*), cell migration (*140, 142*), and inflammation (*136, 139, 141*). MiR-214 is also involved in fibrosis (*12*), epithelial-to-mesenchymal transition (*158*), osteogenic differentiation (*14*), and is correlated to the coronary artery disease (*15*). Thus, miR-214 may play a similarly important role in AV disease. This chapter focuses on investigating the cellular processes activated by miR-214 in fibrosa, in response to OS. Understanding the function of miR-214 can expose potential molecular mechanisms underlying side-dependent AV sclerosis, inflammation, and calcification and possibly serve as AV disease biomarker.

4.3 Hypothesis

The hypothesis of this specific aim is that *miR-214 modulates the genes involved in AV sclerosis, inflammation and calcification in a side- and shear-dependent manner.*

4.4 Materials and methods

4.4.1 Overall work flow and experimental plan

The overall workflow of this specific aim is outlined in Figure 4.1. The miR-214 is a side- and shear-dependent miRNA and is highly expressed in fibrosa when exposed to oscillatory shear, compared to all other shear conditions. The side- and shear-dependency of selected mRNA targets of this miRNA (filtered and identified in specific aim-1) was determined. The *ex vivo* cone and plate shear bioreactor used for these studies is detailed in section 4.4.3 and the shear conditions used are descried in 4.4.4. The general experimental setup is also described in 4.4.5 and specific experimental details are detailed in 4.4.6. The expression of mRNA targets was assessed using qPCR as detailed in sections 4.4.11 through 4.4.14. Based on these experiments, the mRNA targets that showed an inverse relationship with miR-214 expression (in the fibrosa exposed to oscillatory shear) were chosen for further validation.

To assess the functional role of miR-214 in AV pathophysiology, the miR-214 silencing studies were performed. An anti-miR delivery protocol was developed to silence the miRNA *ex vivo* using statically cultured AV leaflets (4.4.7). The delivery efficiency of anti-miR in AV leaflet tissue was assessed using a tagged non-targeting (NT) anti-miR and confocal microscopy. TUNEL stain was done to ensure that the transfection of anti-miR did not affect the cell viability (4.4.10.2). The expression of miR-214 after the silencing experiment was assessed using qPCR (4.4.11 through 4.4.14).

The same miRNA silencing protocol was adapted to silence the miR-214 in fibrosa, when exposed to oscillatory shear (4.4.8), as the miR-214 is upregulated in fibrosa exposed to oscillatory shear compared to all other conditions. Post silencing of miR-214 in sheared leaflets (fibrosa exposed to oscillatory shear), the miR-214, and the selected mRNA targets were assessed using qPCR as well (4.4.11 through 4.4.14). The effect of miR-214 silencing on AV endothelial-to-mesenchymal transition, inflammation and calcification was assessed to further understand the role of miR-214 in AV pathophysiology (4.4.9).

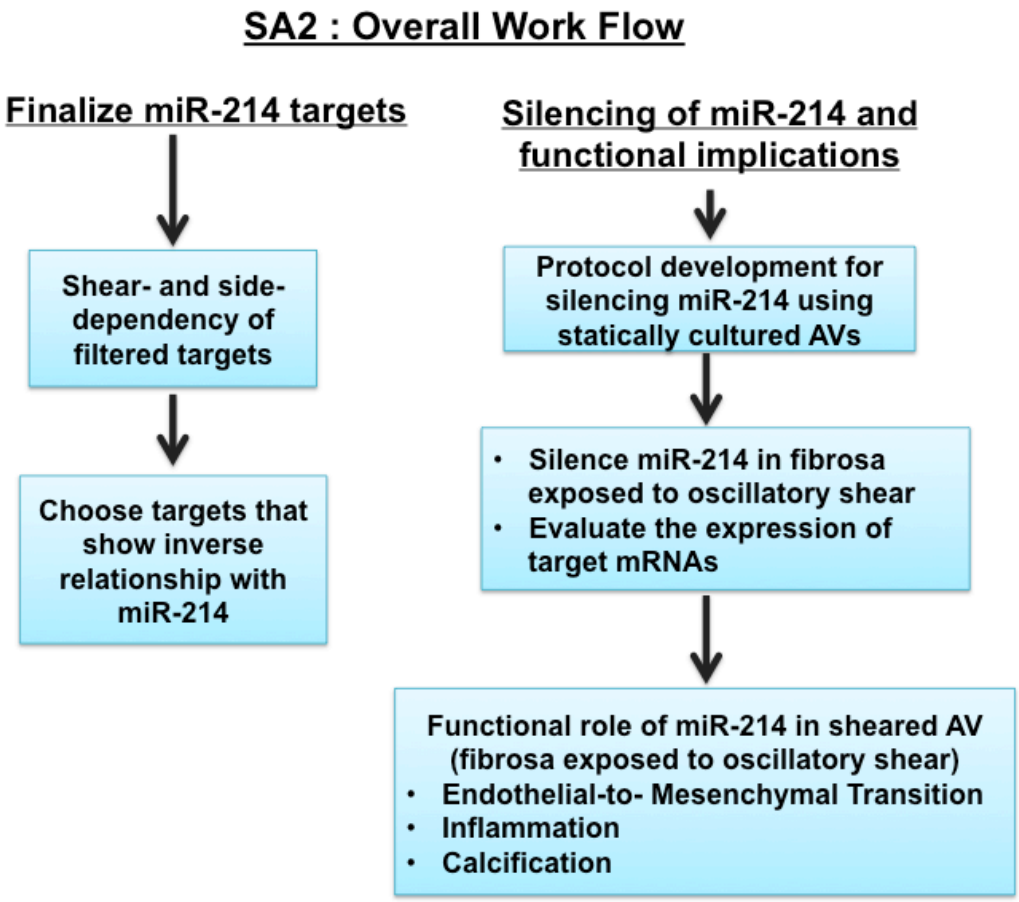

Figure 4.1 Flow chart of overall workflow of specific aim-2.

4.4.2 Aortic valve tissue harvest

Hearts were obtained from healthy, female, non-pregnant pigs (aged 6 to 12 months) immediately after slaughter from a local abattoir (Holifield Farms, Covington, GA). The AV leaflets were immediately excised and thoroughly rinsed in sterile nuclease-free Dulbecco's phosphate buffered solution (dPBS; Sigma-Aldrich, MO) at 4 ^{o}C. Valves were placed in nuclease-free dPBS on ice and transported back to the laboratory. Upon arrival in the laboratory, dissected AVs

were transferred to clean, sterile dPBS at 4 ^{o}C under the sterile laminar flow hood and processed accordingly.

4.4.3 Ex vivo *cone and plate shear stress bioreactor*

An *ex vivo* shear stress bioreactor was used to study the effect of shear stresses on the AV leaflets in a side-dependent manner. This bioreactor has been designed and extensively validated to expose AV tissues to well-defined shear stress profiles (*52*). It is a modification of the cone and plate viscometer. Briefly, as shown in Figure 4.2, the bioreactor consists of a dish with a plate at the bottom, where the valve leaflet tissues are held. In addition, a cone angled at 0.5^{o} is placed at 200 μm above the plate. A programmable servomotor is coupled to this cone and it rotates the cone depending on the specific shear stress program. The device can hold 9 tissue samples of diameter 7 mm. The motors were programmed by the Motion Planner© software (version 4.3.2.0, Parker Hannifin Corp, CA). A perfusion system consisting of a reservoir of media, powered by a slow moving peristaltic pump (Model SP202.100, APT Instruments, IL) was installed to continually re-circulate the media within the cone and plate bioreactor.

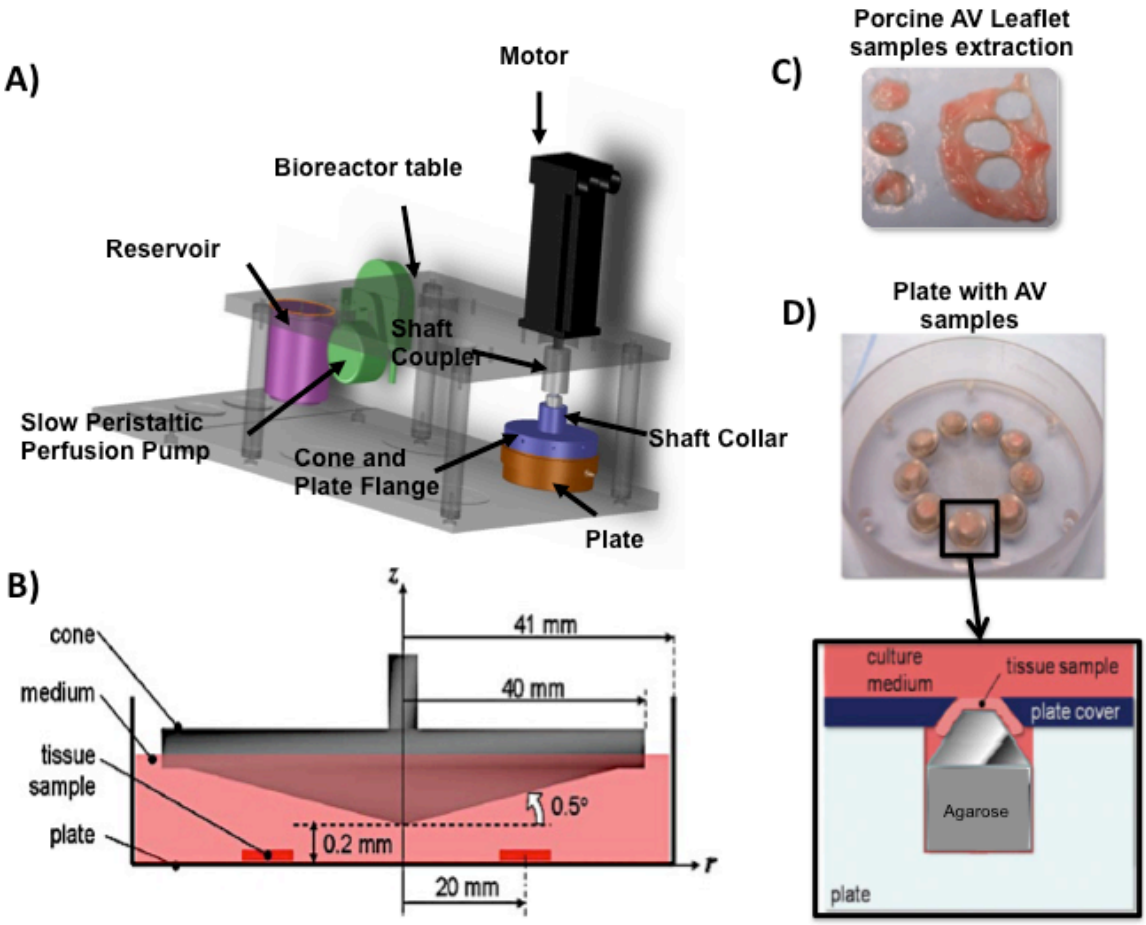

Figure 4.2 Ex vivo shear system for miRNA functional studies.
A) The cone and plate bioreactor setup. It consists of a rotating cone (via motor) on top of a stationary plate (with AV samples). The perfusion system maintains constant flow of media in the cone and plate set up. The whole set up is held in a bioreactor table and can be placed in an incubator. B) Schematic of the cone and plate only. The plate can fit 9 AV samples, all placed at a radial distance of 20 mm from the center of the cone. C) Samples extracted from AV leaflet tissue. D) Plate with 9 samples and the highlighted portion shows agarose filled into the well that holds tissue samples.

The rotating cone rotates the media between the cone and plate and imparts the shear stress to the surface of the AV tissues in the circumferential direction.

Shear stress on the plate is calculated by the formula, $\tau_w = \rho\nu\omega\left|\frac{r}{h+r\alpha}\right|$, where τ_w is the wall shear stress, ρ and v are the density and the viscosity of the fluid, ω is the angular velocity of the cone, and r is the radial coordinate of shear stress calculation on the plate, h is the gap between the apex of the cone and the plate, and α is the cone taper angle, which is 0.5^o. This equation for calculating shear stress experienced by the plate has been validated by computational fluid dynamics simulations of the cone and plate bioreactor, as well as by Laser Doppler Velocimetry measurements of the apparatus (*52*). Further, the actual rotational velocity measured by the tachometer on the motor was shown to match the desired velocity programmed into the controller. The cone was coupled to a servomotor (Model SM232AE-NPSN Brushless Servo Motor, Parker Hannifin Corp., Rohnert Park, CA), which was controlled by a servo drive (Model GV6K Gemini Servo, Parker Hannifin Corp., Rohnert Park, CA). Additional details of this bioreactor are explained in-depth in appendices A.1 and A.2.

4.4.4 Shear stress conditions

The most commonly used idealized shear stress paradigm was used in this specific aim (*48, 102, 112*). The ventricularis side experiences pulsatile unidirectional shear stress (LS) of 0-79 dyne/cm^2, with a peak magnitude 79 dyne/cm^2. An oscillatory shear stress of ± 5 dyne/cm^2 at 1 Hz (OS) was chosen to study the mechanobiology in the fibrosa. As detailed in specific aim-1, this OS induced side-specific calcification in fibrosa but not ventricularis.

4.4.5 Experimental setup

In the laboratory, circular 7-mm radius samples were cut aseptically from the basal region of each leaflet under the sterile laminar flow hood. As detailed by Sucosky et al (*52*), each well of the shear stress bioreactor was filled with approximately 750 µL of 1.2% agarose (Agarose, Thermo Fisher Scientific, NJ), which acted as a tissue holder, and the circularly cut tissue samples were placed on top of the agarose bed (Figure 3.2C, D). Since the thickness of the AV tissue slightly varies from pig to pig, the height of this agarose bed must be adjusted based on the thickness of the tissue. This is to ensure that the tissue samples are flush mounted, i.e., are placed at the same level as the plate that holds all the tissues in place. To verify this, a micro-cover-slide can be slided from the center of the plate to the top of the tissue. If the micro-cover-slide does not move smoothly over the tissue (which happens when the tissues are not flush mounted), the height of the agarose bed must be re-adjusted. These steps are crucial because if the level of the tissue increases relative to the plate (e.g. by 0.1 mm), it decreases the height between the cone and the plate. This variation of the tissue height significantly increases the shear stress experienced by the tissues (1.36 times). This calculation is based on the fact that there are no secondary flows in this cone and plate system and that the velocity profile is linear as detailed by Sucosky et al (*52*). Additional details are also available in Appendix: Cone and Plate manual A.2.

To investigate the changes in expression of miRNA and mRNAs, leaflets were cultured for 48 h using regular DMEM media (*118*). A 48 h culture duration was chosen, as it is well known that this culture duration is sufficient to induce changes in gene expression and makes it possible to investigate the early onset of AV disease (*102*).

For calcification-related studies, 72 h experiments were performed. To accelerate the calcification process that occurs over decades *in vivo*, an osteogenic media was used. This osteogenic media contained normal DMEM supplemented with 1 mmol/L glycerophosphate, 10µmol/L dexamethasone, 3.8 mmol/L PO_4^{3-}, and 1 ng/ml TGF-β1. This media has been previously validated to accelerate the calcification of the porcine AV leaflets in the presence of cyclic stretch (*17*). Media (regular or osteogenic) was changed every 48 h to replenish the nutrients. The entire setup was placed in a 5% CO_2 incubator at 37 °C. Post-culture, the portion of the tissue unexposed to shear stress was carefully excised (without touching the exposed tissue) using sterile tools under the sterile laminar flow hood. Tissues were briefly rinsed in multiple changes of sterile nuclease-free dPBS maintained at 4 ^{o}C until the media was completely removed.

4.4.6 Shear- and side-dependency of filtered targets of miR-214

In specific aim-1, the potential mRNA targets of miR-214 were filtered. To further understand the function of miR-214 in this side-dependent AV disease, six mRNA targets were chosen from its filtered targets, based on their known

functional role in AV pathology. These mRNA targets are *S*ma, *Ctnnb1*, *Enos*, *Klf4*, *Bcl2l11*, and *Col1a1.* Briefly, *Sma*, determines the contractility and phenotype of valvular cells (*143*). Catenin beta-1 or β-catenin **(***Ctnnb1*) is required in embryonic cushion development of the AV (*144*), but its increased expression can induce pathogenesis in adult valves (*145*). A well-known atheroprotective gene, nitric oxide synthase 3 or *Enos*, is anti-inflammatory, and protects the valvular endothelium from calcification (*146*). Apoptosis facilitator, *Bim* or *Bcl2l11* belongs to the family of *Bcl2* and activates the production of reactive oxygen species (*147*). Kruppel-like factor 4, *Klf4* is a well known atheroprotective gene (*148*). Flow-dependent differential expression of *klf4* is also observed in bicuspid compared to tricuspid AV valve (*149*). Finally collagen type I, *Col1a1*, is predominant in AV matrix and its increased expression (observed in calcified AV tissues) indicates high ECM turnover (*150*).

As one can see, these targets are very relevant to AV disease. However, as described earlier, their shear- and side-dependency in AV needs to be determined before proceeding with the miR-214 modulation studies. For this purpose, fibrosa or ventricularis of AV leaflets were exposed to OS or LS for 48h and four conditions were investigated: 1) fibrosa exposed to OS, 2) fibrosa exposed to LS, 3) ventricularis exposed to OS, and 4) ventricularis exposed to LS. Fibrosa exposed to OS and ventricularis exposed to LS are physiologically relevant as the sides' fibrosa/ventricularis are exposed to their respective shear stresses. Thus the fibrosa exposed to OS vs. ventricularis exposed to LS

comparison indicates side-dependency. Fibrosa exposed to LS and ventricularis exposed to OS are referred to as altered conditions as the physiological shear stress profiles are switched between the two sides. Fibrosa exposed to OS vs. LS and ventricularis exposed to OS vs. LS comparisons were used to compare the shear dependency of the fibrosa and the ventricularis, respectively. From specific aim-1, we know that miR-214 showed an increased expression in the fibrosa exposed to OS vs. LS and compared to ventricularis exposed to OS or LS. Based on these experiments, the mRNA targets that showed an inverse relationship with the miR-214 expression were chosen for further functional investigation.

4.4.7 Development of miRNA silencing protocol ex vivo

Since there is no well-established protocol to deliver anti-miR in an *ex vivo* culture, a protocol was developed. This protocol is a modified version of the existing *in vitro* miRNA silencing protocol (*124*). Statically cultured AV tissues were used to optimize the delivery of anti-miR to the tissues. The workflow of this protocol is shown in the Figure 4.3. A fluorescently tagged non-targeting (NT) anti-miR (Exiqon, Denmark) was used to optimize the transfection protocol and also to visualize the extent of transfection. AV leaflets samples were cut as previously described in 4.4.5 and passively transfected with 400 nM tagged NT anti-miR. The samples were then incubated in OptiMEM for 4 h (Life Technologies, NY). After this, the leaflets were quenched with regular DMEM and cultured under static conditions for 48 h. Statically cultured leaflets with no anti-

miR were used as a negative control. After 48 h, each tissue was washed well in nuclease-free sterile dPBS and was cut into two halves for both RNA isolation and imaging. The tissue sections used for imaging were counterstained with DAPI and imaged *en face* to determine the transfection efficiency of tagged NT anti-miR. Total RNA was isolated from the other half of each tissue section and qPCR analysis was done to determine the expression of miR-214 was affected by the NT anti-miR transfection. After which, the same protocol was used to verify the silencing of miR-214 in statically cultured AV leaflets. An *in vivo* grade non-tagged anti-miR-214 was used for this purpose (Exiqon, Denmark). Additional functional studies that were carried out in static culture are detailed in Appendix A.24.

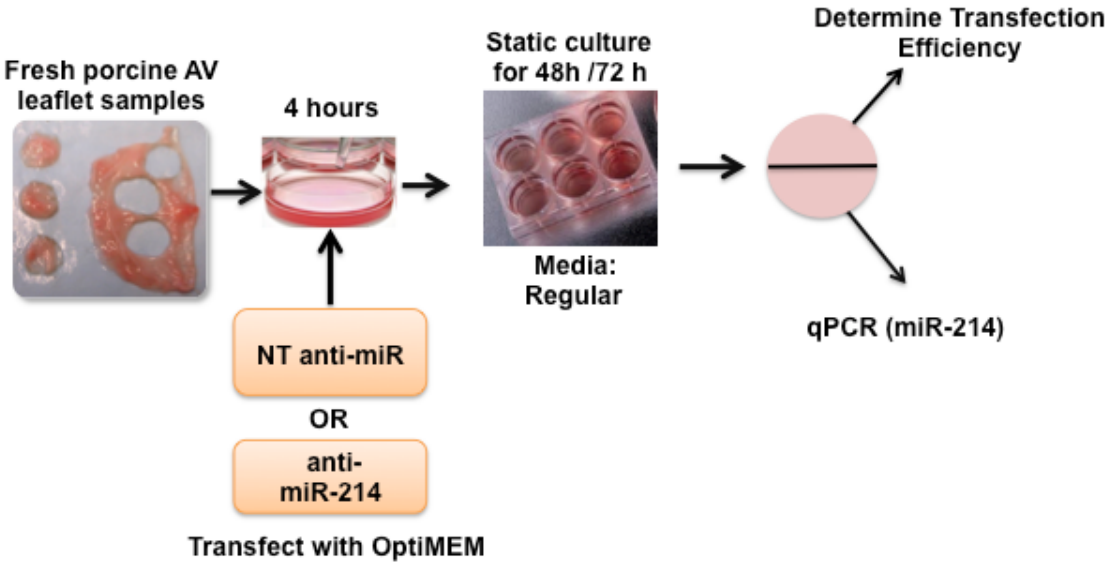

Figure 4.3 Work flow of anti-miR delivery protocol in statically cultured AV. Samples were passively transfected with anti-miR (NT anti-miR or anti-miR-214) for 4 hours. The samples were statically cultured for 48 h. The samples were then imaged to check for transfection efficiency of NT anti-miR and analyzed to check for the expression of miR-214 (qPCR).

4.4.8 Effect of miR-214 silencing on its target mRNAs

It is known from specific aim-1 that the miR-214 is highly expressed when fibrosa is exposed to OS compared to all other shear conditions. Hence, the miR-214 silencing studies were carried out in this shear condition only. The protocol developed using statically cultured tissues (4.4.7) was adapted for use with the shear system. The workflow for silencing the miRNA in sheared samples is shown in the Figure 4.4. Following this protocol, the tissues were then treated with 400 nM of anti-miR-214 or tagged NT anti-miR and then the fibrosa was exposed to OS, for 48 h. To ensure that the anti-miR was retained within the tissue even after shearing, a cross section of the tissue was imaged. The

expression of miR-214 and its target mRNAs (identified from 4.4.6) was then determined using qPCR (4.4.11 through 4.4.14).

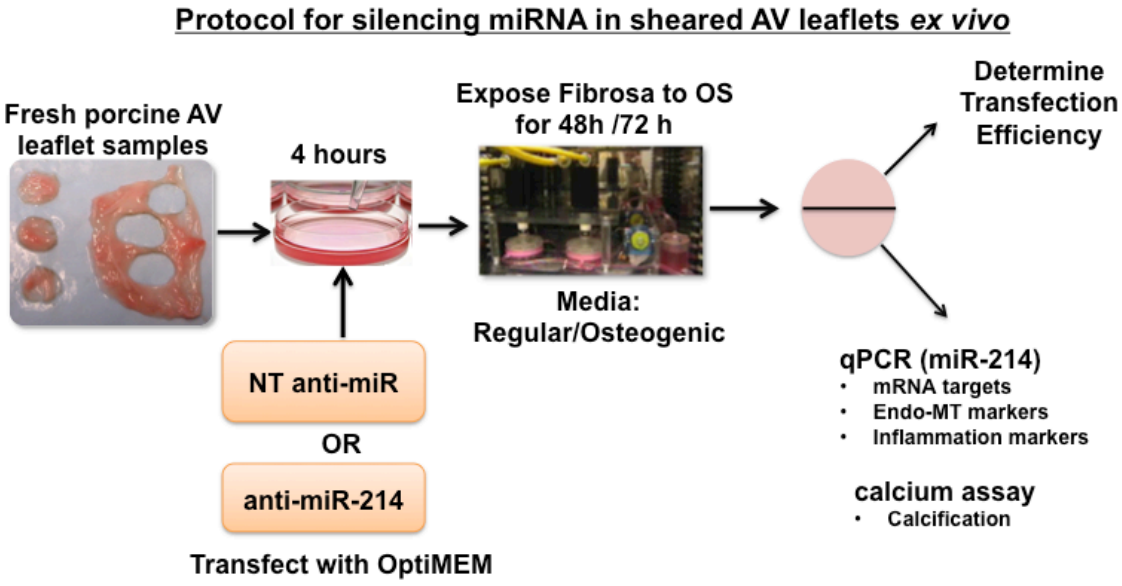

Figure 4.4 Work flow of miR-silencing study in sheared AV.
Samples are passively transfected with anti-miR (tagged NT anti-miR or anti-miR-214) for 4 hours. Fibrosa side of AV are then exposed to OS and cultured for 48 or 72 h. The samples were then assessed for: transfection efficiency, expression of miR-214, mRNA targets, Endo-MT markers, inflammation markers and calcium levels.

4.4.9 Functional role of miR-214 in porcine AV leaflets ex vivo

In addition to identifying the potential targets regulated by miR-214 in AV, the functional role of miR-214 in early (Endo-MT and inflammation) and late (calcification) stages of calcific AV disease was also determined (Figure 4.4).

4.4.9.1 Early stage: endo-MT and inflammation

The role of miR-214 in AV Endo-MT, and inflammation was investigated. Silencing studies with anti-miR-214 were carried out for 48 h when fibrosa was exposed to OS. The gene expression was assessed via qPCR (4.4.11 through 4.4.14). The Endo-MT markers (*159*) such as vascular endothelial cadherin *(VE-Cadherin)*, and monocyte chemoattractant protein-1 (*Mcp1*/*Ccl2*) were tested. To investigate the role of miR-214 in AV inflammation, the inflammation markers tested included intercellular adhesion molecule 1 (*Icam1)*, vascular cell adhesion molecule 1(*Vcam1)*, and bone morphogenetic protein (*Bmp4*) (*56, 160*). A well-known transcription regulator, transforming growth factor beta 1 (*Tgfβ1)* is highly expressed in calcified AVs (*151*) and is known to mediate phenotypic switch (fibroblast to myofibroblast), fibrosis, apoptosis, inflammation and calcification (*145, 159, 161*). So the possible regulation and activation of *Tgfβ1* by miR-214 was also tested. Samples sheared with NT anti-miR (Exiqon, Denmark) were used as a control.

4.4.9.2 Late stage: calcification

The role of miR-214 in AV calcification was investigated. Since OS also induced relatively higher calcium on fibrosa compared to ventricularis, the miR-214 silencing experiments were performed only when fibrosa exposed to OS. The culture duration was 72 h (media changed after 48 h) with osteogenic media. Calcium assay was performed to assess the calcium levels induced (4.4.15). Samples sheared with NT anti-miR were used as a control.

4.4.10 Histology

4.4.10.1 Preparation of frozen sections

The cryopreserved tissue blocks were prepared by embedding the tissue in OCT medium (Electron Microscopy Sciences, PA) and frozen using liquid nitrogen. Sections with thicknesses ranging between 5 to 7 μm were cut. The blocks and tissue sections were stored at -80 ^{o}C. For *en face,* the tissues were directly placed on a tissue slide and imaged.

4.4.10.2 Cell apoptosis stain

A cell apoptosis stain was performed to assess the cell death induced by the transfection of tagged NT anti-miR to statically cultured AV leaflets. A freshly isolated AV leaflet sample was included as a control. This staining was done using the In Situ Cell Death Detection Kit; TMR red, TUNEL kit (Roche Diagnostics, Germany). Cryopreserved tissue sections were fixed with 4% paraformaldehyde (Sigma-Aldrich, MO) in dPBS (pH 7.4) for 20 min, rinsed with dPBS for 30 min, permeabilized with 0.1% Triton X-100 (Sigma-Aldrich, MO) in dPBS (2 min at 4 ^{o}C), and rinsed twice with dPBS. Staining was performed by incubating tissue sections for 1 h at 37 °C in a humidified chamber in the dark in 50 μL of TUNEL reaction mixture followed by counterstaining with DAPI for 5 min. A positive control was prepared by incubating the fixed and permeabilized tissue section with DNAse-I solution (3-3000U/ml RNAse free DNAse-I (Qiagen, CA) in 50mM TrisCl (Sigma-Aldrich, MO), pH 7.5, 1mg/mL BSA (Fisher Scientific, PA) for 10 min prior to labeling with TUNEL reaction mixture. A negative control

was prepared by incubating fixed and permeabilized tissue sections in 50 µl of TUNEL label solution (without terminal transferase). Apoptotic cells appeared red and nuclei appeared blue under fluorescence microscopy.

4.4.10.3 Imaging and analysis

A laser-scanning microscope (710 NLO, Zeiss, Germany) was used for confocal microscopy. The transfection of tagged NT anti-miR was visualized (both *en face* and cross-section) using a confocal microscope. The apoptotic cells within the tissue after the TUNEL stain was also visualized using a confocal microscope. The apoptotic cells in the tissue were counted using ImageJ software (*162*).

4.4.11 RNA isolation

From 48 h shear experiments, total RNA was isolated from whole tissue (both endothelial and interstitial tissue) using the miRNeasy kit (Qiagen, CA). It was not feasible to isolate endothelial-enriched RNA from the sheared AV samples and it was more practical to isolate total RNA from entire tissue (interstitial and endothelial cells). To achieve sufficient RNA yield for qPCR, three sheared tissues were pooled per isolation. In the case of static culture, it was sufficient to pool just two tissue samples.

Post experiment, media from the tissues was completely removed using sterile dPBS, as mentioned earlier. The tissues were then incubated in 700 µL of Qiazol for about 5 min at room temperature. The phenol-chloroform extraction was done

and subsequent purification steps were performed as per the manufacturer's protocol. The concentration and the purity of the samples were measured using the Take 3 plate attachment of Synergy H4 Hybrid Reader (Biotek, VT). Samples showed 260/280 and 260/320 ratios in the range 1.2 to 1.8 and had concentrations ranging from 10-30 ng/ μL (sheared samples) and 200-500 ng/ μL (statically cultured samples).

4.4.12 Preparation of mRNA and miRNA cDNA

To prepare cDNA for mRNA, High-Capacity cDNA Reverse Transcription kit with RNAse inhibitor kit (Life Technologies, NY) was used. To prepare cDNA for miRNA, miScript II RT kit (Qiagen, CA) was used.

4.4.13 Real-time qPCR

Real time qPCR was used to assess the expression miR-214 and mRNA genes (targets, Endo-MT markers, and inflammation markers). The primers for mRNA genes were designed and ordered from Integrated DNA Technologies (IA). The primer sequences for all the genes tested including the endogenous control, 18S, are listed in the Table 4-1. The expression of mRNA targets and functional genes was also assessed via qPCR using the VeriQuest Fast SYBR Green (Affymetrix, CA). The primer for miRNA-214 was purchased from Qiagen (CA) and its level was assessed using qPCR with miScript SYBR Green PCR kit (Qiagen, CA). RNU6B included in this PCR kit was used as the endogenous control.

Table 4-1 Primer sequences of all mRNA genes tested in this specific aim.

Gene	Forward Primer	Reverse Primer
Enos	5- GAG ACT GGC CTT ATT CCT GGG -3	5- CTC CGG AAT ACC ACT GCT GG -3
Bcl2l11	5-TGA GTC GGA TCG CAA CTT GG-3	5-ATC GGT TGA AGC GTT CCT GG-3
Ctnnb1	5-GGA CAT CAC TGA ACC TGC CA-3	5-GGT AGT CCG TAG TGA AGG CG-3
Col1a1	5-GGC CAA GAA GAA GAC ATC CCA-3	5-ACA ACA CAT TGC CGT TGT CG-3
Klf4	5-CTA AGC AGC AGG GAC TGT CA-3	5-GTG GCA TGA GCT CTT GGT AAT G-3
Sma	5- GGT GGG AAT GGG ACA AAA AGA C -3	5- TGG TGA TGA TGC CGT GTT CTA TT -3
18S	5-CCC CAA CTT CTT AGA GGG ACA AG-3	5-AGG GCA TCA CAG ACC TGT TAT TG-3
Vcam1	5- AGT TGC TCC CAG GGA TAC GA -3	5- GGA GCT GGA AAG CCA TCA CT -3
Bmp4	5-CGT CAT CCC AGA TTA CAT -3	5-GAG TCG AAG CTC TGC GGA T-3
Tgfβ1	5-CAA CTA CTG CTT CAG CTC CAC GGA GAA GAA-3	5-GAA CAT CGA TGA CAA GCT TAG GTA TCG ATA-3
Icam1	5-GTC CCC CTC AAA AGT CAT CC-3	5-AAC CCC ATT CAG CGT CAC CT-3
Mcp1	5-TGT CCT AAA GAA GCA GTG ATC TTC-3	5-AGT CAG GCT TCA AGG CTT CG-3
VE-Cadherin	5-AAG AAC ATC GCC CGT GTC AT-3	5-CAC TGA GCC GAT CCA AGG TT-3

4.4.14 Analysis of qPCR data

A sample size of at least 3 to a maximum of 9 was used for data analysis. As mentioned earlier, each sample infact represents 2 (for static) or 3 (for sheared) tissue samples (due pooling of tissues). To analyze qPCR data, ΔCT method was used and fold changes (2^(-ΔCT)) were calculated. When comparing two groups, eg. fibrosa exposed to OS vs. LS, the fold changes were normalized to the mean of the second group (here fibrosa exposed to LS which was set as the baseline) (*14*).

4.4.15 Calcium assessment

The calcium levels were measured in tissues after the miR-214 silencing was carried out in osteogenic media. The tissues were pulverized by mortar and pestle in liquid nitrogen, and collected in pre-weighed vials. After sample collection, the vials were re-weighed before and after drying the samples overnight at 37 ^{o}C. The dry weights of the tissue were then computed. Subsequently, the ground samples were incubated in 1 M acetic acid at 4 ^{o}C for 24 h, to solubilize calcium. The samples were then centrifuged at 15,000 rpm for 9 min, and the supernatant was collected. The supernatant as well as calcium standards were assayed for calcium content by using a calcium specific Arsenazo dye reagent (Fisher-Scientific, MA): 25 µL of the supernatant or the calcium standard was mixed with 300 µL of Arsenazo solution in a 96 well plate. The absorbance of the various samples at a wavelength of 650 nm was measured through spectrophotometry, using a 96 well plate reader (BioTek, VT). The absorption calibration curve was established with the calcium standard spectrophotometry readings, and was thereafter applied to readings from the samples. The amount of calcium per dry weight of sample tissue was then calculated.

4.4.16 Statistical analysis

Data was expressed as mean $\pm$ standard error. All the statistical analyses were done using SPSS Statistics for Mac (Version 20.0, IBM Corp, NY). The normality of all the data was tested using the Anderson-Darling method. Student t-test was

used when only two groups were being compared. Two-way ANOVA was used for analyzing independent sample sets with Tukey's post-hoc test for comparisons between multiple groups. If the data was not normally distributed, Mann-Whitney and Friedman tests were used in place of the student t-tests and ANOVA, respectively. The groups were considered to be significantly different or show trends if the p-value was less than or equal to 0.05 and 0.10, respectively.

4.5 Results

The raw data of all these results is available in Appendix A.19.

4.5.1 Side- and shear-dependent expression of potential mRNA targets of miR-214 in AV leaflets

Of the 6 potential targets tested, four (*Klf4, Enos*, *Ctnnb1*, *Bcl2l1)* showed a downregulation in fibrosa when exposed to OS, but not LS (p=0.1,Figure 4.5A). In contrast, *Col1a1* expression showed an upregulation in fibrosa, suggesting that this gene is unlikely to be a target of miR-214 in AV. However, this increased expression of *Col1a1* could possibly be the explanation for the previously observed increased thickness of fibrosa in response to OS, compared to other conditions. The expression of any of these targets did not change in the ventricularis regardless of the shear stress (OS or LS), suggesting that the gene expression was preserved in ventricularis (Figure 4.5B). When exposed to OS, the expression of *Enos* decreased in fibrosa but not in ventricularis (p=0.1, Figure 4.6A). On the other hand, only *Sma* and *Ctnnb1* showed a downregulation in

fibrosa exposed to OS compared to ventricularis exposed to LS, in a side-dependent manner ($p=0.1$, Figure 4.6B). Thus, overall 5 out of 6 potential targets showed side- and shear-dependency in fibrosa and displayed an inverse relationship with miR-214 expression. These 5 were further investigated in the miR-214 silencing studies.

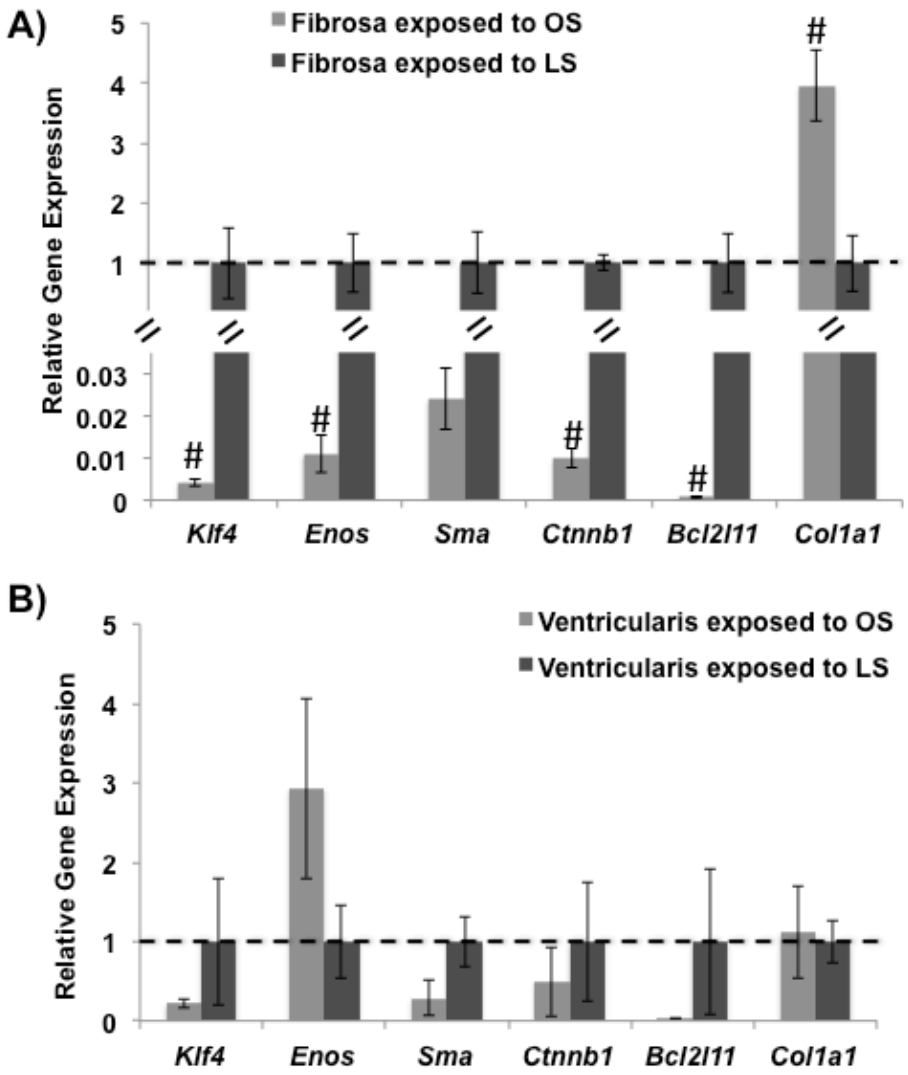

Figure 4.5 Shear-dependency of selected target genes.
A) Four genes: *Klf4, Enos, Ctnnb1,* and *Bcl2l11* showed a lower expression in fibrosa in a shear-dependent manner (OS vs. LS). B) No changes were observed in gene expression in ventricularis in a shear-dependent manner (OS vs. LS). n=3 (pooled 3 samples/isolation), #p≤ 0.1

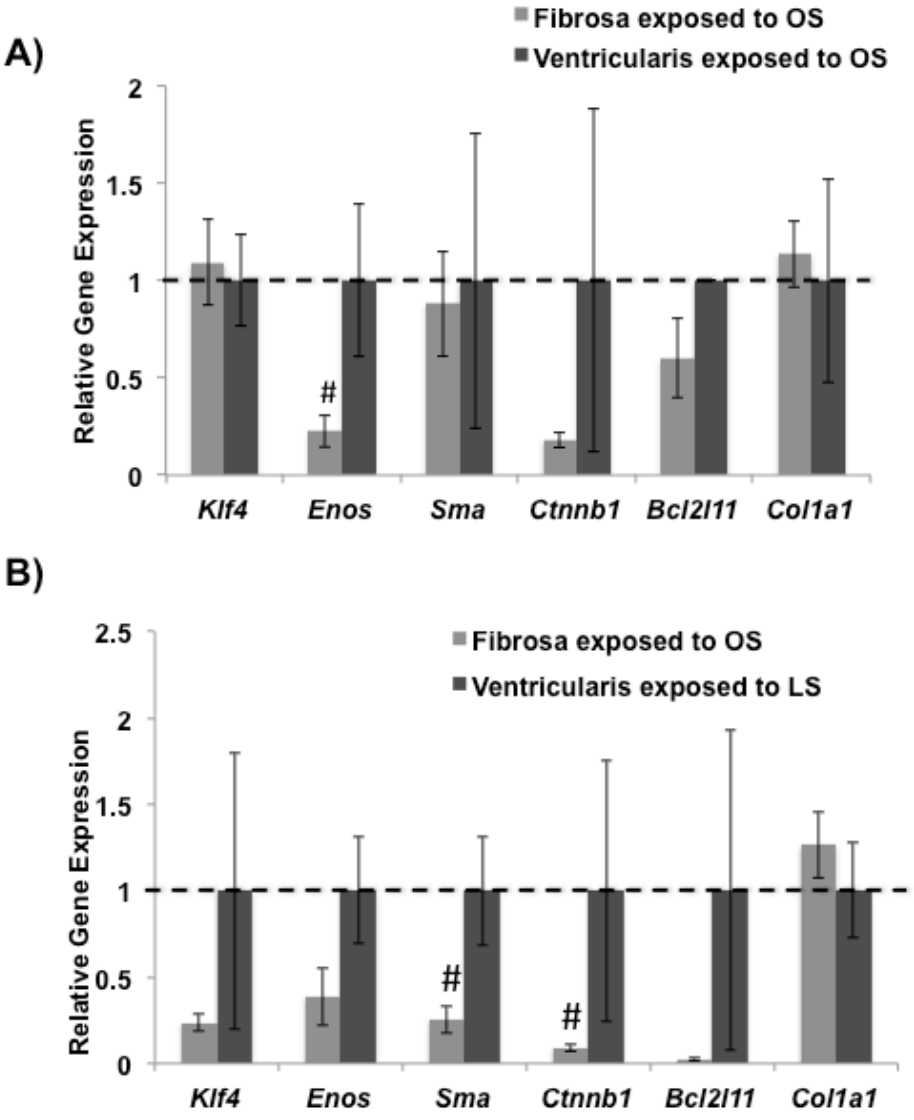

Figure 4.6 Side-dependency of selected gene targets.
A) Only *Enos* showed a lower expression in fibrosa compared to ventricularis, when exposed to OS. B) T*wo genes: Sma and Ctnnb1* showed a lower expression in fibrosa in a side-dependent manner (fibrosa exposed to OS vs. ventricularis exposed to LS). n=3 (pooled 3 samples/isolation), #p≤ 0.1.

4.5.2 Delivery of anti-miR to AV leaflets ex vivo

Modulation studies on miR-214 are needed to confirm its potential gene targets identified in the previous section. For this, a protocol was developed to deliver anti-miR to AV leaflets *ex vivo* (Figure 4.3). The transfection of a tagged NT anti-miR in static cultures compared to the no anti-miR control group was observed not only to endothelial cells, but also to interstitial cells, as shown in Figure 4.7B. Also, this transfection is observed in the entire tissue Figure 4.7B. The TUNEL stain was performed to assess if the transfection of tagged NT anti-miR affected the cell viability. As shown in the Figure 4.8, leaflets transfected with tagged NT-anti-miR showed a few apoptotic cells (fewer than 100 apoptotic cells/1700 total cells, <6%) and thus did not have a significant effect on cell viability. Further, the anti-miR-214 significantly silenced miR-214 in statically cultured AV leaflets ($p=0.05$), compared to the tagged NT-anti-miR, as shown in the Figure 4.9. Thus, a protocol was developed to successfully deliver anti-miR to the AV leaflets *ex vivo* without compromising the cell viability.

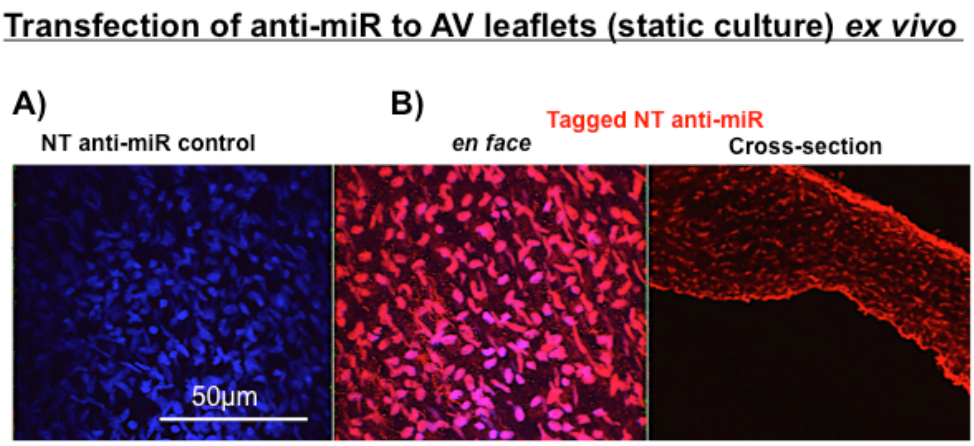

Figure 4.7 Delivery of anti-miR to statically cultured AV leaflets *ex vivo*. A) The anti-miR control with no anti-miR showed nuclei counterstained with DAPI. B) Tagged NT anti-miR (red) showed transfection in both endothelial and interstitial cells of the statically cultured AV (48 h), also showing nuclei counterstained with DAPI.

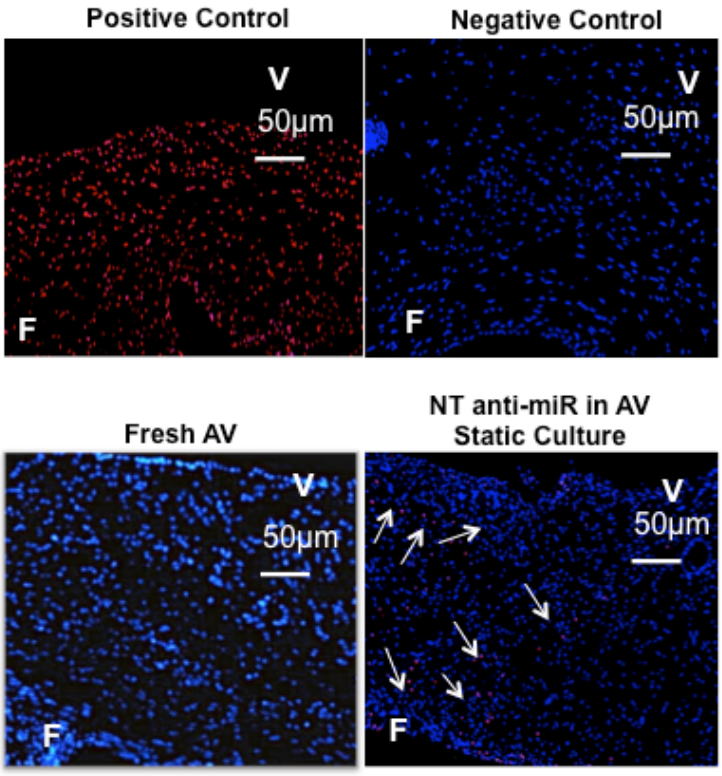

Figure 4.8 Positive control for TUNEL showed excessive apoptosis (red). Negative control for TUNEL stain showed no signs of apoptosis. As expected no apoptotic cells were observed in freshly isolated AV. However, a few apoptotic cells were observed (arrows point to red tagged nuclei) in statically cultured tissues were treated with NT anti-miR. F: fibrosa, V: ventricularis.

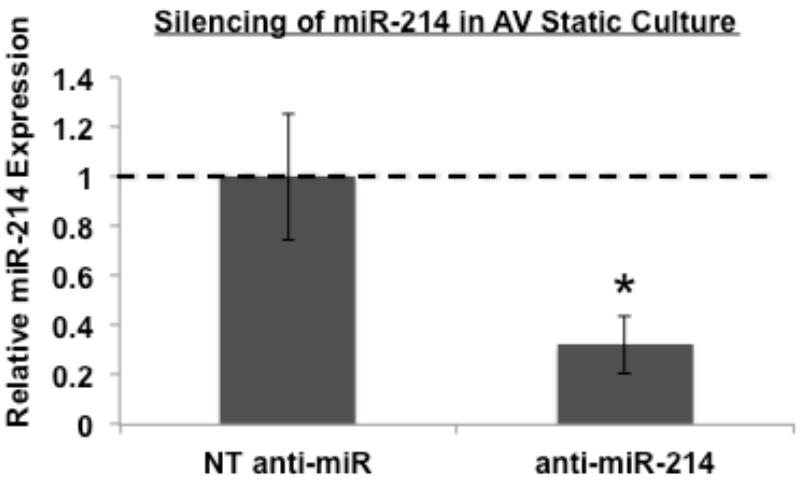

Figure 4.9 Silencing of miR-214 in AV static culture.
Successful silencing of miR-214 in statically cultured AV leaflets by anti-miR-214 compared to NT anti-miR. *p=0.05. n=6 (pooled 2 samples /isolation).

4.5.3 Silencing of miR-214 in sheared AV leaflets ex vivo

The miR-214 silencing was carried out (Figure 4.4) in fibrosa when exposed to OS. As shown in the Figure 4.10A, the transfection of a tagged NT-anti-miR in sheared leaflets was successful and was retained even after 48 h of shear. The miR-214 was also significantly silenced in fibrosa exposed to OS (p=0.004), also shown in the Figure 4.10B.

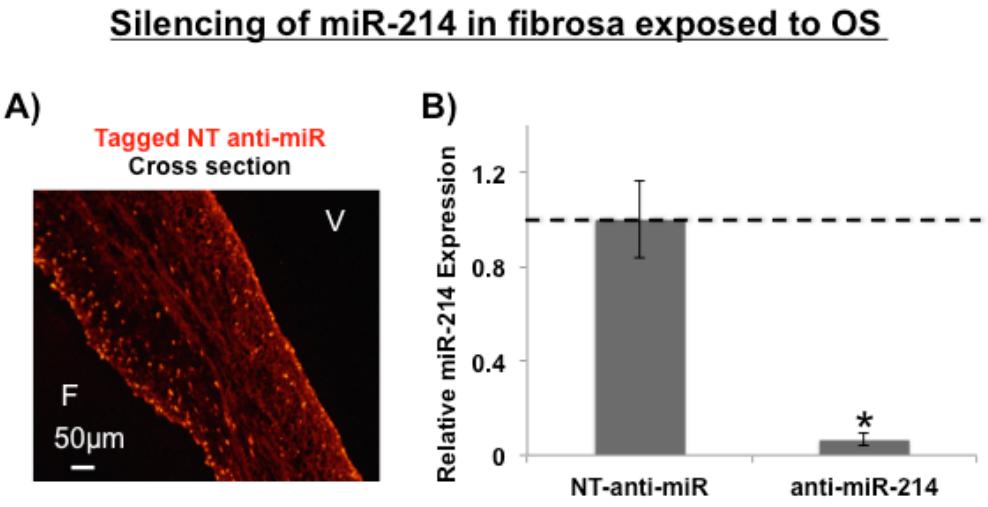

Figure 4.10 Silencing of miR-214 in fibrosa exposed to OS.
A) The cross section image of sheared AV tissue (fibrosa exposed to OS) showed successful transfection and retention of the NT-anti-miR throughout the tissue. B) Successful silencing of miR-214 in fibrosa exposed to OS at 400nM of anti-miR-214 compared to NT anti-miR. n=5 (pooled 3 samples /isolation). $p<0.01$.

4.5.4 Validation of miR-214 targets by silencing miR-214

Following the silencing of miR-214 in fibrosa exposed to OS, the expression of mRNA targets (identified in the earlier section, 4.5.1) was determined. Out of 5 mRNA targets that showed an inverse relationship with miR-214; upon miR-214 silencing, only *Klf4* was significantly upregulated ($p=0.05$) while *Sma* trend did not reach statistical significance ($p=0.11$) (Figure 4.11). This confirms that *klf4* is a potential target of miR-214 in AV.

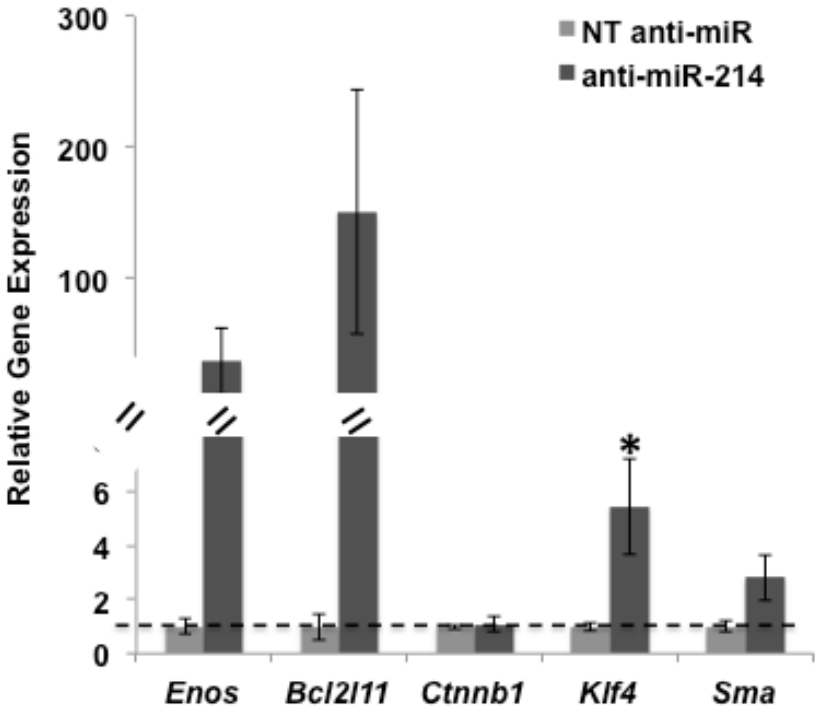

Figure 4.11 Validation of mRNA targets by silencing miR-214 in fibrosa exposed to OS. Out of 5 mRNA targets tested, silencing of miR-214 in fibrosa when exposed to OS, significantly upregulated *Klf4* (p=0.05) and tended to increase *Sma* (p=0.11). n=6-8 (pooled 3 samples/isolation).

4.5.5 OS dependent functional role of miR-214 in AV Endo-MT and inflammation

The functional relevance of silencing miR-214 in fibrosa when exposed to OS was investigated. As shown in Figure 4.12A, silencing of miR-214 tended to restore the expression of *VE-Cadherin* (p=0.1) but not *Mcp1,* in fibrosa exposed to OS. Out of 4 inflammation markers tested, silencing of miR-214 significantly decreased *Tgfβ1* (p=0.03) while moderately decreasing *Icam1* (p=0.08) (Figure 4.12B). Since the miR-214 silencing did not affect the other inflammatory markers *Vcam1*, and *Bmp4*, the miR-214 may be targeting the various other pathways activated or regulated by *Tgfβ1*

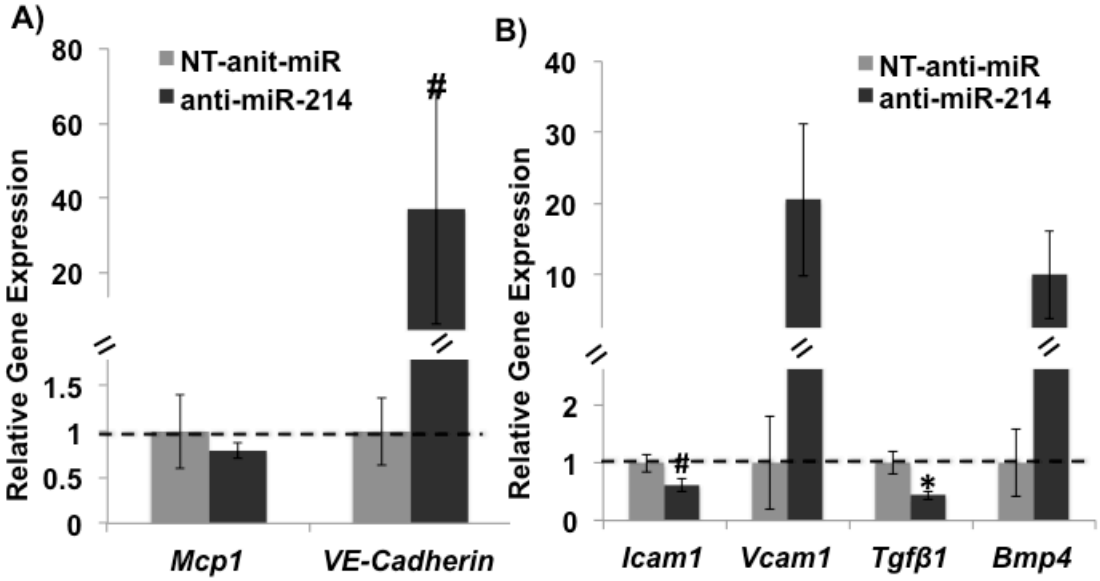

Figure 4.12 miR-214 silencing and AV endo-MT and inflammation. A) Silencing of miR-214 in fibrosa when exposed to OS tended to increase *VE-Cadherin* but not *Mcp1*. B) Silencing of miR-214 in fibrosa when exposed to OS significantly downregulated the *Tgfβ1* and decreased *Icam1*. n=6-8 (pooled 3 samples/isolation). *p≤0.05 and #p≤0.1.

4.5.6 OS dependent functional role of miR-214 in AV calcification

The effect of miR-214 silencing on AV calcification was also investigated. The miR-214 silencing did not alter the calcium levels induced by the OS in the fibrosa compared to the NT anti-miR control group (Figure 4.13). This suggests that miR-214 may not play a direct role in shear–mediated calcification or may require longer culture duration to have a detectable effect on AV calcification.

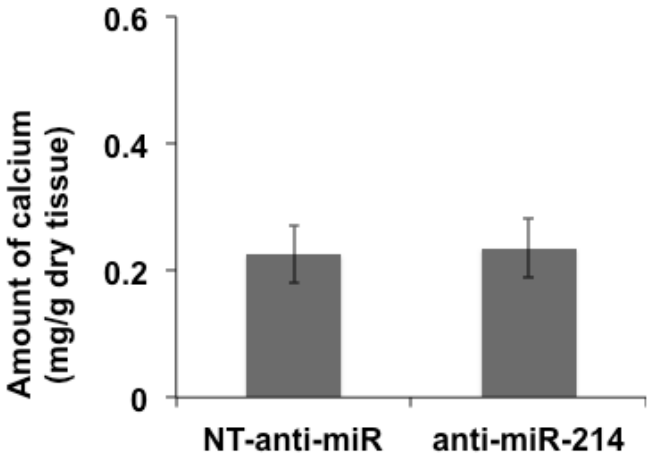

Figure 4.13 The effect of miR-214 silencing on AV calcification.
The silencing of miR-214 did not change the calcium levels in fibrosa induced by OS compared to the NT-anti-miR group. n=18.

4.6 Discussion

This chapter focused on understanding the role of a key shear- and side-dependent miRNA, miR-214 in AV pathophysiology. The major findings of this chapter are: 1) 5 out of 6 potential targets of miR-214 showed an inverse relationship with miR-214 in a side- and shear-dependent manner, 2) silencing of miR-214 in fibrosa exposed to OS significantly increased *klf4*, confirming *Klf4* as a target and 3) shear-dependent functional role of miR-214 in AV pathophysiology by knocking down its expression.

The calcific AV disease is a side-dependent disease preferentially occurring in the fibrosa and we have previously shown that the low magnitude oscillatory

shear stress can possibly contribute to this side-dependency. The OS also altered the AV ECM by increasing the thickness of the fibrosa but not the ventricularis, also observed in sclerotic valves (*9*). However, to understand the mechanism by which the OS contributes to these pathological changes that lead to AV disease, the functional role of a key side- and shear- dependent miRNA, miR-214 was investigated. It is well known that the miRNAs are critical regulators of gene expression and their involvement in cardiovascular diseases and congenital AV diseases have been recently recognized (*94, 106*). Hence, understanding the OS dependent regulation of miR-214 and its functional relevance in AV pathophysiology, will improve our current knowledge of shear-dependent mechanisms that lead to AV disease.

4.6.1 OS significantly increased miR-214 while decreasing its potential targets in the fibrosa

As mentioned previously, the miR-214 is a key side- and shear-dependent miRNA as its expression was significantly increased in the fibrosa when exposed to OS but not LS. The expression of miR-214 is also not shear-dependent in the ventricularis side. A detailed bioinformatics analysis showed that miR-214 potentially regulates the genes that play an important role in AV pathogenesis. Interestingly, the expression of 5 of 6 potential mRNA targets of miR-214 (except for *Col1a1*) was downregulated in fibrosa when exposed to OS, and thus, inversely correlated with the increased expression of miR-214. Nevertheless, the downregulation of anti-inflammatory genes: *Enos,* and *Klf4*, and upregulation of

Col1a1 (collagen turnover) in the fibrosa, are pathological and make the fibrosa more susceptible to disease. Thus, OS creates a pro-inflammatory environment, preferentially in the fibrosa side (*48, 56, 102*), that may be correlated with the higher expression of miR-214 observed in fibrosa.

4.6.2 Increased expression of miR-214 in fibrosa in response to OS can activate the Klf4 *and* Tgfβ1 *dependent pathways*

Successful transfection of anti-miR to AV endothelial and interstitial cells in sheared AV leaflets was demonstrated without compromising the cell viability. The increased expression of miR-214 in response to OS in the fibrosa was also successfully silenced using anti-miR-214. Out of 5 potential targets tested, one anti-inflammatory gene, *Klf4* was confirmed as a potential target of miR-214. As mentioned earlier, *Klf4* is an atheroprotective gene, and protects vascular endothelium by regulating the promoter activity of anti-inflammatory and anti-thrombotic factors (*148*). The disturbed shear stresses are known to decrease *Klf4* and therefore induce a pro-atherogenic environment in arterial bifurcations (*163*). Since the role of *kfl4* is not well defined in AV, a similar mechanism can be speculated that miR-214 regulates *Klf4*, and is involved in the OS dependent inflammation (*155, 164*) induced in fibrosa. Thus, the oscillatory shear stress can potentially induce inflammation in fibrosa by decreasing the expression of *Klf4* via increase in miR-214.

Since silencing of miR-214 did not significantly affect the expression of *Icam1, Vcam1*, and *Bmp4*, miR-214 may not be directly involved in AV inflammation. However, miR-214 silencing significantly decreased *Tgfβ1* indicating that miR-214 may be involved in pathways regulated by *Tgfβ1* such as fibrosis, EndoMT, apoptosis, etc. (*143, 145, 151, 159, 161*). The increased expression of *VE-Cadherin* in response to miR-214 silencing in fibrosa exposed to OS, raised this possibility.

On the other hand, in vasculature, the increased expression of *klf4* inhibits the epithelial-to-mesenchymal transition by targeting the expression of *Tgfβ*1 (*165, 166*). However, the exact mechanism as to how *klf4* regulates the expression of *Tgfβ1* (and vice versa) in AV pathogenesis is unknown. One hypothesis could be that *Tgfβ1* can accelerate the AV fibrosis, by activating the differentiation of quiescent valvular interstitial cells into osteoblast like phenotype (*145*), and this activation may require the downregulation of *klf4* (*167*). Also, TGF-β1 has been shown to regulate the expression of miR-214 in renal injury and fibrosis (*12*). Thus, the increased expression of *Tgfβ1* in response to OS can further increase the miR-214 and decrease *Klf4, a*nd this process can form a feedback loop. This feedback effect can increase the tendency of trans-differentiation of valvular cells in the fibrosa. Although the downregulation of *Tgfβ1* observed here is significant, but not severe (less than 2 fold) in response to miR-214 silencing, it is likely that this effect will be more pronounced with longer culture durations. Thus, the possibility of this feedback response cannot be denied and must be investigated

in future studies. On the contrary, miR-214 did not seem to have a direct effect on OS induced AV calcification. As discussed earlier, by silencing miR-214 with anti-miR-214, we rescued one of the important anti-inflammatory genes, *Klf4* while also potentially inducing pro-calcific genes such as *Vcam1* and *Bmp4 (*high fold changes, Figure 4.12, although not statistically significant). It is possible that this increased expression of pro-inflammatory and pro-calcific markers competed with the anti-inflammatory marker, to slow down the overall anti-calcific effect of anti-miR-214. It is also possible that miR-214 may regulate calcification via a different mechanism or there might be other miRNAs involved.

Also as observed in specific aim-1, in addition to side-dependent calcification in fibrosa, the OS induced changes in ECM (collagen and elastin), increased thickness of fibrosa as well as increased the expression of *Col1a1*, all showing the signs of altered ECM remodeling.

Thus, based on all of our results, a side- and shear- dependent role of miR-214 in the AV endothelium is proposed (Figure 4.14): the oscillatory shear stress increases the thickness of the fibrosa, alters the ECM, and creates a pro-fibrotic environment via a miR-214 - *Klf4* - *Tgfβ1* dependent pathway. This activation likely results in AV fibrosis, Endo-MT and eventually sclerosis. Thus miR-214 is a key miRNA involved in AV pathogenesis in a side- and shear- dependent manner.

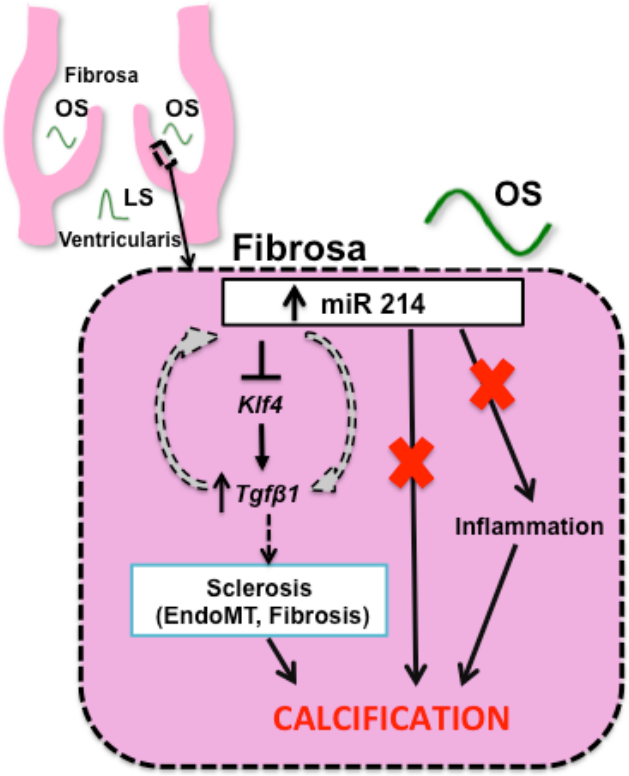

Figure 4.14 The proposed mechanism of action of miR-214 in AV. Fibrosa exposed to OS increases expression of miR-214 that targets *klf4* and activates *Tgfβ1.* This activation likely results in AV fibrosis, EndoMT and thus sclerosis. The dashed lines show the possible mechanisms and a possible feedback loop between miR-214 and *Tgfβ1.*

4.7 Limitations

An idealized shear stress paradigm as opposed to realistic shear stresses was used. In the presence of altered hemodynamics such as low heart rate and cardiac output, the magnitude of shear stress experienced by the fibrosa side can decrease to about 3 dyne/cm^2 from 13 dyne/cm^2, indicating that the valve does experience low magnitude shear stress (*111*). However, the lack of flow reversal on the fibrosa side according to this paradigm may change the response

of miR-214. The mRNA targets of miR-214 identified in this study were not validated at the protein level. It is because it was challenging to isolate good quality protein from the sheared tissue, post inhibition. This would not have been a problem in *in vitro* cell culture studies. This limitation was addressed by picking experimentally validated targets of miR-214 instead of predicted targets. The experiments were also repeated atleast 3 times to make sure the results are repeatable - both with and without the inhibitor experiments.

Additionally, to gain more insight into the mechanisms regulated by miR-214, the modulation studies should be carried out with pre-miR-214 as well. The upregulation of miR-214 due to pre-miR-214 may have had an effect on AV calcification, which was not observed when anti-miR-214 was used. However, longer culture durations (7 to 14 days) may also be necessary to observe the effect of anti-miR-214 on AV calcification. Finally, the differential gene expression pattern observed in this study may differ in humans due to the species (pig vs. human). Since the side-dependent miRNAs identified in this study are conserved in humans, investigating the functional role of these miRNAs in porcine AV leaflets will still provide us clues about their role in AV pathogenesis. Thus, despite these limitations, our data shows a possibility of the involvement in miR-214 in side-dependent AV disease.

4.8 Conclusions

The oscillatory shear stress predisposes the fibrosa to the early onset of disease by decreasing the expression of anti-inflammatory markers (*Enos*, and *Klf4*) and increasing the turnover of collagen (*Col1a1*). This OS induced pathology in the fibrosa is mediated via miR-214, *klf4 and Tgfβ1* dependent pathway that can lead to AV fibrosis, Endo-MT and eventually sclerosis. Thus, miR-214 plays a key role in the early onset of side- and shear- dependent AV disease and has a potential to serve as a disease biomarker.

CHAPTER 5 INVESTIGATION OF THE ROLE OF INORGANIC PYROPHOSPHATE IN AORTIC VALVE CALCIFICATION

5.1 Summary

Aortic valve calcification is a major cause of morbidity and mortality but the underlying molecular mechanisms are poorly understood. In this specific aim, an *ex vivo* model of calcification in intact AVs has been developed in order to investigate the role of PPi in AV ectopic calcification. Porcine AV leaflets were cultured in serum-free medium under static conditions for 8 days, over which time architecture and viability were preserved. Calcification occurred predominantly on the fibrosa side, and required both a high phosphate concentration (3.8 mM) and removal of PPi with alkaline phosphatase (ALP) or inorganic pyrophosphatase (IP). Calcification was arrested by the bisphosphonate etidronate, a non-hydrolyzable analog of PPi. Leaflets actively released PPi into the medium and this was enhanced by MLS38949, a specific inhibitor of tissue non-specific alkaline phosphatase (TNAP). Furthermore, leaflets synthesized PPi from extracellular ATP, which was reduced by β, γ-methylene-ATP, an inhibitor of ENPP1. Thus extracellular PPi is a key endogenous inhibitor of calcification and its levels appear to be controlled through synthesis by ENPP1 and hydrolysis by TNAP. Future preventative therapeutics to treat AV disease could be similarly based on bisphosphonates or inhibitors of TNAP.

5.2 Introduction

Aortic valve disease is a common condition and a strong risk factor for cardiovascular deaths (*16*). Unfortunately at present, the only therapeutic option is repair or replacement of diseased valves; to avoid surgery, there is a need for preventative strategies. While the initial events in valvular disease are poorly understood and may be multifactorial, calcification is a common endpoint that leads to valve failure (*168*). Thus targeting the calcification may be a useful therapeutic strategy. Calcification likely results from an imbalance between promoters and inhibitors of mineralization; understanding these mechanisms is a crucial step in developing medical therapies and tissue-engineering applications.

Mineralization in other soft tissues such as arteries is controlled in large part by the concentrations of calcium and phosphate and by endogenous inhibitors of hydroxyapatite formation. Foremost among these inhibitors is PPi, which is present in bodily fluids at concentrations sufficient to prevent hydroxyapatite crystal formation (*169*). Removal of PPi induces vascular calcification *ex vivo* (*170*). Direct administration of PPi can prevent calcification in vascular system *ex vivo* and *in vivo* (*42*), and in AV interstitial cells *in vitro*(*171*).

PPi is produced extracellularly from ATP through ENPP1 (*172*) and absence of this enzyme results in fatal arterial calcification (*173*). PPi may also be transported out of cells via the membrane protein ANK, absence of which also causes ectopic calcification (*174*). A key determinant of extracellular PPi levels

and mineralization is TNAP, an ecto-enzyme that hydrolyzes PPi. It is the robust expression of TNAP by osteoblasts that lowers local PPi levels and enables bone formation to occur (*175*). However, increased activity of TNAP in vascular smooth muscle may contribute to the vascular calcification that occurs in renal failure (*176*). This mechanism is illustrated in Figure 5.1.

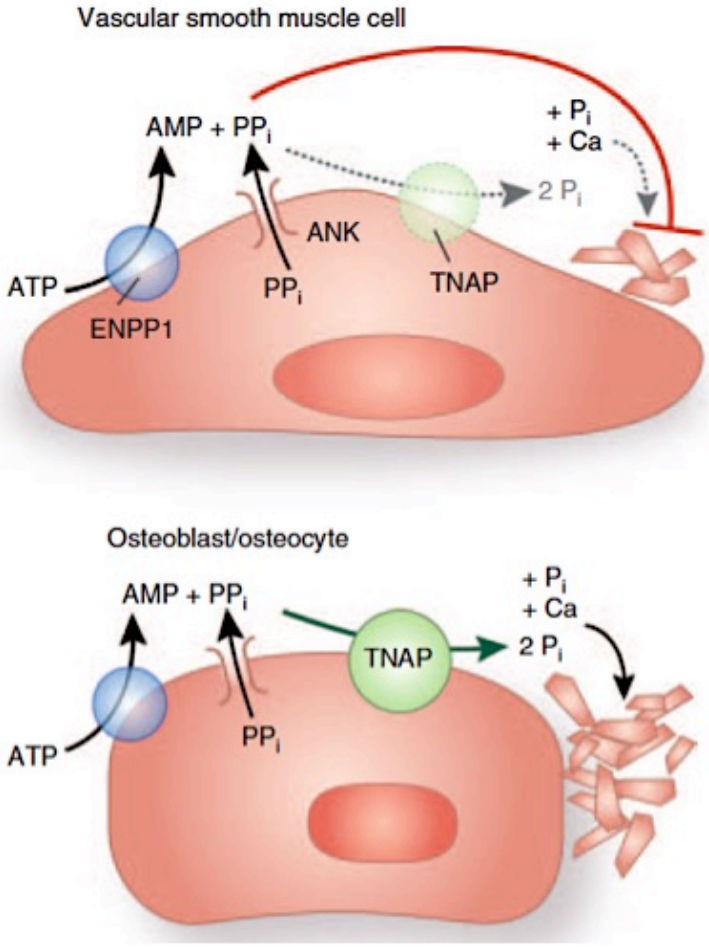

Figure 5.1 Tissue non-specific alkaline phosphatase and pyrophosphate induce and inhibit mineralization respectively, in vascular smooth muscle cells and bone cells(*177*).

5.3 Hypothesis

It is hypothesized that *PPi has a similarly important role in preventing AV calcification*. While pyrophosphate was found to inhibit calcification in interstitial cells cultured from AV leaflets (*171*), cell culture does not reflect events and metabolism in intact tissues. Therefore, an *ex vivo* calcification model was developed as part of this work using cultured porcine AV leaflets and used to examine PPi metabolism and its effect on calcification.

5.4 Materials and methods

5.4.1 Tissue harvest and preparation

Hearts were obtained from healthy, female pigs immediately after slaughter from a local abattoir (Holifield Farms, Covington, GA). The AV leaflets were immediately excised, thoroughly rinsed, and stored in sterile Dulbecco's phosphate buffered solution (dPBS; Sigma-Aldrich, MO) at 4 ^{o}C for transport to the laboratory. Upon arrival in the laboratory, five pieces (5 mm square) were cut aseptically from the basal region of each leaflet in a laminar flow hood. Each leaflet sample was placed in a separate well of a 12-well tissue culture plate with 2.4 mL of DMEM (Mediatech, VA) containing penicillin and streptomycin. These tissues were statically cultured for 8 days in a 5% CO_2 incubator at 37 °C with media changes every 2 days. The DMEM contains 1.8 mM calcium and 0.8 mM phosphate, and the phosphate concentration was increased by adding NaH_2PO_4. For use as a positive control for the calcification model, the valves were devitalized prior to culture by repetitive freezing and thawing (5 to 6 cycles) or

injured by rubbing the tissues with a cotton swab. The following additives were used when indicated: 1) inorganic pyrophosphatase (from Bakers' yeast; Sigma-Aldrich, MO), 1000 units/mL stock solution in Hanks buffered salt solution; 2) calf intestinal alkaline phosphatase (Promega, WI), 1000 units/mL suspension; 3) etidronic acid (TCI America, OR), 1 mM stock solution in distilled water; 4) Transforming Growth Factor-beta1 (TGF-β1) (Sigma-Aldrich, MO), 1ng/mL of culture media; 5) dexamethasone (Sigma-Aldrich, MO), 100 μM; 6) fetal bovine serum (Fisher Scientific, GA), 10% of culture media; and 7) warfarin (Sigma-Aldrich, MO), 6.7mM stock solution in 0.5 M NaOH, pH adjusted to 7.5 to 8.0.

5.4.2 Calcium incorporation

The assay to quantify calcium incorporation was performed as previously described (*170*). Approximately 0.3 μCi/mL of $^{45}CaCl_2$ (DuPont-NEN, MA) was added to the culture medium. At the end of the culture, the tissues were washed briefly twice to completely remove the culture media. The tissues were then incubated for an hour in a physiologic salt solution such as Hank's balanced salt solution (HBSS) at room temperature to remove any soluble tissue calcium. The samples were then dried in an oven, weighed; and then extracted overnight in 500 μL of 1N HCl to remove incorporated ^{45}Ca for measurement by liquid scintillation. Results are expressed as nanomoles of calcium per mg, calculated from the specific activity of ^{45}Ca in the medium.

5.4.3 Histological assessment

5.4.3.1 Preparation of paraffin or frozen sections

To prepare paraffin sections, the tissues were fixed in 10% neutral buffered formalin (Fisher Scientific, PA) for at least 24 h, then saturated in 70% ethanol (VWR, GA), processed in ascending grades of ethanol, embedded in paraffin, and cut into 5 μm sections. The blocks and the tissue sections were stored at room temperature. Paraffin sections were deparaffinized in xylene and then in descending grades of ethanol before they were used for staining. The cryopreserved tissue blocks were prepared by embedding the tissue in OCT medium (Electron Microscopy Sciences, PA) and were frozen using liquid nitrogen. 5 to 7 μm sections were cut. The blocks and tissue sections were stored at -80 ^{o}C. These cryo sections were warmed to room temperature before use.

5.4.3.2 Alizarin Red stain

Alizarin Red staining was performed with to visualize the calcification within the tissue. Briefly, deparaffinized paraffin sections were incubated with a 2% Alizarin Red (Sigma-Aldrich, MO) solution in distilled water at pH 4.1 to 4.3 for up to 5 min. The sections were then rinsed in acetone-xylene solution and coverslipped. Calcium deposits appeared red when viewed under normal bright field microscope.

5.4.3.3 Verhoeff-Van Gieson elastin stain

To visualize the overall architecture of the AV leaflet tissue a Verhoeff-Van Gieson elastin stain was performed. AV leaflet samples stained with this elastin stain distinctly show the tri-layered components of AV ECM, fibrosa, spongiosa and ventricularis layers. Elastin fibers stain blue-black to black, nuclei stains blue to black, collagen stains red, and muscle and other matrix components stain yellow. ACCUSTAIN Elastic kit (Sigma-Aldrich, MO) was used according to the manufacturer's directions.

5.4.3.4 Cell viability and apoptosis stains

Cell viability staining was performed by incubating tissues with 0.5 mg/mL methylthiazoletetrazolium (MTT, Sigma-Aldrich, MO) in DMEM at the end of the culture period for 3 h at 37 °C. The tissues were then washed with PBS 3 times and embedded for cryopreservation. Tissue sections of 5 to 7 μm were cut and then coverslipped. Viable cells appeared blue-brown when viewed under normal bright field microscopy. Dead cells, on the other hand, appeared colorless.

Cell apoptosis stain was performed to assess the cell death of cultured AV leaflet tissues. This staining was done using the In Situ Cell Death Detection Kit; TMR red, TUNEL kit (Roche Diagnostics, Germany). Cryopreserved tissue sections were fixed with 4% paraformaldehyde (Sigma-Aldrich, MO) in dPBS (pH 7.4) for 20 min, rinsed with dPBS for 30 min, permeabilized with 0.1% Triton X-100 (Sigma-Aldrich, MO) in dPBS (2 min at 4 ^{o}C), and rinsed twice with dPBS.

Staining was performed by incubating tissue sections for 1 h at 37 °C in a humidified chamber in the dark in 50 µL of TUNEL reaction mixture followed by counterstaining with DAPI for 5 min. Positive control was prepared by incubating the fixed and permeabilized tissue section with DNAse-I solution (3-3000U/ml RNAse free DNAse-I (Qiagen, CA) in 50mM TrisCl (Sigma-Aldrich, MO), pH 7.5, 1mg/mL BSA (Fisher Scientific, PA) for 10 min prior to labeling with TUNEL reaction mixture. A negative control was prepared by incubating fixed and permeabilized tissue sections in 50 µL of TUNEL label solution (without terminal transferase). Apoptotic cells appeared red and nuclei appeared blue under fluorescence microscopy.

5.4.4 Imaging

A Nikon E600 microscope (Nikon Inc., NY) coupled to a Retiga 1300C camera (I-Cube, MD) and its bundled software Q-Capture Pro were used to acquire images.

5.4.5 Pyrophosphate production

Fresh AV leaflets were incubated in DMEM (3 leaflets in 1 mL) in a 5% CO_2 incubator at 37 °C with or without 30 µM MLS38949 a specific inhibitor of TNAP (*178*) (PubChem ID 2931238, kindly provided by Dr. Jose Luis Millan, Sanford-Burnham Biomedical Research Institute, La Jolla, CA, USA). PPi content in the medium was measured enzymatically using uridinediphospho (UDP) glucose

pyrophosphorylase and UDP[^{14}C]glucose as substrate as previously described (*179*). Synthesis of PPi from ATP was measured by incubating fresh leaflets in physiologic salt solution (2 leaflets in 1 mL) containing 3 nM ATP and tracer [γ ^{32}P] ATP with or without 300 μM β, γ-methylene ATP (an inhibitor of ENPP1) or 30 μM MLS38949. Samples of the medium were spotted on polyethyleneimine cellulose plates (Sigma-Aldrich, MO) followed by development with 650 mM KH_2PO_4 (pH 3). Spots identified by autoradiography were scraped into distilled water and counted as Cerenkov radiation by liquid scintillation. PPi production was normalized to the dry weight of the leaflets.

5.4.6 Statistical analysis

Data were expressed as mean $\pm$ standard error of at least 6 samples. Normality of all the data was tested using the Anderson-Darling method. Student's t-test was used for comparison of two groups and one-way ANOVA with Tukey's post-hoc test was used for comparisons between multiple groups. If not normally distributed, the data were analyzed by the Mann-Whitney or Kruskal-Wallis tests. Differences between samples were considered significant when the p-value was ≤ 0.05.

5.5 Results

Raw data for all the results are included in Appendix A.20.

5.5.1 Effect of phosphate and phosphatase on AV calcification ex vivo

A dose-response study (0.1, 0.2, 0.4, 0.8 units/mL) demonstrated that 0.4 units/mL of IP resulted in calcification that is detectable both quantitatively and qualitatively, as shown in Figure 5.2. The incorporation of ^{45}Ca into AV leaflets cultured with different phosphate concentrations for 8 days is shown in Figure 5.3. A small uptake of ^{45}Ca occurred without added phosphate that probably represents equilibration with cellular stores as previously described for cultured aortas (*170*). Incorporation of ^{45}Ca increased at 3.2 mM phosphate and became significant at 3.8 mM ($p<0.05$ vs. 0.8 mM) but no staining was apparent with Alizarin Red. Incorporation of ^{45}Ca was markedly increased by the addition of 0.4 units/mL of inorganic pyrophosphatase (*171*) to the medium and resulted in positive Alizarin Red staining, indicating that this represented calcification.

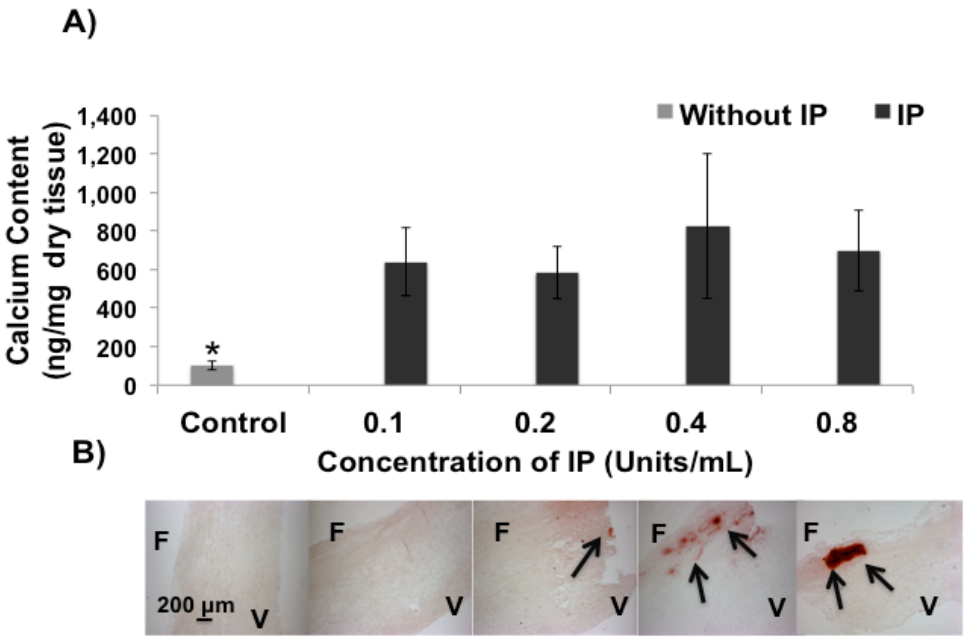

Figure 5.2 Effect of pyrophosphatase on AV calcification: dose response. A) Incorporation of ^{45}Ca in valve tissues over 8 days at different phosphate concentrations of inorganic pyrophosphatase at 3.8 mM phosphate. Control refers to leaflets cultured in 3.8 mM phosphate alone. *$p<0.05$ vs. any dose of IP., n=6-8. B) Corresponding Alizarin Red stains. F: fibrosa; V: ventricularis. Arrows point to calcified areas.

Time course study showed that the increased ^{45}Ca incorporation was apparent by 2 days (Figure 5.4) and visible by Alizarin Red staining by 4 days. Staining occurred predominantly on the fibrosa side of the leaflet with occasional minor staining of the ventricularis.

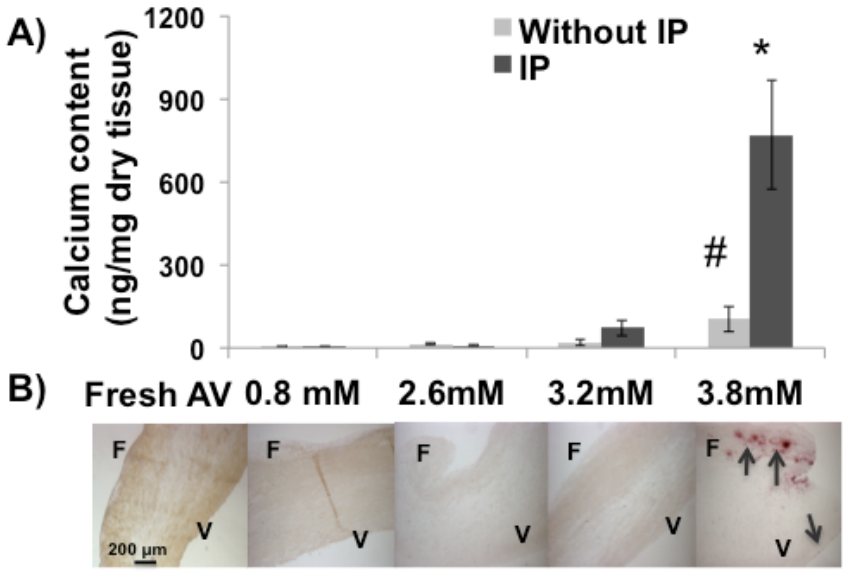

Figure 5.3 Effect of phosphate and pyrophosphatase on AV calcification. A) Incorporation of ^{45}Ca in valve tissues over 8 days at different phosphate concentrations with or without inorganic pyrophosphatase. #$p<0.05$ vs. 0.8mM phosphate alone, *$p<0.05$ vs. 3.8 mM phosphate alone., n=6-8. B) Corresponding Alizarin Red stains for valves cultured in IP. A freshly isolated leaflet is included as a negative control (far left). F: fibrosa; V: ventricularis. Arrows point to calcified areas.

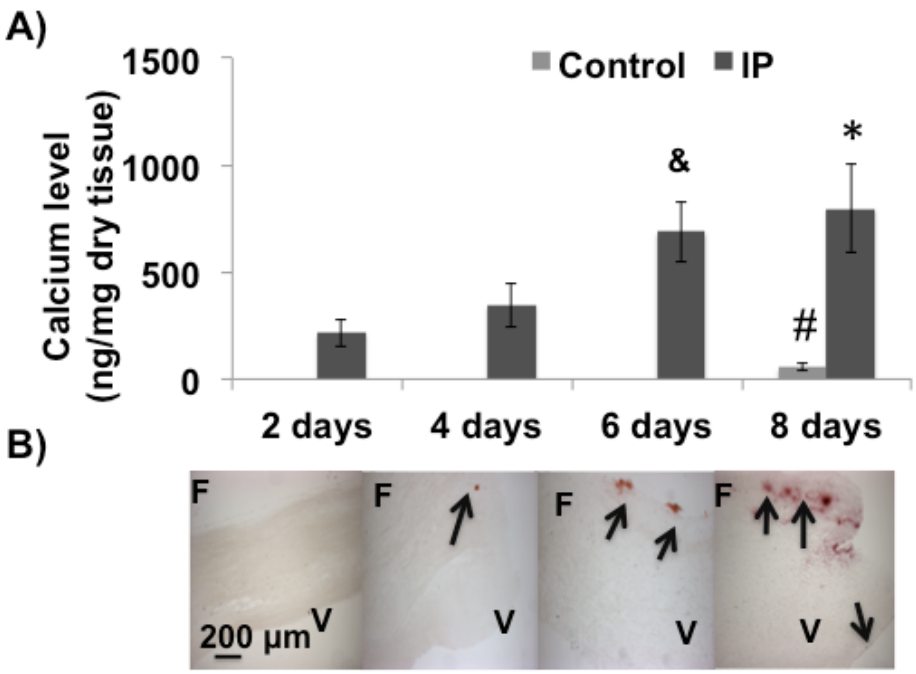

Figure 5.4 Time course of AV calcification.
A) ^{45}Ca incorporation in valve tissues cultured with or without IP and 3.8 mM phosphate in 2, 4, 6 and 8 days. *p<0.05 vs. 2, 4 days, &p<0.1 vs. 4 days, #p<0.05 vs. 4, 6, 8 days; n=16. B) Corresponding Alizarin Red stains. F: fibrosa, V: ventricularis. Arrows point to calcified areas.

Similar results were obtained when ALP was added to the cultures as shown in Figure 5.5. ALP also hydrolyzes PPi but is less specific and hydrolyzes other phosphorylated compounds as well (*3*). ALP + IP did not produce any further calcification beyond IP alone, indicating that this effect was solely through removal of PPi. Addition of TGF-β1, dexamethasone and serum to the culture media along with ALP also did not produce additional calcification beyond ALP alone or IP alone. However, the regions of calcification differed as evident in Alizarin Red staining. Finally, devitalization of the leaflets by repetitive freezing and thawing also induced significant calcification (p=0.05 vs. control).

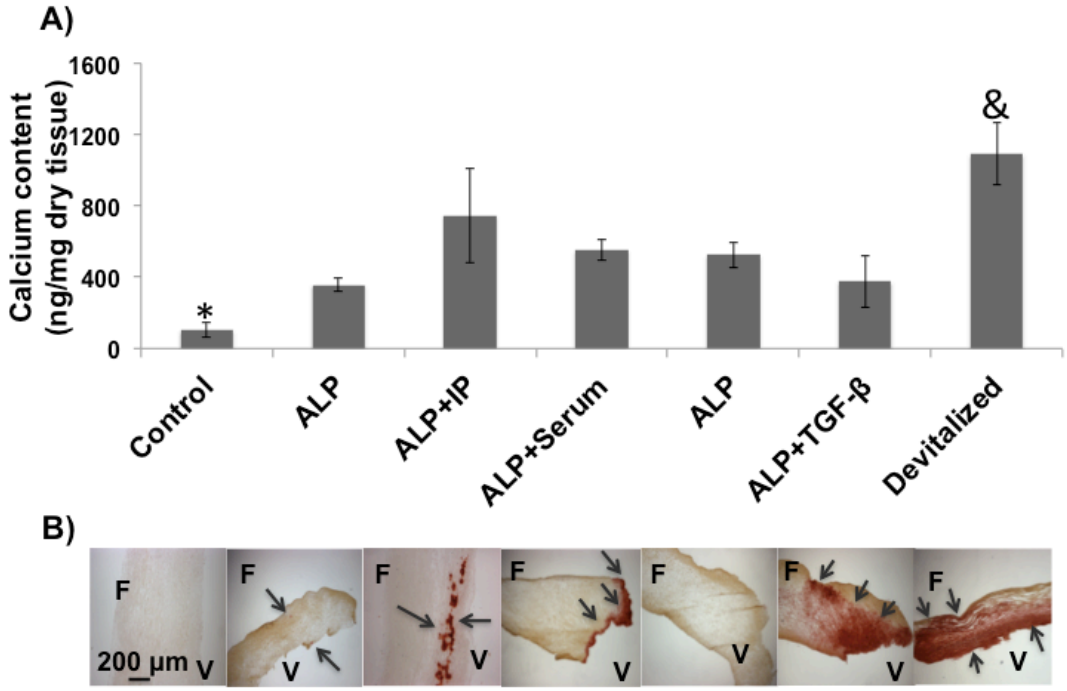

Figure 5.5 Effect of alkaline phosphatase, TGF-β1, serum, dexamethasone, and devitalization on AV calcification. A) Incorporation of 45Ca into AV leaflets cultured in different conditions as indicated. Control refers to leaflets cultured in 3.8 mM phosphate alone. Leaflets were devitalized by freezing and thawing several times. *$p<0.05$ vs. all groups, and &$p<0.05$ vs. all groups; n=6-8. B) Corresponding Alizarin Red stains. F: fibrosa, V: Ventricularis. Arrows point to calcified areas.

Warfarin was also added to the culture with or without IP and as shown in the Figure 5.6, warfarin induced significant calcification only when combined with IP. However, the extent of calcification in the leaflets was intense in the presence of both warfarin and IP compared to either warfarin or IP alone, as seen in the Alizarin Red staining.

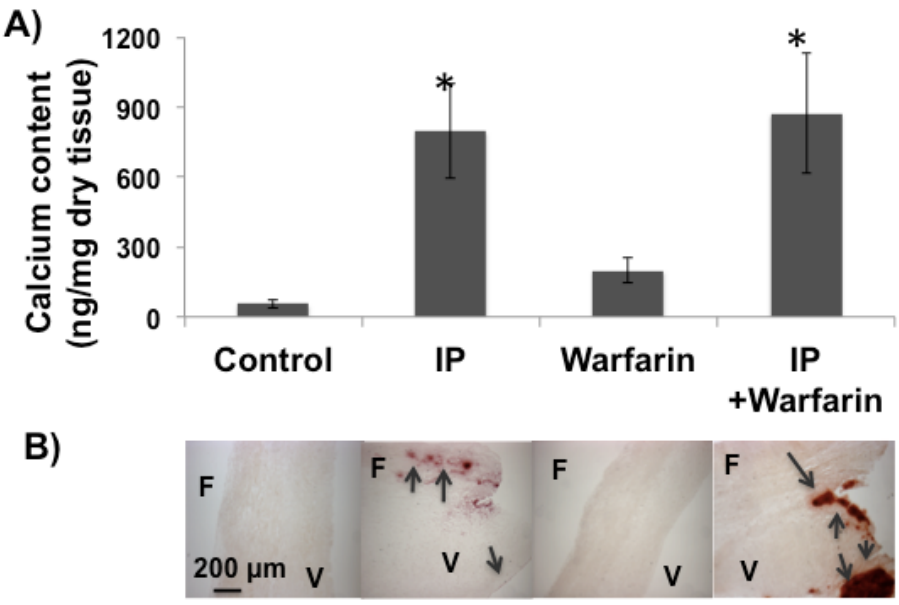

Figure 5.6 Effect of warfarin on AV calcification.
A) Incorporation of ^{45}Ca into AV leaflets cultured in the presence of warfarin with and without the inorganic pyrophosphatase. Control refers to leaflets cultured with 3.8 mM phosphates only. *p<0.05 vs. control; n =16. B) Corresponding Alizarin Red stains. F: fibrosa; V: ventricularis. Arrows point to calcified areas.

5.5.2 Effect of etidronate on AV calcification ex vivo

To confirm that the effect of IP was indeed due to removal of PPi, the bisphosphonate etidronate, a non-hydrolyzable analog of PPi (*180*) was added to the culture medium. As shown in Figure 5.7, etidronate completely prevented AV leaflet calcification at a concentration as low as 0.07 µM.

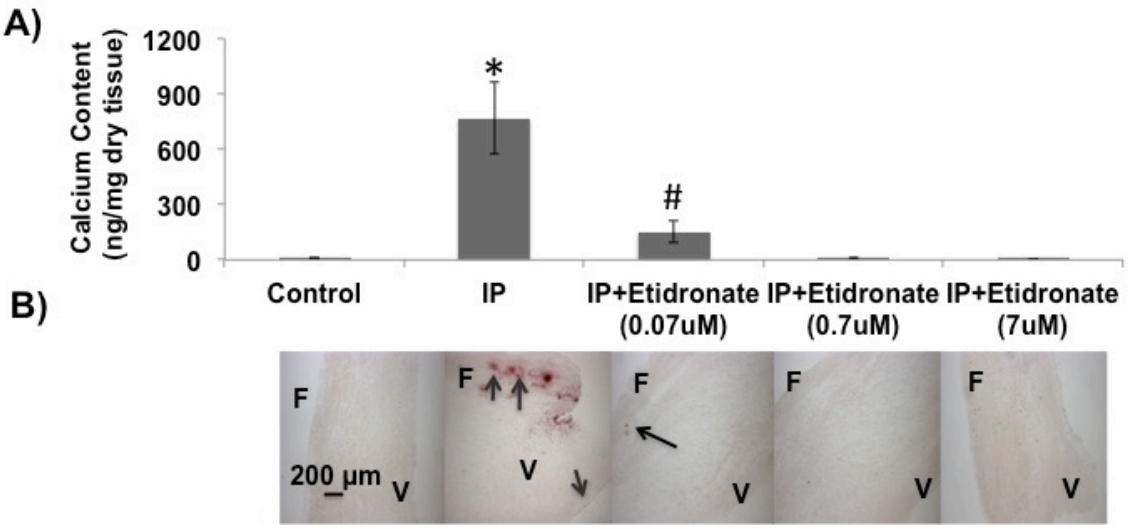

Figure 5.7 Effect of Etidronate on calcification of AV leaflets.
A) Incorporation of ^{45}Ca in valve leaflets over 8 days at different concentrations of etidronate with inorganic pyrophosphate. *p<0.05 vs. all other groups, #p<0.05 vs. 3.8 mM phosphates only and other concentrations of etidronate. B) Corresponding Alizarin Red stains. Arrows point to calcified areas. F: fibrosa; V: ventricularis.

5.5.3 AV structure and cell viability ex vivo

There were no apparent histologic changes in the leaflets after culture for 8 days as revealed by staining with Verhoeff-Van Gieson staining for elastin (Figure 5.8). Staining with methylthiazoletetrazolium, MTT (Figure 5.9) indicated that cell viability of AV tissues was maintained during culture. As expected there was no staining in devitalized leaflets. Consistent with MTT staining results, TUNEL staining did not reveal any apoptotic cells (Figure 5.10). Addition of phosphate, IP, ALP or etidronate did not alter histology or viability. However, cell viability or

apoptosis in the presence of TGF-β1, dexamethasone, serum and warfarin was not tested.

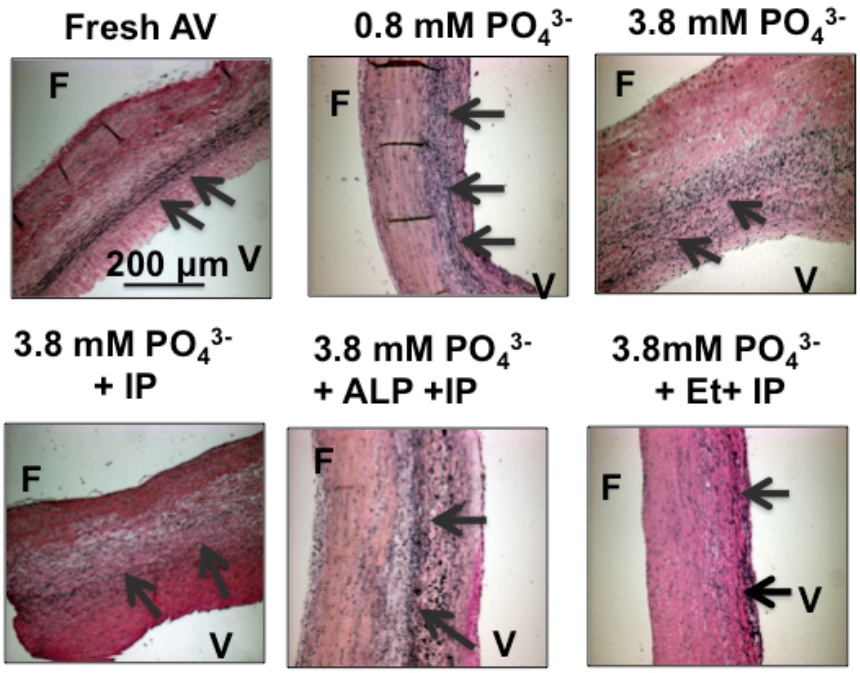

Figure 5.8 Verhoeff-Van Gieson elastin stain shows preserved AV structure under various culture conditions. Arrows point to elastin fibers oriented along the length of the tissue. F: fibrosa, V: ventricularis. A freshly isolated AV is included as a control.

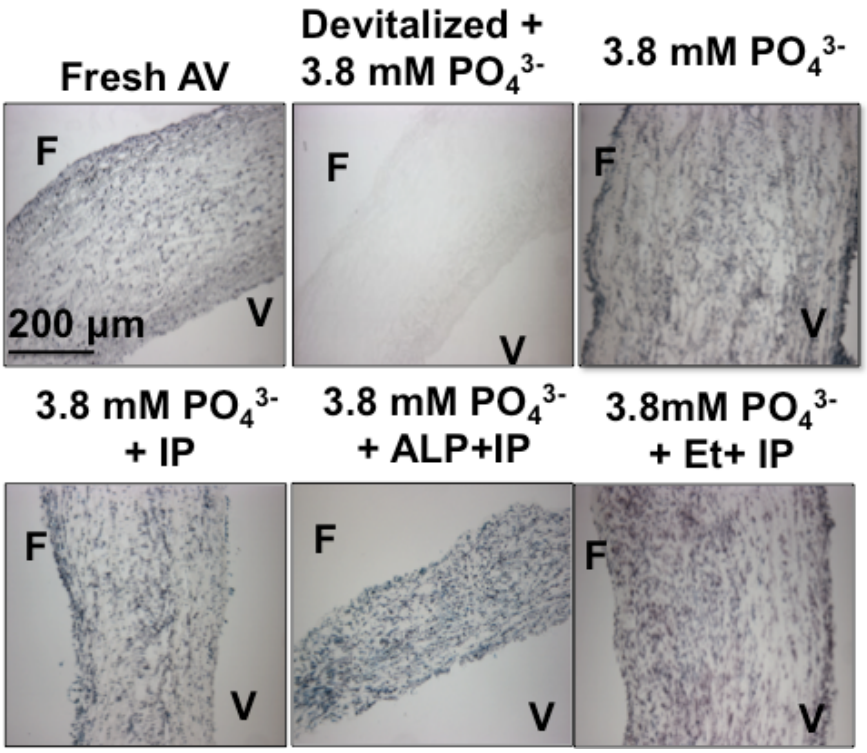

Figure 5.9 MTT stain shows preserved viability of AV tissue under various culture conditions. Leaflets devitalized (positive control) by freezing and thawing several times show no staining. F: fibrosa, V: ventricularis. A freshly isolated AV is included as a control.

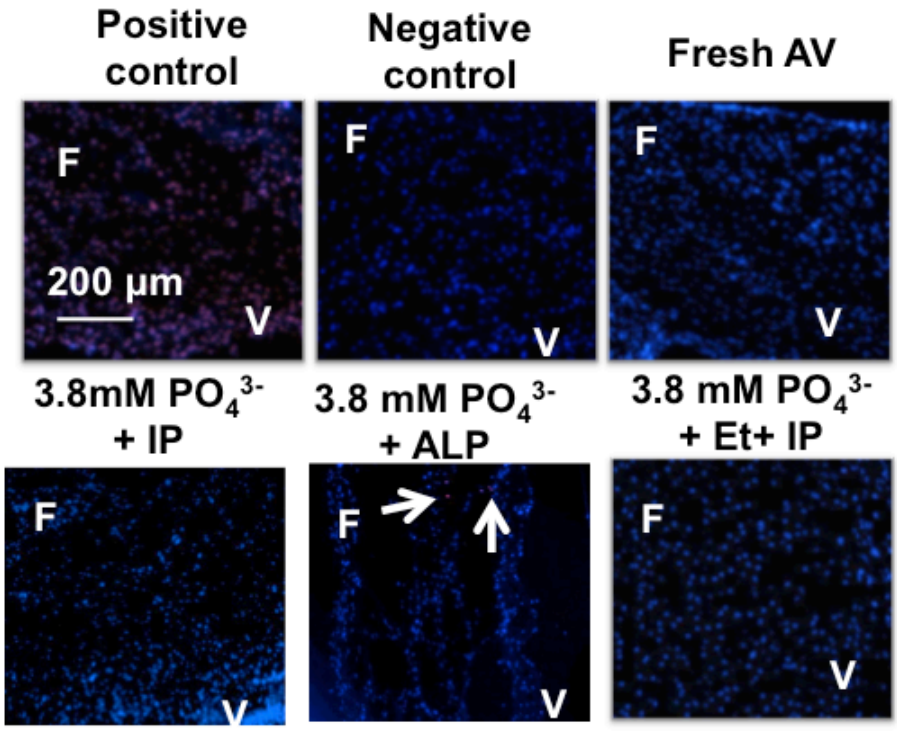

Figure 5.10 TUNEL stain for apoptosis.
Apoptotic nuclei stain red superimposed on the blue DAPI counterstain. Positive control: after treatment with DNase; negative control: without TMR red stain. Arrows point to apoptotic cells. Fresh and cultured leaflets each had less than 0.2% positive cells (out of >500 counted). F: fibrosa, V: ventricularis.

5.5.4 Synthesis of Pyrophosphate from AV Leaflets

Leaflets were capable of producing PPi, as shown by the appearance of PPi (measured by enzyme assay) in the medium (Figure 5.11A). MLS38949, an inhibitor of TNAP, was added to prevent hydrolysis of PPi. There was rapid appearance of PPi within the first hour and, in the presence of MLS38949, this continued to increase.

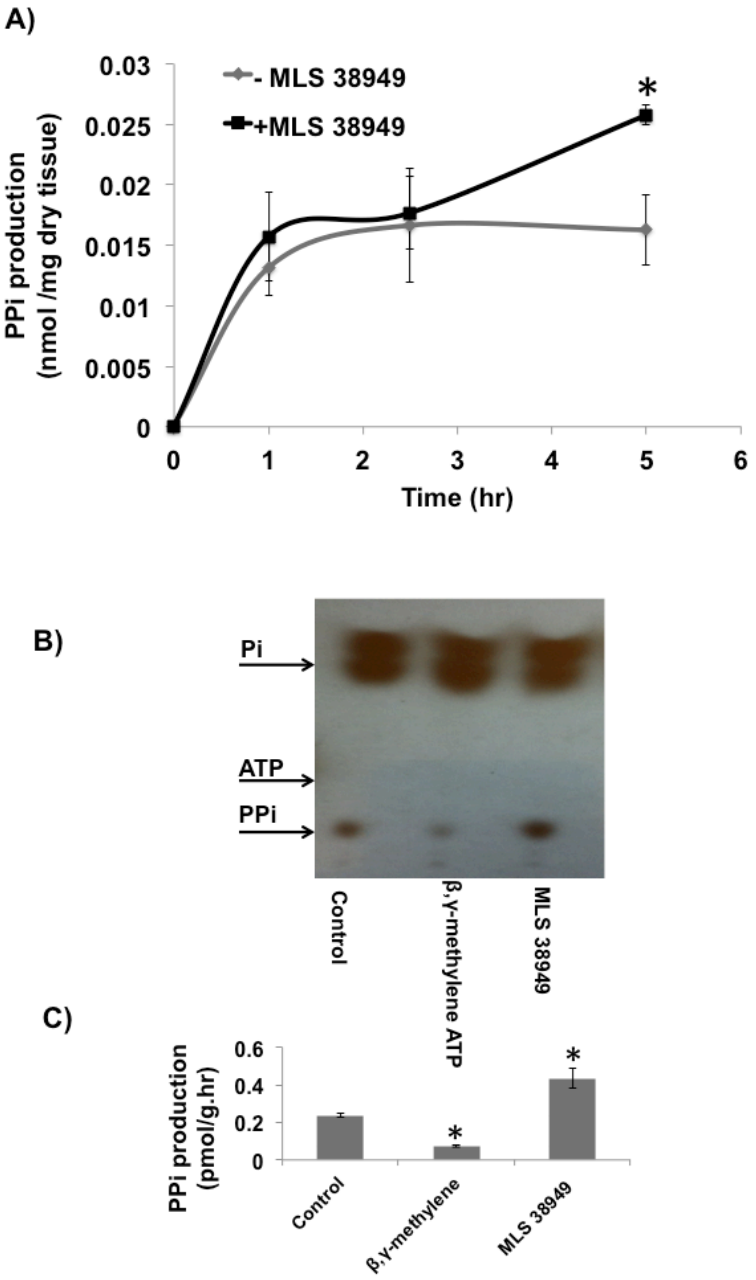

Figure 5.11 Synthesis of pyrophosphate from AV leaflets.
A) Quantification of PPi released into the medium from AV leaflets incubated with or without 30uM MLS38949 (an inhibitor of TNAP as a function of time). *$p<0.05$ vs. no MLS38949 at 5 h. n=4. B) Autoradiogram of a representative thin-layer chromatogram after incubation of valve leaflets with [γ^{32}P] ATP in 3 nM ATP with or without 30 μM MLS38949, an inhibitor of TNAP or 300 μM β,γ-methylene ATP, an inhibitor of ENPP1. All the exogenous ATP was consumed in 5 min. Control leaflets were incubated without any inhibitors. C) Quantification of PPi production by AV tissue from ATP. *$p<0.05$ vs. control.

ENPP1 is the sole enzymatic source of extracellular PPi. To determine whether it is active in valve tissue, freshly isolated leaflets were incubated with [γ^{32}P] ATP. Disappearance of ATP was rapid and complete by 5 min, with most of the ATP hydrolyzed to orthophosphate (Figure 5.11B, and C). However, a small amount of ^{32}PPi was apparent and this was reduced upon addition of β, γ-methylene ATP, an inhibitor of ENPP1 (*181*), indicating that ^{32}PPi was being synthesized by the leaflets and was not merely a contaminant of the [γ^{32}P]ATP. The amount of ^{32}PPi was significantly increased when the TNAP inhibitor MLS38949 was added.

5.6 Discussion

Valve leaflets cultured under serum-free conditions maintained viability and normal morphology for at least 8 days. Under these conditions, calcification required an elevated phosphate concentration and the addition of inorganic pyrophosphatase. This calcification occurred mostly in the fibrosa as seen in humans *in vivo*, although there was occasional calcification of the ventricularis side. This is consistent with previous clinical and experimental findings that have shown that fibrosa is more prone to mineralization compared to ventricularis (*1*). In AVs from patients with end-stage renal disease, a hyperphosphatemic, low pyrophosphate condition (*182*), calcification is also primarily within the fibrosa with occasional involvement of the ventricularis (O'Neill, W.C., unpublished data).

The effect of phosphate is likely due to promotion of CaH_2PO_4 crystallization and subsequent hydroxyapatite formation (*169*) but phosphate may also induce

cellular changes including osteogenic differentiation that may promote mineralization (*38*). Serum phosphate is a known risk factor for valvular calcification in CKD (*27, 37*). The requirement of IP is probably related to removal of PPi, a critical endogenous inhibitor of calcification. Inhibition of calcification by etidronate, a non-hydrolyzable PPi analog is consistent with this. Unlike IP, which selectively hydrolyzes PPi, ALP can hydrolyze other phosphorylated compounds as well such as osteopontin, another endogenous inhibitor of calcification (*3*). The fact that ALP did not produce additional calcification when added with IP suggests that other phosphorylated inhibitors are not active in cultured AV leaflets.

TGF-β1, dexamethasone and serum are commonly used additives in osteogenic media to induce calcification in AV leaflets (*17, 102, 151, 183*) were added to the culture medium to determine their calcification potential independent of each other. Although the addition of neither of these compounds induced higher calcification compared to that of ALP or IP alone, the distribution of calcification nodules within the AV leaflet tissue differed. This suggests that the underlying mechanisms by which these compounds induce calcification might be different. However, no further experiments were carried out to understand these different mechanisms, as the focus of this aim is to specifically understand the role of pyrophosphate in AV calcification. As expected, the significant calcification after devitalization is consistent with loss of calcification inhibitors although cell necrosis could become a nidus for dystrophic calcification (*5*).

Warfarin is a commonly administered anti-coagulant to patients receiving vascular devices or grafts. Warfarin, a vitamin K antagonist can induce arterial and valvular calcification by potentially inhibiting MGP, an endogenous inhibitor of calcification (*184, 185*). This process inactivates the putative calcification-inhibitory activity of MGP. Although addition of warfarin did not induce further calcification quantitatively, the amount of calcification within the tissue was severe compared to the control group or IP alone, as seen in the Alizarin Red staining. The investigation on warfarin induced AV calcification in this study is only to demonstrate a possibility, and a proof of concept. Further in-depth studies are warranted to understand this response and specifically the role of warfarin, and its possible interactions with PPi or TNAP or other regulators of calcification.

Thus, the role of PPi in inhibiting AV calcification observed in this study is consistent with a previous study in cultured valvular interstitial cells and with the known inhibitory role of PPi in vascular calcification. Similar effects of IP and ALP were observed in cultured aortas (*170, 176*). Bisphosphonates, which are non-hydrolyzable analogs of PPi, also prevent vascular calcification in culture and in vivo (*186, 187*). Although PPi is present in the circulation at concentrations that can inhibit calcification (*169*), it is clear from the results that valve tissue can synthesize PPi that could act locally. Valve leaflets generated PPi from added ATP, which significantly decreased in the presence of β, γ methylene ATP, an

inhibitor of ENPP1. This enzyme is a major source of extracellular PPi and deficiency of ENPP1 results in severe arterial calcification in humans (*188*) and mice (*173*). Since β,γ methylene ATP interferes with the assay of PPi, it is not possible to determine the contribution of ENPP1 to net PPi synthesis by the leaflets. Another potential source of extracellular PPi is the putative membrane transporter ANK but since there are no known inhibitors, its contribution cannot be determined.

Paradoxically, ENPP1 expression is increased in calcified valves (*189*) and has been proposed to promote calcification by reducing extracellular ATP levels (thereby promoting apoptosis) and increasing phosphate levels. However, the studies supporting this were performed in cultured cells and the amount of phosphate that could be generated from extracellular ATP is minimal compared to ambient phosphate levels. While this remains a possible mechanism, the current results demonstrate that simple removal of PPi without altering ENPP1 is sufficient to produce calcification, indicating that ENPP1 activity is required to prevent calcification. It is possible that the increased ENPP1 expression in calcified valves is a compensatory response to the calcification or a local deficiency of PPi.

TNAP hydrolyzes PPi and also regulates the availability of PPi in the vascular tissues (*175*), being responsible for almost 50% of the PPi hydrolysis in vascular smooth muscle. Inhibition of TNAP significantly increased the production of PPi

by AV leaflets, indicating that this enzyme also influences the levels of PPi in the AV. Consistent with this, elevated ALP activity has also been reported in calcified valves (*190*).

This tissue-based model offers substantial advantages over cultured cells because a normal extracellular matrix and both valve interstitial and endothelial cells are present. In addition, the serum-free culture medium avoids potential problems related to the myriad of growth factors, cytokines, and compounds present in serum. The absence of serum did not affect cell viability (Figure 5.9 MTT stain shows preserved viability of AV tissue).

5.7 Limitations

In this study, the cultures were performed under static conditions, which do not reflect the dynamic mechanical environment *in vivo* that differs on either side of the leaflets. Even in static cultures, our results show that AV leaflets are capable of producing PPi, the levels of which are intricately regulated by the expression of ENPP1 and TNAP. Since mechanical stimuli have significant effects on cell metabolism in valve tissue (*10*), the metabolism of PPi is likely to be affected as well and will require further study.

5.8 Conclusions

The results of this study demonstrate a critical role for pyrophosphate in AV calcification and suggest important roles for ENPP1 and TNAP in controlling PPi levels in valvular tissue.

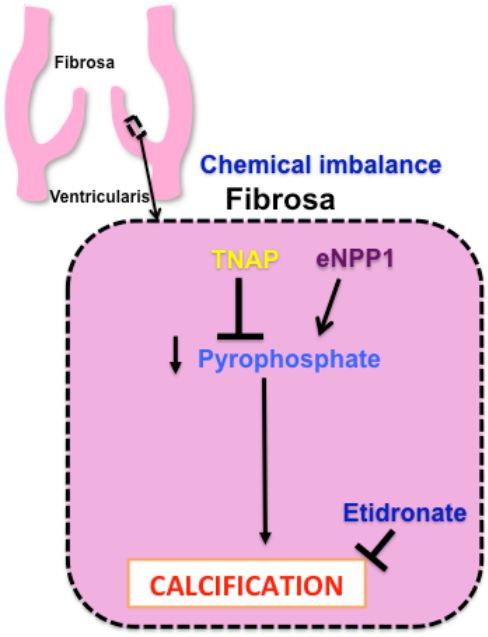

Figure 5.12 Schematic showing the conclusions of specific aim 3.

Thus agents that enhance ENPP1 activity or inhibit TNAP could be potential therapies. Although PPi could be administered to treat AV calcification, it is subject to rapid hydrolysis *in vivo* (*42*). Bisphosphonates, which are non-hydrolyzable analogs of pyrophosphate, have been shown to inhibit vascular calcification in animal models. These are a potential alternative, but could have unknown effects on bone metabolism.

CHAPTER 6 DISCUSSION

Calcific aortic valve disease is a multifactorial disease and a major risk factor for cardiovascular related deaths in elderly population (*16, 168*). Calcified AV leaflets show signs of endothelial damage, inflammation, macrophage infiltration, and bone formation preferentially in the fibrosa compared to ventricularis (*9*). The focus of this thesis was to improve our current understanding of the molecular mechanisms involved in this preferential pathogenesis in the fibrosa. The overall hypothesis of this work was *"sclerosis, inflammation, and calcification preferentially occur in the fibrosa compared to the ventricularis due to differential gene expression and oscillatory shear stress".* This hypothesis is represented in a schematic (Figure 6.1) and was tested by three specific aims using porcine AV leaflets with an ex vivo approach: 1) identification of the side- and shear-dependent miRNAs (miR-181a, and miR-214) involved in AV sclerosis, inflammation and calcification, 2) determination of the relationship between a key side- and shear-dependent miRNA, miR-214 and AV pathogenesis, and 3) investigation of the role of pyrophosphate in AV calcification. This chapter discusses the key findings of these specific aims in the context of the overall hypothesis of this dissertation.

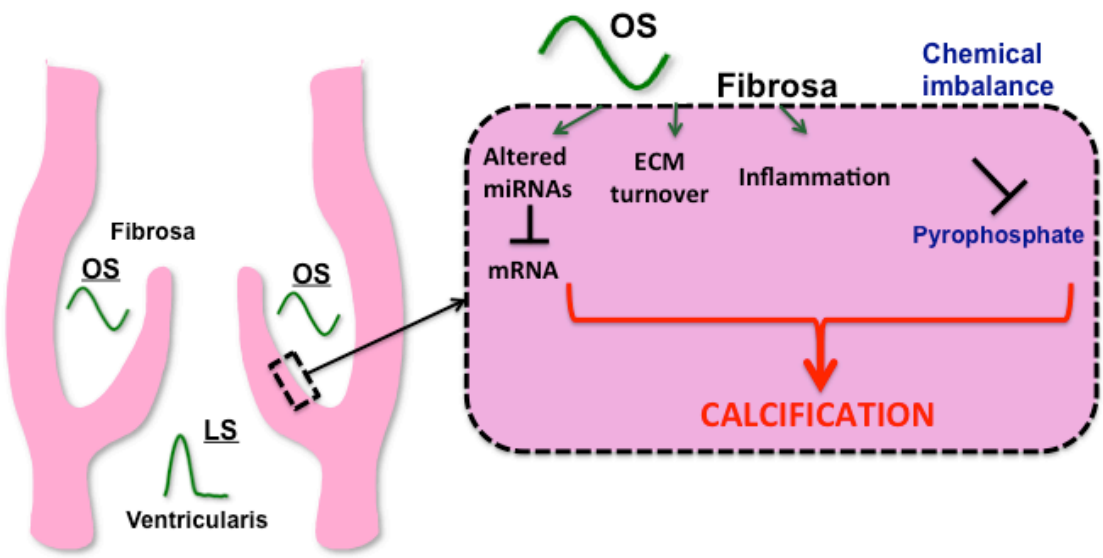

Figure 6.1 Schematic showing the overall hypothesis of this dissertation.

6.1 Low magnitude oscillatory shear stress induced a pro-sclerotic, -inflammatory and -calcific environment in the fibrosa compared to the ventricularis

The oscillatory shear stress (OS) induced calcification in the fibrosa compared to the ventricularis, similar to the calcified valves (*9*). The OS also changed the collagen composition (decreased mature, and increased young, nascent collagen fibers), increased collagen turnover (*Col1a1*) in the fibrosa compared to the ventricularis exposed to OS or LS. These changes constitute active remodeling in the fibrosa and can explain the observed OS induced increase in thickness of the fibrosa. Further, OS also decreased the atheroprotective markers (*Enos*, *Klf4*) in the fibrosa creating a pro-inflammatory environment. Selective ECM remodeling and loss of anti-inflammatory markers in the fibrosa are also observed in sclerotic valves (*1*). These findings suggest that OS promoted

calcification in the fibrosa by altering the ECM and inducing a pro-inflammatory environment.

6.2 Side-and shear-dependent miRNA, miR-214 is potentially involved in AV sclerosis but not inflammation and calcification

As the miRNAs are recognized as key regulators of gene expression in both cardiovascular and valvular diseases (*22, 156*), their involvement in OS induced AV pathogenesis was investigated. Further, the active ECM remodeling observed in the fibrosa exposed to OS, can also affect the miRNA expression (*121*), gene expression changes and vice versa (*25, 145*). In response to OS, two miRNAs (miR-181a and 214) showed side-dependency as they were highly expressed in the fibrosa but not ventricularis. The side- and shear-dependency of these two miRNAs corroborate the previous observation that the miRNAs are differentially expressed on either side of the valve and are mechanosensitive (*22*).

Of the 5 potential mRNA targets tested, only *Klf4* was significantly upregulated upon silencing miR-214. It can be speculated that miR-214 regulates *Klf4*, and is involved in the OS dependent inflammation (*155, 164*) induced in the fibrosa. Since silencing of miR-214 did not significantly affect the expression of *Icam1, Vcam1*, and *Bmp4*, or calcium levels, miR-214 may not be directly involved in AV inflammation and calcification. However, miR-214 silencing significantly decreased *Tgfβ1* indicating that miR-214 may be involved in pathways regulated by *Tgfβ1* such as fibrosis and EndoMT (*143, 145, 151, 159, 161*). It is interesting

to note that anti-miR-214 inhibited some markers of EndoMT inducers such as *Tgfβ1* while rescuing expression of anti-Endo-MT markers (*VE-Cadherin* and *Klf4*), supporting the potential role of miR-214 in Endo-MT pathway. However, anti-miR-214 showed no effect on *Sma*, another key EndoMT marker. These results suggest the complex role of miR-214 and that it may work in concert with other miRNAs to regulate the AV pathophysiology.

Thus, the miR-214 can mediate OS induced fibrosis and Endo-MT (changes in *Tgfβ1*, *Klf4, VE-Cadherin, Col1a1*, and ECM architecture and fibrosa thickening) (Figure 6.2). Also, the increased expression of miR-214 in response to OS may be indicative of the early stages of AV pathogenesis. Given the critical role for *Tgfβ1* and *Klf4* in cardiovascular pathophysiology, we propose that miR-214 is a key miRNA involved in early AV pathogenesis in a side- and shear- dependent manner. Further research is warranted to understand the complex functional role of miR-214 in mediating AV inflammation and calcification.

6.3 Cyclic stretch and hypertensive pressure can cause greater damage to AV compared to the OS

As discussed previously (section 6.1), the OS initiated calcification in the AV leaflets, preferentially in the fibrosa compared to the ventricularis. Under similar culture conditions (media: osteogenic, culture duration: 7 or 8 days), the extent of calcification in AV leaflets as a result of elevated cyclic stretch (15%) and severe hypertension (160/100 mmHg) alone was remarkably higher than that induced by the OS. It is well known that hypertension and elevated leaflet stretch are

associated with the calcific AV disease (*17, 78*). It appears that the increased strain of the leaflets as a result of hypertension (*64*) can possibly induce more damage to the AV leaflets than the OS. This is an interesting result from this dissertation and warrants further investigation.

6.4 Inorganic pyrophosphate prevents the AV ectopic calcification

Inorganic pyrophosphate is well known to inhibit the ectopic calcification of blood vessels (*170*). Pyrophosphate appeared to play a similarly important role in AV as its removal lead to calcification in AV leaflets. The specificity of PPi was demonstrated when etidronate (a synthetic non-hydrolyzable analog of PPi) prevented this calcification induced by the removal of PPi. Similar to the vasculature (*170*), the levels of PPi in AV leaflets seemed to be regulated by the TNAP as the production of PPi increased markedly when TNAP was inhibited. Moreover, a significant amount of PPi came from ATP in AV leaflets via the action of an enzyme, ENPP1. Based on these findings, the increased expression of ENPP1 observed in calcified AVs (*171*) could be a compensatory response to the calcification or a local deficiency of PPi induced by the high expression of TNAP (*190*). The pyrophosphate thus, protects the valve from calcification and its expression is likely regulated through the synthesis by ENPP1 and hydrolysis by TNAP. Furthermore, the synthetic analogs of PPi or inhibitors of TNAP could be good candidates as therapeutics to prevent AV calcification.

6.5 Proposed AV disease mechanisms

We believe that AV calcification is a multifactorial disease and thus, based on our findings, two distinct, yet plausible mechanisms are proposed as shown in the

Figure 6.2. The dashed lines in the schematic show the possible feedback mechanisms as previously explained in section 6.2.

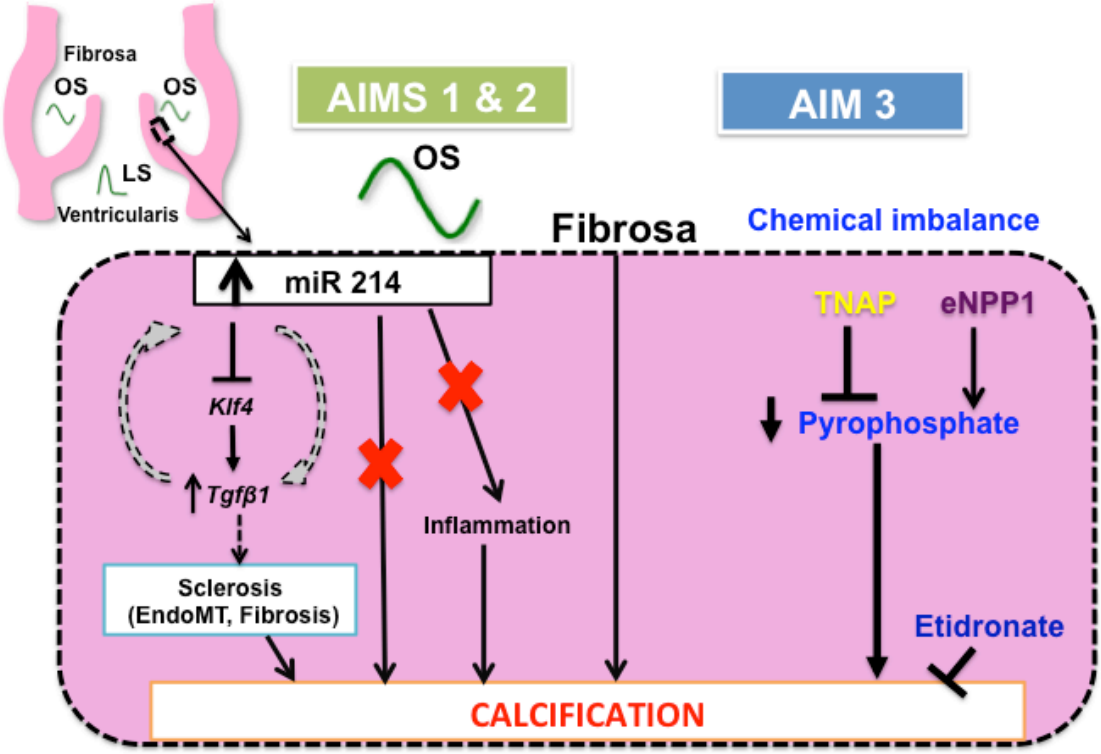

Figure 6.2 The proposed pathways that lead to calcific AV disease.
The dashed lines show the possible mechanisms and feedback loop.

CHAPTER 7 CONCLUSIONS

The focus of this thesis was to understand the basis for this increased susceptibility of the fibrosa to sclerosis, inflammation, and calcification. The calcification model developed by Balachandran et.al (*17*) was used in conjunction with the *ex vivo* shear system to induce side-dependent calcification.

The oscillatory nature of the shear stress at a low magnitude induced calcification preferentially in the fibrosa compared to the ventricularis, in a manner consistent with the calcification patterns observed in diseased human AVs (*1, 9*). The low magnitude oscillatory shear stress (OS) possibly predisposed fibrosa to side-dependent calcification via increasing collagen turnover (*Col1a1*), and thickening of the ECM (fibrosis) and decreasing the expression of genes that protect endothelial function (*Klf4* and *Enos*). The unidirectional pulsatile shear, LS, however, preserved the ECM and gene expression in the ventricularis.

The involvement of miRNAs in OS mediated AV pathogenesis was also investigated. Several groups have investigated the function of miRNAs in an *in vitro* setting (*22, 107, 191, 192*); however, the cell culture does not reflect events and metabolism in intact tissues. In this work, we are the first to investigate the role of a miRNA in AV pathogenesis in an *ex vivo* setting in a shear-dependent manner. The miR-214 was found to play a role in this OS induced pathogenesis in fibrosa but not ventricularis. An *ex vivo* miR silencing protocol was also

developed to perform the miRNA functional studies. The anti-miR was successfully delivered to both endothelial and interstitial cells of the AV tissue without compromising the cell viability. The miR-214 silencing studies showed that this OS induced pathology in the fibrosa is likely to be mediated via miR-214, *klf4 and Tgfβ1* dependent pathway that can lead to AV fibrosis, Endothelial-to-mesenchymal transition and eventually sclerosis. The miR-214, however, did not play a role in shear-induced inflammation and calcification. The miR-214, as such, is likely to play a key role in the early onset of side- and shear- dependent AV disease and has a potential to serve as a disease biomarker.

This dissertation also focused on understanding the role of pyrophosphate in inhibiting AV calcification. The protective role of PPi is well known in vascular calcification (*4, 170*), and in calcified AVs (*171*). For the first time, this work showed that AV leaflets actively synthesize PPi from ATP through an enzyme, ENPP1. The PPi in turn protects AV leaflets from calcification. Calcified AVs contain elevated levels of tissue non-specific ALP (*190*), TNAP that hydrolyzes PPi and decreases its protective action. The PPi is rapidly hydrolyzed in vivo as such, PPi cannot be administered directly to treat AV calcification (*42*). The synthetic non-hydrolyzable analogs of PPi such as Etidronate can be used to treat or slow down AV calcification, as shown in our study. Thus, the agents that inhibit TNAP activity or increase the ENPP1 activity could be potential therapies.

To conclude, the role of miRNA(s) in OS mediated side-dependent AV pathogenesis was studied in this work. This thesis provided preliminary evidence

that stretch and hypertension may be the major players inducing calcification in AV compared to the OS. The potential of synthetic analogs of PPi for use as a drug to inhibit AV calcification was also demonstrated. These findings add more knowledge to the existing information on the molecular mechanisms involved in AV calcification. Furthermore, the findings from this thesis can be used as a basis in future studies targeted towards developing preventative therapies.

CHAPTER 8 RECOMMENDATIONS AND FUTURE WORK

This chapter details the recommended future work – both short tem and long term, based on the findings in this dissertation.

8.1 Short term projects

8.1.1 Role of miRNAs in pathogenesis of AV calcification

The miRNAs are key regulators of gene expression and serve as biomarkers for cardiovascular diseases. Our findings corroborate recent evidence that miRNAs also play an important role in AV pathogenesis (*22, 106*). Further, the findings and methods developed in this dissertation opened several new avenues for this exciting new area of research. Of the two side- and shear-sensitive miRNAs (miR-181a and miR-214) identified in this thesis, only miR-214 was further investigated as part of this dissertation. Interestingly, miR-214 seemed to be involved in oscillatory shear stress, OS mediated AV sclerosis but not inflammation and calcification. However, shear studies should be carried out for longer culture durations in both regular and calcification media (at least 7 days) to confirm this observation. Alternatively a pre-miR-214 can also be transfected in fibrosa exposed to OS to determine if the overexpression of miR-214 aggravates inflammation and calcification of AV. One of the challenges of this work was that the size of the sheared tissue was not large enough to isolate

good quality and quantity of protein. This is the major reason why the targets were only validated at the mRNA level but not at protein level. In future studies, the *ex vivo* cone and plate shear system should be modified to accommodate an AV tissue size greater than 7 mm dia (current size).

In addition, it would also be interesting to see how miR-214 behaves in elevated stretch and hypertension mediated AV inflammation and calcification Also, since miR-181ais strongly involved in inflammation and lipid metabolism in vasculature (*125, 126, 129*), future studies can also focus on understanding the role of miR-181a in AV inflammation and calcification.

8.1.2 Synthesis and regulation of pyrophosphate by the dynamic mechanical environment experienced by the AV

AV leaflets actively synthesize PPi, which inhibits calcification. The PPi levels are regulated by the TNAP. We also showed that AV leaflets synthesize PPi from ATP through the enzymatic action of ENPP1. A transmembrane protein, ANK, maintains the circulating levels of PPi and the absence of ANK results in ectopic calcification (*174*). The function of ANK and its regulation of PPi in AV leaflets were not verified in this dissertation and should be pursued in future studies.

This dissertation is the first to report a systematic investigation of the role of PPi in healthy porcine AV leaflets. These studies were carried out using freshly isolated and statically cultured AVs. However, the AV experiences a dynamic

mechanical environment, which likely changes the mechanism by which the PPi and TNAP are regulated. Since ANK and ENPP1 are mechanosensitive (*193*), their enzymatic activity will also possibly change in the presence of physiological and altered mechanical stimuli. As synthetic analogs of PPi offer great potential to treat or slow down AV calcification, understanding how PPi is regulated in a mechanical environment, will aid in developing therapeutics to treat AV calcification.

8.1.3 Warfarin and AV calcification

Warfarin (common name: Coumadin) is a widely used anti-coagulant in patients receiving cardiovascular or valvular devices. However, warfarin administration is associated with several side effects and has been shown to interfere with the calcification process (*185*). It is a vitamin K antagonist that can induce arterial and valvular calcification by potentially inhibiting gamma-carboxylation of matrix Gla protein, an endogenous inhibitor of calcification (*184, 185*). This dissertation presented some evidence that use of warfarin can increase the tendency of AV leaflets to calcify. Further in-depth studies are warranted to understand this response. Specifically the role of warfarin or any vitamin K antagonist drug and that drug's possible interactions with PPi, TNAP, or other regulators of calcification could be investigated.

8.2 Long term projects

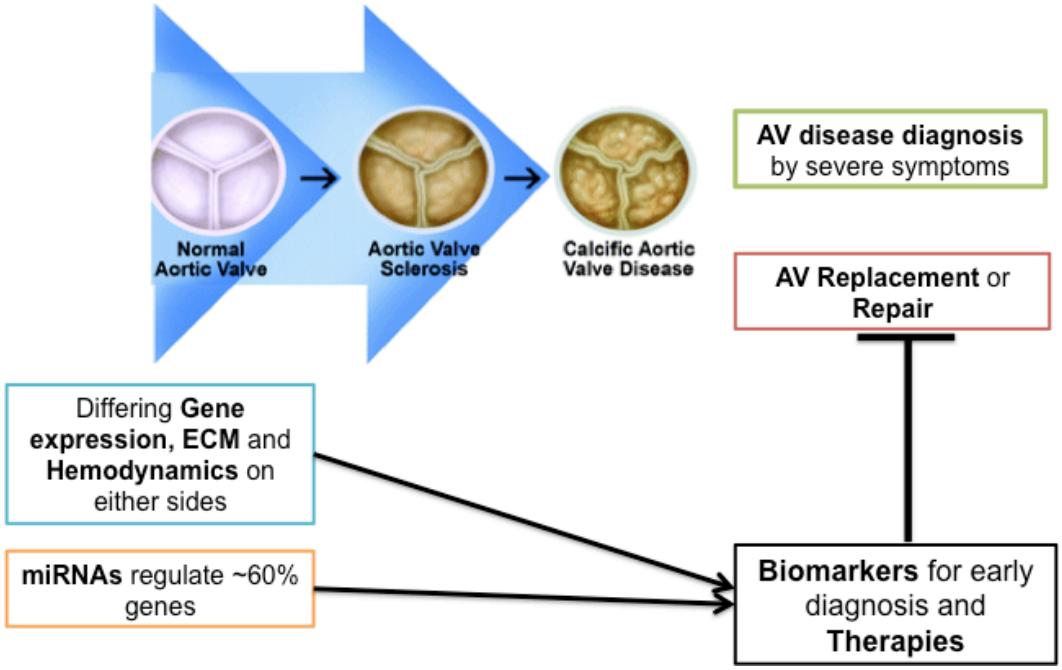

Figure 8.1 Understanding the miRNAs involved in side-dependent AV disease will aid in identification of biomarkers for early AV disease detetction and therapies.

8.2.1 Effect of combined mechanical stimuli: stretch, pressure and shear in mediating aortic valve pathogenesis

Independent reports on isolated effects of elevated stretch, pressure and shear stress on AV are available (*17, 22, 83, 84, 102*). However, different culture conditions prevent us from making a holistic comparison. This dissertation showed preliminary evidence that under similar culture conditions (media: osteogenic media, duration: 7 or 8 days), elevated stretch and hypertensive pressure induced significantly higher calcification in AV leaflets compared to the OS. However, supplementary studies need to be performed to understand if elevated stretch and hypertension activated additional mechanisms that resulted

in this increased calcification compared to the OS. For these purposes, future studies could start by looking at the extracellular matrix characterization and remodeling, activation of valvular interstitial cells, and expression of pro- and anti- inflammatory markers in response to each of these mechanical stimuli.

Additionally, future studies can also focus on developing a tissue bioreactor that can expose the entire valve and its aortic root to its native and altered dynamic mechanical environment. This enables us to look at the combined effect of each of the stimuli (stretch, pressure and shear) and to understand how these stimuli act in synergy. For instance, a recent study showed that isolated stretch increased the expression of α-SMA in AV leaflets, whereas pressure decreased it (*83*). When both stretch and pressure were combined, the expression of α-SMA was comparable to that of freshly isolated AV leaflets. Thus, these studies definitely provide us additional cues on AV calcification mechanisms.

8.2.2 miRNA based biomarkers and therapies for AV calcification

The regulation of gene expression by miRNAs is complex and is cell, tissue, mechanics and time dependent. The expression of miRNAs is precisely controlled in physiological state, and is sensitive to changes such as development, environment changes, diseases, and therapies. As such, the miRNAs have great potential to serve, as biomarkers for early identification of pathogenesis for a variety of cardiovascular diseases (*88*). For example, based on the findings in this dissertation, miR-214 can be potentially linked to the early

shear-dependent AV pathogenesis. Since calcific AV disease is a multifactorial disease, further investigations as to how this miRNA is regulated in conjunction with other miRNAs and cytokines *in vivo* are warranted. Thus, a complete understanding of the regulatory mechanisms of miRNAs and the gene expression is the most important issue at present as this knowledge is essential for the development of genomic-based therapeutics.

APPENDIX

A.1. Cone and plate system drawings

A.1.1 Overall bioreactor assembly

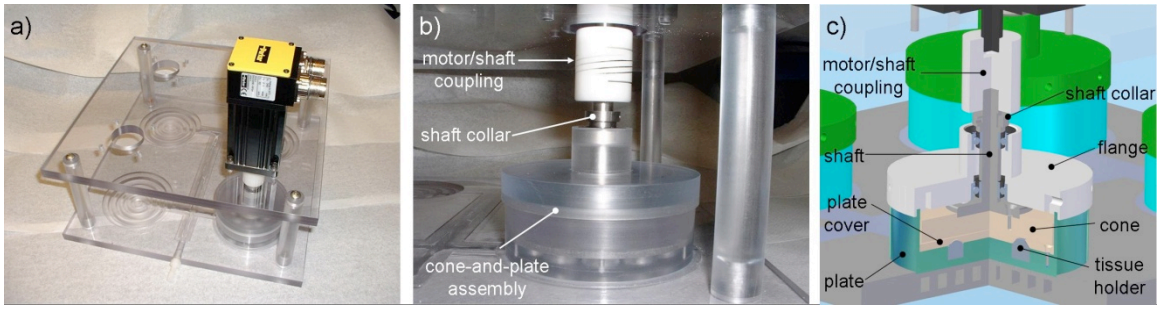

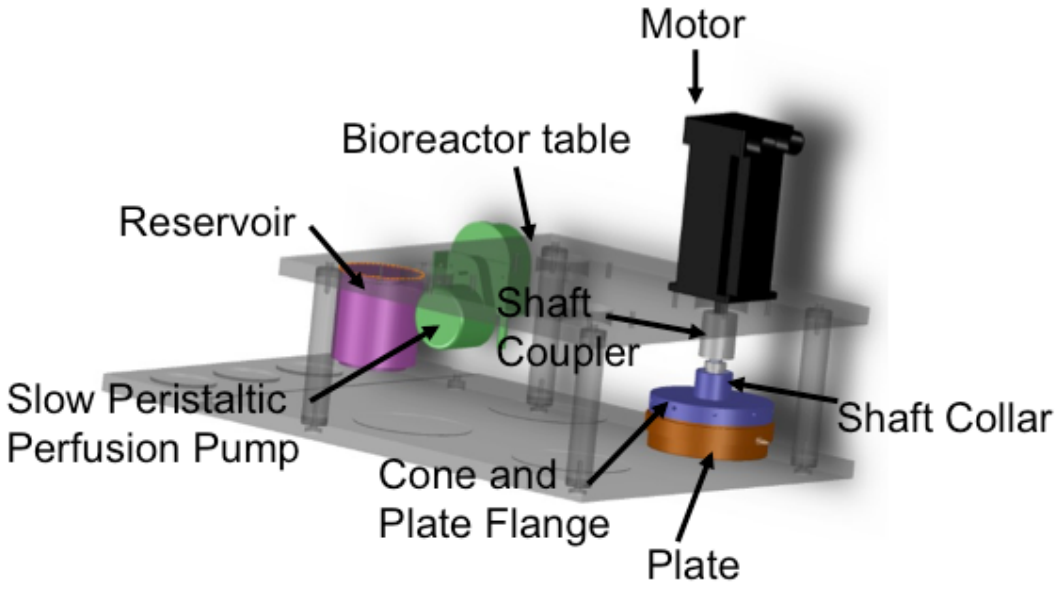

A.1.2 Cone

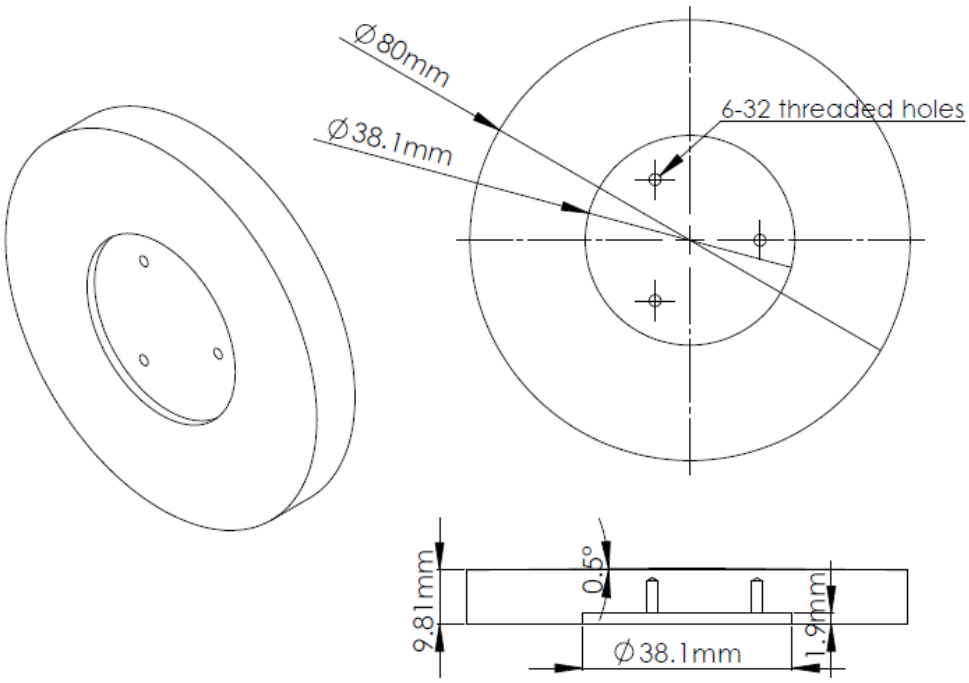

A.1.3 Shaft collar

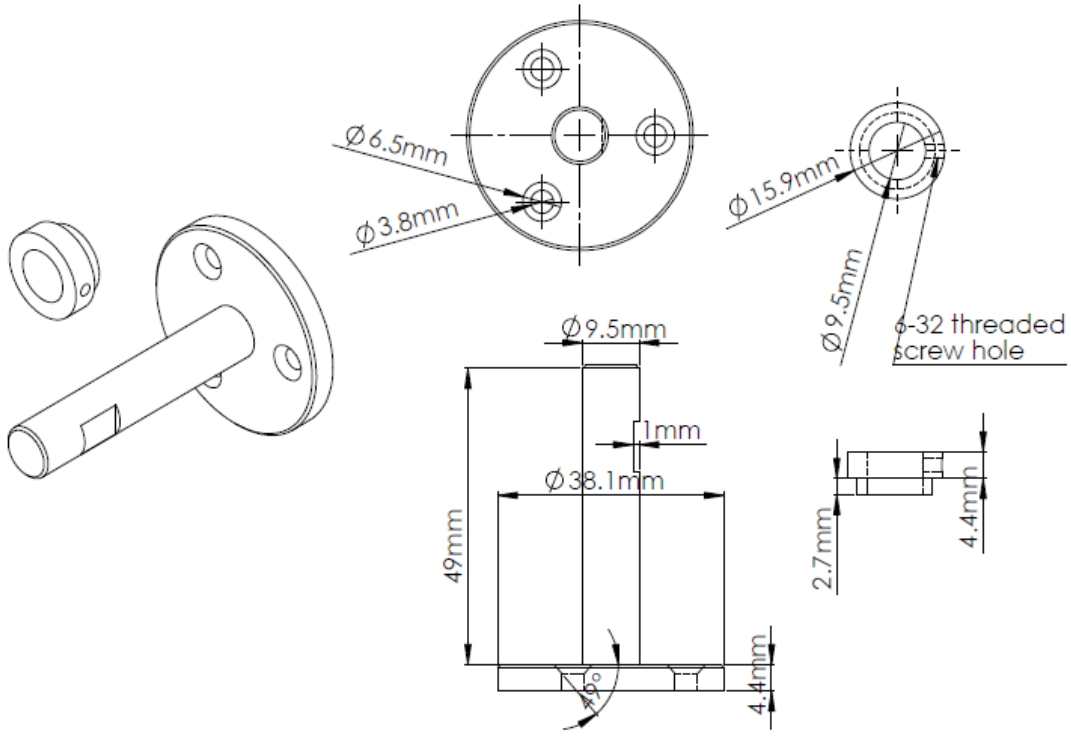

A.1.4 Cone flange

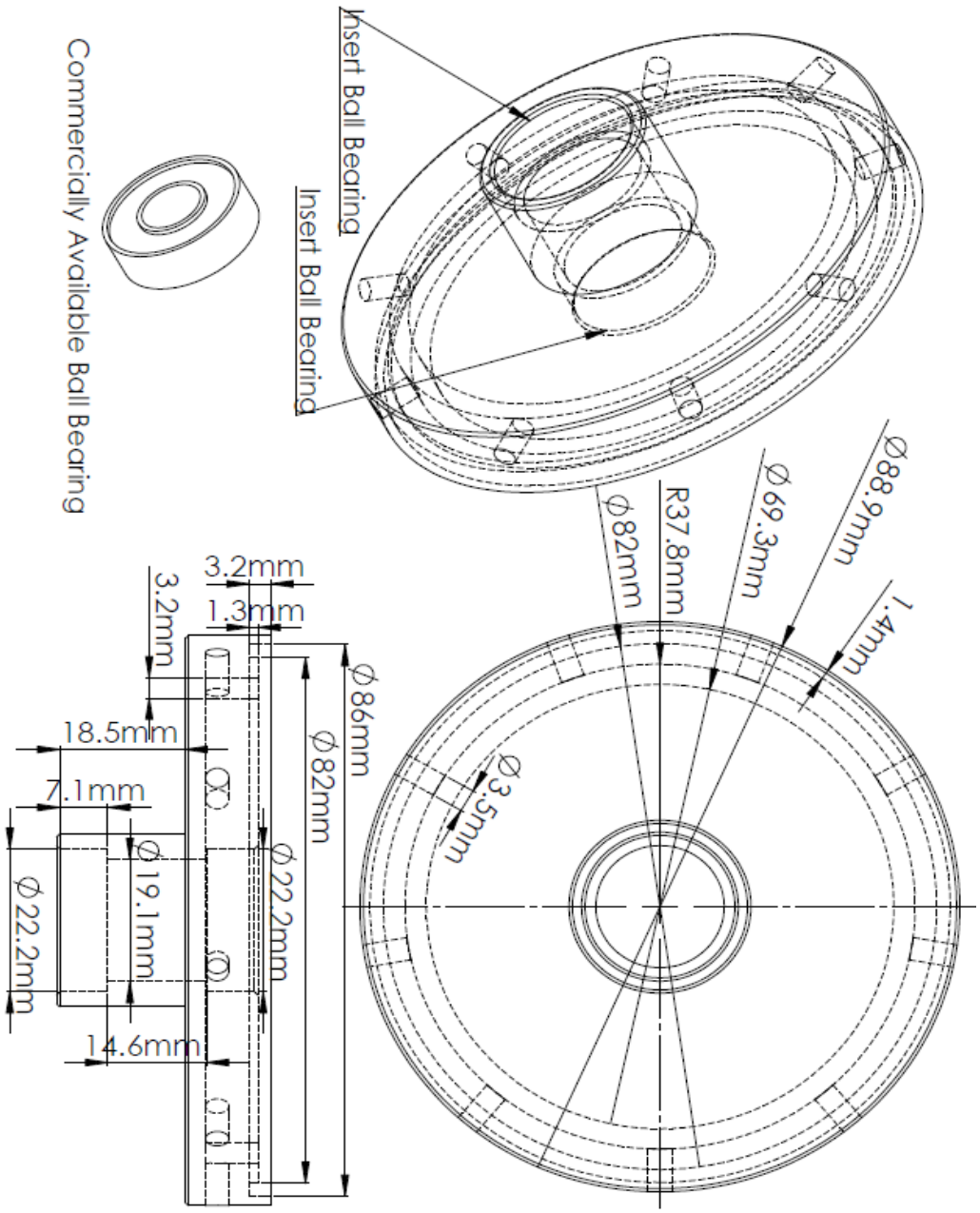

A.1.5 Plate

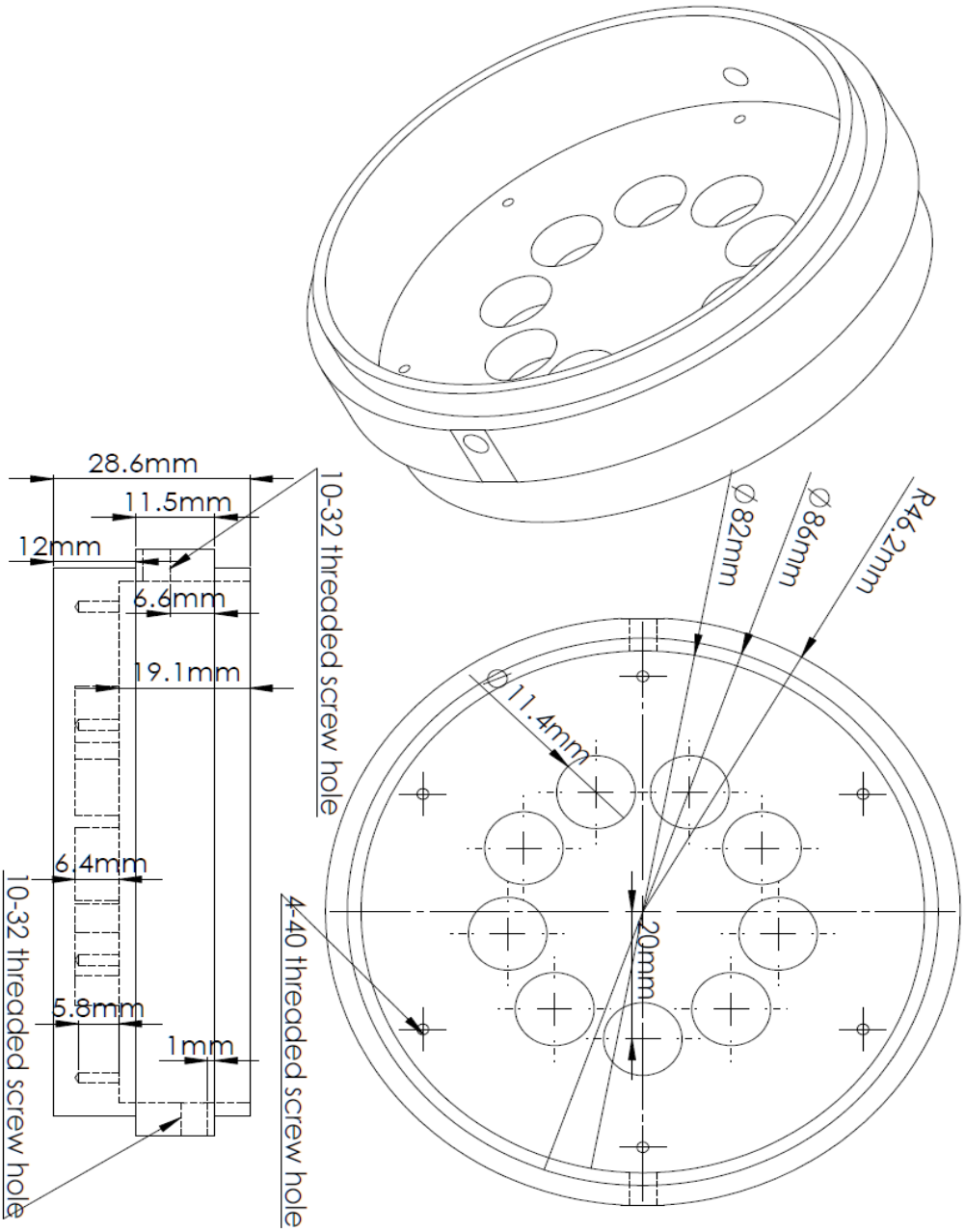
28.6mm
11.5mm
12mm
6.6mm
19.1mm
6.4mm
5.8mm
1mm
10-32 threaded screw hole
10-32 threaded screw hole
4-40 threaded screw hole
Ø82mm
Ø86mm
R46.2mm
Ø11.4mm
20mm

A.1.6 Plate cover

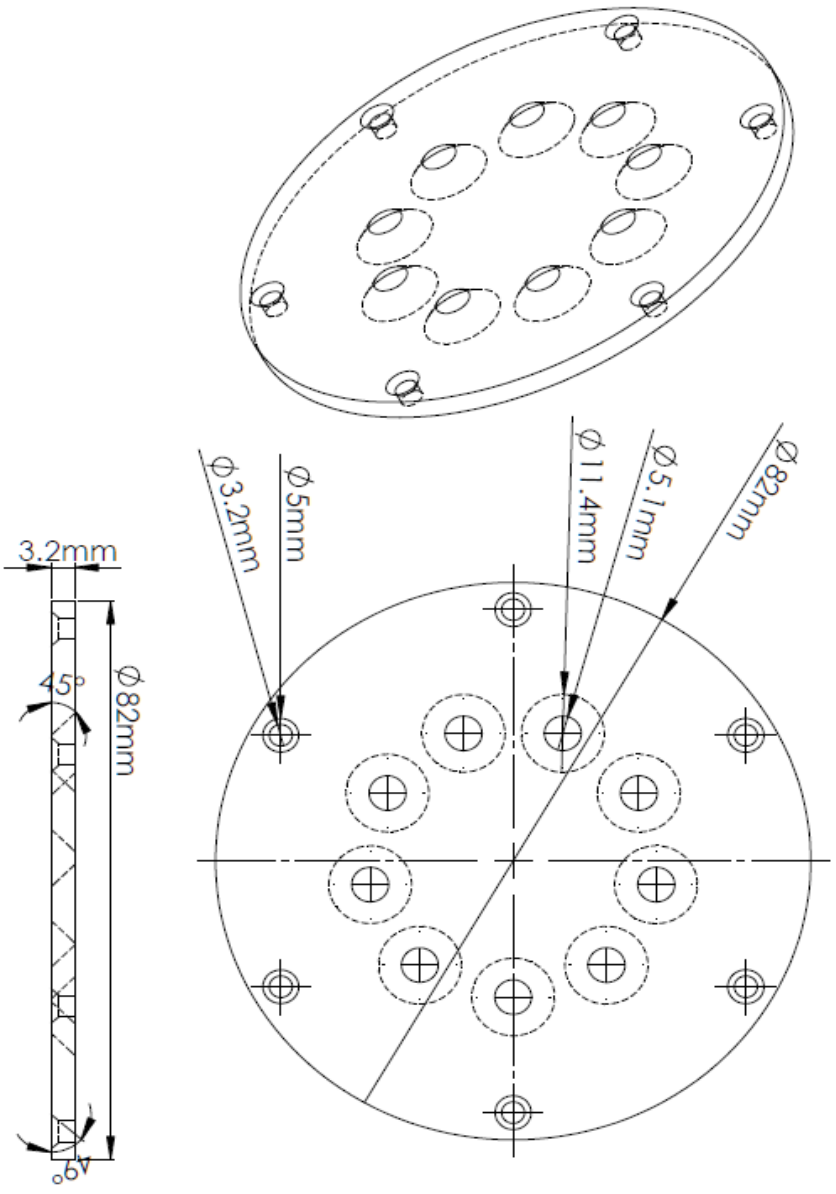

A.1.7 Bioreactor assembly frame

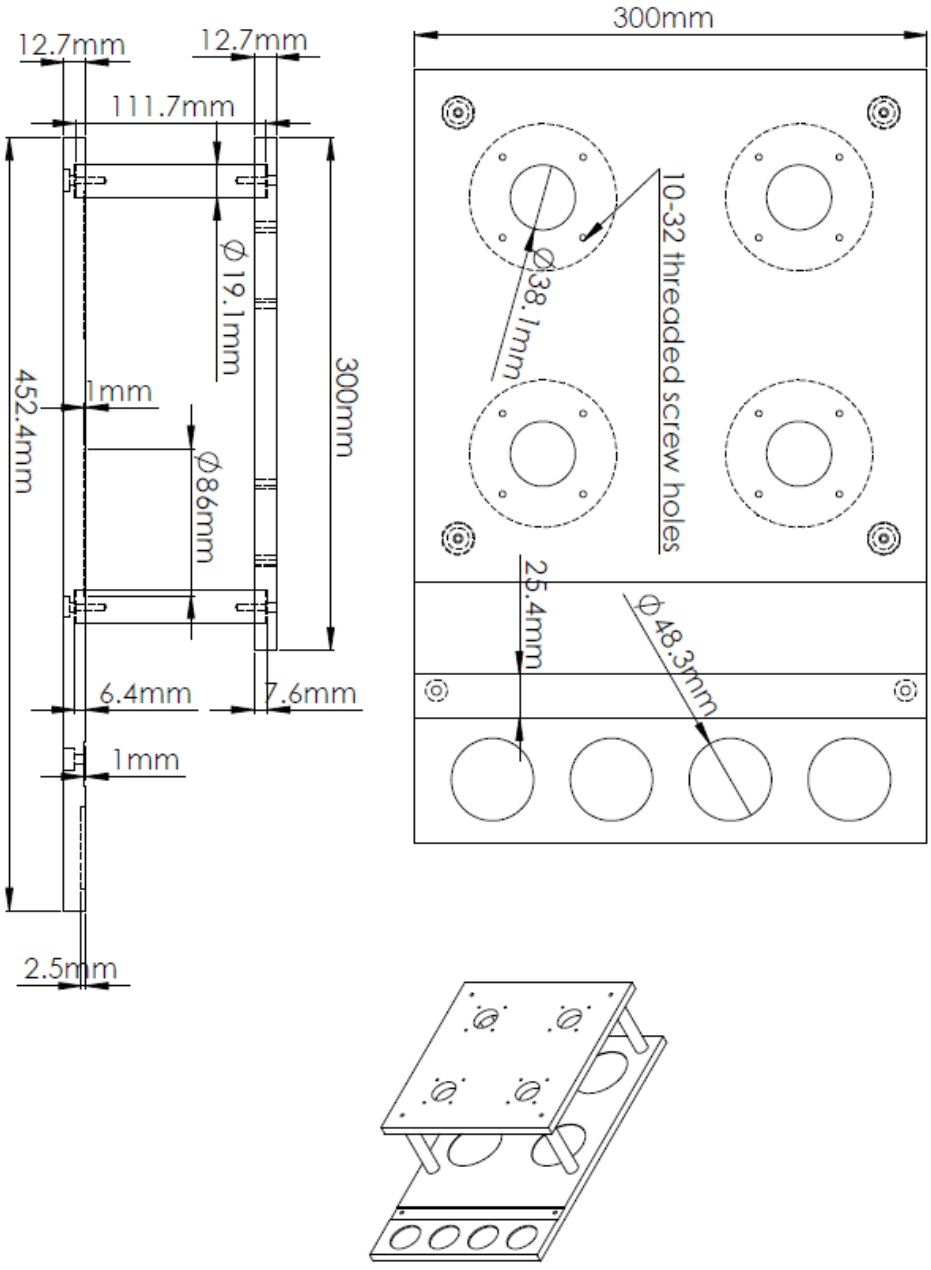

A.1.8 Perfusion reservoir

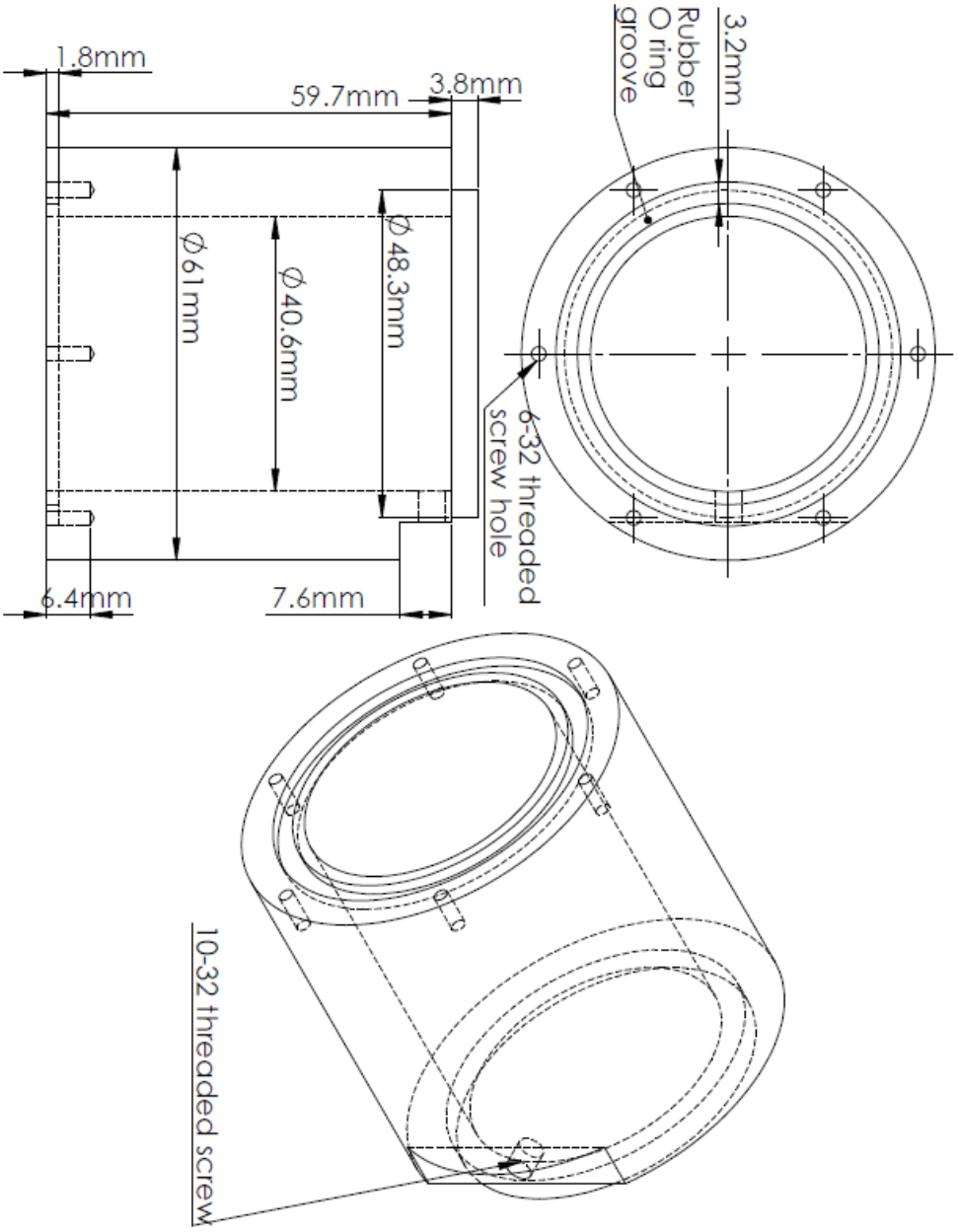

A.1.9 Perfusion reservoir lid

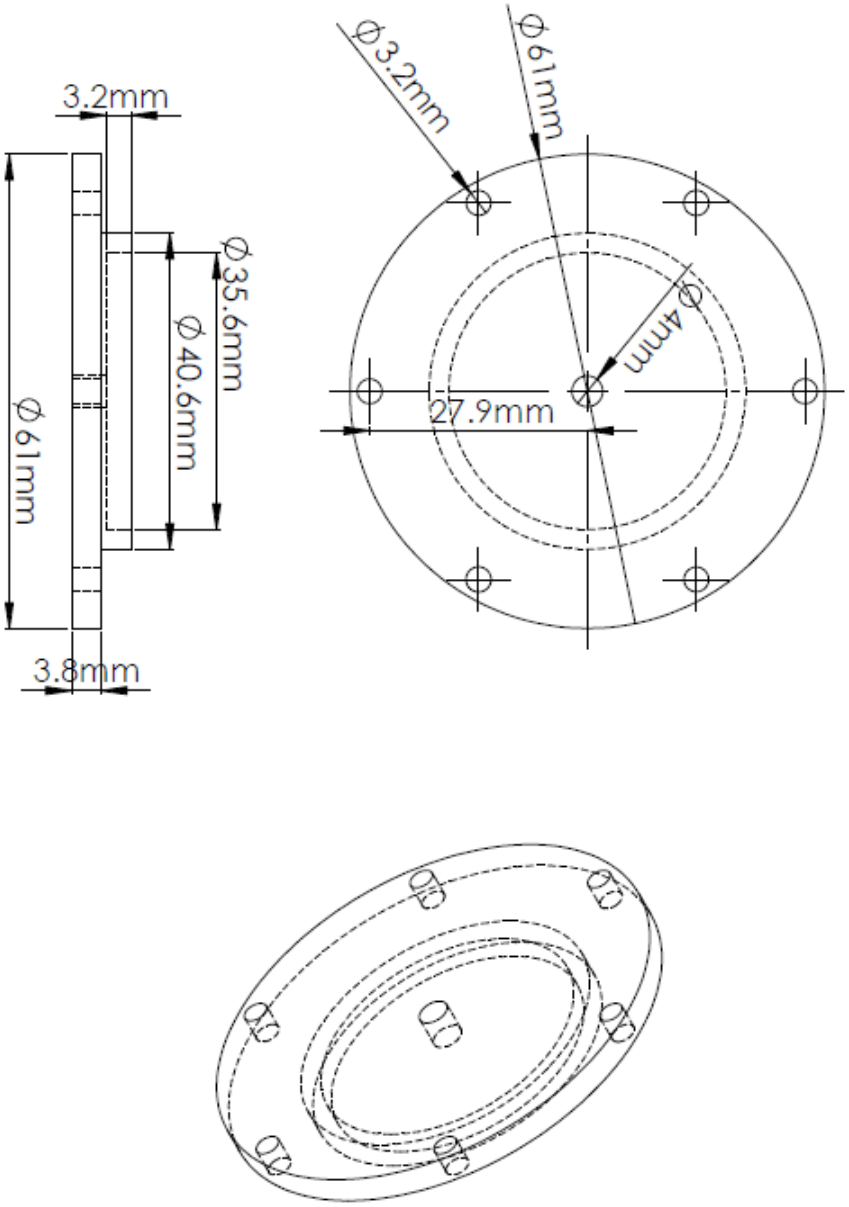

A.2. Cone and plate bioreactor user manual

Prepared

4/11/2008

Philippe Sucosky. Email: philippe.sucosky@gmail.com

Adnan Elhammali. Email: adnan.elhammali@gmail.com

Revised

4/22/2011

Choon Hwai Yap. Email: choonhwai@gmail.com

Revised

5/8/2015

Swetha Rathan. Email: swetha@gatech.edu

A.2.1 System description

Ex vivo tissue studies require the maintenance of mechanical and biochemical environments close to physiologic conditions. The present cone-and-plate tissue culture system has been designed to expose tissue samples to well-defined shear stress conditions. The design consists of a servo motor coupled to a cone placed on top of a stationary dish. The motor is controlled by a servo drive programmed via a computer. Fluid flows within the gap between the cone and the plate. In the present design, the cone features an angle of 0.5° and is located 200 microns above the surface of the plate.

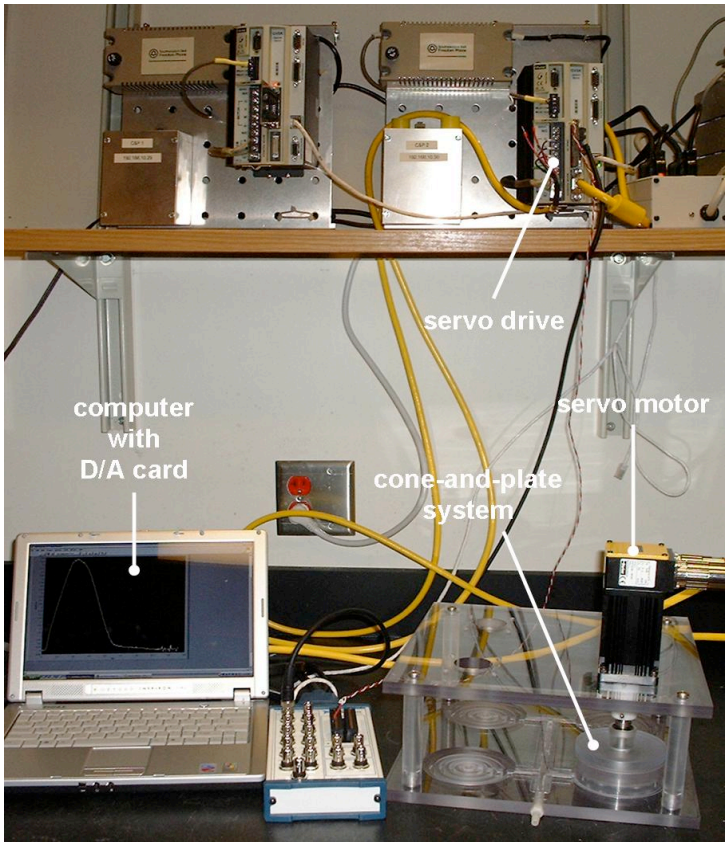

Figure A. 2. 1 Cone and plate shear stress bioreactor set up.

This particular geometry allows for the production of a nearly-uniform shear stress environment in the flow, and more particularly at the surface of the plate. Since the shear stress level is directly related to the cone angular velocity, desired temporal shear stress variations can be imposed by rotating the cone at specific angular velocity waveforms. The production of a desired angular velocity waveform can be monitored in real time via a digital/analog acquisition card interfacing between the computer and the servo motor.

Although similar devices have already been used extensively in biomedical research to subject cells to uniform shear stress environments, they have not been adapted to accommodate whole pieces of tissue. The present novel design can accommodate circular tissue samples (7 mm diameter) flush mounted in the bottom plate to avoid any perturbation to the surrounding flow, and thus, to the uniformity of the surrounding shear stress environment. Nine equi-angularly spaced cylindrical wells are machined in the plate, each accommodating a sample holder. The tissue sample placed at the top of the holder is clamped in position by a plate cover such that the top surface of the sample coincides with that of the plate cover. The particular geometry of the plate cover exposes a circular sample region of 5 mm in diameter. The system can be used to expose various types of tissues to steady, pulsatile or oscillatory shear stress. A picture of the complete apparatus is shown in Figure A. 2. 1.

A.2.2 Cone assembly

As shown in the Figure A. 2. 2, the cone assembly consists of a cone attached to a shaft. The cone is made of Delrin plastic while the shaft is made of stainless steel. The cone is coupled to the shaft via three screws. The cone features an angle of 0.5° and the conical surface is polished to ensure a maximum smoothness.

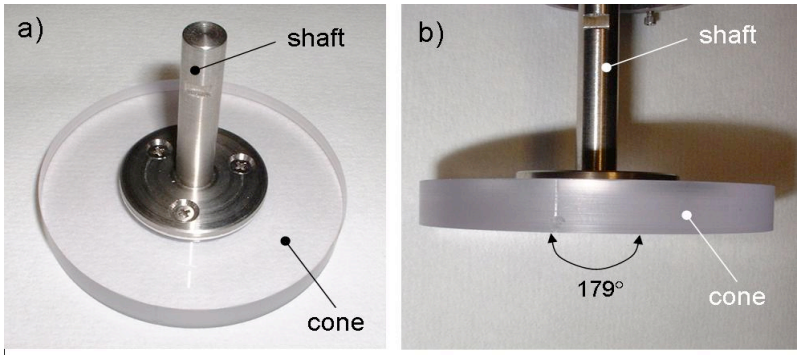

Figure A. 2. 2 Cone assembly: top view (A) and front view (B) showing the nearly flat angle of the cone.

A.2.3 Plate

The plate (Figure A. 2. 3) is machined in a cylindrical rod of polycarbonate. Nine equi-angularly spaced cylindrical wells (7-mm diameter) are located at a radius r = 20 mm from the center. The internal and external lateral surfaces can be polished to enhance optical access, if needed. Each well can accommodate a tissue sample holder.

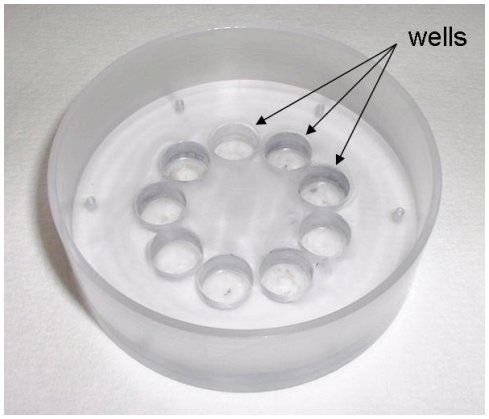

Figure A. 2. 3 Plate with the nine equi-angularly spaced cylindrical wells.

A.2.4 Plate cover

The function of the plate cover is two-fold: to expose a smooth flat piece of tissue to the flow, and to clamp the tissue samples in position on top of the holders. The plate cover is a thin circular plate of polycarbonate screwed on top of the tissue wells located in the plate. Nine equi-angularly spaced holes are machined in the plate cover, aligned with the wells of the plate.

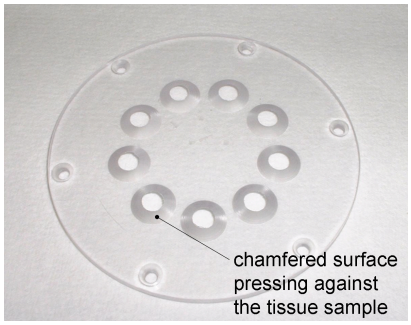

Figure A. 2. 4 Plate cover with nine equi-angularly spaced holes that align with the wells in the plate.

The holes are chamfered at an angle of 45° such that the hole diameter on the lower surface of the plate cover is equal to the diameter of the well machined in the plate, and the hole diameter on the upper surface of the plate cover is equal to the diameter of the circular surface at the top of the holder (i.e., 5 mm) (Figure A. 2. 4). The chamfered surface presses on the tissue sample to maintain it in position on top of the holder.

A.2.5 Agarose bed within tissue wells

The function of the agarose bed is to position the circular tissue samples at the center of the wells and to maintain them at a certain distance from the plate surface. 1.2% agarose was found to be well suited for this purpose. The agarose can be autoclaved to ensure sterility. Thereafter, they should be stored in a 4^{o}C refrigerator until use. Before insertion into the cone and plate, the bottle of agarose is first microwaved to liquefy the agarose for manipulation. To ensure the agarose bed had the suitable shape within the well, the plate cover is first coupled with the plate, such that the wells are empty spaces accessible through holes in the plate cover. About 715-800 µL of agarose is then pipetted into each well, and allowed to solidify for atleast 15 min. The plate cover is then removed, leaving the agarose in the required shape within the wells. However, care must be taken to minimize breakage of the agarose pieces during removal of the plate cover. To achieve this, a curved tweezer can be gently inserted between the plate cover and the agarose to loosen the contact before removing the plate cover. At this stage, however, the agarose has a meniscus to its top surface. 2 drops of agarose can be placed into this meniscus to flatten it after removing the place cover. Once the additional agarose solidifies, trimmed valve leaflets can be placed on the agarose, and the plate cover can be re-attached to the plate. The agarose height may have to be adjusted depending on the thickness of the tissues. Figure A. 2. 5 shows a picture of the plate, agarose bed, tissues and cover assembly.

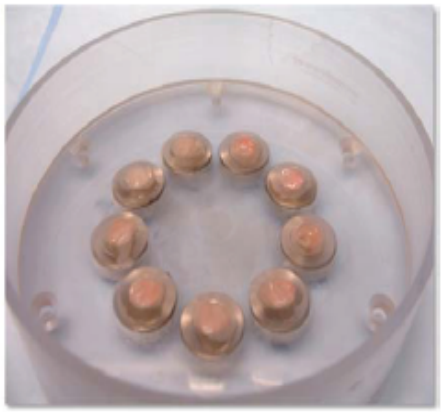

Figure A. 2. 5 Plate, agarose, tissues and cover assembly.

A.2.6 Flange

The flange closes the system to ensure sterility and accommodates the two ball bearings driving the cone and shaft assembly in rotation. The lip machined on the edge ensures a correct centering of the flange with respect to the plate and the rest of the system. The flange is made of polycarbonate. A shaft collar placed on the cone shaft allows the adjustment of the vertical distance between the cone apex and the surface of the plate cover. The collar is maintained in position via a setscrew. The first prototype is shown in Figure A. 2. 6A. A new flange has been designed. In this new design, nine holes are machined around the perimeter of the flange and intersect with a groove machined in the flat circular surface located at the bottom of the flange. The function of those channels is to ensure proper gas exchange by bringing air from the surroundings into the device. The axes of the holes machined on the perimeter of the flange are horizontal to prevent contamination (Figure A. 2. 6B).

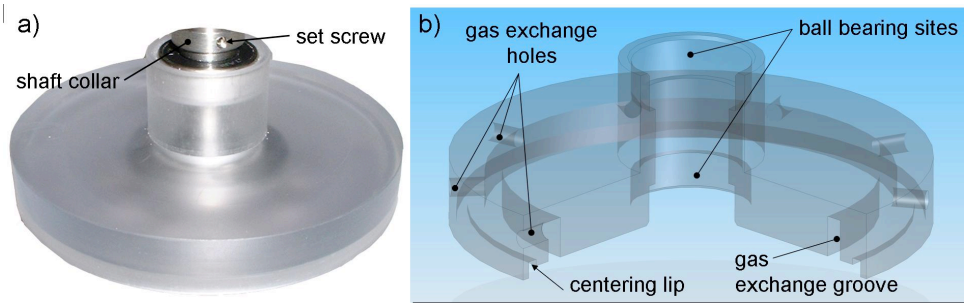

Figure A. 2. 6 Flange design: A) picture of the prototype (no gas exchange capability); and B) clipped CAD rendering of the newly designed flange (with gas exchange capability).

A.2.7 The perfusion system

Since the cone and plate system has orifices to allow gas exchange, the small amount of media fluid within the bioreactor can easily dry out. To prevent this, a reservoir is attached to the system, allowing at least 50 ml of media to be stored, and a slow peristaltic pump (SP200FO, APT Instruments, Rochester, IL) is used to circulate the media into and out of the cone and plate system. Threaded luer lock fittings were installed on the plate portion of the bioreactor, and the reservoir, such that small diameter (1/8” ID) tygon® tubing (B-44-3, McMaster Carr, Atlanta, GA) can be used to connect the reservoir to the pump, from the pump to the plate portion of the bioreactor, and from the plate back to the reservoir (Figure A. 2. 7).

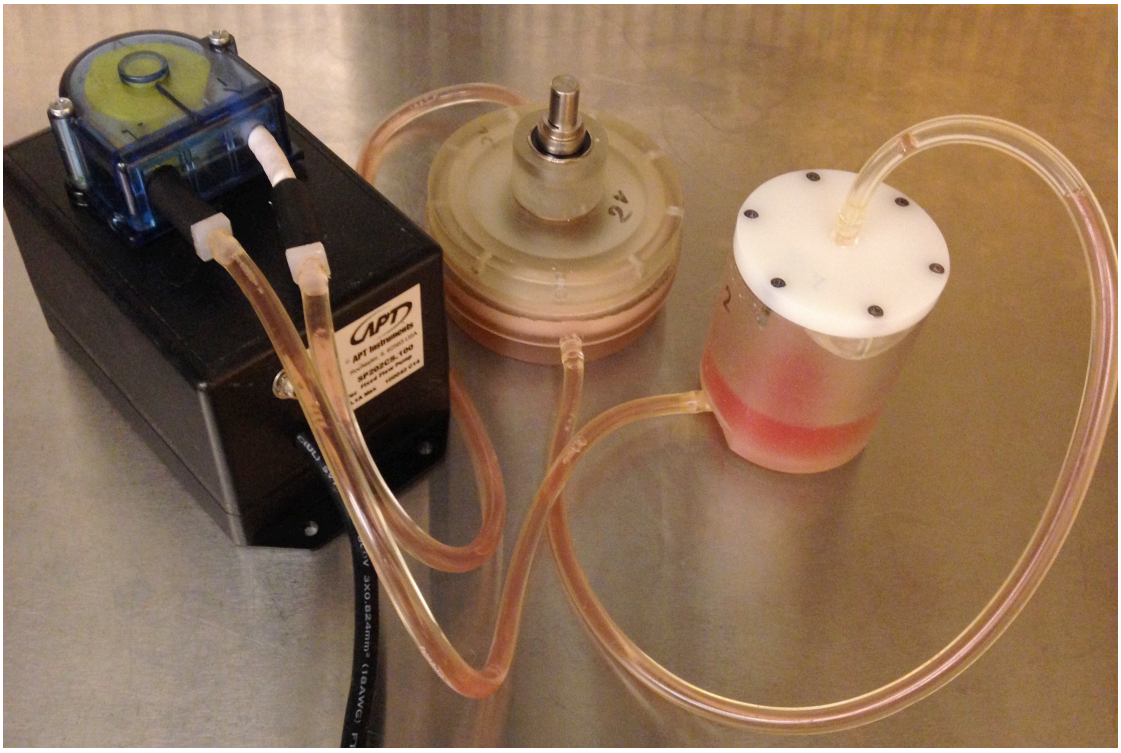

Figure A. 2. 7 Schematic of the perfusion system.

A.2.8 Suction table, suction lid and motor table

A suction table has been designed to maintain the system in position while the cone is rotating. The table is made of polycarbonate and can accommodate four cone-and-plate systems. Four sets of concentric suction channels are machined in the table. Those channels are connected by two transversal channels and a central channel with inlet located at the front of the suction table. Four polycarbonate rods are screwed in at the corners of the suction table to support the motor table (Figure A. 2. 8). The diameter of the rods (19 mm) is large enough to stabilize the entire assembly even in presence of the inherent

vibrations produced by the servo motor. Figure A. 2. 9 shows the different elements assembled and mounted on the motor and suction tables.

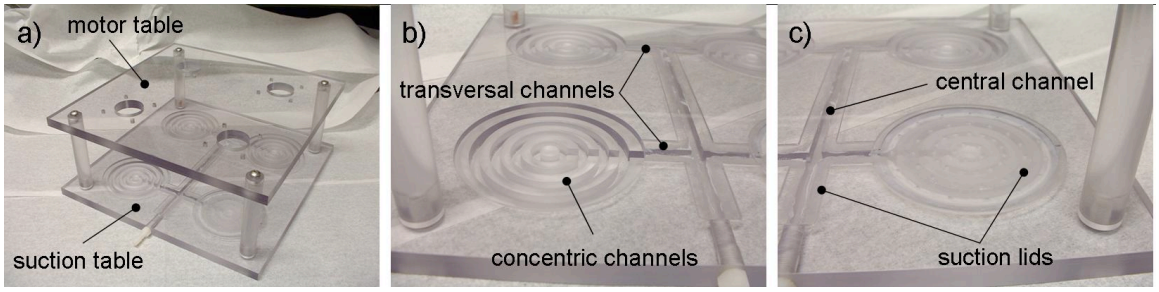

Figure A. 2. 8 Design of the suction table.
A) suction table and motor table; B) detail of the concentric channels; and C) suction lids covering the suction channels.

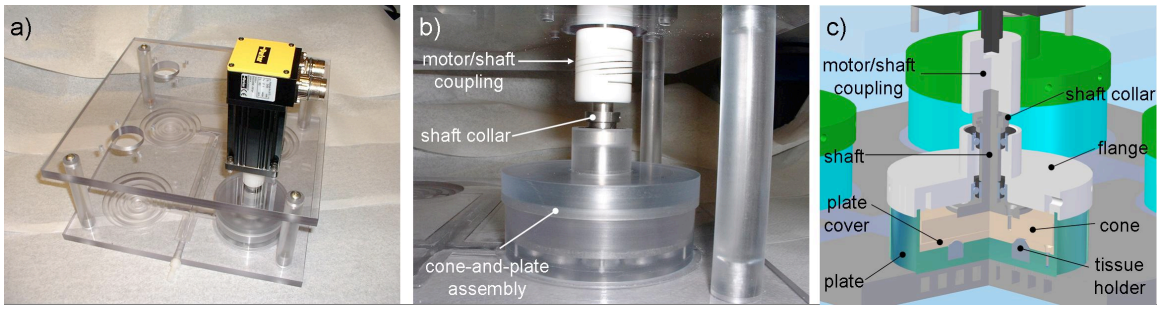

Figure A. 2. 9 Complete system.
A) different elements assembled and mounted on the motor and suction tables; B) details of the cone-and-plate assembly mounted on the suction lid; and C) clipped CAD rendering of the whole assembly.

A.2.9 Driving system

The driving system used to rotate the cone at the desired angular velocity waveforms consists of a rotary servo motor and a servo drive/controller. The single-axis controller/drive used in the present setup (Figure A. 2. 10) offers

complex program and I/O capabilities. The servo drive/controller powered by a DC power block can be programmed using a commercial software package supplied with the product. The rotary servo motor chosen in the current setup was dimensioned to provide the necessary torque and velocity to subject the tissue samples to a maximum shear stress of 100 dyn/cm^2.

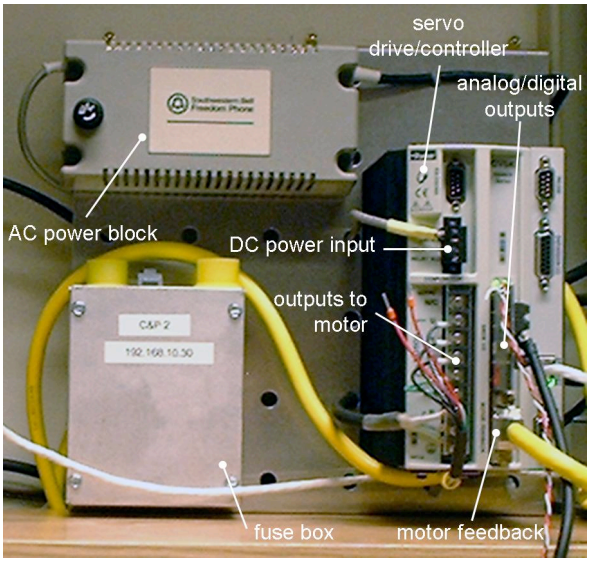

Figure A. 2. 10 Driving system set up.

A.2.10 Programming the servo drive

We use the compiled waveform method to program all of our shear stress waveforms. This involves the sectioning off of the waveform into hundreds of small segments. For each segment, the velocity and the distance traversed under that velocity are programmed into the drive. A second program will then need to be created to compile the first program and then loop it.

Program 1

del name ---> This deletes anything stored under this program name.

def name ---> This assigns the program the new name

mc01

A400 ---> Defines acceleration at which motor switches between velocities

V0.82133 ---> Velocity in RPS

D28 ---> Distance traversed at this velocity (note: 4000 units per rotation, double check that this is the setting for your specific motor)

GOBUF1 ---> Command to complete segment

V2.0095 ---> Start of a new segment

D69

GOBUF1

V4.9618

D171

GOBUF1

V6.4744

D223

GOBUF1

end

The distance D has to be a whole number. To rotate in the opposite direction, enter a negative distance. Once the maximum desired velocity is reached, you will need to enter a deceleration command (ad instead of A as we did in line 4) right after the last GOBUF1 command of the accelerating segment and before

inserting the new decelerating segments. This must be done every time the acceleration changes from positive to negative or vice versa.

Program 2

del rname

DEF rname

PCOMP name ---> compiles the segments of program “name”

L0 ---> begin loop

PRUN tauh ---> run program

T0.31 ---> inserts a time delay of .31 seconds. Insert delay as needed.

LN ---> defines the infinite loop

END

Write these programs in the program editor and download to the servo drive. Once downloaded, you will only need to run the second program (type rname in the terminal). You will need to read the manual or contact tech support to learn the basic operations of the servo drive and motor (how to turn on and off and how to activate the motor).

A.2.11 Analog monitoring

To monitor the waveform in real time, you will need to connect two sets of cables to the Data acquisition card. This is not being actively carried out all the time,

since this shear system and its servo motor components have been well established over years. However, in case there is a need to troubleshoot and monitor the output of the motor, follow this protocol. The analog cable which will output a voltage is connected from pin 21 and 25 (ground). Refer to page 75 of the hardware installation manual for a schematic. The digital output will be used as a trigger. This trigger will be programmed to function when the motor stops and starts running. Refer to page 73 of the hardware installation guide for a schematic of the digital outputs.

A.2.12 Analog outputs

There are a few commands to activate the analog output. Analog output A is on pin 21 and analog output B is on pin 22. They both do the same thing. Ground is on pin 25. A cable should connect these pins to the Analog In connections on the DAQ card (Figures 1 and 2 of the hardware installation guide).

The commands are:

DMONAV 5 – programs output A to velocity.

DMONBV 5- same as above but for output B

DMONAS- scaling factor 2000 corresponds to 1rps=.975V;

1000 corresponds to 1rps=.487

Determining the scaling is a bit tricky since it is drive specific. The easiest thing to do is run the motor at 1 rps and connect the probes of a voltage meter directly to pins 21 and 25 and measure the voltage. Alter the ratio of voltage/velocity with

the DMONAS command. Remember, your max and min voltage has to be within -10 to +10 so scale in a manner such that you're max and min velocities are included.

DMONAV 24- This command will allow you to test if the outputs are functioning properly. Enter this command and rotate the shaft with your hand. You should notice voltage fluctuation on the instrument being used to measure (make sure you enter the drive0 command to deactivate the drive otherwise the shaft won't turn)

DMONBV 24- same as above but for output B.

Now you should have your analog outputs activated and should know the ratio of velocity to output voltage.

A.2.13 Digital outputs

You will need to connect two cables from pin 41 and 42 of the servo drive to the digital and timing I/O connections of the DAQ BNC block (Figures II.1 and II.2). 42 is the ground. Once connected, use the following command:

outfnc1-B

The 1 corresponds to pin 41 and the B defines the motion trigger. This trigger is initiated when the motor starts moving after a halt. When reading the waveform in LabView, we can use this trigger such that collection of data will begin only when the motor starts moving. This is appropriate for our purposes because it

guarantees that our data corresponds to the beginning of the waveform. You do not need the trigger for continuous waveforms that have no halts.

A.2.14 Feedback

We are using LabView 8 to carry out feedback. Open LabView and in the "Getting Started" section choose "vi from template". Then under "DAQ", choose "Data Acquisition with NI-DAQ.mx".

Follow the given instructions. On the screen for Analog data acquisition, you will see the trigger tab by double clicking on the DAQ block. Set it to digital and choose the appropriate inputs from the card. Be sure to program the appropriate slope under "custom scaling" in the configuration window. The slope should have been determined when running the DMONAS command as described above. Finally, make sure the timing settings are set so as to read at least one period of the waveform.

When back on the DAQ block, right click on the data tab and choose "create" and "graph indicator". Then right click on the white region, choose "File I/O" under programming and then choose "write spreadsheet file". Drag and place this next to the graph indicator and connect the two. (Note: You may want to wait to add the spreadsheet writing function until you have properly configured the feedback mechanism and can clearly see the graph in LabView)

Now, when you open the graph indicator and hit the arrow tab, the waveform will be read and you will be prompted to save the information immediately (assuming you created the spreadsheet write function as described above). Once saved, you will have to rename the file with the .txt extension. You will be given a series of velocity measurements. The number of measurements given will correspond to the frequency chosen in the “timing section” when double clicking on the DAQ block.

A.2.15 Tuning

Tuning can be very tedious since it must be carried out manually. Once you obtain a set of data from LabView, plot in Excel and compare with the original programmed waveform. Make adjustments to the Program as necessary. It is very common for the output velocity to come out one or two units lower than the programmed velocity. Keep in mind that when raising the velocity of a segment in the program, you must also increase the distance D for that segment by the appropriate distance. Not doing so will result in the shortening of the period of the waveform (Increasing V but not D will decreased the time).

A.2.16 Servo drive codes

One can use RS232 cable and a USB connector to upload the servo drive codes in the motor. Alternatively, IP address mapping of the motors can be done. For this, a batch file is required to activate the connection between the laptop and the

servo-motor controllers (connected through the LAN cables). This batch file's contents are as follows:

Filename:6KARP.bat

Contents:

arp -s 192.168.10.30 00-90-55-00-56-E6 192.168.10.31

arp -s 192.168.10.29 00-90-55-00-56-E7 192.168.10.31

A.2.17 Motor reset and installation protocol

Typically, before running the programs, it is recommended to reset the servo motors. This is done in order to clear the memory of the motor and ensure there are no memory related errors that can sometimes cause the motor to fail. Start the servo motor controller program, "Motion Planner, version 4.3 and make sure the servo motor is connected to the system and is communicating. Then open a new terminal window (small blue square icon on upper left of the tabs of motion planner). Type RFS in the command line and press enter. RFS means Restore Factory Settings. After a short time (approx. half a minute) the terminal will output several lines of code (shown right below RFS command) once it is done as shown in Figure A. 2. 11.

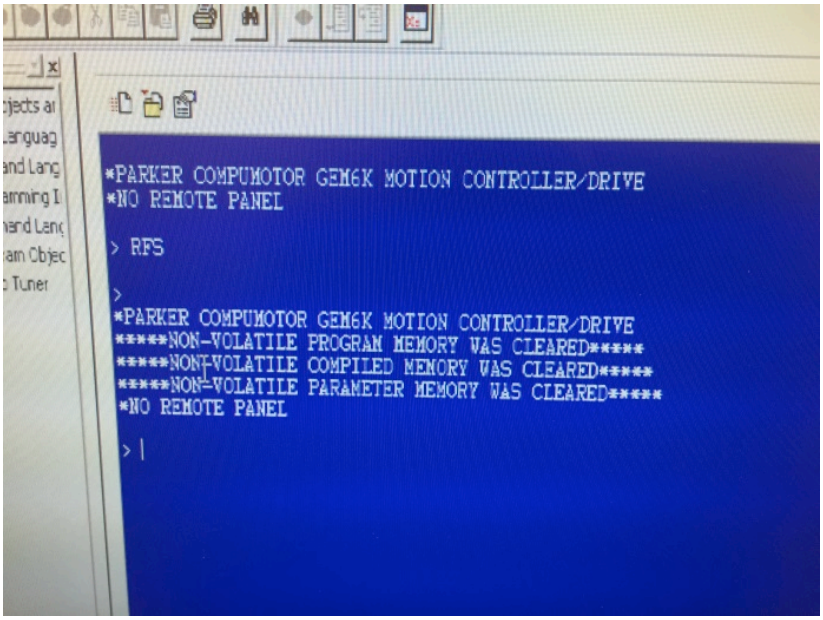

Figure A. 2. 11 Instructions to reset the servo motor to factory settings.

The servo motor has now been restored to factory settings and must be installed to be able to use it. Click file and select new. Then among the options, select the program editor (left image) and press OK. Then select the Gemini tab and install the motor by following the instructions in Figure A. 2. 12 and Figure A. 2. 13. Enter the series, frame, and part for the motors we use. For our motors this is SM232AE. This code can be found written on each of the motor heads. Press “Yes” when asked to require DRESET to be activated. Now, if you open a new terminal and enter TDIR to the command line, you should find that there are no programs detected when checking the motor memory.

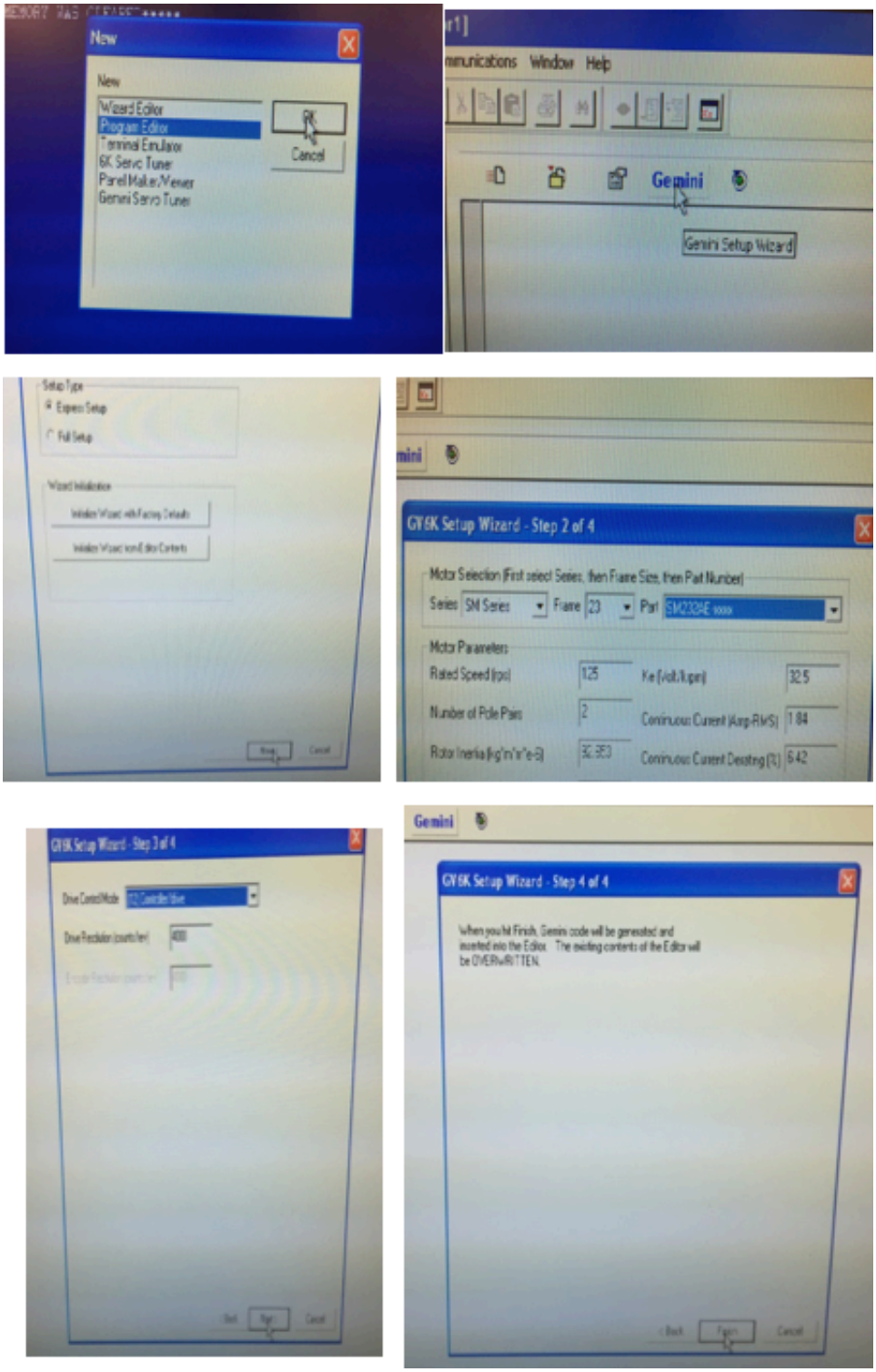

Figure A. 2. 12 Installation of servo motor after resetting.

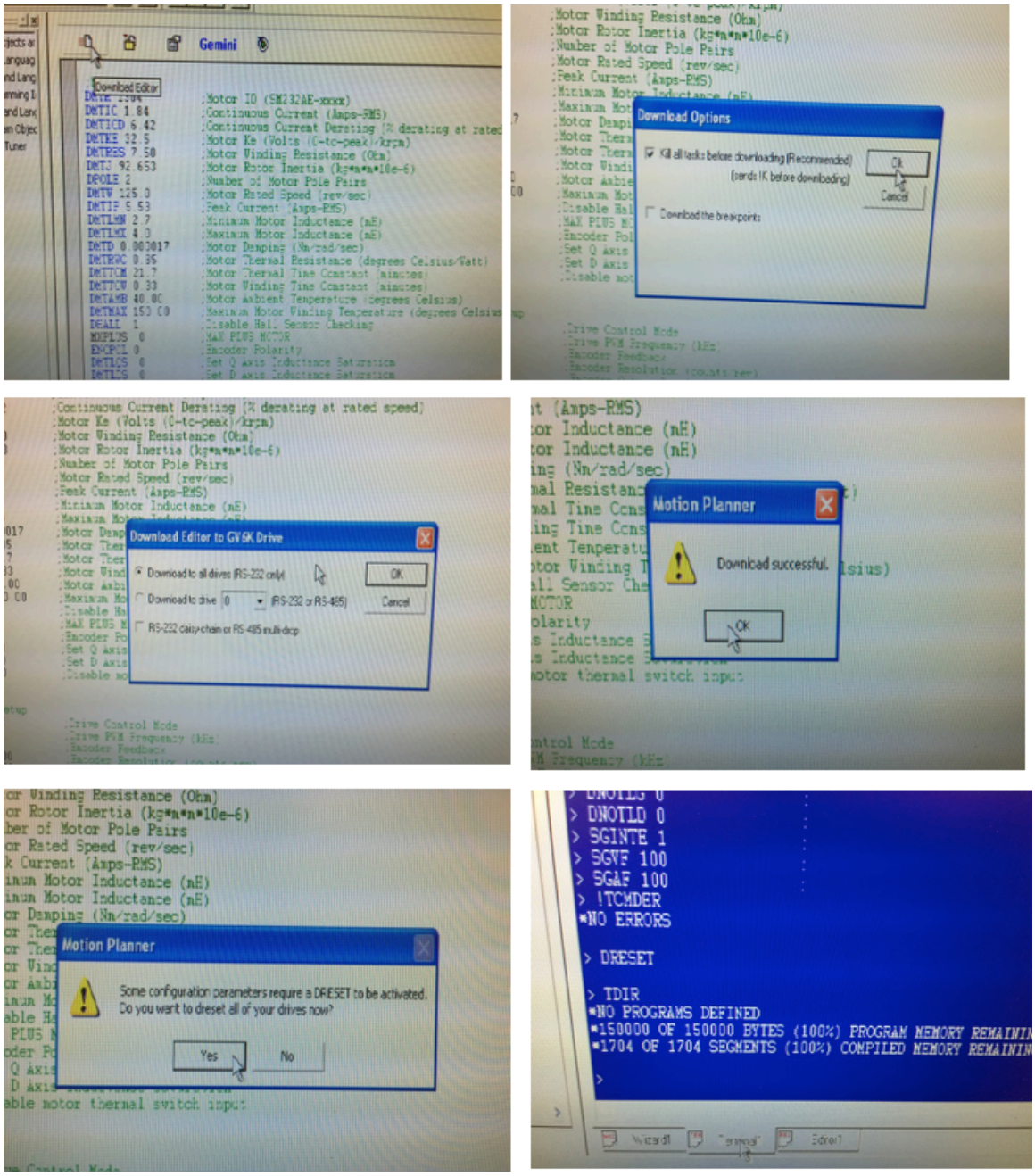

Figure A. 2. 13 Instructions to install the Gemini GV 6K servo motor

A.2.18 System operation

Connect the cone and plate apparatus (Figure A. 2. 7) to the servomotor, and plug in the peristaltic perfusion pump. Turn on the laptop; plug in the RS232 cable between the laptop and the servo motor controller. Allow some time for the laptop to detect the connection. Start the servo motor controller program, “Motion Planner, version 4.3. You can now upload / download shear stress waveforms through the laptop program. To run the waveforms, enter command: “drive1” to engage the motor, and then enter the command to run the waveform, which would be the name of the waveform file. Usually cyclic programs start with a “r”. To stop the program, press Ctrl-K, and then enter command “drive0” to dis-engage the motor.

Now that the motor memory has been wiped, you can go ahead and download the program to the servo motor. Next, you have to download the programs to the motor for either oscillatory (sin5, rsin5) or pulsatile shear (tauh, rtauh), depending on the experiment you are running.

Hit the “download file” icon (left image). Download the two programs required for the experiments that will be run on that motor. Here sin5 is downloaded. You can also find the programs required on the yellow post-it notes above the motor. To trace the program running on the motor, type command trace1 (to turn the trace on) and trace0 (to turn the trace off) while programming the code to the

motor. Always disable the limits using command lh0. Typically the commands should follow this order

drive1

lh0

trace1

rsin5

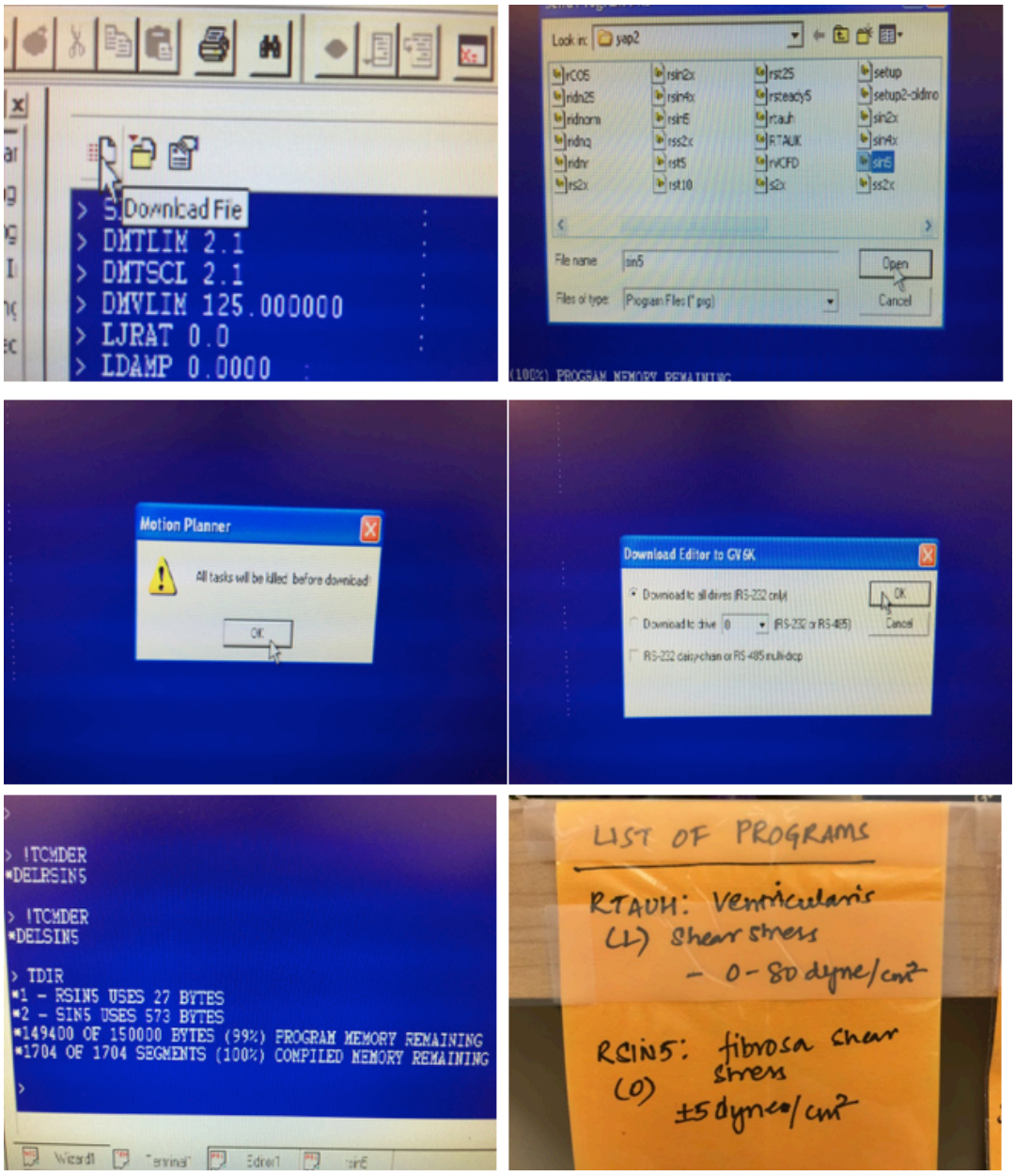

Figure A. 2. 14 Instructions to upload a program to servo motor using motion planner

A.2.19 List of parts and supplies

Cone and Plate apparatus (please see Appendix A.1 for mechanical drawings) is custom machined by the ChBE machine shop or GTRI. The parts needed to machine this bioreactor as well as the motors, and pump part numbers are listed in the tables below. Other than the parts listed, we also need the following:

a. Incubator: Model 3110 CO_2 water Jacketed Incubator, Forma Scientific, Marrietta, OH.
b. Laptop: Dell Inspiron 710m, Dell, Round rock, TX.

Table A. 2. 1 Motor and controller – assemble and set up

Part Description	**Company**	**Part number**	**Price per Unit**
Cover - Bottom Plate	Newark	05M4430	$31.23
AC Power Cord	Newark	98K6011	$4.34
Fuse Holder	Newark	84K0273	$2.11
Power Entry Module	Newark	48M7013	$10.69
AC Power Cord to Drive	Newark	17B6600	$5.15
AC Input Fuse	Newark	26K7958	$1.34
24V Power Supply	Digikey	T1206-P5P-N	$21.76
Fuse Block	Digikey	F4928-ND	$3.07
2.5A Fuse	Digikey	507-1631-ND	$0.29
6.0 A Fuse	Digikey	507-1636-ND	$0.29
Rubber Feet (Bag of 64)	Digikey	SJ5508-0-ND	$3.92
DC Connector	Digikey	CP-5-ND	$2.43

Table A. 2. 2 Peristaltic pump

Part Description	**Company**	**Part number**	**Price per Unit**
Fixed-Flow Cased Peristaltic PumpTubing size ID: 3mm, Material: Viton, gen purpose, motor: 3 rpm synchronous, continuous Standard enclosure with on/off switch	APT Instruments	SP200	$135

Table A. 2. 3 Materials for 2 sets of cone and plate set up

Part Description	Company	Part number	Price per Unit
O rings - AS568A Dash Number 031	Mcmaster	9396K111	$4.92
Scratch and UV resistant poly carbonate sheet	Mcmaster	8707K112	$35.19
Impact Resistant Polycarbonate Rod, 4" Diameter, Semi-Clear Gray - 1 ft	Mcmaster	8571K41	$107
white delrin rod (3-1/2" Dia, Length 12")	Mcmaster	8572K35	$60
Polycarbonate rod (2.1/2 " Dia, Length 12")	Mcmaster	8571K39	$48.81
Steel ball bearing	Mcmaster	6138K66	$13.27

Laboratory clear Tygon PVC tubing-10ft-4	Mcmaster	5155T17	$28
Clear polycarbonate barbed fitting	Mcmaster	5117K83	$4.96
18-8 stainless steel 82degree flat head philips machine screw	Mcmaster	96877A121	$7.72
1808 Stainless steel knurl grip cup point set screw	Mcmaster	93445A170	$10.92
316/316L Stainless Steel Rod, 5/8" Diameter-1'	McMaster	89325K83	$9.68
316/316L Stainless Steel Rod, 2" Diameter-1'	Mcmaster	89325K63	$58.04
Acetal Helical Flexible Shaft Coupling, 3/8" x 3/8" Diameter Shaft, 1-1/4" Length, 1" OD	McMaster	2505K133	$43.17
Optically Clear Cast Acrylic Sheet, 1/2" Thick, 12" x 24"	McMaster	8560K266	$52.58
Miscellaneous Screws and Parts (for buffer)	McMaster		$100

A.3. Sterilization techniques

All materials for the experiments (including surgical tools, bottles, bioreactors etc) were sterilized by one or more of the following methods.

A.3.1 Autoclaving at 120°C for 30 min

Gravity cycle was chosen for autoclaving metallic surgical tools, pipette tips, glassware and plastics (autoclavable only). All the contents were placed in autoclavable pouches (VWR #11213-038, #11213-025) and taped with autoclave indicator tape (VWR #58752-781). Liquid cycle was chosen for autoclaving liquids only. Liquids such as DI water, DPBS, and agarose were autoclaved using this method.

A.3.2 Ethylene oxide (EtOH) sterilization for 24 hrs

This method was employed for sterilizing materials that are not autoclavable. All the plastic parts of the shear stress bioreactor parts, including the reservoir pumps and the tools that are not autoclavable were packed in gas sterilization pouches (VWR #11213-226) and sterilized using this method. EtOH ampoules and bags were purchased from Anderson sterilizers (AN #79).

A.3.3 Sterile filtering using 0.1 μm filter

Media and other solutions are filtered using media filters (Corning) or syringe filters (VWR).

A.4. Post experiment tissue handling

A.4.1 Supplies

- 6 well plate (1) (Fisher #08-772-1B)
- Ice Pack (pre-frozen at -20^{o}C)
- Scalpel handle (1) and sterile scalpel (1)
- Sterile ice cold DPBS (Sigma #D5773)
- Sterile ice cold DEPC (Sigma # D5758-25ML) treated DPBS (for RNA analysis) – Prepared by adding 0.1% v/V DEPC to DPBS, vortex at medium heat for atleast 12 hrs and sterilize using autoclave liquid cycle for atleast 30 minutes.

A.4.2 Procedure

- Autoclave surgical tools and DPBS** well in advance. Refrigerate dPBS**.
- Fill the wells of 6 well plate or petri dishes with ice cold DPBS** and place them on ice pack to ensure that DPBS remains cold. This will ensure that the gene expression pattern in the cells is preserved.
- Use motion planner to stop the motors and take only one cone and plate system out at a time and return to the sterile laminar flow hood. Handle tissues from one set up at a time. Please refer to the cone and plate system operation protocol for more details on operating the motors.
- Remove the tissues from the base plate of the cone and plate system, using forceps. Place them on the petri dish cover/6-well plate and cut the excess tissue, ensuring the portion of the tissue that is exposed to shear is

untouched (this portion of the tissue has a faint circular mark from the cover plate).

- Quickly rinse the tissues in 2 to 3 changes of ice cold DPBS** (step 2) until the tissue loses most of the pink color from the media before proceeding to next steps of the appropriate tissue saving protocol. Media contains ascorbic acid so it is important to ensure that the media is completely removed from the tissue, as it may interfere with some of the assays (protein, calcium, MMP assays, etc.).
- Typically for RNA and protein isolation, the tissues are ground and homogenized before adding the appropriate lysis buffer. However, if the RNA content of the tissue is very low, the grinding and homogenization step can be skipped. Add lysis buffer directly to the tissue, incubate for 5 min at room temperature and then proceed with the miRNeasy kit (Qiagen) isolation procedure. This will not improve the RNA concentration, however, the degradation of the RNA due to handling can be minimized.

A.5. Cryopreservation of tissues

Cryopreservation of tissues is recommended only for immunohistochemistry analysis, as the antibody binding sites are well preserved. However, tissue structure is not very well preserved.

A.5.1 Supplies

- Plastic molds (Electron microscopy sciences #EMS 70182)
- OCT compound (Electron microscopy sciences #EMS 62550-01)

- Long hemostat
- Vacuum flask (TEP core lab)
- Liquid Nitrogen (TEP Biohazard Room/Core lab)
- Methanol (BDH1135-19L)
- Plastic weighing boats
- Small styrofoam box

A.5.2 Procedure

- Have the liquid nitrogen ready in the vacuum flask. Pour sufficient amount of liquid nitrogen in a small styrofoam box (make sure the opening of the box is proportionate with the plastic weighing boats).
- Pour methanol in the plastic weighing boats (after which technically it should float on liquid nitrogen, but just in case, it is better to ensure that the opening of the styrofoam box is just enough to fit the weighing boat).
- Label plastic molds with the experimental details and sides that face the fibrosa/ventricularis. Put the label at the top of the sides of the plastic mold so that the methanol does not remove the ink. This way, it is much easier to identify the sides during imaging. Fill plastic mold with OCT compound and allow the air bubbles to settle down, for about 5 minutes.
- Arrange tissue samples at the base of plastic mold in appropriate orientation. For aortic valve tissues, the collagen and elastin fibers (or the ridges on the fibrosa side) should always be parallel to the base of the plastic molds. Also ensure that the fibrosa of the tissue faces the label

fibrosa on the mold. Allow the tissues to “sit” in OCT compound for at least 5 to 10 minutes, to make sure all the water in the tissue is replaced with OCT compound. If not, the water within the valve tissue freezes creating lots of gaps within the tissue.

- Using forceps ensure that the tissues “stand” in the OCT compound while keeping track of the tissue orientation. Place the mold (with the tissue) on a weighing boat containing methanol. Take a small styrofoam box with the opening that is just enough to fit the weighing boat. Fill the styrofoam box with liquid nitrogen up to the brim (use extreme caution and wear thermal gloves, safety glasses and a lab coat) and place the weighing boat in liquid nitrogen (flask/Styrofoam box). The methanol will be cold enough to freeze the mold. This ensures slow and uniform freezing of the tissue sections and at the same time, the liquid nitrogen does not get into the mold, which can crack it. Store the frozen molds in -80°C freezer.

A.6. Tissue paraffin embedding

Paraffin embedding of tissues is recommended for tissue structure visualization stains. Antibody retrieval must be done on paraffin embedded slides, if these were to be used for immunohistochemistry analysis.

A.6.1 Supplies

- Paraffin embedding cassettes (IBB histology core)
- Microcentrifuge vials or 15mL falcon tubes

- 10% neutral buffered formalin (IBB histology core)
- Straight forceps (1)
- 70% Reagent Alcohol (IBB histology core)

A.6.2 Procedure

- Have 10% formalin ready in micro centrifuge vials or 15mL falcon tubes depending on the size of the tissue. Typically, the volume of the formalin used should be atleast 20 times more than the volume of the sample.
- Leave the samples in formalin for at least 24 hours before further processing.
- When ready, transfer the samples in the paraffin embedding cassettes (one per cassette) and label the cassettes accordingly with a pencil only!!! (Because the ink from the pen will be erased due to the heavy alcohol related processing).
- Transfer all the cassettes (with tissue) in a container with 70% reagent alcohol, label the container with PI, name of the user and the date and leave it in 4^{o}C fridge in Histology core lab in IBB.
- Sign up for paraffin processing on the sign up sheet (typically found on the same fridge where the container with the tissue cassettes is stored) and let Aqua Asberry know about this.
- Once processed, please pick up the samples promptly and embed the tissues in paraffin blocks. This step requires prior training and approval from Aqua Asberry in IBB.

- After embedding, leave the samples on ice block for at least 6 hours before beginning the slicing using a microtome either in IBB or in TEP.

A.7. Pulverization of heart valve tissue

A.7.1 Supplies

- Long hemostat (1).
- Vacuum flask (TEP Core lab).
- Liquid nitrogen (TEP Biohazard Room/Core lab).
- Lysis buffer (RIPA buffer or Qiazol lysis buffer).
- Homogenization vials/Cryovials.
- Small funnel with a hole big enough to insert into homogenization or cryovials.
- Mortar and pestle – the size of a Chinese tea cup.
- Thermal gloves.
- 70% reagent alcohol.
- Small plastic cup.

A.7.2 Procedure

- Have the liquid nitrogen ready in the vacuum flask. Wear thermal gloves to avoid contact with liquid nitrogen. A small plastic cup can be used to transfer the liquid nitrogen.

- Thoroughly clean mortar and pestle, funnel and the bench with 100% alcohol (histology reagent alcohol can be used) and then with autoclaved DI water. This is to ensure that the samples do not get contaminated.
- Place the funnel on the pre-labeled cryovial into which the ground tissue will be transferred. Add a small amount of liquid nitrogen to the cryovial as well to maintain the same temperature as the ground tissue.
- Place the tissue in the mortar and add liquid nitrogen to immerse the tissue completely for at least a minute. Leave the pestle in the mortar to keep it at the same temperature as the tissue.
- Using the pestle and a twisting and pulsating downwards motion, push down the tissue and grind it until it is a very fine granular powder. Never let the tissue thaw and keep adding liquid nitrogen while grinding.
- Don’t push the tissue too hard because there is a chance that the liquid nitrogen will spill along with some of the sample.
- Add enough liquid nitrogen to make tissue slurry and quickly pour it in the pre-cooled cryovial via funnel. If there is any left over tissue, repeat this step until all the ground tissue is transferred. However, ensure that excess liquid nitrogen is not added to the cryovial while transferring the tissue, because the liquid nitrogen might pop out along with some tissue.
- At this point, the tissue can be further homogenized for protein or RNA isolation or can be used directly for various quantitative assays.
- If RNA/protein is not isolated immediately, add appropriate lysis buffer (RIPA or Qiazol) and save the cryovial with ground tissue in -80°C freezer.

RIPA buffer must contain protease and phosphatase inhibitors (add the product number).

- Ground tissues should never be allowed to thaw!!! Only take them out when it is ready to be ground and homogenized for protein isolation. For use, thaw the vial only on ice (Very Important!!) and use the same vial to hold the ground tissue and add additional buffer for homogenization and sonication.
- For western blots, gently tap/scoop out about 0.1g of ground tissue (more than 0.3g is overkill) and homogenize it.

A.8. Primer design protocol

Primers for miRNA qPCR must be ordered from Qiagen as these work best compared to the primers designed using this protocol. For mRNA qPCR primers, follow this protocol.

A.8.1 Get mRNA transcript

- Go to NCBI and under the drop down search menu select gene. Search for the gene of interest, for example eNPP1.
- From the results, select the one that is specific to the species of interest, sus scrofa (pig).
- Go all the way down to the mRNA and proteins and get the NM or XM accession number for mRNA.

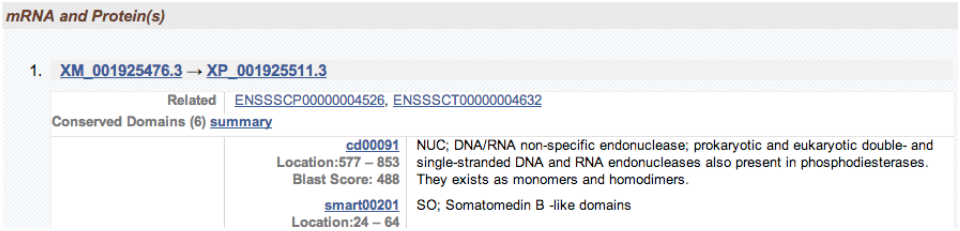

- The XM corresponds to the gene data obtained from predictive models. This could be due the fact that not all genes in pig are validated. In general, validated genes are labeled as NM. Since we only have this option, we will use the XM sequence. In case, if both the NM and XM sequence are available, always use NM as the website provides the information on predictive models as well (if available). Copy this sequence number, here XM_001925476.3.

A.8.2 Design primers

- To design the primer, use the free tool from NCBI: http://www.ncbi.nlm.nih.gov/tools/primer-blast/ and use the NM or XM number to search for specific primers.

A.8.3 Selection criteria

- Adjust other parameters in this tool to make the search more stringent.
- PCR primer length or product size: 100 to 200 (<100 –cannot be purified, >100-cycle wont be efficient); PCR melting temperature: Min: 58, Opt: 60, Max: 62; max Tm difference is 2 degrees. This is specific to this tool, and can change depending on the software or specific equipment we use.

- Choose the Refseq database. Exon junction span: Select the exon-exon mapping, but if it does not produce any result, select no-preference. For some of the reference genes, for example, 18S is a ribosomal RNA so it has no exon junctions, so no preference must be chosen.
- Select the organism: Sus scrofa (if looking in pig).
- Click the advance parameters and check the primer size, min: 18, max: 24, opt: 20.
- GC content min: 30, max: 80.
- Something else to keep in mind: Make the lengths and compositions of the primers designed for all the genes as similar as possible. This will help in running multiple genes in the same plate.
- Search will yield primers and also indicate its specificity for the gene of interest. Choose 3 to 4 primers from the list. Make sure that when you input the primers, only your mRNA of interest comes up. If others come up, redesign primers.

A.8.4 Verification of the primers

- To ensure that the primers designed here work as expected, they need to be verified. To double check if we got the proper gene expression amplified, we can predict the amplicon temperature at oligo calc: http://www.basic.northwestern.edu/biotools/oligocalc.html
- Primer can also be designed to go over an intron/exon border so that the genomic DNA is not amplified. This is generally not done because it is assumed that all the genomic DNA is eliminated with a separate DNase I

treatment (available through Qiagen used in conjunction with the miRNeasy kit).

- GC Clamp: The presence of G or C bases within the last five bases from the 3' end of primers (GC clamp) helps promote specific binding at the 3' end due to the stronger bonding of G and C bases. More than 3 G's or C's should be avoided in the last 5 bases at the 3' end of the primer.
- Repeats: A repeat is a di-nucleotide occurring many times consecutively and should be avoided because they can misprime. For example: ATATATAT. A maximum number of di-nucleotide repeats acceptable in an oligo is 4 di-nucleotides.
- Runs: Primers with long runs of a single base should generally be avoided as they can misprime. For example, AGCGGGGGATGGGG has runs of base 'G' of value 5 and 4. A maximum number of runs accepted is 4bp.
- 3' End Stability: It is the maximum ΔG value of the five bases from the 3' end. An unstable 3' end (less negative ΔG) will result in less false priming.
- Avoid Template Secondary Structure**:** A single stranded nucleic acid sequence is highly unstable and fold into conformations (secondary structures). The stability of these template secondary structures depends largely on their free energy and melting temperatures(T_m). Consideration of template secondary structures is important in designing primers, especially in qPCR. If primers are designed on a secondary structure which is stable even above the annealing temperatures, the primers are unable to bind to the template and the yield of PCR product is significantly

affected. Hence, it is important to design primers in the regions of the templates that do not form stable secondary structures during the PCR reaction. Our products determine the secondary structures of the template and design primers avoiding them.

- Avoid Cross Homology: To improve specificity of the primers it is necessary to avoid regions of homology. Primers designed for a sequence must not amplify other genes in the mixture.
- Primer Secondary Structures**:** Presence of the primer secondary structures produced by intermolecular or intramolecular interactions can lead to poor or no yield of the product. They adversely affect primer template annealing and thus the amplification. They greatly reduce the availability of primers to the reaction.
- Hairpins: It is formed by intramolecular interaction within the primer and should be avoided. Optimally a 3' end hairpin with a ΔG of -2 kcal/mol and an internal hairpin with a ΔG of -3 kcal/mol is tolerated generally.

- ΔG definition**:** The Gibbs Free Energy G is the measure of the amount of work that can be extracted from a process operating at a constant pressure. It is the measure of the spontaneity of the reaction. The stability of hairpin is commonly represented by its ΔG value, the energy required to break the secondary structure. Larger negative value for ΔG indicates

stable, undesirable hairpins. Presence of hairpins at the 3' end most adversely affects the reaction.

- $\Delta G = \Delta H - T\Delta S$
- Self Dimer: A primer self-dimer is formed by intermolecular interactions between the two (same sense) primers, where the primer is homologous to itself. Generally a large amount of primers are used in PCR compared to the amount of target gene. When primers form intermolecular dimers much more readily than hybridizing to target DNA, they reduce the product yield. Optimally a 3' end self dimer with a ΔG of -5 kcal/mol and an internal self dimer with a ΔG of -6 kcal/mol is tolerated generally.
- Cross Dimer: Primer cross dimers are formed by intermolecular interaction between sense and antisense primers, where they are homologous. Optimally a 3' end cross dimer with a ΔG of -5 kcal/mol and an internal cross dimer with a ΔG of -6 kcal/mol is tolerated generally.

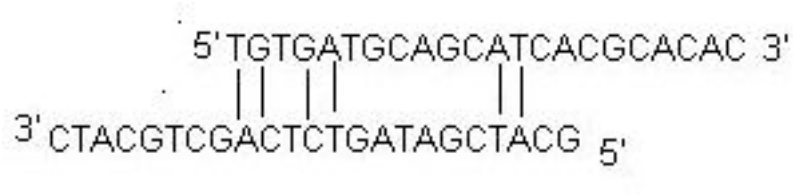

A.8.5 Ordering

- The smallest quantity can be ordered from either Invitrogen or Integrated DNA Technologies and use standard desalting.
- Order forward and reverse primer as separate primers. They can be

prepared for qPCR later. The primers will be shipped in its lyophilized (powdered) form.

- As soon as the primers arrive, proceed with the reconstitution steps.

A.8.6 Reconstitution of primers for real-time qPCR

- Spin the lyophilized primers at room temperature using mini centrifuge. Only spin briefly a few times to collect the sample at the bottom of the tube.
- Add water based on the yield of the primer. For example, if the yield is 32.3 nm, then add 323 µL of nuclease free water. Note: Always use nuclease free water only!.
- The stock primers can be aliquoted to minimize the free thaw cycles.

A.8.7 Preparation of primer aliquots for real-time qPCR

Total Volume of Primer Aliquot: 200µL

- Add 10 µL of forward primer.
- Add 10 µL of reverse primer.
- Add 180 µL of nuclease free water to bring volume to 200 µL.
- Vortex briefly and spin using the microcentrifuge.
- Note: Primer Aliquots can be stored at $4^{o}C$ for a month.

A.9. MTT Cell viability stain

A.9.1 Supplies

- Thiazolyl Blue Tetrazolium Bromide (MTT) (Sigma #M5655).
- DPBS or PBS or Hanks Buffered Saline solution.
- Media (ascorbic acid free)
- Syringe filters.
- Mounting media
- Cover slips.
- Tissue Cryopreservation supplies.

A.9.2 Procedure

- Prepare the MTT stock solution (5mg/mL) in PBS or Hanks Balanced Salt Solution. Solution must be sterilized by filtering after adding MTT. Stock solution can be stored in fridge (4^{o}C) for up to a month and must be protected from light.
- For positive controls, dead porcine AV tissues were used. To obtain these dead tissues, healthy porcine AVs were cut and left under UV for about 3 days and were subjected to 3 to 4 freeze-thaw cycles using liquid nitrogen.
- In a 6 well plate, place either fresh, cultured tissues or dead tissues in each well. Two tissues per well were used.
- Add at least 3mL of media per well and add 0.5mg/mL of MTT.

- The culture was incubated at 37°C for 3 hrs in a CO_2 incubator. Always use a CO_2 incubator to maintain sterility and the pH of the media.
- After the culture, rinse the tissues in dPBS for up to 2 to 3 minutes to remove the media. If the cells are viable, the tissues look purple in color and no color if the tissues are dead (positive). It is important to use ascorbic acid free media because the ascorbic acid can reduce MTT and can give a false positive result.
- Cryopreserve the blocks in OCT following the cryopreservation protocol.
- Slice and coverslip using the water based medium and allow to dry before imaging.

A.10. TUNEL apoptosis stain

A.10.1 Supplies

- In Situ Cell Death Detection Kit, Fluorescein (Roche).
- Permeabilization Solution (0.1% Triton-X100) (Dilute 10% Triton-X100 solution 1:100 in PBS (10% Solution: 1mL of Triton X in 9mL of PBS). Make enough for slide holder (200mL).
- DNase Solution (3-3000U/ml of DNAse (from miRNeasy kit, Qiagen) in 50mM TrisCl, pH 7.5, 1mg/mL BSA).
- 1X PBS.
- 4 % Paraformaldehyde (pH 7.4).
- PAP pen (VWR).

A.10.2 Procedure

- Section frozen slides (7um). Circle the tissue sections with a PAP pen. The contents of PAP pen are hydrophilic and will help hold the reaction mixture on tissue sections.
- Wash with 1x PBS for 5min.
- Fix slides with 4% PFA for 10min at room temperature.
- Three times - Wash with 1x PBS for 5 min each.
- Permeabilize with permeabilization solution for 2 min in fridge at $4^{o}C$.
- Three times - Wash with 1x PBS for 5 min each.
- Prepare positive control by incubating slide with DNase for 10min at RT.
- Prepare negative control by incubating a tissue section with 50uL labeling solution without enzyme solution.
- For rest of samples, scale appropriately: add total 50uL of enzyme solution to 450uL of labeling solution (totaling 500uL TUNEL reaction mixture).
- Add 50uL of TUNEL reaction mixture to each slide.
- Include in a humidifying chamber at 37°C for 60 min.
- Rinse with 1x PBS (3 times for 5 min each).

- Stain with DAPI (1:2000 for 8 min).
- Rinse with 1x PBS (3 times for 5 min each).
- Mount and image for fluorescein using traditional microscopy.
- Save the slides in 4^{o}C, protected from light and air (can seal the slides with nail polish) if imaging later.

A.11. Von Kossa Stain

A.11.1 Supplies

- Add 5% silver nitrate solution (add 25 g of Silver nitrate (Sigma #S8157) to 500 mL of dH_2O. Mix well and pour into clean brown bottle and store in refrigerator at 4°C. Stable for 1 year).
- 5% sodium thiosulfate solution (add 5 g of sodium thiosulfate (Sigma #S7026) to 100 mL of dH_2O. Make fresh).
- Nuclear fast red (Kemechtrot) solution (dissolve 5 g of aluminum sulfate (Sigma #368458) in 100 mL of dH_2O. Add 0.1 g nuclear fast red (Sigma #229113) and slowly heat to boil and cool. Filter and add a grain of thymol (Sigma #T0501) as a preservative.

A.11.2 Procedure

- Slice paraffin sections at 5-7 um. Deparaffinize slides and rehydrate to dH2O at RT.

- Circle the tissue sections with a PAP pen. The contents of PAP pen are hydrophilic and will help hold the reaction mixture on tissue sections.
- Incubate slides in 5% silver nitrate solution placed under bright sunlight or under a 60W lamp. It is wise to add 100ul of this silver nitrate solution to the tissue sections encircled with PAP pen.
- Place foil or mirror behind the jar/tray to reflect the light. Leave for 1 hour or until calcium turns black. For best results use UV lamp.
- Wash 3x dH2O for 5 min at RT.
- Wash 1x in 5% sodium thiosulfate for 5 min at RT.
- Wash 1x in tap water, 1x in dH2O.
- Incubate slides in Nuclear Fast Red for 5 min at RT.
- Wash briefly in dH2O.
- Dehydrate and clear.
- Coverslip and store at RT.

A.12. Alizarin Red stain

A.12.1 Supplies

- 1 % Alizarin Red S (Sigma-Aldrich, Cat. No.A5533), pH 4.2 with ammonium hydroxide. Lasts for approx. 1 month.
- Xylene (VWR, histology grade)
- Acetone (VWR, histology grade)
- Toluene based tissue mounting media (Electron microscopy sciences)

A.12.2 Procedure

- Warm slides to room temperature for 10 minutes.
- Wash 3 min in dH2O.
- Stain sections in 1% Alizarin Red for 5 minutes. Calcium deposits should turn orange-red in color.
- Rinse in acetone 1 minute with dipping.
- Rinse in acetone-xylene for 3 minutes.
- Clear in xylene for 3 minutes.
- Coverslip and store at RT.

A.13. Silencing of miRNA in AV leaflets *ex vivo*

This protocol was primarily developed primarily to silence miR-214 in AV leaflets ex vivo. This protocol can be adapted to transfect any anti-miR or pre-miR to AV leaflets. However, transfection of pre-miR might require some troubleshooting.

These experiments must be performed in a sterile laminar flow hood and if using the tagged anti-miR (either anti-miR-214 or NT anti-miR), all the steps must be carried out in DARK!!.

A.13.1 Resuspension calculations for anti-miR-214

- Yield of anti-miR 214 oligo: 5 nmol (*in vivo* grade power inhibitor, Exiqon, Germany).
- To obtain stock Concentration: 20 µM, add 250 µL of Tris EDTA 7.5-8 buffer

(Sigma) to the anti-miR.

- Aiquot 50 µL of re-suspended anti-miR-214 and store in -20 °C for upto 6 months without loss in activity.

A.13.2 Resuspension calculations for scrambled anti-miR

- Yield of scrambled or NT tagged anti-miR oligo: 238.2 nmol (*in vivo* grade power inhibitor, Exiqon, Germany). Here TEX615 (texas red) was used as the fluorescent tag.
- To obtain stock Concentration: 100 µM, add 2338.2 µL of Tris EDTA 7.5-8 buffer (Sigma) to the anti-miR.
- Aliquot 100 µL of re-suspended and store in -20 °C for upto 6 months without loss in activity.
- Tagged anti-miRs are light sensitive and **must be protected from light**.

A.13.3 Dilution of anti-miR for transfection

- For anti-miR-214, the concentration that worked well is 400 nM. So the same concentration of tagged NT-anti-miR was used.
- Minimum amount of OptiMEM (Life Technologies, NY) needed to transfect anti-miR to a 7mm dia. AV tissue sample is 600 µL without causing appreciable hypoxia. This is the size of the tissue used in the cone and plate shear bioreactor.

- Work out the volume of anti-miR-214 and tagged NT-anti-miR needed to transfect to achieve a final concentration of 400nM based on the amount of OptiMEM used. **Remember,** the amount of anti-miR-214 and tagged NT-anti-miR added will differ since the stock concentrations are different.

A.13.4 Passive transfection of anti-miR to AV leaflets ex vivo

- Incubate the tissues with OptiMEM + anti-miR (anti-miR-214 or tagged NT-anti-miR) for 4 hours.
- After 4 hours incubation, quench the samples with regular media (atleast 4 mL/ tissue sample).
- Load the samples in the shear system with fibrosa facing up. Expose fibrosa to OS for 2 days.
- Post shear, save samples in Qiazol for RNA isolation. Pool atleast 3 samples or more for better yield of RNA.
- Each time the silencing of miR-214 in both groups (anti-miR-214 and tagged NT-anti-miR) must be verified before proceeding to further target investigation.
- Additionally, two to three tissues from tagged NT-anti-miR shear group must be cryopreserved. Frozen sections can be prepared to check for transfection efficiency and apoptosis (using TUNEL stain).

A.14. Quantification of ECM layers from elastin stain

Prepared by Kartik Balachandran in 2010.

Refined by Pouria Hosseini in 2015.

A.14.1 Procedure

- Turn on microscope and computer, start up ZEN Software, click on live, place the slide under 10x lens.
- Focus the image.
- Adjust exposure and white balance as necessary. The image should look like those shown above. You may change these values for each image as you see fit.
- Snap the picture.
- Open the image with imageJ (an opensource software) or your favorite image processing software.
- Make note of the resolution of the image.
- Open one or more images with imageJ to make sure the dimensions are consistent.
- Use the line tool to measure the length of each of the three layers of the tissue
    - Fibrosa layer: the fibrosa layer is defined as the collagen rich layer closest to the aorta. It is characterized by red squiggly lines on the image. Measure the thickness from the edge of the tissue to where the collagen ends. Measure the collagen layer at its thickest and thinnest in each image and then average the two values.

- Ventricularis layer: the ventricularis layer is defined as the elastin rich layer closest to the left ventricle. Black vertical lines on the image characterize it. Measure the thickness from the start of the black elastin lines to the edge of the tissue. Measure the ventricularis layer at its thickest and thinnest in each image and then average the two values.
- Spongiosa layer: the spongiosa layer is defined as the water rich region composed of sulfated glycosaminoglycans and proteoglycans in between the two other layers. It is characterized by the lightest colors in the tissue and appears between the edge of the collagen and the elastin lines.
- An example is shown below:

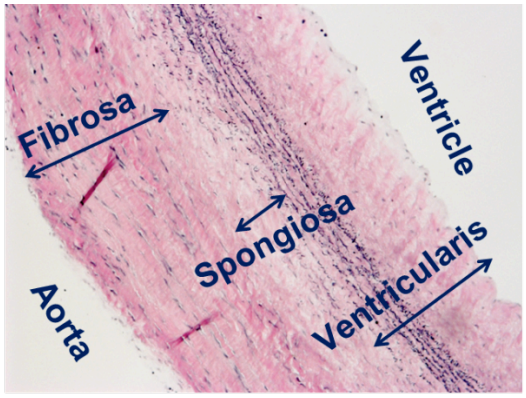

- The following screenshots may help in navigating the imageJ software.

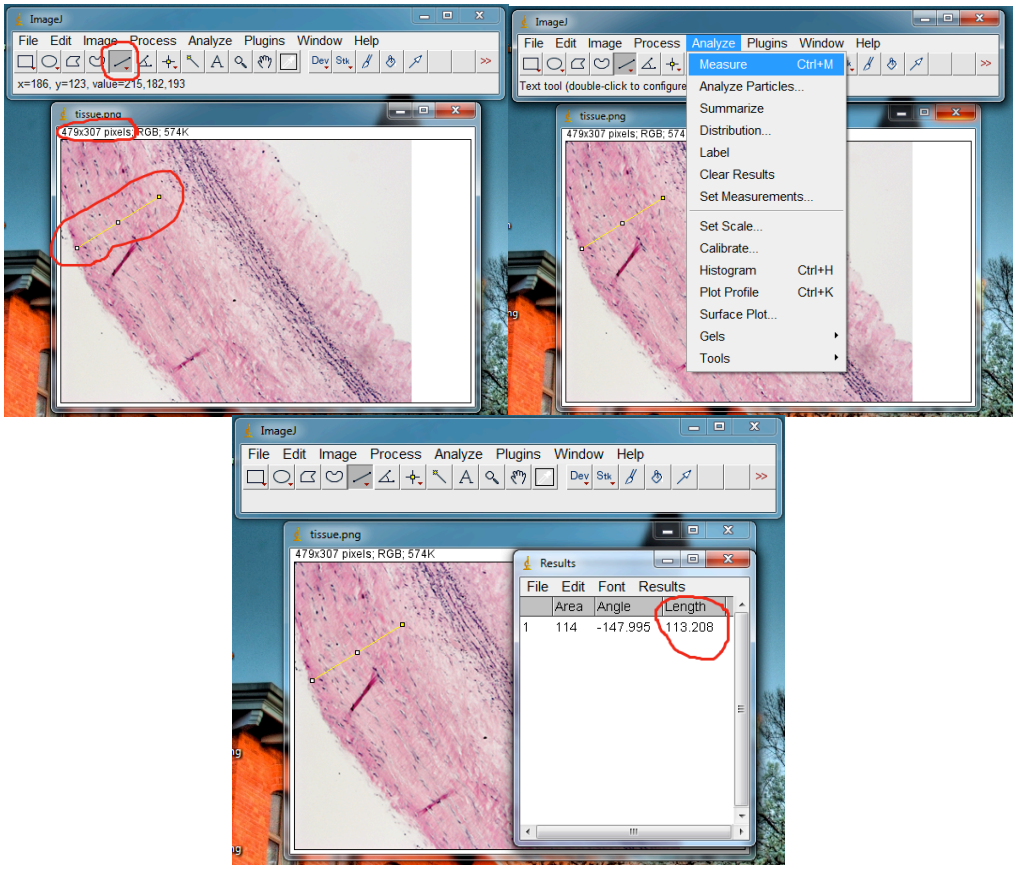

- If many images are averaged, be sure to normalize the data with respect to itself by dividing the average percent thickness of each layer by the sum of the average percent thicknesses of all three layers so that the percent thicknesses add up to 1.

A.15. Matlab Codes

A Matlab R2009 b (The Mathworks, Natick, MA) was used to run these codes.

A.16. Matlab code to program the servo with desired shear stress

File name: writeprgfile.m

This code was written by Philip Sucosky and Kartik Balachandran. This matlab code converts the shear stress vs. time data into a format that is readable by the servo motor. Additional details on how to load this program on the servo are available for reference in the cone and plate user manual (Appendix A.2).

```
function writeprgfile

hratefactor=1;
cycletime=1/hratefactor;
velfactor=1;
A=dlmread('/Users/Swetha/Cone and Plate experiments/ Fibrosa Shear stress/OS.txt');  %Input file is the text file containing shear stress vs. time (0.860 seconds or cardiac cycle)
A(:,2)=A(:,2)*0.1; %Pa
A(:,1)=A(:,1)/1000; %seconds
ro=1000; %kg/m3
```

```
mu=10^-6; %m2/s

r= 0.02; %m (Diameter of cone)

th=0.5/180*pi; %radians

h=0.0002; %m

timestep=0.0297; %seconds


w=A(:,2)/mu/ro/r*(h+th*r)/2/pi*hratefactor*velfactor; %rounds/s

D=w*timestep/hratefactor*4000; %4000 units = 1 round. D is in units.

w=[w;w];

D=[D;D];

count=0;

i=1;

while i<length(A(:,1))

    count=count+1;

    if abs(D(i))>2

        w2(count)=w(i);

        D2(count)=D(i);

        i=i+1;

    else

        DD=D(i);

        WW=w(i);

        count2=0;

        while abs(DD)<2
```

```
            count2=count2+1;
            i=i+1;
            DD=DD+D(i);
            WW=WW+w(i);
        end
        if i<length(A(:,1))
            w2(count)=WW/count2;
            D2(count)=DD;
        end
    end
end
tpt=[];
tpt2=[];
for i=1:length(A(:,2))-1
    if A(i,2)~=0 & A(i+1,2)==0
        tpt=[tpt; i+1];
    elseif A(i,2)==0 & A(i+1,2)~=0
        tpt2=[tpt2;i];
    end
end
tpt2=[tpt2;length(A(:,2))];
if sum(D2./w2/4000) < cycletime %change this if needed...!! this is cycle time
    addtime=cycletime-sum(D2./w2/4000);
```

```
    D2(end)=D2(end)+w2(end)*addtime*4000;
end
%D(find(D>0 & D<2))=2;
%D(find(D<=0 & D>-2))=-2;
D2=round(D2);
D=D2;
w=w2;
fid=fopen('/Users/Swetha/Cone and Plate experiments/ Fibrosa Shear stress/OS.prg','wt'); %This is the folder where the programmable code that is generated by this matlab code is saved.
fprintf(fid,'del sin5\n'); %This is the name of the user defined program name and can be anything. I have used sin5 for OS of 5 dyne/cm2.
fprintf(fid,'def sin5\n');
fprintf(fid,'mc01 \n');
if w(1)>0
    fprintf(fid,'A400 \n');
    sign=1;
else
    fprintf(fid,'AD400 \n');
    sign=-1;
end
for i=1:length(w)
    %[w(i) sign  w(i)*sign]
```

```
if sign*w(i) >0
    if i>1
        fprintf(fid,'GOBUF1\n');
    end
    fprintf(fid,'V%f\n',abs(w(i)));
    fprintf(fid,'D%d\n',D(i));
elseif w(i)>0
    fprintf(fid,'VF0 \n');
    if i>1
        fprintf(fid,'GOBUF1\n');
    end
    fprintf(fid,'A400 \n');
    sign=1;
    fprintf(fid,'V%f\n',abs(w(i)));
    fprintf(fid,'D%d\n',D(i));
elseif w(i)<0
    fprintf(fid,'VF0 \n');
    if i>1
        fprintf(fid,'GOBUF1\n');
    end
    fprintf(fid,'AD400 \n');
    sign=-1;
    fprintf(fid,'V%f\n',abs(w(i)));
```

```
        fprintf(fid,'D%d\n',D(i));
    end
end

fprintf(fid,'GOBUF1\n');
fprintf(fid,'end');
fclose all
```

A.17. Analysis of picrosirius red images

File name: picrosirius_analysis-modified.m

This code was written by Kartik Balachandran and modified by Pouria Hosseini.

```
% % This program reads in picrosirius red image files and calculates
    % percentage of red, orange, yellow and green fibers in the
    % image.
    function
[redpercent,orangepercent,yellowpercent,greenpercent,num_red,num_orange,nu
m_yellow,num_green] = picrosirius_analysis(filename)
    [stain,map]=imread(filename); %Image file name
    stain = stain(:,:,1:3);
    stain_cropped=imcrop(stain);
    figure;
```

```
% Magnifies image to simplify the selection of area of intest
    imshow(stain_cropped)
    stain_cropped=double(stain_cropped);
    stain_cropped_norm = stain_cropped./255; % We get 3 images - R,B,G --
Each image is a gray scale representing the intensity of color in the respective
channels
    stain_cropped_thres= stain_cropped_norm > 0.1; % check this value..!1
    stain_cropped_thres=double(stain_cropped_thres);
    stain1=stain_cropped_norm.*stain_cropped_thres; % To get the image with
intensities greater than the threshold value
    stain_hsv=rgb2hsv(stain1);% convert rgb image to hsv image
    hue_mat=stain_hsv(:,:,1); % get only the hue matrix (the true color)
    hue_mat1= hue_mat .* 255;
    [height width]=size(hue_mat1);
% Defines the hue values for a particular color
H1=double(hue_mat1 > 2 & hue_mat1 < 9) + double(hue_mat1 >230 &
hue_mat1 <256);
    H2=double(hue_mat1 > 10 & hue_mat1 < 38); % figure out the hue and color
range !!
    H3= double(hue_mat1 > 39 & hue_mat1 < 51);
    H4= double(hue_mat1 > 52 & hue_mat1 < 128);
    figure;
% Shows the individual red, orange, yellow, green images based on the above
```

```
mentioned criteria
    imshow(H1)
    figure;
    imshow (H2)
    figure;
    imshow (H3)
    figure;
    imshow (H4)
    num_red=0;
    num_orange=0;
    num_yellow=0;
    num_green=0;
    num_total = height .* width;
    for i=1:height % counting the number of non-zero entries in each matrix
       for j=1:width
          if(hue_mat1(i,j) > 2) && (hue_mat1(i,j) < 9)
num_red = num_red + 1;
          elseif(hue_mat1(i,j)  >  230)  &&  (hue_mat1(i,j)  < 256)
             num_red = num_red + 1;
          elseif(hue_mat1(i,j) > 10) && (hue_mat1(i,j) < 38)
             num_orange = num_orange + 1;
          elseif(hue_mat1(i,j) > 39) && (hue_mat1(i,j) < 51)
             num_yellow = num_yellow + 1;
```

```
            elseif(hue_mat1(i,j) > 52) && (hue_mat1(i,j) < 128)
                num_green = num_green + 1;
            end
        end
    end
    % Displays the percentage of fibers that are red, orange, yellow, or green
    redpercent = (num_red/num_total).*100;
    orangepercent = (num_orange/num_total).*100;
    yellowpercent = (num_yellow/num_total).*100;
    greenpercent = (num_green/num_total).*100;

    data = {'','Raw
Value','Percent';'Red',num_red,redpercent;'orange',num_orange,orangepercent;'
Yellow',num_yellow,yellowpercent;'Green',num_green,greenpercent};
    close all
end
```

A.18. Raw Data for specific aim1

A.18.1 Calcification of AV induced by OS and steady shear (Figure 3.7A)

	3 days		
Fresh	**Fibrosa exposed to OS**	**Fibrosa exposed to steady shear**	**Static**
0.74	3.79	1.81	1.25
0.31	1.45	0.50	2.21
1.14	1.73	0.55	1.14
0.36	2.99	0.54	1.31
2.24	3.69	0.88	1.12
0.63	0.74	0.22	0.80
1.53	0.75	0.15	1.31
1.05	0.77	0.39	1.24
	2.55	0.44	1.35

A.18.2 Time course of AV calcification induced by OS (Figure 3.8A)

	3 days		7 days	
Fresh	**Fibrosa exposed to OS**	**Ventricularis exposed to OS**	**Fibrosa exposed to OS**	**Ventricularis exposed to OS**
0.74	3.79	0.30	9.18	2.60
0.31	1.45	0.49	3.41	2.28
1.14	1.73	0.34	3.99	2.85
0.36	2.99	0.55	7.02	3.37
2.24	3.69	0.31	3.46	3.39
0.63	0.74	0.36	3.77	3.18
1.53	0.75	2.08	3.72	4.96
1.05	0.77	0.49	5.72	2.24
	2.55	0.60	3.92	3.22
		1.76		

A.18.3 Realistic shear stress and AV calcification (Figure 3.9A)

	7 days		
Fresh	**Normal**	**Low CO**	**High HR**
0.66	0.62	0.79	0.29
0.97	0.71	0.75	1.27
0.58	0.89	0.83	0.60
1.57	0.88	0.93	0.62
0.64	0.62	0.99	0.43
0.64	0.46	0.91	0.37
1.38	0.81	0.82	1.02
1.20	0.56	0.84	0.75
1.37			

A.18.4 AV calcification due to different mechanical stimuli (Figure 3.10)

	7 days		8 days		
Fresh	**Fibrosa exposed to OS**	**Ventricularis exposed to OS**	**15% Stretch**	**160/100 mmHg**	**15% Stretch +160/100 mmHg**
0.74	9.18	2.60	25.91	32.56	138.57
0.31	3.41	2.28	32.16	41.41	88.47
1.14	3.99	2.85	15.44	23.66	73.99
0.36	7.02	3.37	1.00	33.25	79.53
2.24	3.46	3.39	13.02	32.40	
0.63	3.77	3.18	31.80	67.08	
1.53	3.72	4.96	57.48	37.38	
1.05	5.72	2.24	28.56	46.16	
	3.92	3.22			

A.18.5 AV Extracellular matrix thickness (Figure 3.12B)

Fibrosa					
Fresh	**Static**	**Fibrosa exposed to OS**	**Fibrosa exposed to LS**	**Ventricularis exposed to OS**	**Ventricularis exposed to LS**
0.393	0.347	0.465	0.388	0.434	0.501
0.452	0.452	0.461	0.432	0.401	0.386
0.405	0.448	0.502	0.444	0.370	0.404
0.455	0.431	0.580	0.500	0.358	0.463
Spongiosa					
Fresh	**Static**	**Fibrosa exposed to OS**	**Fibrosa exposed to LS**	**Ventricularis exposed to OS**	**Ventricularis exposed to LS**
0.177	0.322	0.315	0.362	0.239	0.262
0.175	0.261	0.346	0.271	0.403	0.279
0.218	0.307	0.312	0.215	0.363	0.269
0.199	0.310	0.254	0.187	0.375	0.346
Ventricularis					
Fresh	**Static**	**Fibrosa exposed to OS**	**Fibrosa exposed to LS**	**Ventricularis exposed to OS**	**Ventricularis exposed to LS**
0.389	0.296	0.186	0.221	0.277	0.187
0.346	0.243	0.186	0.295	0.164	0.283
0.401	0.219	0.179	0.287	0.240	0.302
0.363	0.242	0.150	0.306	0.225	0.222

A.18.6 Relative proportion of collagen fibers (Figure 3.13B)

Condition/Fiber	Red/Orange	Yellow	Green
Fresh	0.749	0.027	0.224
Fibrosa exposed to OS	0.761	0.047	0.193
Ventricularis exposed to OS	0.721	0.016	0.263
Fibrosa exposed to OS	0.764	0.030	0.206
Ventricularis exposed to OS	0.699	0.024	0.277
Static	0.772	0.023	0.206

A.18.7 Fold changes of Sma and Col1a1 (Figure 3.14)

Sma		***Col1a1***	
Fibrosa exposed to OS	**Fibrosa exposed to LS**	**Fibrosa exposed to OS**	**Fibrosa exposed to LS**
0.023	1.693	4.789	0.795
0.012	1.302	2.820	1.898
0.037	0.005	4.271	0.308

Sma		***Col1a1***	
Fibrosa exposed to OS	**Ventricularis exposed to LS**	**Fibrosa exposed to OS**	**Ventricularis exposed to LS**
0.243	0.547	1.528	1.234
0.125	1.611	0.900	0.453
0.391	0.842	1.362	1.313

Sma		***Col1a1***	
Fibrosa exposed to OS	**Ventricularis exposed to OS**	**Fibrosa exposed to OS**	**Ventricularis exposed to OS**
0.845	0.490	1.374	0.962
0.434	0.018	0.809	0.115
1.361	2.492	1.225	1.923

Sma		***Col1a1***	
Ventricularis exposed to OS	**Ventricularis exposed to LS**	**Ventricularis exposed to OS**	**Ventricularis exposed to LS**
0.141	0.547	1.234	1.070
0.005	1.611	0.453	2.138
0.717	0.842	1.313	0.128

A.18.8 Side- and shear-dependent expression of miRNAs (Figure 3.15)

miR -181a		miR -181b	
Fibrosa exposed to	**Fibrosa exposed to**	**Fibrosa exposed to**	**Fibrosa exposed to**
OS	**LS**	**OS**	**LS**
37.93	0.01	7.39	0.00
79.83	1.13	366.43	1.87
8.61	1.86	2.00	1.13
4.85	1.05	3.55	0.97
8.79	0.78	221.47	0.60
2.89	1.17	4.47	1.43
2.12		0.44	
2.58		0.76	
3.74		0.85	

miR -199a-5p		miR -214	
Fibrosa exposed to	**Fibrosa exposed to**	**Fibrosa exposed to**	**Fibrosa exposed to**
OS	**LS**	**OS**	**LS**
6.79	0.06	1.75	0.04
6.43	0.84	3.32	1.76
2.92	2.10	0.17	1.21
0.20	1.09	6.54	1.25
2.42	0.92	52.14	0.52
0.31	0.99	8.40	1.23
0.77		2.21	
0.28		3.46	
1.06		0.02	
		6.07	
		4.90	
		13.52	

miR -181a		miR -181b	
Ventricularis exposed to	Ventricularis exposed to	Ventricularis exposed to	Ventricularis exposed to
OS	LS	OS	LS
6.73	1.09	5.45	1.01
5.75	0.96	5.79	0.93
19.89	0.95	46.36	1.06
0.14	2.07	0.07	1.57
0.15	0.65	0.14	0.57
0.18	0.28	0.13	0.86
0.63		0.15	
0.60		0.09	
0.38		0.14	

miR -199a-5p		miR -214	
Ventricularis exposed to	Ventricularis exposed to	Ventricularis exposed to	Ventricularis exposed to
OS	LS	OS	LS
101.77	1.01	0.82	0.90
49.19	0.93	0.09	1.00
20.63	1.06	1.73	1.10
76.71	1.57	4.01	1.01
34.81	0.57	6.17	0.98
44.61	0.86	18.85	1.00
13.87		0.27	1.19
13.12		0.32	0.81
16.05		0.44	1.00

miR -181a		miR -181b	
OS		OS	
Fibrosa	Ventricularis	Fibrosa	Ventricularis
4.55	0.62	1.59	0.28
9.58	0.53	78.88	0.30
1.03	1.84	0.43	2.41
19.33	0.92	8.92	0.59
6.36	0.94		1.24
12.12	1.13	11.24	1.17
1.66	1.17	1.01	1.20
2.40	1.12	1.73	0.71
1.81	0.71	1.94	1.09

miR -199a-5p		miR -214	
OS		OS	
Fibrosa	Ventricularis	Fibrosa	Ventricularis
4.08	1.78	2.02	0.41
3.86	0.86	3.82	0.64
1.75	0.36	0.19	1.95
0.21	1.47	19.87	0.78
2.59	0.67	158.36	0.93
0.33	0.86	25.51	1.29
2.99	0.97	6.70	
1.10	0.91	10.50	
4.10	1.12		

miR -181a		miR -181b	
Fibrosa exposed to	Ventricularis exposed to	Fibrosa exposed to	Ventricularis exposed to
OS	LS	OS	LS
49.13	1.09	30.56	1.01
103.38	0.96	1514.57	0.93
11.16	0.95	8.26	1.06
1.68	2.07	1.03	1.57
3.04	0.65	64.20	0.57
1.00	0.28	1.30	0.86
0.73		0.13	
0.89		0.22	
1.29		0.25	

miR -199a-5p		miR -214	
Fibrosa exposed to	Ventricularis exposed to	Fibrosa exposed to	Ventricularis exposed to
OS	LS	OS	LS
6.77	0.89	19.58	1.01
6.40	0.85	37.01	0.98
2.91	1.26	1.88	1.00
0.29	1.00	6.76	1.19
3.57	1.39	53.88	0.81
0.45	0.61	8.68	1.00
1.14		2.28	
0.42		3.57	
1.56			

A.18.9 Expression of miRNAs in fresh and static conditions (Figure 3.16)

miR -181a			miR -181b		
Fibrosa exposed to OS	Fresh	Static	Fibrosa exposed to OS	Fresh	Static
26.64	0.79	2.02	25.13	0.90	14.34
56.05	1.13	241.89	1245.58	1.21	357.88
6.05	1.09	12.30	6.79	0.89	18.50
3.94			4.85		
7.14			302.89		
2.35			6.11		
1.72			0.61		
2.10			1.04		
3.04			1.17		

miR -199a-5p			miR -214		
Fibrosa exposed to OS	**Fresh**	**Static**	**Fibrosa exposed to OS**	**Fresh**	**Static**
1.46	1.12	0.27	7.56	0.72	7.86
1.38	0.91	0.37	14.30	1.19	17.01
0.63	0.96	0.30	0.73	1.09	19.74
0.39			4.96		
4.82			39.50		
0.61			6.36		
1.53			1.67		
0.57			2.62		
2.10					

A.19. Raw data for specific aim 2

A.19.1 Shear-dependency of selected target genes (Figure 4.5)

Condition/ Gene	*Klf4*	*Enos*	*Sma*	*Ctnnb1*	*Bcl2l11*	*Col1a1*
Fibrosa exposed to OS	0.006	0.004	0.023	0.006	0.000	4.789
	0.003	0.009	0.012	0.009	0.001	2.820
	0.004	0.019	0.037	0.014	0.001	4.271
Fibrosa exposed to LS	2.133	0.046	1.693	1.054	1.939	0.795
	0.736	1.648	1.302	1.191	0.282	1.898
	0.132	1.306	0.005	0.756	0.779	0.308

Condition/ Gene	*Klf4*	*Enos*	*Sma*	*Ctnnb1*	*Bcl2l11*	*Col1a1*
Ventricularis exposed to OS	0.257	0.477	0.547	0.203	0.005	1.234
	2.603	1.934	1.611	2.514	2.851	0.453
	0.140	0.589	0.842	0.282	0.144	1.313
Ventricularis exposed to LS	0.317	5.056	0.141	0.095	0.036	1.070
	0.163	1.159	0.005	0.022	0.036	2.138
	0.167	2.564	0.717	1.367	0.036	0.128

A.19.2 Side-dependency of selected targets genes (Figure 4.6)

Condition/Gene	*Klf4*	*Enos*	*Sma*	*Ctnnb1*	*Bcl2l11*	*Col1a1*
Fibrosa exposed to OS	1.458	0.117	0.845	0.121	0.279	1.374
	0.693	0.178	0.434	0.170	0.551	0.809
	1.127	0.389	1.361	0.258	0.971	1.225
Ventricularis exposed to OS	1.470	1.728	0.490	0.192	1.000	0.962
	0.757	0.396	0.018	0.045	1.000	0.115
	0.773	0.876	2.492	2.764	1.000	1.923

Condition/Gene	*Klf4*	*Enos*	*Sma*	*Ctnnb1*	*Bcl2l11*	*Col1a1*
Fibrosa exposed to OS	0.314	0.341	0.243	0.060	0.010	1.528
	0.149	0.521	0.125	0.084	0.020	0.900
	0.243	1.139	0.391	0.128	0.035	1.362
Ventricularis exposed to LS	0.257	0.477	0.547	0.203	0.005	1.234
	2.603	1.934	1.611	2.514	2.851	0.453
	0.140	0.589	0.842	0.282	0.144	1.313

A.19.3 Silencing of miR-214 in AV static culture (Figure 4.9)

Static	
NT anti-miR	**anti-miR-214**
0.593	0.071
0.801	0.355
1.606	0.615
1.734	0.028
0.102	0.685
1.164	0.170

A.19.4 Silencing of miR-214 in fibrosa exposed to OS (Figure 4.10B)

Fibrosa exposed to OS	
NT anti-miR	**anti-miR-214**
1.342	0.001
0.658	0.000
1.109	0.093
0.575	0.140
1.316	0.105

A.19.5 Validation of mRNA targets using anti-miR-214 (Figure 4.11)

Condition/Gene	***Enos***	***Bcl2l11***	***Ctnnb1***	***Klf4***	***Sma***
Fibrosa exposed to OS: NT-anti-miR	2.097	0.269	1.383	1.630	0.556
	0.035	0.850	0.591		1.474
	0.868	1.880	1.025	0.370	0.970
	2.093	0.001	1.155	0.800	0.782
	0.246	2.997	1.036	1.172	1.043
	0.661	0.001	0.809	1.028	1.175
	1.194		0.573	1.000	
	0.806		1.199		0.012
			1.228		1.988
Fibrosa exposed to OS: anti-miR-214	116.024	89.295	2.957	3.675	5.801
	8.769	573.779	0.652	13.118	1.082
	2.065	238.842	0.824	0.628	0.527
	0.000	0.038	0.902	0.707	0.518
	0.004	0.058	0.758	1.350	6.918
	0.001	0.000	0.841	13.773	2.932
	200.014		0.707	3.564	2.051
	1.825			6.832	
	0.027				

A.19.6 Role of miR-214 in AV Endo-MT, and Inflammation (Figure 4.12)

Condition/Gene	*Mcp1*	*VE-Cadherin*
Fibrosa exposed to OS: NT-anti-miR	1.796	0.301
	0.476	1.562
	0.728	1.136
	1.425	1.000
	0.863	2.471
	0.712	0.400
	0.539	0.128
	1.286	
	1.175	
Fibrosa exposed to OS: anti-miR-214	37.072	15.168
	0.587	0.726
	0.892	27.151
	0.976	2.302
	1.123	10.060
	0.540	0.149
	0.641	

Condition/Gene	*Icam1*	*Vcam1*	*Tgfβ1*	*Bmp4*
Fibrosa exposed to OS: NT anti-miR	1.215	0.297	1.337	0.284
	1.168	2.611	1.170	1.055
	0.618	0.092	0.493	1.661
	1.389		1.566	0.003
	1.177		1.091	2.997
	0.434		0.343	0.000
Fibrosa exposed to OS: anti-miR-214	0.435	23.532	0.416	28.543
	0.588	37.398	0.605	20.549
	0.639	0.647	0.574	10.832
	1.173		0.622	0.000
	0.396		0.214	0.000
	0.469		0.196	0.002

A.19.7 Role of miR-214 in AV calcification (Figure 4.13)

Fibrosa exposed to OS	
NT anti-miR	**anti-miR-214**
0.819	0.336
0.279	0.302
0.195	0.300
0.392	0.264
0.240	0.113
0.293	0.121
0.093	0.145
0.088	0.219
0.084	0.909
0.406	0.038
0.065	0.287
0.092	0.127
0.227	0.046
0.045	0.004
0.281	0.182
0.331	0.228
0.064	0.312
0.069	0.311

A.20. Raw data for specific aim 3

A.20.1 Pyrophosphatase and AV calcification (Figure 5.2A)

Control	0.1U/mL	0.2U/mL	0.4U/mL	0.8U/mL
12.36	1280.60	403.54	3370.09	670.44
94.32	621.27	117.43	526.44	174.57
95.67	31.05	1204.41	266.62	288.16
91.35	46.09	396.39	1077.63	1021.61
164.76	1260.74	295.60	432.31	1024.07
224.71	602.81	500.08	234.17	355.26
104.49	1008.94	667.88	373.59	175.97
26.08	267.01	1074.21	328.24	1887.25

A.20.2 Phosphate, pyrophosphatase and AV calcification (Figure 5.3A)

Without Inorganic Pyrophosphatase (IP)				With Inorganic Pyrophosphatase (IP)			
0.8mM	2.6mM	3.2mM	3.8mM	0.8mM	2.6mM	3.2mM	3.8mM
6.30	4.91	9.73	5.66	5.27	6.41	7.60	1002.28
5.83	8.83	6.51	212.25	3.07	5.02	7.17	280.81
8.95	24.66	8.31	10.86	3.12	24.18	251.36	42.82
9.40	20.40	6.07	7.66	3.10	3.71	110.38	888.66
4.98	6.71	11.96	22.59	1.93	3.94	0.37	1691.43
4.72	7.75	79.97	187.50	3.24	3.36	68.42	1195.99
6.34	14.69		274.52	2.39	4.78	68.98	222.76
				3.47	2.66	70.98	821.44

A.20.3 Time course of AV calcification (Figure 5.4A)

With Inorganic Pyrophosphatase (IP)				Control
2 days	**4 days**	**6 days**	**8 days**	**8 days**
288.72	1211.73	518.00	3370.09	8.77
490.97	476.78	1087.07	526.44	8.19
370.29	74.45	373.25	266.62	10.15
490.31	528.37	93.31	1077.63	5.51
36.32	536.21	40.23	432.31	4.73
575.76	1395.85	676.08	234.17	9.53
21.49	37.95	246.34	373.59	10.44
684.28	296.32	162.74	328.24	7.73
12.28	49.73	45.16	1002.28	12.36
7.79	34.28	1479.15	280.81	94.32
5.97	44.55	1395.76	42.82	95.67
5.86	174.16	907.09	888.66	91.35
6.62	289.55	63.91	1691.43	164.76
52.35	94.84	1403.36	1195.99	224.71
9.06	157.52	1531.79	222.76	104.49
375.97		990.71	821.44	26.08

A.21. Effect of different chemokines on AV calcification (Figure 5.5A)

Control	ALP	ALP+IP	Devitalized	ALP+ Serum	ALP+ Dexamethasone	ALP+ TGF-β
5.66	278.40	453.06	952.05	551.34	842.57	1054.86
212.25	283.08	1295.44	1628.90	424.62	275.42	17.06
10.86	539.08	10.42	448.17	747.73	429.37	490.66
7.66	272.66	16.53	743.91	581.80	796.23	29.69
22.59	477.83	14.91	1690.94	435.43	364.62	113.23
187.50	352.07	1117.43	617.65	437.01	540.01	541.96
274.52	385.15	2025.46	1035.91	831.58	444.26	
	268.78	1020.14	1606.95	384.20	502.15	

A.21.1 Warfarin and AV calcification (Figure 5.6A)

Control	IP	Warfarin	IP+Warfarin
8.77	3370.09	15.04	2295.75
8.19	526.44	719.05	15.37
10.15	266.62	22.64	143.55
5.51	1077.63	15.02	15.02
4.73	432.31	25.39	3207.43
9.53	234.17	16.05	2352.85
10.44	373.59	155.03	2160.51
7.73	328.24	23.18	41.53
12.36	1002.28	117.99	210.84
94.32	280.81	316.86	370.62
95.67	42.82	158.46	340.21
91.35	888.66	503.25	275.16
164.76	1691.43	186.22	415.38
224.71	1195.99	254.92	1251.85
104.49	222.76	186.07	588.14
26.08	821.44	460.42	287.82

A.21.2 Etidronate and AV calcification (Figure 5.7A)

Control	IP only	0.07 µM Et+IP	0.7 µM Et+IP	7 µM Et+IP
8.77	1002.28	460.75	2.97	3.73
8.19	280.81	317.47	23.12	3.51
10.15	42.82	141.74	2.27	4.62
5.51	888.66	10.17	1.93	7.39
4.73	1691.43	35.97	2.72	2.03
9.53	1195.99	34.95	7.20	2.20
10.44	222.76	12.41	3.08	2.98
7.73	821.44	185.27	37.10	2.86

A.21.3 Synthesis of pyrophosphate from AV leaflets (Figure 5.11)

Control			MLS		
1.00	**2.50**	**5.00**	**1.00**	**2.50**	**5.00**
0.0186	0.0228	0.0222	0.0106	0.0117	0.0266
0.0155	0.0261	0.0204	0.0179	0.0210	0.0248
0.0103	0.0058	0.0115	0.0251	0.0243	0.0241
0.0083	0.0118	0.0110	0.0092	0.0137	0.0276

pmol/g/h		
Control	**β,γ-methylene ATP**	**MLS 38949**
0.2357	0.0664	0.3407
0.2551	0.0880	0.5233
0.2209	0.0712	0.4430

A.22. Target list of miR-214 and miR-181a

A.22.1 Targets of miRs-181a and -214 identified using online databases

miRNA	Experimentally validated mRNA targets
	miRWalk +miRTarBase
hsa-miR-181a-5p	SSSCA1
	THRB
	ITGAX
	ZAP70
	HSPA5
	SYF2
	ATM
	NANOS2
	ATG5
	RDX
	ADM
	IL10
	SDC1
	GPI
	BCL2L2
	TLR4
	CNTN3
	LCT
	NCAM1
	TCL1A
	NBN
	GRIA2
	AFP
	SOD2
	WT1
	ODZ1
	BCL2L11
	SOCS1
	CREBBP
	MECP2
	TGFB1
	TIMM8A
	NPM1

MCL1
DCTN6
CD4
CD83
H2AFX
BAX
TP53
CDKN1B
TACSTD1
TP73
TNF
NTS
DMPK
FLT3
BAALC
BCR
AHSA1
RC3H1
PTEN
NDUFA2
CCL27
PML
PSMD9
PDCD4
CD40
DDX20
HPRT1
NLK
YES1
CASP4
COX8A
IL6
RGS4
ALAS1
CDKN1A
FASN
EIF2C2
LMX1A
PCAF
TSPO
CASP3
CD36
CD8A

EPHB6
SIRT1
DICER1
MAPK8
SMAD4
TGFBI
YAP1
FOS
STMN1
ASCL1
CEBPA
ESR1
NLRP1
CCND1
SPP1
TRIM13
MAPK3
TGFBR1
MMP9
CDH17
RNASEN
CISH
GEMIN4
STAT1
NR4A2
RASSF1
GYPA
ZFPM1
ZNF501
CD3EAP
CARS
TGFBRAP1
HRSP12
PDK4
PARP1
RNPC3
MT4
PITX3
BDNF
TFRC
EPOR
SLC27A4
CFD

CD19
TIMP3
PECAM1
CDKN2A
ERBB2
DGCR8
GADD45A
LYZ
HOXA11
POU3F2
TARBP2
ERG
HLA-A
APOE
RRBP1
STIP1
CDX2
HIPK2
GPAM
SEMA4C
WNT1
KRAS
HLA-E
CTTNBP2
LYN
LIN28
PRR6
SCD
F8
TWIST1
GATA1
GATA6
PLAG1
RALA
ZNF763
LFNG
LRRC17
CHRFAM7A
CD46
RASSF6
FXYD6
KCTD3
TSHR

ZNF558
C8A
ARL6IP6
ZNF426
ATF7IP2
PRR4
TCF21
PHOX2A
PROSC
PTPLAD1
GSTM2
FSIP1
KBTBD3
PTPRZ1
WNT3A
TUSC1
LRRN3
TMEM45A
ARF6
C1orf109
TAF15
PLXDC2
NMRK2
WNT2
ATG10
PRDX3
ZNF652
RTEL1-TNFRSF6B
GCNT1
PCDHB8
ENAH
ZNF25
S100A1
PLA2G4C
NOL4
SIX6
FKBP10
SMCHD1
OR11A1
INCENP
LPGAT1
CLUAP1
LYSMD3

CCDC6
BAG2
GPR83
PTGS2
ANKRD13C
RLF
NRP1
FAM47B
CCNG1
BRMS1L
OTUD1
ATP6V0E1
WNT16
CST5
SH3BGRL
GPR137B
OFCC1
IQCG
NKX3-2
OTX2
ROPN1L
TMEM14A
TAF2
IDS
FRA10AC1
COL27A1
EPHA5
DCST1
ZNF562
EYA4
CHL1
TAAR6
SLCO2A1
TMEM257
HMGB2
HERC3
BTBD3
SRPK2
DNAJC7
ANKRD1
CFI
MRPS14
HEY2

	MTMR12
	ACOT12
	KIAA0101
	USP28
	AMMECR1
	BPGM
	DSCR8
	UGT3A1
	HSD17B3
	GADD45G
	FBXO34
	C1QTNF9
	KLRC4
	MOB3B
	FKBP7
	TBX4
	TMPRSS11A
	SNAI2
	SLC7A11
	NUDT12
	COPS2
	ZNF12
	PRLR
	PLCL2
	ZNF594
	METAP1
	Bcl2
	Cd69
	Tcra
	Egr1
	Tox
	Runx1
	OPN
	PUM1
hsa-miR-214-3p	ACTA2
	AKT1
	AMELX
	APC
	ATP2A2
	BCL2
	BIRC3

BMP2
CALB1
CCND1
CCND2
CD28
CD44
CDC42
CDKN1A
CDKN2A
COL1A1
COX8A
CTNNB1
DCT
DICER1
EGFL7
EIF2C1
EIF2C2
ENAM
EZH2
FUT4
HDGF
IK
IKBKB
ITGB1
JAG1
JUN
KLF4
KRAS
LBR
MAP2K3
MAPK8
MCL1
MOCOS
MYC
MYH11
MYOD1
NBN
NEUROG3
NOS3
NRAS
PAK1
PITX2
PRNP

PTEN
RAB22A
RAG2
ROBO2
RUNX2
SH2B2
SOX9
SRGAP2
STMN2
SYNE1
TACSTD1
TCF3
TGFBR2
THBS1
TIMM8A
TOP2B
TUBE1
TWIST1
VEGFA
ZEB1
ZEB2
ZNRD1
PTEN
DAPK1
MAP2K3
MAPK8
PLXNB1
GALNT7
FLOT1
MAP2K5
HSPD1
AHSA1
CPNE7
RASA1
YWHAQ
ARL2
AP3B1

A.23. Stretch and pressure – AV calcification *ex vivo*

A.23.1 Rationale and hypothesis

Aortic valve sclerosis leads to leaflet calcification and results in aortic stenosis and regurgitation. It has been shown that hypertension is significantly associated with AV sclerosis with odds ratio ranging from 1.23 to 1.74 (*78*); however the molecular mechanisms are not understood well. It is hypothesized that pathological hypertensive pressure can lead to earlier AV calcification compared to normal disease progression. The role of combined effects of both physiological and pathological cyclic stretch and pressure on AV calcification was investigated.

A.23.2 Methods

Fresh porcine AV leaflets were cultured in a novel *ex vivo* cyclic stretch and pressure bioreactor (*83*) under different conditions for 2, 4, 6 and 8 days. Osteogenic media was used to accelerate the calcification process (*17*). Six conditions tested were tested: 1) 10% stretch alone, 2) 120/80 mmHg pressure alone, 3) combined 10% stretch and 120/80 mmHg pressure, 4) 15% stretch alone, 5) 160/100 mmHg pressure alone, and 6) combined 15% stretch and 160/100 mmHg pressure. The first three conditions correspond to the physiological stretch and pressure, whereas, the last three conditions represent severe hypertension. The leaflets were assayed for calcium using quantitative calcium arsenazo assay. Statistical analysis was carried out as discussed previously.

A.23.3 Results

Calcium levels increased significantly in the presence of 10% cyclic stretch after 6 and 8 days culture (Figure A.23. 1). On the other hand, the isolated pressure alone induced significant calcification only after 8 days; however, its effect was about 2.5 folds significantly lower than the 10% stretch. Interestingly, combined stretch and pressure maintained the calcium levels throughout, even after 8 days.

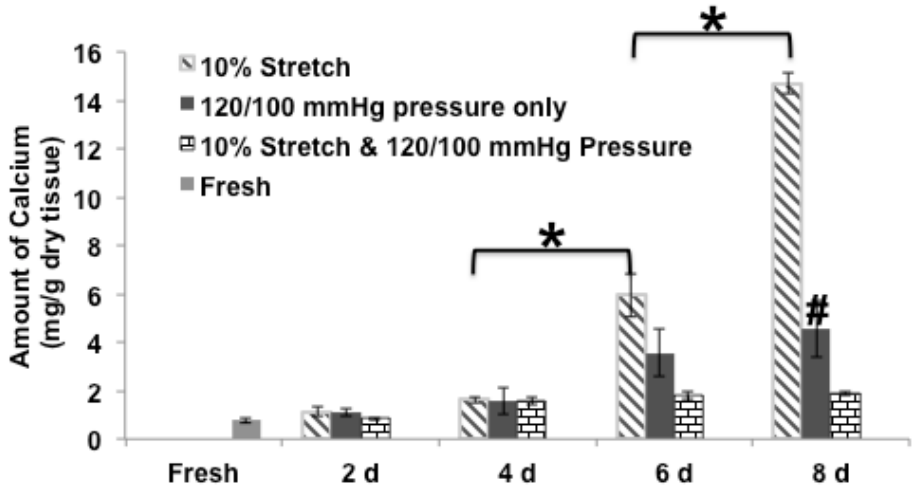

Figure A.23. 1 Time course of AV calcification induced by physiological stretch and pressure ex vivo**.** Calcium induced by 10% stretch alone increased significantly with culture duration after 6 days, and continued to increase after 8 days culture. Calcium induced after 8 days culture in the presence of 10% stretch alone was statistically higher compared to the isolated pressure. However when stretch and pressure was combined, no calcification was observed even after 8 days culture in osteogenic media. *$p<0.05$, #$p<0.05$ vs. 10% stretch, 120 mmHg pressure at 2 and 4 days, n=4.

As expected, the amount of calcium significantly increased in case of isolated 15% stretch or isolated hypertensive pressure of 160/100 mmHg after 8 days culture compared to that of 4 days ($p<0.05$) (Figure A.23. 2). However, the calcification induced by the combined 15% stretch and 160/100 mmHg was significantly higher ($p<0.05$) than the isolated stimuli after 8 days culture.

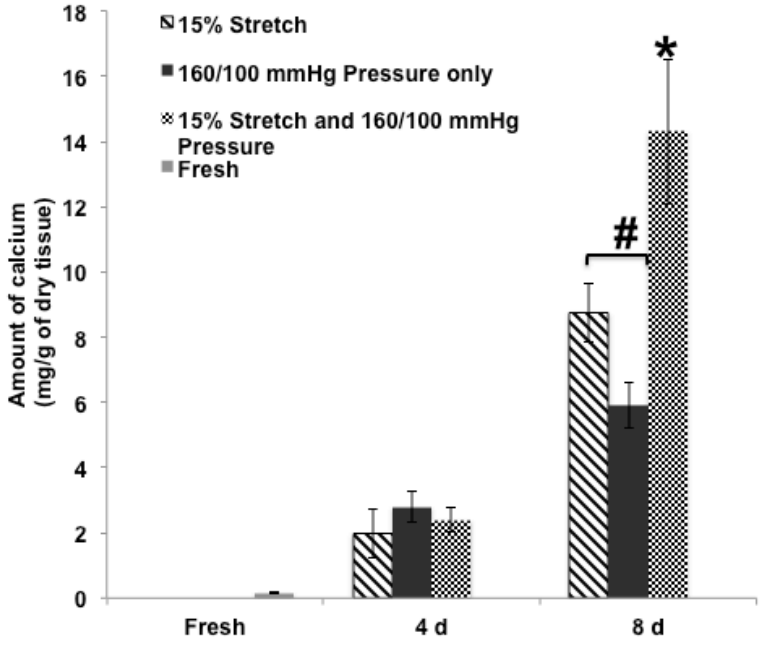

Figure A.23. 2 Time course of AV calcification induced by pathological stretch andpressure *ex vivo***.** Calcium induced by 15% stretch alone or 160/100 mm Hg pressure alone or by combined 15% stretch and 160/100 mmHg pressure significantly increased after 4 days culture and continued to increase after 8 days. After 8 days culture, the calcium induced by combined 15% stretch and 160/100 mmHg pressure was significantly higher than the 15% stretch or 160/100 mmHg pressure. *$p<0.05$, #$p<0.05$ vs. 10% stretch, n=4.

A.23.4 Discussion and conclusions

Our results suggest that cyclic stretch alone upregulates calcification, perhaps due to deformational trauma, while the concurrent presence of normal pressure depressed this calcification response suggesting that different physiological forces play a role to maintain healthy valve physiology. However, exposure to hypertensive pressure increased the calcification significantly compared to isolated stretch, indicating that the altered mechanical environment as a result of hypertension may be an important step in the pathway linking hypertension to clinically observed increased risk of calcification. Additional investigation is required to test this hypothesis, and was not pursued as part of this thesis work.

A.24. Functional role of miR-214 in AV static culture

A.24.1 Approach

The delivery of anti-miR to the AV tissues was optimized using statically cultured leaflets (specific aim-2). After successful silencing of miR-214, the selected targets genes of miR-214 were then validated. Also the functional effect of miR-214 silencing on AV endothelial-to-mesenchymal transition (Endo-MT) and inflammation was tested. This appendix includes all the results from these studies, which were not part of the specific aim-2.

A.24.2 Methods

The workflow of this protocol is shown in the Figure A.24.1. Freshly isolated AV leaflets were passively transfected with 400 nM tagged non-targeting (NT) anti-miR or anti-miR-214 (Exiqon, Denmark). The samples were then incubated in OptiMEM for 4 h (Life Technologies, NY). After this, the leaflets tissues were quenched with regular DMEM and cultured under static conditions for 48 h. Each sample was then washed well in nuclease-free sterile dPBS. Total RNA was isolated from the other half of each of the tissues and qPCR analysis was done. Selected mRNA target genes of miR-214 (*Klf4, Enos, Ctnnb1, Col1a1, Sma* and *Bcl2l11*) were validated. The effect of miR-214 silencing on AV Endo-MT (*Mcp1* and *VE-Cadherin*) and inflammation (*Tgfβ1*, *Icam1, Bmp4* and *Vcam1)* was also investigated. Statistical analysis was carried out as discussed previously.

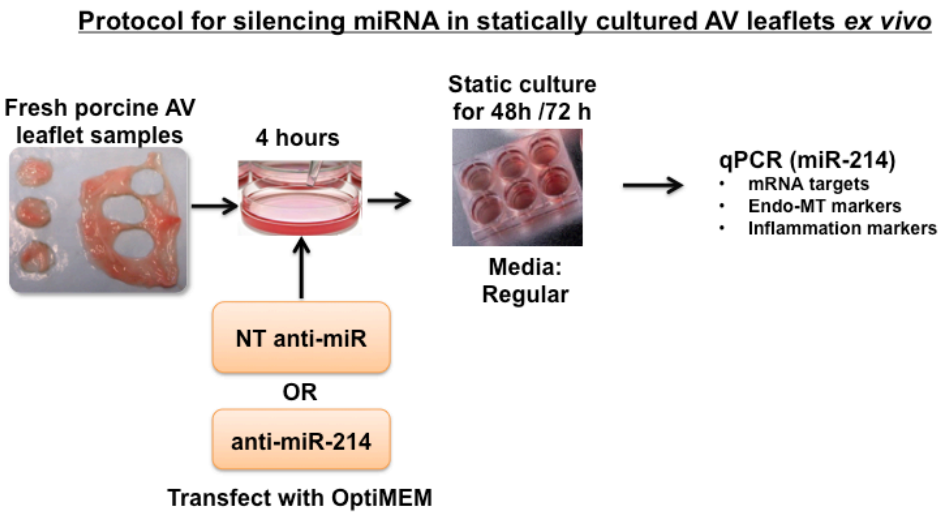

Figure A.24.1 Silencing protocol of miR-214 in statically cultured AV.

A.24.3 Results

As shown in the Figure A.24. 2, out of 6 targets tested, only *Klf4* was significantly upregulated (p=0.05). This confirms that *klf4* is a potential target of miR-214 in AV. Also, upon miR-214 silencing, the expression of *Mcp1* increased significantly (p=0.04) while the expression of *VE-Cadherin* did not change (Figure A.24. 3A). Silencing of miR-214 tended to increase an inflammation marker (also a key transcription factor) *Tgfβ1* (p=0.09), but did not affect the expression of *Icam1, Bmp4* and *Vcam1* (Figure A.24. 3B).

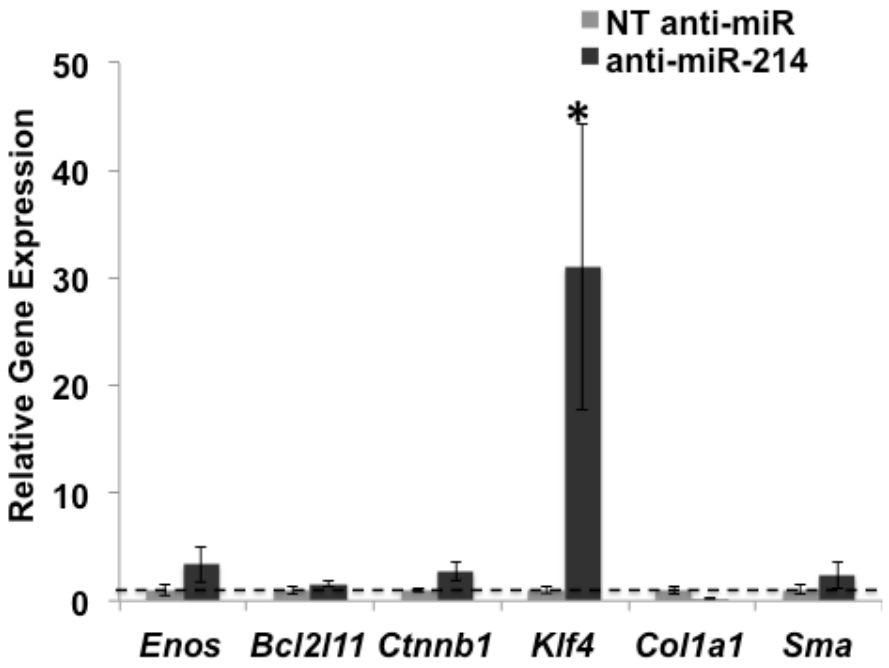

Figure A.24. 2 Validation of mRNA targets by silencing miR-214 in statically cultured AVs. Out of 6 mRNA targets tested, only *Klf4* appeared to be a target of miR-214. *p=0.05. n=6 (pooled 2 samples/isolation).

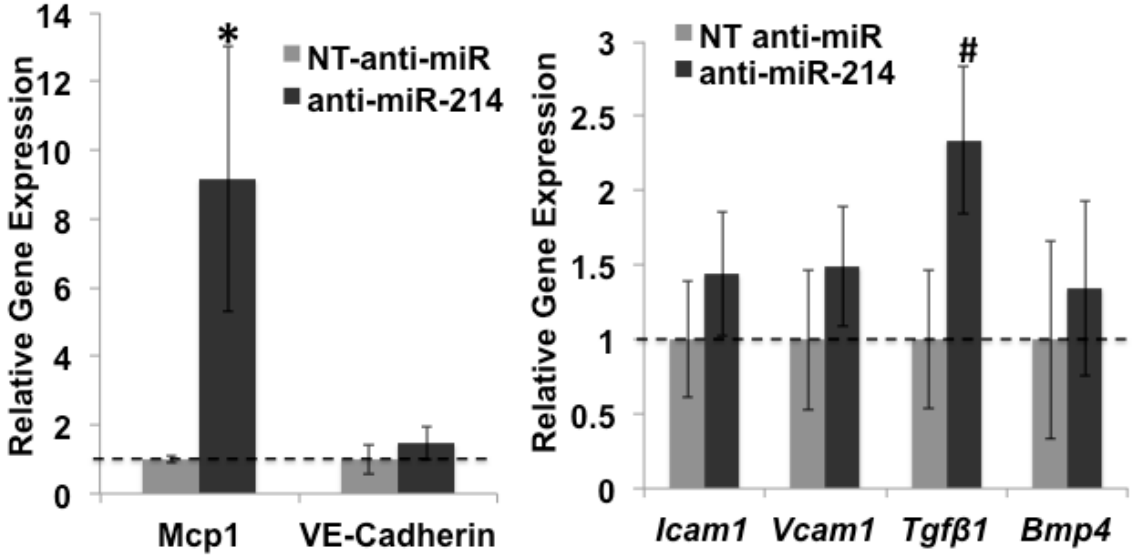

Figure A.24. 3 The effect of miR-214 silencing on AV Endo-MT and inflammation in static conditions. **A)** Silencing of miR-214 significantly increased Mcp1 levels. **B)** Silencing of miR-214 downregulated *Tgfβ1* only. *p=0.04, #p=0.09. n=6 (pooled 2 samples/isolation).

A.24.4 Discussion and conclusions

The findings in this study can be summarized as follows: 1) *klf4* is a validated target of miR-214, 2) miR-214 plays a role in AV Endo-MT via *Mcp1* via *Tgfβ1,* 3) miR-214 may not play a significant role in AV inflammation. Similar results were observed in specific aim-2 when miR-214 was silenced in fibrosa exposed to OS. Silencing of miR-214 significantly upregulated the expression of *klf4, Tgfβ1,* but did not affect the Endo-MT markers. Further, the regulation of *Mcp1* by miR-214 is mechanical stimuli dependent (static vs. oscillatory shear). Overall, miR-214 may be involved in AV Endo-MT via *klf4 and Tgfβ1* dependent pathway. Additional investigation is required to support this speculation, and was not pursued as part of this thesis work.

REFERENCES

1. R. V. Freeman, C. M. Otto, Spectrum of Calcific Aortic Valve Disease: Pathogenesis, Disease Progression, and Treatment Strategies. *Circulation* **111**, 3316-3326 (2005).

2. S. E. P. New, E. Aikawa, Molecular Imaging Insights Into Early Inflammatory Stages of Arterial and Aortic Valve Calcification. *Circulation Research* **108**, 1381-1391 (2011).

3. E. E. Golub, K. Boesze-Battaglia, The role of alkaline phosphatase in mineralization. *Current Opinion in Orthopaedics* **18**, 444-448 410.1097/BCO.1090b1013e3282630851 (2007).

4. D. A. Towler, Inorganic Pyrophosphate. *Arteriosclerosis, Thrombosis, and Vascular Biology* **25**, 651-654 (2005).

5. K. Amann, Media Calcification and Intima Calcification Are Distinct Entities in Chronic Kidney Disease. *Clinical Journal of the American Society of Nephrology* **3**, 1599-1605 (2008).

6. N. M. Rajamannan, M. Subramaniam, D. Rickard, S. R. Stock, J. Donovan, M. Springett, T. Orszulak, D. A. Fullerton, A. J. Tajik, R. O. Bonow, T. Spelsberg, Human Aortic Valve Calcification Is Associated With an Osteoblast Phenotype. *Circulation* **107**, 2181-2184 (2003).

7. B. Stewart, D. Siscovick, B. Lind, J. Gardin, J. Gottdiener, V. Smith, D. Kitzman, C. Otto, Clinical factors associated with calcific aortic valve disease. Cardiovascular Health Study. *J Am Coll Cardiol* **29**, 630-634 (1997).

8. C. M. Otto, B. K. Lind, D. W. Kitzman, B. J. Gersh, D. S. Siscovick, S. The Cardiovascular Health, Association of Aortic-Valve Sclerosis with Cardiovascular Mortality and Morbidity in the Elderly. *N Engl J Med* **341**, 142-147 (1999).

9. C. Otto, J. Kuusisto, D. Reichenbach, A. Gown, K. O'Brien, Characterization of the early lesion of 'degenerative' valvular aortic

stenosis. Histological and immunohistochemical studies. *Circulation* **90**, 844-853 (1994).

10. S. Arjunon, S. Rathan, H. Jo, A. Yoganathan, Aortic Valve: Mechanical Environment and Mechanobiology. *Annals of Biomedical Engineering*, 1-16 (2013).

11. Y. Agmon, B. K. Khandheria, I. Meissner, J. D. Sicks, W. M. O'Fallon, D. O. Wiebers, J. P. Whisnant, J. B. Seward, A. J. Tajik, Aortic valve sclerosis and aortic atherosclerosis: different manifestations of the same disease?: Insights from a population-based study. *J Am Coll Cardiol* **38**, 827-834 (2001).

12. L. Denby, V. Ramdas, R. Lu, B. R. Conway, J. S. Grant, B. Dickinson, A. B. Aurora, J. D. McClure, D. Kipgen, C. Delles, E. van Rooij, A. H. Baker, MicroRNA-214 Antagonism Protects against Renal Fibrosis. *Journal of the American Society of Nephrology : JASN* **25**, 65-80 (2014).

13. G. Yin, R. Chen, A. B. Alvero, H.-H. Fu, J. Holmberg, C. Glackin, T. Rutherford, G. Mor, *TWISTing stemness, inflammation and proliferation of epithelial ovarian cancer cells through MIR199A2/214*. (2010), vol. 29, pp. 3545-3553.

14. X. Wang, B. Guo, Q. Li, J. Peng, Z. Yang, A. Wang, D. Li, Z. Hou, K. Lv, G. Kan, H. Cao, H. Wu, J. Song, X. Pan, Q. Sun, S. Ling, Y. Li, M. Zhu, P. Zhang, S. Peng, X. Xie, T. Tang, A. Hong, Z. Bian, Y. Bai, A. Lu, Y. Li, F. He, G. Zhang, Y. Li, miR-214 targets ATF4 to inhibit bone formation. *Nat Med* **19**, 93-100 (2013).

15. H.-Q. Lu, C. Liang, Z.-Q. He, M. Fan, Z.-G. Wu, Circulating miR-214 is associated with the severity of coronary artery disease. *Journal of Geriatric Cardiology : JGC* **10**, 34-38 (2013).

16. M. Lindroos, M. Kupari, J. Heikkila, R. Tilvis, Prevalence of aortic valve abnormalities in the elderly: an echocardiographic study of a random population sample. *J Am Coll Cardiol* **21**, 1220-1225 (1993).

17. K. Balachandran, P. Sucosky, H. Jo, A. P. Yoganathan, Elevated Cyclic Stretch Induces Aortic Valve Calcification in a Bone Morphogenic Protein-Dependent Manner. *The American Journal of Pathology* **177**, 49-57 (2010).

18. K. Balachandran, Dissertation, Georgia Institute of Technology (2010).

19. C. M. Otto, Evaluation and Management of Chronic Mitral Regurgitation. *New England Journal of Medicine* **345**, 740-746 (2001).

20. H.-W. Sung, A. P. Yoganathan, Axial flow velocity patterns in a normal human pulmonary artery model: Pulsatile in vitro studies. *Journal of Biomechanics* **23**, 201-214 (1990).

21. D. Wiltz, C. A. Arevalos, L. R. Balaoing, A. A. Blancas, M. C. Sapp, X. Zhang, K. J. Grande-Allen, *Extracellular Matrix Organization, Structure, and Function*. Calcific Aortic Valve Disease (2013).

22. C. J. Holliday, R. F. Ankeny, H. Jo, R. M. Nerem, Discovery of shear- and side-specific mRNAs and miRNAs in human aortic valvular endothelial cells. *American Journal of Physiology - Heart and Circulatory Physiology* **301**, H856-H867 (2011).

23. J. T. Butcher, S. Tressel, T. Johnson, D. Turner, G. Sorescu, H. Jo, R. M. Nerem, Transcriptional profiles of valvular and vascular endothelial cells reveal phenotypic differences - Influence of shear stress. *Arteriosclerosis Thrombosis and Vascular Biology* **26**, 69-77 (2006).

24. C. A. Simmons, G. R. Grant, E. Manduchi, P. F. Davies, Spatial Heterogeneity of Endothelial Phenotypes Correlates With Side-Specific Vulnerability to Calcification in Normal Porcine Aortic Valves. *Circulation Research* **96**, 792-799 (2005).

25. M. Miragoli, M. H. Yacoub, I. El-Hamamsy, J. L. Sanchez-Alonso, A. Moshkov, N. Mongkoldhumrongkul, M. Padala, S. Paramagurunathan, P. Sarathchandra, Y. E. Korchev, J. Gorelik, A. H. Chester, Side Specific Mechanical Properties of Valve Endothelial Cells. *American Journal of Physiology - Heart and Circulatory Physiology* **307**, H15-H24 (2014).

26. J.-H. Chen, C. A. Simmons, Cell–Matrix Interactions in the Pathobiology of Calcific Aortic Valve Disease. *Circulation Research* **108**, 1510-1524 (2011).

27. D. Petrovic´, R. Obrenovic´, B. Stojimirovic´, Risk factors for aortic valve calcification in patients on regular hemodialysis. *The International Journal Of Artificial Organs* **32**, 173-179 (2009).

28. H. Baumgartner, Hemodynamic Assessment of Aortic Stenosis Are There Still Lessons to Learn? *Journal of the American College of Cardiology* **47**, 138-140 (2006).

29. C. Ward, Clinical significance of the bicuspid aortic valve. *Heart* **83**, 81-85 (2000).

30. A. J. Barker, M. Markl, J. Burk, R. Lorenz, J. Bock, S. Bauer, J. Schulz-Menger, F. von Knobelsdorff-Brenkenhoff, Bicuspid Aortic Valve Is Associated with Altered Wall Shear Stress in the Ascending Aorta. *Circulation: Cardiovascular Imaging* **5**, 457-466 (2012).

31. M. B. Lewin, C. M. Otto, The Bicuspid Aortic Valve: Adverse Outcomes From Infancy to Old Age. *Circulation* **111**, 832-834 (2005).

32. E. R. Mohler Iii, Mechanisms of aortic valve calcification. *The American Journal of Cardiology* **94**, 1396-1402 (2004).

33. N. M. Rajamannan, B. Gersh, R. O. Bonow, Calcific aortic stenosis: From bench to the bedside, emerging clinical and cellular concepts *Heart* **89**, 801-805 (2003).

34. M. H. Yacoub, J. J. M. Takkenberg, Will heart valve tissue engineering change the world? *Nat Clin Pract Cardiovasc Med* **2**, 60-61 (2005).

35. J. A. Leopold, Cellular Mechanisms of Aortic Valve Calcification. *Circulation: Cardiovascular Interventions* **5**, 605-614 (2012).

36. A. C. Liu, V. R. Joag, A. I. Gotlieb, The Emerging Role of Valve Interstitial Cell Phenotypes in Regulating Heart Valve Pathobiology. *Am J Pathol* **171**, 1407-1418 (2007).

37. K. A. Hruska, S. Mathew, R. Lund, P. Qiu, R. Pratt, Hyperphosphatemia of chronic kidney disease. *Kidney Int* **74**, 148-157 (2008).

38. A. Peng, T. Wu, C. Zeng, D. Rakheja, J. Zhu, T. Ye, J. Hutcheson, N. D. Vaziri, Z. Liu, C. Mohan, X. J. Zhou, Adverse Effects of Simulated Hyper- and Hypo-Phosphatemia on Endothelial Cell Function and Viability. *PLoS ONE* **6**, e23268 (2011).

39. J. L. Reynolds, J. N. Skepper, R. McNair, T. Kasama, K. Gupta, P. L. Weissberg, W. Jahnen-Dechent, C. M. Shanahan, Multifunctional Roles for Serum Protein Fetuin-A in Inhibition of Human Vascular Smooth Muscle Cell Calcification. *Journal of the American Society of Nephrology* **16**, 2920-2930 (2005).

40. R. T. Franceschi, G. Xiao, D. Jiang, R. Gopalakrishnan, S. Yang, E. Reith, Multiple Signaling Pathways Converge on the Cbfa1/Runx2 Transcription Factor to Regulate Osteoblast Differentiation. *Connective Tissue Research* **44**, 109-116 (2003).

41. D. A. Towler, Molecular and Cellular Aspects of Calcific Aortic Valve Disease. *Circulation Research* **113**, 198-208 (2013).

42. W. C. O'Neill, K. A. Lomashvili, H. H. Malluche, M.-C. Faugere, B. L. Riser, Treatment with pyrophosphate inhibits uremic vascular calcification. *Kidney Int* **79**, 512-517 (2011).

43. C. A. S. Jonathan Butcher, James N Warnock, Mechanobiology of the Aortic Heart Valve. *The Journal of Heart Valve Disease* **17**, 62-73 (2008).

44. J. T. Butcher, R. M. Nerem, Valvular endothelial cells regulate the phenotype of interstitial cells in co-culture: effects of steady shear stress. *Tissue engineering* **12**, 905-915 (2006).

45. J.-J. Chiu, S. Chien, Effects of Disturbed Flow on Vascular Endothelium: Pathophysiological Basis and Clinical Perspectives. *Physiological Reviews* **91**, 327-387 (2011).

46. W. L. Lim, Y. T. Chew, T. C. Chew, H. T. Low, Pulsatile flow studies of a porcine bioprosthetic aortic valve in vitro: PIV measurements and shear-induced blood damage. *Journal of Biomechanics* **34**, 1417-1427 (2001).

47. Nandy, S., Tarbell, J. M., *Flush mounted hot film anemometer measurement of wall shear stress distal to a tri-leaflet valve for newtonian*

and non-newtonian blood analog fluids. (IOS Press, Amsterdam, PAYS-BAS, 1987), vol. 24.

48. L. Ge, F. Sotiropoulos, Direction and Magnitude of Blood Flow Shear Stresses on the Leaflets of Aortic Valves: Is There a Link With Valve Calcification? *Journal of Biomechanical Engineering* **132**, 014505 (2010).

49. S. Chandra, N. Rajamannan, P. Sucosky, Computational assessment of bicuspid aortic valve wall-shear stress: implications for calcific aortic valve disease. *Biomech Model Mechanobiol* **11**, 1085-1096 (2012).

50. C. H. Yap, N. Saikrishnan, G. Tamilselvan, N. Vasilyev, A. P. Yoganathan, The congenital bicuspid aortic valve can experience high-frequency unsteady shear stresses on its leaflet surface. *American Journal of Physiology - Heart and Circulatory Physiology* **303**, H721-H731 (2012).

51. M. J. Levesque, R. M. Nerem, The Elongation and Orientation of Cultured Endothelial Cells in Response to Shear Stress. *Journal of Biomechanical Engineering* **107**, 341-347 (1985).

52. P. Sucosky, M. Padala, A. Elhammali, K. Balachandran, H. Jo, A. P. Yoganathan, Design of an Ex Vivo Culture System to Investigate the Effects of Shear Stress on Cardiovascular Tissue. *Journal of Biomechanical Engineering* **130**, 035001 (2008).

53. L. Sun, N. Rajamannan, P. Sucosky, Design and Validation of a Novel Bioreactor to Subject Aortic Valve Leaflets to Side-Specific Shear Stress. *Annals of Biomedical Engineering* **39**, 2174-2185 (2011).

54. M. O. Platt, Y. Xing, H. Jo, A. P. Yoganathan, Cyclic pressure and shear stress regulate matrix metalloproteinases and cathepsin activity in porcine aortic valves. *Journal of Heart Valve Disease* **15**, 622-629 (2006).

55. R. F. Ankeny, V. H. Thourani, D. Weiss, J. D. Vega, W. R. Taylor, R. M. Nerem, H. Jo, Preferential Activation of SMAD1/5/8 on the Fibrosa Endothelium in Calcified Human Aortic Valves - Association with Low BMP Antagonists and SMAD6. *PLoS ONE* **6**, e20969 (2011).

56. L. Sun, S. Chandra, P. Sucosky, Ex Vivo Evidence for the Contribution of Hemodynamic Shear Stress Abnormalities to the Early Pathogenesis of Calcific Bicuspid Aortic Valve Disease. *PLoS ONE* **7**, e48843 (2012).

57. M. J. Thubrikar, S. P. Nolan, J. Aouad, J. D. Deck, Stress Sharing Between the Sinus and Leaflets of Canine Aortic Valve. *The Annals of Thoracic Surgery* **42**, 434-440 (1986).

58. K. Ragaert, F. De Somer, P. Somers, I. De Baere, L. Cardon, J. Degrieck, Flexural mechanical properties of porcine aortic heart valve leaflets. *Journal of the Mechanical Behavior of Biomedical Materials* **13**, 78-84 (2012).

59. G. C. Engelmayr Jr, D. K. Hildebrand, F. W. H. Sutherland, J. E. Mayer Jr, M. S. Sacks, A novel bioreactor for the dynamic flexural stimulation of tissue engineered heart valve biomaterials. *Biomaterials* **24**, 2523-2532 (2003).

60. M. Thubrikar, *The aortic valve*. (CRC Press, Boca Raton, Fla. :, 1990).

61. G. W. Christie, B. G. Barratt-Boyes, Age-dependent changes in the radial stretch of human aortic valve leaflets determined by biaxial testing. *The Annals of Thoracic Surgery* **60, Supplement 2**, S156-S159 (1995).

62. R. J. Brewer, R. M. Mentzer, Jr., J. D. Deck, R. C. Ritter, J. S. Trefil, S. P. Nolan, An in vivo study of the dimensional changes of the aortic valve leaflets during the cardiac cycle. *The Journal Of Thoracic And Cardiovascular Surgery* **74**, 645-650 (1977).

63. M. Thubrikar, S. P. Nolan, L. P. Bosher, J. D. Deck, The cyclic changes and structure of the base of the aortic valve. *American Heart Journal* **99**, 217-224 (1980).

64. C. H. Yap, H.-S. Kim, K. Balachandran, M. Weiler, R. Haj-Ali, A. P. Yoganathan, Dynamic deformation characteristics of porcine aortic valve leaflet under normal and hypertensive conditions. *American Journal of Physiology - Heart and Circulatory Physiology* **298**, H395-H405 (2010).

65. A. S. John, S. S. Michael, On the Biaxial Mechanical Properties of the Layers of the Aortic Valve Leaflet. *Journal of Biomechanical Engineering* **129**, 757-766 (2007).

66. E. J. Weinberg, M. R. Kaazempur Mofrad, A multiscale computational comparison of the bicuspid and tricuspid aortic valves in relation to calcific aortic stenosis. *Journal of Biomechanics* **41**, 3482-3487.

67. S. Katayama, N. Umetani, T. Hisada, S. Sugiura, Bicuspid aortic valves undergo excessive strain during opening: A simulation study. *The Journal of Thoracic and Cardiovascular Surgery* **145**, 1570-1576 (2013).

68. K. Balachandran, P. Sucosky, H. Jo, A. P. Yoganathan, Elevated cyclic stretch alters matrix remodeling in aortic valve cusps: implications for degenerative aortic valve disease. *Am J Physiol Heart Circ Physiol* **296**, H756-764 (2009).

69. S. Helske, S. Syvaranta, K. A. Lindstedt, J. Lappalainen, K. Oorni, M. I. Mayranpaa, J. Lommi, H. Turto, K. Werkkala, M. Kupari, P. T. Kovanen, Increased expression of elastolytic cathepsins S, K, and V and their inhibitor cystatin C in stenotic aortic valves. *Arteriosclerosis Thrombosis and Vascular Biology* **26**, 1791-1798 (2006).

70. R. A. Peña-Silva, J. D. Miller, Y. Chu, D. D. Heistad, Serotonin produces monoamine oxidase-dependent oxidative stress in human heart valves. *American Journal of Physiology - Heart and Circulatory Physiology* **297**, H1354-H1360 (2009).

71. K. Balachandran, M. A. Bakay, J. M. Connolly, X. Zhang, A. P. Yoganathan, R. J. Levy, Aortic Valve Cyclic Stretch Causes Increased Remodeling Activity and Enhanced Serotonin Receptor Responsiveness. *The Annals of Thoracic Surgery* **92**, 147-153 (2011).

72. C.-H. Ku, P. H. Johnson, P. Batten, P. Sarathchandra, R. C. Chambers, P. M. Taylor, M. H. Yacoub, A. H. Chester, Collagen synthesis by mesenchymal stem cells and aortic valve interstitial cells in response to mechanical stretch. *Cardiovasc Res* **71**, 548-556 (2006).

73. R. A. Gould, K. Chin, T. P. Santisakultarm, A. Dropkin, J. M. Richards, C. B. Schaffer, J. T. Butcher, Cyclic strain anisotropy regulates valvular

interstitial cell phenotype and tissue remodeling in three-dimensional culture. *Acta Biomaterialia* **8**, 1710-1719 (2012).

74. P. S. Robinson, R. T. Tranquillo, Planar Biaxial Behavior of Fibrin-Based Tissue-Engineered Heart Valve Leaflets. *Tissue Eng. Part A* **15**, 2763-2772 (2009).

75. P. Poggio, R. Sainger, E. Branchetti, J. B. Grau, E. K. Lai, R. C. Gorman, M. S. Sacks, A. Parolari, J. E. Bavaria, G. Ferrari, Noggin attenuates the osteogenic activation of human valve interstitial cells in aortic valve sclerosis. *Cardiovascular Research* **98**, 402-410 (2013).

76. K. Smith, S. Metzler, J. Warnock, Cyclic strain inhibits acute pro-inflammatory gene expression in aortic valve interstitial cells. *Biomech Model Mechanobiol* **9**, 117-125 (2010).

77. K. Haerten, G. Dohn, V. Dohn, L. Seipel, F. Loogen, [Natural history of patients with severe aortic valve disease under medical therapy (author's transl)]. *Zeitschrift Für Kardiologie* **69**, 757-762 (1980).

78. S. W. Rabkin, The association of hypertension and aortic valve sclerosis. *Blood Pressure* **14**, 264-272 (2005).

79. R. Ceravolo, R. Maio, A. Pujia, A. Sciacqua, G. Ventura, M. C. Costa, G. Sesti, F. Perticone, Pulse pressure and endothelial dysfunction in never-treated hypertensive patients. *J Am Coll Cardiol* **41**, 1753-1758 (2003).

80. K. Hishikawa, T. Nakaki, T. Marumo, M. Hayashi, H. Suzuki, R. Kato, T. Saruta, Pressure promotes DNA synthesis in rat cultured vascular smooth muscle cells. *The Journal of Clinical Investigation* **93**, 1975-1980 (1994).

81. K. Hishikawa, T. Nakaki, T. Marumo, H. Suzuki, R. Kato, T. Saruta, Pressure Enhances Endothelin-1 Release From Cultured Human Endothelial Cells. *Hypertension* **25**, 449-452 (1995).

82. Y. Xing, J. N. Warnock, Z. He, S. L. Hilbert, A. P. Yoganathan, Cyclic Pressure Affects the Biological Properties of Porcine Aortic Valve Leaflets in a Magnitude and Frequency Dependent Manner. *Annals of Biomedical Engineering* **32**, 1461-1470 (2004).

83. P. Thayer, K. Balachandran, S. Rathan, C. Yap, S. Arjunon, H. Jo, A. Yoganathan, The Effects of Combined Cyclic Stretch and Pressure on the Aortic Valve Interstitial Cell Phenotype. *Annals of Biomedical Engineering* **39**, 1654-1667 (2011).

84. J. N. Warnock, S. C. Burgess, A. Shack, A. P. Yoganathan, Differential immediate-early gene responses to elevated pressure in porcine aortic valve interstitial cells. *The Journal of heart valve disease* **15**, 34-41; discussion 42 (2006).

85. S. Konduri, Y. Xing, J. N. Warnock, Z. He, A. P. Yoganathan, Normal Physiological Conditions Maintain the Biological Characteristics of Porcine Aortic Heart Valves: An Ex Vivo Organ Culture Study. *Annals of Biomedical Engineering* **33**, 1158-1166 (2005).

86. G. Engelmayr, L. Soletti, S. Vigmostad, S. Budilarto, W. Federspiel, K. Chandran, D. Vorp, M. Sacks, A Novel Flex-Stretch-Flow Bioreactor for the Study of Engineered Heart Valve Tissue Mechanobiology. *Annals of Biomedical Engineering* **36**, 700-712 (2008).

87. J. Kortsmit, N. J. B. Driessen, M. C. M. Rutten, F. P. T. Baaijens, Nondestructive and Noninvasive Assessment of Mechanical Properties in Heart Valve Tissue Engineering. *Tissue Eng. Part A* **15**, 797-806 (2009).

88. J. Bauersachs, T. Thum, Biogenesis and Regulation of Cardiovascular MicroRNAs. *Circulation Research* **109**, 334-347 (2011).

89. E. Berezikov, W.-J. Chung, J. Willis, E. Cuppen, E. C. Lai, Mammalian Mirtron Genes. *Molecular Cell* **28**, 328-336 (2007).

90. K. Miyoshi, T. Miyoshi, H. Siomi, Many ways to generate microRNA-like small RNAs: non-canonical pathways for microRNA production. *Mol Genet Genomics* **284**, 95-103 (2010).

91. A. Kuehbacher, C. Urbich, A. M. Zeiher, S. Dimmeler, Role of Dicer and Drosha for Endothelial MicroRNA Expression and Angiogenesis. *Circulation Research* **101**, 59-68 (2007).

92. G. T. Torrezan, E. N. Ferreira, A. M. Nakahata, B. D. F. Barros, M. T. M. Castro, B. R. Correa, A. C. V. Krepischi, E. H. R. Olivieri, I. W. Cunha, U.

Tabori, P. E. Grundy, C. M. L. Costa, B. de Camargo, P. A. F. Galante, D. M. Carraro, Recurrent somatic mutation in DROSHA induces microRNA profile changes in Wilms tumour. *Nat Commun* **5**, (2014).

93. B. Lewis, C. Burge, D. Bartel, Conserved seed pairing, often flanked by adenosines, indicates that thousands of human genes are microRNA targets. *Cell* **120**, 15-20 (2005).

94. E. Bronze-da-Rocha, MicroRNAs Expression Profiles in Cardiovascular Diseases. *BioMed Research International* **2014**, 23 (2014).

95. B. N. Davis, A. C. Hilyard, G. Lagna, A. Hata, SMAD proteins control DROSHA-mediated microRNA maturation. *Nature* **454**, 56-61 (2008).

96. Y. Ye, J. R. Perez-Polo, J. Qian, Y. Birnbaum, *The role of microRNA in modulating myocardial ischemia-reperfusion injury*. (2011), vol. 43, pp. 534-542.

97. E. Van Rooij, L. B. Sutherland, N. Liu, A. H. Williams, J. McAnally, R. D. Gerard, J. A. Richardson, E. N. Olson, A signature pattern of stress-responsive microRNAs that can evoke cardiac hypertrophy and heart failure. *Proceedings of the National Academy of Sciences of the United States of America* **103**, 18255-18260 (2006).

98. L. Poliseno, A. Tuccoli, L. Mariani, M. Evangelista, L. Citti, K. Woods, A. Mercatanti, S. Hammond, G. Rainaldi, MicroRNAs modulate the angiogenic properties of HUVECs. *Blood* **108**, 3068-3071 (2006).

99. T. A. Harris, M. Yamakuchi, M. Ferlito, J. T. Mendell, C. J. Lowenstein, MicroRNA-126 regulates endothelial expression of vascular cell adhesion molecule 1. *Proceedings of the National Academy of Sciences* **105**, 1516-1521 (2008).

100. K. D. Obrien, D. D. Reichenbach, S. M. Marcovina, J. Kuusisto, C. E. Alpers, C. M. Otto, Apolipoproteins B, (a), and E accumulate in the morphologically early lesion of 'degenerative' valvular aortic stenosis. *Arteriosclerosis Thrombosis and Vascular Biology* **16**, 523-532 (1996).

101. R. Koos, T. Krueger, R. Westenfeld, H. P. Kühl, V. Brandenburg, A. H. Mahnken, S. Stanzel, C. Vermeer, E. C. M. Cranenburg, J. Floege, M.

Kelm, L. J. Schurgers, Relation of circulating matrix Gla-protein and anticoagulation status in patients with aortic valve calcification. *Thrombosis and Haemostasis* **101**, 706-713 (2009).

102. P. Sucosky, K. Balachandran, A. Elhammali, H. Jo, A. P. Yoganathan, Altered Shear Stress Stimulates Upregulation of Endothelial VCAM-1 and ICAM-1 in a BMP-4- and TGF-β1-Dependent Pathway. *Arterioscler Thromb Vasc Biol* **29**, 254-260 (2009).

103. X. Qin, X. Wang, Y. Wang, Z. Tang, Q. Cui, J. Xi, Y.-S. J. Li, S. Chien, N. Wang, MicroRNA-19a mediates the suppressive effect of laminar flow on cyclin D1 expression in human umbilical vein endothelial cells. *Proceedings of the National Academy of Sciences*, (2010).

104. K.-C. Wang, L. X. Garmire, A. Young, P. Nguyen, A. Trinh, S. Subramaniam, N. Wang, J. Y. Shyy, Y.-S. Li, S. Chien, Role of microRNA-23b in flow-regulation of Rb phosphorylation and endothelial cell growth. *Proceedings of the National Academy of Sciences*, (2010).

105. Y. Fang, C. Z. Shi, E. Manduchi, M. Civelek, P. F. Davies, MicroRNA-10a regulation of proinflammatory phenotype in athero-susceptible endothelium in vivo and in vitro. *Proceedings of the National Academy of Sciences of the United States of America* **107**, 13450-13455 (2010).

106. V. Nigam, H. H. Sievers, B. C. Jensen, H. A. Sier, P. C. Simpson, D. Srivastava, S. A. Mohamed, Altered MicroRNAs in Bicuspid Aortic Valve: A Comparison Between Stenotic and Insufficient Valves. *Journal of Heart Valve Disease* **19**, 459-465 (2010).

107. B. Yanagawa, F. Lovren, Y. Pan, V. Garg, A. Quan, G. Tang, K. K. Singh, P. C. Shukla, N. P. Kalra, M. D. Peterson, S. Verma, miRNA-141 is a novel regulator of BMP-2–mediated calcification in aortic stenosis. *The Journal of Thoracic and Cardiovascular Surgery* **144**, 256-262.e252 (2012).

108. S. Rathan, A. R. Anita Rajamani, H. Gorti, S. Arjunon, H. Jo, A. Yoganathan, Calcification of Aortic Valve leaflets is Shear Dependent and Side-specific. *QScience Proceedings* **2012**, 58 (2012).

109. H. Dweep, C. Sticht, P. Pandey, N. Gretz, miRWalk – Database: Prediction of possible miRNA binding sites by “walking” the genes of three genomes. *Journal of Biomedical Informatics* **44**, 839-847 (2011).

110. S.-D. Hsu, Y.-T. Tseng, S. Shrestha, Y.-L. Lin, A. Khaleel, C.-H. Chou, C.-F. Chu, H.-Y. Huang, C.-M. Lin, S.-Y. Ho, T.-Y. Jian, F.-M. Lin, T.-H. Chang, S.-L. Weng, K.-W. Liao, I.-E. Liao, C.-C. Liu, H.-D. Huang, miRTarBase update 2014: an information resource for experimentally validated miRNA-target interactions. *Nucleic Acids Research* **42**, D78-D85 (2014).

111. C. H. Yap, N. Saikrishnan, G. Tamilselvan, A. P. Yoganathan, Experimental measurement of dynamic fluid shear stress on the aortic surface of the aortic valve leaflet. *Biomech Model Mechanobiol* **11**, 171-182 (2012).

112. D. Hoehn, L. Sun, P. Sucosky, Role of Pathologic Shear Stress Alterations in Aortic Valve Endothelial Activation. *Cardiovascular Engineering and Technology* **1**, 165-178 (2010).

113. C. H. Yap, N. Saikrishnan, A. P. Yoganathan, Experimental measurement of dynamic fluid shear stress on the ventricular surface of the aortic valve leaflet. *Biomech Model Mechanobiol* **11**, 231-244 (2012).

114. Y. Choon Hwai, Dissertation, Georgia Institute of Technology (2011).

115. F. Custodis, S. H. Schirmer, M. Baumhakel, G. Heusch, M. Bohm, U. Laufs, Vascular Pathophysiology in Response to Increased Heart Rate. *J Am Coll Cardiol* **56**, 1973-1983 (2010).

116. R. Maio, S. Miceli, A. Sciacqua, G. Leone, R. Bruni, P. Naccarato, F. Martino, G. Sesti, F. Perticone, Heart rate affects endothelial function in essential hypertension. *Intern Emerg Med*, 1-9 (2011).

117. G. M. London, B. Pannier, S. J. Marchais, A. P. Guerin, Calcification of the Aortic Valve in the Dialyzed Patient. *Journal of the American Society of Nephrology* **11**, 778-783 (2000).

118. K. Balachandran, S. Konduri, P. Sucosky, H. Jo, A. Yoganathan, An Ex Vivo Study of the Biological Properties of Porcine Aortic Valves in

Response to Circumferential Cyclic Stretch. *Annals of Biomedical Engineering* **34**, 1655-1665 (2006).

119. K. J. Rodriguez, L. M. Piechura, A. M. Porras, K. S. Masters, Manipulation of valve composition to elucidate the role of collagen in aortic valve calcification. *BMC Cardiovascular Disorders* **14**, 29-29 (2014).

120. J. K. Mouw, Y. Yui, L. Damiano, R. O. Bainer, J. N. Lakins, I. Acerbi, G. Ou, A. C. Wijekoon, K. R. Levental, P. M. Gilbert, E. S. Hwang, Y.-Y. Chen, V. M. Weaver, Tissue mechanics modulate microRNA-dependent PTEN expression to regulate malignant progression. *Nat Med* **20**, 360-367 (2014).

121. H. R. Shcherbata, E. Edeleva, Stress-induced ECM alteration modulates cellular microRNAs that feedback to readjust the extracellular environment and cell behaviour. *Frontiers in Genetics* **4**, (2013).

122. L. C. U. Junqueira, G. Bignolas, R. R. Brentani, Picrosirius staining plus polarization microscopy, a specific method for collagen detection in tissue sections. *Histochem J* **11**, 447-455 (1979).

123. E. Aikawa, P. Whittaker, M. Farber, K. Mendelson, R. F. Padera, M. Aikawa, F. J. Schoen, Human Semilunar Cardiac Valve Remodeling by Activated Cells From Fetus to Adult: Implications for Postnatal Adaptation, Pathology, and Tissue Engineering. *Circulation* **113**, 1344-1352 (2006).

124. C. J. Holliday, Dissertation, Georgia Institute of Technology (2012).

125. B. Chu, T. Wu, L. Miao, Y. Mei, M. Wu, MiR-181a regulates lipid metabolism via IDH1. *Scientific Reports* **5**, 8801 (2015).

126. N. Dong, X. Tang, B. Xu, miRNA-181a Inhibits the Proliferation, Migration, and Epithelial–Mesenchymal Transition of Lens Epithelial CellsmiRNA-181a in the Treatment of PCO. *Investigative Ophthalmology & Visual Science* **56**, 993-1001 (2015).

127. Y. Li, C. Kuscu, A. Banach, Q. Zhang, A. Pulkoski-Gross, D. Kim, J. Liu, E. Roth, E. Li, K. R. Shroyer, P. I. Denoya, X. Zhu, L. Chen, J. Cao, microRNA-181a-5p Inhibits Cancer Cell Migration and Angiogenesis via

Downregulation of Matrix Metalloproteinase-14. *Cancer Research*, (2015).

128. Y.-B. Ouyang, Y. Lu, S. Yue, R. G. Giffard, miR-181 targets multiple Bcl-2 family members and influences apoptosis and mitochondrial function in astrocytes. *Mitochondrion* **12**, 213-219 (2012).

129. W. Xie, Z. Li, M. Li, N. Xu, Y. Zhang, miR-181a and inflammation: miRNA homeostasis response to inflammatory stimuli in vivo. *Biochemical and Biophysical Research Communications* **430**, 647-652 (2013).

130. K.-H. Shin, S. D. Bae, H. S. Hong, R. H. Kim, M. K. Kang, N.-H. Park, miR-181a shows tumor suppressive effect against oral squamous cell carcinoma cells by downregulating K-ras. *Biochem. Biophys. Res. Commun.* **404**, 896-902 (2011).

131. X. Sun, B. Icli, A. K. Wara, N. Belkin, S. He, L. Kobzik, G. M. Hunninghake, M. P. Vera, T. S. Blackwell, R. M. Baron, M. W. Feinberg, MicroRNA-181b regulates NF-κB–mediated vascular inflammation. *The Journal of Clinical Investigation* **122**, 1973-1990 (2012).

132. L. Shi, Z. Cheng, J. Zhang, R. Li, P. Zhao, Z. Fu, Y. You, hsa-mir-181a and hsa-mir-181b function as tumor suppressors in human glioma cells. *Brain Research* **1236**, 185-193 (2008).

133. Z. F. Duan, E. Choy, D. Harmon, X. Z. Liu, M. Susa, H. Mankin, F. Hornicek, MicroRNA-199a-3p Is Downregulated in Human Osteosarcoma and Regulates Cell Proliferation and Migration. *Molecular Cancer Therapeutics* **10**, 1337-1345 (2011).

134. G. A. Song, H. Z. Zeng, J. A. Li, L. F. Xiao, Y. Z. He, Y. H. Tang, Y. R. Li, miR-199a Regulates the Tumor Suppressor Mitogen-Activated Protein Kinase Kinase Kinase 11 in Gastric Cancer. *Biological & Pharmaceutical Bulletin* **33**, 1822-1827 (2010).

135. F. Fornari, M. Milazzo, P. Chieco, M. Negrini, G. A. Calin, G. L. Grazi, D. Pollutri, C. M. Croce, L. Bolondi, L. Gramantieri, MiR-199a-3p Regulates mTOR and c-Met to Influence the Doxorubicin Sensitivity of Human Hepatocarcinoma Cells. *Cancer Res.* **70**, 5184-5193 (2010).

136. G. Yin, R. Chen, A. B. Alvero, H. H. Fu, J. Holmberg, C. Glackin, T. Rutherford, G. Mor, TWISTing stemness, inflammation and proliferation of epithelial ovarian cancer cells through MIR199A2/214. *Oncogene* **29**, 3545-3553 (2010).

137. E. A. Lin, L. Kong, X.-H. Bai, Y. Luan, C.-j. Liu, miR-199a*, a Bone Morphogenic Protein 2-responsive MicroRNA, Regulates Chondrogenesis via Direct Targeting to Smad1. *J. Biol. Chem.* **284**, 11326-11335 (2009).

138. Y. Feng, J. H. Cao, X. Y. Li, S. H. Zhao, Inhibition of miR-214 expression represses proliferation and differentiation of C2C12 myoblasts. *Cell Biochemistry and Function* **29**, 378-383 (2011).

139. P. T. Jindra, J. Bagley, J. G. Godwin, J. Iacomini, Costimulation-Dependent Expression of MicroRNA-214 Increases the Ability of T Cells To Proliferate by Targeting Pten. *Journal of Immunology* **185**, 990-997 (2010).

140. E. Penna, F. Orso, D. Cimino, E. Tenaglia, A. Lembo, E. Quaglino, L. Poliseno, A. Haimovic, S. Osella-Abate, C. De Pitta, E. Pinatel, M. B. Stadler, P. Provero, M. G. Bernengo, I. Osman, D. Taverna, microRNA-214 contributes to melanoma tumour progression through suppression of TFAP2C. *Embo Journal* **30**, 1990-2007 (2011).

141. L. M. Li, D. X. Hou, Y. L. Guo, J. W. Yang, Y. A. Liu, C. Y. Zhang, K. Zen, Role of MicroRNA-214-Targeting Phosphatase and Tensin Homolog in Advanced Glycation End Product-Induced Apoptosis Delay in Monocytes. *Journal of Immunology* **186**, 2552-2560 (2011).

142. L. S. Chan, P. Y. K. Yue, N. K. Mak, R. N. S. Wong, Role of MicroRNA-214 in ginsenoside-Rg1-induced angiogenesis. *European Journal of Pharmaceutical Sciences* **38**, 370-377 (2009).

143. N. Latif, P. Sarathchandra, A. H. Chester, M. H. Yacoub, Expression of smooth muscle cell markers and co-activators in calcified aortic valves. *European Heart Journal* **36**, 1335-1345 (2015).

144. S. Liebner, A. Cattelino, R. Gallini, N. Rudini, M. Iurlaro, S. Piccolo, E. Dejana, β-Catenin is required for endothelial-mesenchymal transformation during heart cushion development in the mouse. *The Journal of Cell Biology* **166**, 359-367 (2004).

145. J.-H. Chen, W. L. K. Chen, K. L. Sider, C. Y. Y. Yip, C. A. Simmons, β-Catenin Mediates Mechanically Regulated, Transforming Growth Factor-β1–Induced Myofibroblast Differentiation of Aortic Valve Interstitial Cells. *Arteriosclerosis, Thrombosis, and Vascular Biology* **31**, 590-597 (2011).

146. J. Richards, I. El-Hamamsy, S. Chen, Z. Sarang, P. Sarathchandra, M. H. Yacoub, A. H. Chester, J. T. Butcher, Side-Specific Endothelial-Dependent Regulation of Aortic Valve Calcification. *The American Journal of Pathology* **182**, 1922-1931.

147. J. Hagenbuchner, A. Kuznetsov, M. Hermann, B. Hausott, P. Obexer, M. J. Ausserlechner, FOXO3-induced reactive oxygen species are regulated by BCL2L11 (Bim) and SESN3. *Journal of Cell Science* **125**, 1191-1203 (2012).

148. A. Hamik, Z. Lin, A. Kumar, M. Balcells, S. Sinha, J. Katz, M. W. Feinberg, R. E. Gerszten, E. R. Edelman, M. K. Jain, Kruppel-like Factor 4 Regulates Endothelial Inflammation. *Journal of Biological Chemistry* **282**, 13769-13779 (2007).

149. S. Maleki, H. M. Björck, L. Folkersen, R. Nilsson, J. Renner, K. Caidahl, A. Franco-Cereceda, T. Länne, P. Eriksson, Identification of a novel flow-mediated gene expression signature in patients with bicuspid aortic valve. *Journal of Molecular Medicine (Berlin, Germany)* **91**, 129-139 (2013).

150. H. A. Eriksen, J. Satta, J. Risteli, M. Veijola, P. Väre, Y. Soini, Type I and type III collagen synthesis and composition in the valve matrix in aortic valve stenosis. *Atherosclerosis* **189**, 91-98.

151. B. Jian, N. Narula, Q.-y. Li, E. R. Mohler Iii, R. J. Levy, Progression of aortic valve stenosis: TGF-β1 is present in calcified aortic valve cusps and promotes aortic valve interstitial cell calcification via apoptosis. *The Annals of Thoracic Surgery* **75**, 457-465 (2003).

152. D. N. Ku, D. P. Giddens, C. K. Zarins, S. Glagov, Pulsatile flow and atherosclerosis in the human carotid bifurcation - Positive correlation between plaque location and low and oscillatory shear stress *Arteriosclerosis* **5**, 293-302 (1985).

153. M. Weston, A. Yoganathan, Biosynthetic Activity in Heart Valve Leaflets in Response to In Vitro Flow Environments. *Annals of Biomedical Engineering* **29**, 752-763 (2001).

154. Y. B. Lee, I. Bantounas, D. Y. Lee, L. Phylactou, M. A. Caldwell, J. B. Uney, Twist-1 regulates the miR-199a/214 cluster during development. *Nucleic acids research* **37**, 123-128 (2009).

155. G. J. Mahler, C. M. Frendl, Q. Cao, J. T. Butcher, Effects of shear stress pattern and magnitude on mesenchymal transformation and invasion of aortic valve endothelial cells. *Biotechnology and Bioengineering* **111**, 2326-2337 (2014).

156. C. Urbich, A. Kuehbacher, S. Dimmeler, *Role of microRNAs in vascular diseases, inflammation, and angiogenesis*. (2008), vol. 79, pp. 581-588.

157. S. Kumar, C. W. Kim, R. D. Simmons, H. Jo, Role of Flow-Sensitive microRNAs in Endothelial Dysfunction and Atherosclerosis: Mechanosensitive Athero-miRs. *Arteriosclerosis, Thrombosis, and Vascular Biology* **34**, 2206-2216 (2014).

158. B. Li, Q. Han, Y. Zhu, Y. Yu, J. Wang, X. Jiang, Down-regulation of miR-214 contributes to intrahepatic cholangiocarcinoma metastasis by targeting Twist. *FEBS Journal* **279**, 2393-2398 (2012).

159. S. Piera-Velazquez, Z. Li, S. A. Jimenez, Role of Endothelial-Mesenchymal Transition (EndoMT) in the Pathogenesis of Fibrotic Disorders. *The American Journal of Pathology* **179**, 1074-1080 (2011).

160. G. P. Sorescu, M. Sykes, D. Weiss, M. O. Platt, A. Saha, J. Hwang, N. Boyd, Y. C. Boo, J. D. Vega, W. R. Taylor, H. Jo, Bone Morphogenic Protein 4 Produced in Endothelial Cells by Oscillatory Shear Stress Stimulates an Inflammatory Response. *Journal of Biological Chemistry* **278**, 31128-31135 (2003).

161. L. Kim, D. K. Kim, W. I. Yang, D. H. Shin, I. M. Jung, H. K. Park, B. C. Chang, Overexpression of Transforming Growth Factor-β1 in the Valvular Fibrosis of Chronic Rheumatic Heart Disease. *Journal of Korean Medical Science* **23**, 41-48 (2008).

162. C. A. Schneider, W. S. Rasband, K. W. Eliceiri, NIH Image to ImageJ: 25 years of image analysis. *Nat Meth* **9**, 671-675 (2012).

163. C.-W. Ni, H. Qiu, A. Rezvan, K. Kwon, D. Nam, D. J. Son, J. E. Visvader, H. Jo, Discovery of novel mechanosensitive genes in vivo using mouse carotid artery endothelium exposed to disturbed flow. *Blood*, (2010).

164. P. F. Davies, M. Civelek, Y. Fang, I. Fleming, The atherosusceptible endothelium: endothelial phenotypes in complex haemodynamic shear stress regions in vivo. *Cardiovascular Research* **99**, 315-327 (2013).

165. X. Xiao, W. Tang, Q. Yuan, L. Peng, P. Yu, Epigenetic repression of Krüppel-like factor 4 through Dnmt1 contributes to EMT in renal fibrosis. *International Journal of Molecular Medicine* **35**, 1596-1602 (2015).

166. N. Tiwari, N. Meyer-Schaller, P. Arnold, H. Antoniadis, M. Pachkov, E. van Nimwegen, G. Christofori, Klf4 Is a Transcriptional Regulator of Genes Critical for EMT, Including Jnk1 (*Mapk8*). *PLoS ONE* **8**, e57329 (2013).

167. B. N. Davis-Dusenbery, M. C. Chan, K. E. Reno, A. S. Weisman, M. D. Layne, G. Lagna, A. Hata, Down-regulation of Krüppel-like Factor-4 (KLF4) by MicroRNA-143/145 Is Critical for Modulation of Vascular Smooth Muscle Cell Phenotype by Transforming Growth Factor-β and Bone Morphogenetic Protein 4. *Journal of Biological Chemistry* **286**, 28097-28110 (2011).

168. K. D. O'Brien, Pathogenesis of Calcific Aortic Valve Disease: A Disease Process Comes of Age (and a Good Deal More). *Arterioscler Thromb Vasc Biol* **26**, 1721-1728 (2006).

169. J. L. Meyer, Can biological calcification occur in the presence of pyrophosphate? *Archives of Biochemistry and Biophysics* **231**, 1-8 (1984).

170. K. A. Lomashvili, S. Cobbs, R. A. Hennigar, K. I. Hardcastle, W. C. O'Neill, Phosphate-Induced Vascular Calcification: Role of Pyrophosphate and Osteopontin. *Journal of the American Society of Nephrology* **15**, 1392-1401 (2004).

171. N. Côté, D. El Husseini, A. Pépin, S. Guauque-Olarte, V. Ducharme, P. Bouchard-Cannon, A. Audet, D. Fournier, N. Gaudreault, H. Derbali, M. D.

McKee, C. Simard, J.-P. Després, P. Pibarot, Y. Bossé, P. Mathieu, ATP acts as a survival signal and prevents the mineralization of aortic valve. *J. Mol. Cell. Cardiol.* **52**, 1191-1202 (2012).

172. D. Harmey, L. Hessle, S. Narisawa, K. A. Johnson, R. Terkeltaub, J. L. Millán, Concerted Regulation of Inorganic Pyrophosphate and Osteopontin by Akp2, Enpp1, and Ank: An Integrated Model of the Pathogenesis of Mineralization Disorders. *The American Journal of Pathology* **164**, 1199-1209 (2004).

173. K. Johnson, M. Polewski, D. van Etten, R. Terkeltaub, Chondrogenesis Mediated by PPi Depletion Promotes Spontaneous Aortic Calcification in NPP1 -/- Mice. *Arteriosclerosis, Thrombosis, and Vascular Biology* **25**, 686-691 (2005).

174. A. M. Ho, M. D. Johnson, D. M. Kingsley, Role of the Mouse ank Gene in Control of Tissue Calcification and Arthritis. *Science* **289**, 265-270 (2000).

175. M. Murshed, D. Harmey, J. L. Millán, M. D. McKee, G. Karsenty, Unique coexpression in osteoblasts of broadly expressed genes accounts for the spatial restriction of ECM mineralization to bone. *Genes & Development* **19**, 1093-1104 (2005).

176. K. A. Lomashvili, P. Garg, S. Narisawa, J. L. Millan, W. C. O'Neill, Upregulation of alkaline phosphatase and pyrophosphate hydrolysis: Potential mechanism for uremic vascular calcification. *Kidney Int* **73**, 1024-1030 (2008).

177. V. P. Persy, M. D. McKee, Prevention of vascular calcification: is pyrophosphate therapy a solution. *Kidney Int* **79**, 490-493 (2011).

178. R. Dahl, E. A. Sergienko, Y. Su, Y. S. Mostofi, L. Yang, A. M. Simao, S. Narisawa, B. Brown, A. Mangravita-Novo, M. Vicchiarelli, L. H. Smith, W. C. O,ÄôNeill, J. L. MillaÃÅn, N. D. P. Cosford, Discovery and Validation of a Series of Aryl Sulfonamides as Selective Inhibitors of Tissue-Nonspecific Alkaline Phosphatase (TNAP). *Journal of Medicinal Chemistry* **52**, 6919-6925 (2009).

179. W. C. O'Neill, M. K. Sigrist, C. W. McIntyre, Plasma pyrophosphate and vascular calcification in chronic kidney disease. *Nephrology Dialysis Transplantation* **25**, 187-191 (2010).

180. H. Fleisch, Bisphosphonates: Mechanisms of Action. *Endocrine Reviews* **19**, 80-100 (1998).

181. S. M. Joseph, M. A. Pifer, R. J. Przybylski, G. R. Dubyak, Methylene ATP analogs as modulators of extracellular ATP metabolism and accumulation. *British Journal of Pharmacology* **142**, 1002-1014 (2004).

182. K. A. Lomashvili, W. Khawandi, W. C. O'Neill, Reduced Plasma Pyrophosphate Levels in Hemodialysis Patients. *Journal of the American Society of Nephrology* **16**, 2495-2500 (2005).

183. L. Kyllonen, S. Haimi, B. Mannerstrom, H. Huhtala, K. Rajala, H. Skottman, G. Sandor, S. Miettinen, Effects of different serum conditions on osteogenic differentiation of human adipose stem cells in vitro. *Stem Cell Research & Therapy* **4**, 17 (2013).

184. J. Danziger, Vitamin K-dependent Proteins, Warfarin, and Vascular Calcification. *Clinical Journal of the American Society of Nephrology* **3**, 1504-1510 (2008).

185. C. Palaniswamy, A. Sekhri, W. S. Aronow, A. Kalra, S. J. Peterson, Association of Warfarin Use With Valvular and Vascular Calcification: A Review. *Clinical Cardiology* **34**, 74-81 (2011).

186. H. A. Fleisch, R. G. G. Russell, S. Bisaz, R. C. Mühlbauer, D. A. Williams, The Inhibitory Effect of Phosphonates on the Formation of Calcium Phosphate Crystals in vitro and on Aortic and Kidney Calcification in vivo. *European Journal of Clinical Investigation* **1**, 12-18 (1970).

187. K. A. Lomashvili, M.-F. Marie-Claude, W. Xiaonan, H. M. Hartmut, W. C. O'Neill, Effect of bisphosphonates on vascular calcification and bone metabolism in experimental renal failure. *Kidney International* **75**, 617-625 (2009).

188. F. Rutsch, S. Vaingankar, K. Johnson, I. Goldfine, B. Maddux, P. Schauerte, H. Kalhoff, K. Sano, W. A. Boisvert, A. Superti-Furga, R. Terkeltaub, PC-1 Nucleoside Triphosphate Pyrophosphohydrolase Deficiency in Idiopathic Infantile Arterial Calcification. *The American Journal of Pathology* **158**, 543-554 (2001).

189. N. Côté, D. El Husseini, A. Pépin, C. Bouvet, L.-A. Gilbert, A. Audet, D. Fournier, P. Pibarot, P. Moreau, P. Mathieu, Inhibition of ectonucleotidase with ARL67156 prevents the development of calcific aortic valve disease in warfarin-treated rats. *European Journal of Pharmacology* **689**, 139-146 (2012).

190. J. N. Clark-Greuel, J. M. Connolly, E. Sorichillo, N. R. Narula, H. S. Rapoport, E. R. Mohler III, J. H. Gorman III, R. C. Gorman, R. J. Levy, Transforming growth factor-beta1 mechanisms in aortic valve calcification: increased alkaline phosphatase and related events. *The Annals of Thoracic Surgery* **83**, 946-953 (2007).

191. L. Qian, L. W. Van Laake, Y. Huang, S. Liu, M. F. Wendland, D. Srivastava, miR-24 inhibits apoptosis and represses Bim in mouse cardiomyocytes. *The Journal of Experimental Medicine* **208**, 549-560 (2011).

192. L. Sun, J. Zhu, M. Wu, H. Sun, C. Zhou, L. Fu, C. Xu, C. Mei, Inhibition of MiR-199a-5p Reduced Cell Proliferation in Autosomal Dominant Polycystic Kidney Disease through Targeting CDKN1C. *Medical Science Monitor : International Medical Journal of Experimental and Clinical Research* **21**, 195-200 (2015).

193. H. G. Xu, C. J. Hu, H. Wang, P. Liu, X. M. Yang, Y. U. Zhang, L. T. Wang, Effects of mechanical strain on ANK, ENPP1 and TGF-β1 expression in rat endplate chondrocytes in vitro. *Molecular Medicine Reports* **4**, 831-835 (2011).